Universidade de Aveiro Departamento de Engenharia Cerâmica e do Vidro
2005

Harvey Amorín González

Preparação e propriedades de cristais e de cerâmicos de perovesquites ferroeléctricas com camadas de bismuto

Preparation and properties of ferroelectric single crystals and ceramics of bismuth layered perovskites

Universidade de Aveiro Departamento de Engenharia Cerâmica e do Vidro
2005

Harvey Amorín González

Preparação e propriedades de cristais e de cerâmicos de perovesquites ferroeléctricas com camadas de bismuto

Preparation and properties of ferroelectric single crystals and ceramics of bismuth layered perovskites

Dissertação apresentada à Universidade de Aveiro para cumprimento dos requisitos necessários à obtenção do grau de Doutor em Ciência e Engenharia de Materiais, realizada sob a orientação científica da Doutora Maria Elisabete J. V. Costa, Professora Auxiliar do Departamento de Engenharia Cerâmica e do Vidro da Universidade de Aveiro, e do Doutor Andrei L. Kholkin, Investigador principal da Universidade de Aveiro

Dissertation presented to de University of Aveiro to obtain the Doctor degree in Materials Science and Engineering, under the scientific guidance of Dr. Maria Elisabete J. V. Costa, Auxiliary Professor of the Department of Ceramics and Glass Engineering of the University of Aveiro, and Dr. Andrei L. Kholkin, Principal Researcher of the University of Aveiro

o júri

presidente

Prof. Dr. José Joaquim de Almeida Grácio
Professor Catedrático da Universidade de Aveiro

Prof. Dr. José Narciso Marat-Mendes
Professor Associado Aposentado da Universidade Nova de Lisboa

Prof. Dr. Igor P. Raevsky
Full Professor of the Rostov State University, Russia

Prof. Dr. Paula Maria Lousada Silveirinha Vilarinho
Professora Associada da Universidade de Aveiro

Prof. Dr. Senentxu Lanceros-Méndez
Professor Auxiliar da Universidade do Minho

Prof. Dr. Maria Elisabete Jorge Vieira Costa
Professora Auxiliar da Universidade de Aveiro

Prof. Dr. Andrei Leonidovitch Kholkine
Investigador Principal da Universidade de Aveiro

acknowledgments

It would not be fair to finish this thesis without mentioning all those people whose support has been very important during these years. Certainly, there are many to whom I must be grateful, and the doubt that somebody is forgotten in these few words is always present. That is why, in the first place, I want to send a message of general gratefulness to all those who surround me and in some way have contributed with this work, as well as with my scientific and human development.

First of all, I am deeply grateful to my supervisor Prof. Dr. Maria Elisabete J. V. Costa for her continuous support and encouragement, for her frequent suggestions and discussions in many subjects, especially in materials science, for her careful revision and criticism of the manuscript, and more importantly, for her confidence in me to perform this thesis with the necessary freedom. I am also very grateful to my co-supervisor Dr. Andrei L. Kholkin, for his scientific support and revision of the manuscript, cordial advice, and useful discussions in many subjects of this work.

I acknowledge the Portuguese Foundation for Science and Technology (FCT) for their financial support through a PhD grant (SFRH/BD/6619/2001), and also express my gratitude to the University of Aveiro for the facilities to carry out this work, and this opportunity to live in Portugal for four unforgettable years.

I would like to express my sincere gratitude to all my colleagues from the Department of Ceramics and Glass Engineering for their valuable help, empathy and friendship during all these years, from the administrative and technical staff to all the PhD and Postdoc students of the 3rd floor, as well as all the members of the Ferroelectric Group, for the excellent atmosphere of work and scientific interchange, in particular, to Prof. Dr. João L. Baptista for have brought me to this outstanding group, and also to Rosário, Vladimir, Nikolai, Igor and Rafael for the scientific collaboration.

I express my gratitude to Dr. Carlos Zaldo for his kindly invitation to perform piezoelectric measurements in the ICMM-CSIC in Madrid, and to Jose Manuel for his great help with these measurements and hospitality during my stay in Madrid. Moreover, I would like to thanks to Dr. Nicolay A. Pertsev, from the Ioffe Institute in St. Petersburg, for his useful remarks and suggestions in the discussion of ferroelectric domains, and also to Dr. Juanjo Manjarin, from the UAM in Madrid, for his valuable support in the theoretical approach.

I want to express my grateful thanks to my best friends in Aveiro, Javier, Gerardo, Cheo and David (almost Cuban) for their sincere friendship and our necessary “scientific meetings” in the *Praça do Peixe*. I am also fortunate for having many excellent friends during these years in Portugal, Rosalia, Merche, Laura, Claudia Miranda, Xana, Rogerio e Mariana, Kaka, Paula Valente and Rogerio, Chus and Glenn, Duncan, Flori… my sincere gratitude to all this international group for their friendship and for sharing many parties and meals, for the stress relief after a working day.

I am exceedingly grateful to all my family, the main source of love and support during all my life, the primary inspiration since my first day in this scientific life, which will be with me wherever I am. Special gratitude goes to my parents Gladys and Nelson, who knew it from the beginning, to my brother Harold, my other half, to my sister Claudia, who follows our steps, and to all my wonderful family…

I am also very grateful to my family-in-law for accepting me as a son. To my fathers-in-law: Adela and Santiago, for their continuous support and care, to my brothers-in-law, for every day…

Last but not least, the most special gratitude is for my wife Eva, who has become a special part of my life, who encourages me every day and trusts in me continually, who takes the main decisions at my side. Thank you Eva for your patience, your understanding in the most difficult moments, and your absolute support… in other words, thank you for loving me…

palavras-chave

cristais de $SrBi_2Ta_2O_9$ e de $SrBi_2Nb_2O_9$, cerâmicos texturizados, propriedades dieléctricas, ferroeléctricas, piezoeléctricas, domínios

resumo

Impulsionado pelo interesse em conhecer as propriedades intrínsecas dos compostos $SrBi_2Ta_2O_9$ (SBT) e $SrBi_2Nb_2O_9$ (SBN) que se apresentam como os materiais mais promissores para substituir o titanato de zircónio e de chumbo (PZT) nas memórias ferroeléctricas de acesso aleatório, surgiu a necessidade de monocristais destes compostos com dimensões e qualidade adequadas à medição de propriedades. No presente trabalho, fizeram-se crescer cristais simples de SBT e de SBN com qualidade e dimensões elevadas, usando um método de solução a alta temperatura, com um fluxo de Bi_2O_3 modificado com B_2O_3 e uma razão molar de 60/40 entre SBT (ou SBN) e fluxo (35 % em peso de Bi_2O_3 e 5 % em peso de B_2O_3). Primeiramente optimizaram-se as condições de processamento, testando-se diferentes perfis de temperatura para promover o crescimento e melhorar a qualidade dos cristais de SBT. As condições identificadas como óptimas foram usadas para fazer crescer cristais de SBN. Os cristais obtidos evidenciaram um hábito lamelar com morfologia de plaquetas com dimensões típicas de $\sim 7 \times 5 \times 0.2$ e $5 \times 5 \times 0.4$ mm^3 para SBT e SBN, respectivamente. De acordo com as análises de topografia e de difracção de raios-X, ambos os cristais se apresentaram naturalmente orientados com a direcção [001] (eixo *c*) perpendicular à face de maior área do cristal e lados paralelos à direcção [110] da fase ortorrômbica (inclinação de 45º relativamente a ambos os eixos *a* e *b*).

As primeiras medidas fiáveis sobre estrutura de domínios de cristais de SBT de boa qualidade foram realizadas no presente trabalho por microscopia de força piezoeléctrica. Ambos os domínios ferroeléctricos de 180º e ferroelásticos de 90º foram observados à temperatura ambiente após tratamento térmico dos cristais a 750 ºC, durante 10 horas. Os domínios apresentaram uma estrutura em "espinha" com paredes de domínios de 90º predominantemente planas. As paredes de domínios de 90º mostraram-se paralelas às arestas laterais do cristal [110], o que se coaduna com a orientação preferencial observada. A largura dos domínios de 90º situa-se entre 0,7 e 1,5 μm ao passo que a dos domínios de 180º varia entre 250 e 500 nm. A formação deste complexo padrão de domínios é atribuída a um processo de transição de fases em duas etapas, ou seja, a ocorrência não simultânea das transições de fase ferroelástica e ferroelétrica em SBT.

A qualidade dos cristais de SBT e SBN foi também confirmada por medidas diélectricas, ferroelétricas e piezoeléctricas realizadas paralelamente ao eixo *c* (direcção [001]) e paralelamente ao plano *ab* (segundo a direcção [110]) demonstrando-se a elevada anisotropia das propriedades intrínsecas de ambos os cristais, *i.e.*, a razão entre o valor médio de permitividade dieléctrica medida paralelamente ao plano *ab* e o valor medido paralelamente ao eixo *c* foi de cerca de 10 à temperatura de Curie, T_C, diminuindo para 2 à temperatura ambiente. As baixas perdas dieléctricas acima e abaixo de T_C ($\tan\delta < 0.04$) indicaram uma baixa concentração de defeitos nos cristais.

Observaram-se ciclos de histerese saturados quando se aplicou um campo eléctrico alterno paralelamente ao plano ab do cristal SBT. A polarização espontânea segundo o eixo ferroeléctrico a foi estimada em cerca de $\approx 20\ \mu C/cm^2$ para o SBT. Porém, no caso dos cristais de SBN, não foi possível obter ciclos de histerese saturados mesmo aplicando um campo eléctrico com o valor máximo de 100 kV/cm. O coeficiente piezoeléctrico d_{33} medido segundo a direcção [100] (eixo polar) é de $\approx$ 30 e de 62 pm/V para o SBT e o SBN, respectivamente.

Os materiais ferroeléctricos com estrutura em camadas de bismuto (compostos BLSF) apresentam grande interesse para aplicações piezoeléctricas de elevada temperatura embora seja necessário prepará-los na forma texturizada devido à sua elevada anisotropia. O presente trabalho estuda a possibilidade de usar os cristais de SBT como sementes para induzir a texturização de cerâmicos de SBT pela via de template grain growth (TGG). Produziram-se cerâmicos de SBT texturizados com propriedades dieléctricas e ferroeléctricas melhoradas, usando sementes anisométricas e de morfologia lamelar, com tamanho médio de $\sim 40 \times 40 \times 8\ \mu m^3$. Dispersou-se uma pequena quantidade de sementes anisométricas de SBT numa matrix de partículas finas de SBT contendo um excesso de Bi_2O_3 para formar fase líquida e alinharam-se essas sementes por prensagem unidireccional. Avaliaram-se os efeitos de vários parâmetros de processamento tais como o excesso de Bi_2O_3, as sementes de SBT, as condições de prensagem e de sinterização, tentando obter-se cerâmicos densos, com elevada textura e propriedades melhoradas. Correlacionou-se a evolução da microestructura dos cerâmicos com as condições de processamento recorrendo a uma análise estereológica.

Demonstrou-se a existência de anisotropia nas propriedades dieléctricas e no ciclo de histerese e a sua dependência do grau de textura. Mediram-se propriedades dieléctricas e ferroeléctricas melhoradas segunda uma direcção perpendicular à da prensagem unidirecional, observando-se valores de permitividade e de polarização acima dos apresentados pelos cerâmicos sem sementes. Mostrou-se que esta melhoria de propriedades resultou da orientação do grão, da anisotropia de propriedades dos monocristais e do grau de textura dos cerâmicos. Apresentou-se um modelo para descrever a polarização espontânea máxima de cerâmicos de SBT com orientação de grão aleatória ou com textura, em função do grau de textura, usando uma análise de textura baseada na distribuição da orientação dos grãos grandes e anisométricos. Seleccionou-se a equação de March-Dollase para descrever os dados experimentais referentes à distribuição de orientação e discutiu-se a distribuição espacial do vector polarização em grãos lamelares de materiais BLSF. A aplicação do referido modelo aos cerâmicos texturizados de SBT permitiu a comparação dos valores de polarização espontânea previstos pelo modelo com os valores experimentais obtidos a partir do ciclo de histerese ferroeléctrica dos mesmos cerâmicos.

keywords

$SrBi_2Ta_2O_9$ and $SrBi_2Nb_2O_9$, single crystals, textured ceramics, templated grain growth, dielectric, ferroelectric, piezoelectric properties, domains

abstract

The interest in the understanding of the intrinsic properties of $SrBi_2Ta_2O_9$ (SBT) and $SrBi_2Nb_2O_9$ (SBN), which are the most promising materials for substituting lead zirconate titanate in non-volatile ferroelectric random access memories, arouse the need of single crystals of these compounds with suitable size and quality for the properties measurement. In this work, high-quality SBT and SBN single crystals were successfully grown by a high-temperature self-flux solution method, using a B_2O_3 modified Bi_2O_3 flux and a molar ratio of 60/40 of SBT (or SBN) powder to flux (35 wt% Bi_2O_3 and 5 wt% B_2O_3). The processing conditions were optimized by testing different thermal profiles to increase the size and improve the quality of the grown SBT crystals. The optimized conditions were then applied for the growth of SBN crystals. The grown crystals showed a layered habit with a platelet morphology and typical sizes of ~ 7 × 5 × 0.2 and 5 × 5 × 0.4 mm^3 for SBT and SBN, respectively. According to x-ray diffraction and topography analyses, both crystals were naturally oriented with [001] direction (*c*-axis) perpendicular to the major face and edges parallel to [110] direction (45º to both *a*- and *b*-axes) of the orthorhombic phase.

The first reliable measurements of the domain structure of high-quality SBT single crystals were performed in this work by piezoelectric force microscopy. Both ferroelectric 180º domains and ferroelastic 90º domains (twins) were revealed at room temperature after annealing the crystals at 750 ºC for 10 h. The coexisting domains form a well-defined “herringbone” structure with mostly flat 90º walls. The ferroelastic 90º walls were parallel to the single crystal edges [110], which agree with the observed preferential orientation. The width of 90º domains (twins) lies in the range of 0.7 - 1.5 μm, while that of 180º domains, which were oriented parallel to the [100] direction (polar axis), exhibited a periodicity of about 250 to 500 nm. Formation of the observed complex domain pattern was attributed to a two-stage process associated with the presence of separate ferroelastic and ferroelectric phase transitions in SBT.

The high quality of the grown SBT and SBN single crystals was confirmed by dielectric, ferroelectric and piezoelectric measurements, which were performed in the *ab*-plane (along the [110] direction) and along the *c*-axis (the [001] direction), demonstrating the large anisotropy in the intrinsic properties of both crystals, *i.e.*, the ratio between average permittivity along the [110] (*ab*-plane) and the [001] direction (*c*-axis) was about 10 at T_C and decreased to ~ 2 at room temperature. The low dielectric losses above and below T_C ($\tan\delta < 0.04$) indicate a low concentration of defects in the crystals.

Saturated hysteresis loops were observed for switching in the *ab*-plane of the SBT single crystal and the spontaneous polarization along the ferroelectric *a*-axis was estimated to be $P_S \approx 20\ \mu C/cm^2$ for SBT. However, for SBN crystals, saturated hysteresis loops were not obtained for a maximum electric field of 100 kV/cm. The longitudinal piezoelectric coefficient d_{33} was measured along the [100] direction (polar-axis) in both crystals, and was estimated as ≈ 30 and 62 pm/V for SBT and SBN, respectively.

Bi-layer structured ferroelectric (BLSF) materials like SBT present significant interest for high-temperature piezoelectric applications, though they are required to be prepared in a textured form due to their high anisotropy. This work studies the possibility of using the grown SBT crystals as seeds for the fabrication of textured SBT ceramics by templated grain growth (TGG). Seeded SBT ceramics with improved dielectric and ferroelectric properties were produced by using plate-like anisometric SBT templates with average sizes of ~ $40 \times 40 \times 8\ \mu m^3$. A small amount of the anisometric SBT templates was distributed in a fine-grained matrix of SBT powder containing Bi_2O_3 excess as liquid phase, and then aligned by conventional uniaxial pressing. Several processing parameters, *e.g.*, the Bi_2O_3 excess, the amount of templates, or the processing and sintering conditions including the uniaxial pressure, the sintering temperature and time, were examined in order to produce textured SBT ceramics with enhanced properties. The ceramics microstructure evolution was correlated with the processing parameters via a stereological analysis.

Anisotropy in the dielectric and ferroelectric properties of the seeded SBT specimens and its dependence on the degree of texture were demonstrated. Enhanced properties were measured perpendicularly to the uniaxial pressing direction revealing permittivity and polarization values above those of unseeded SBT ceramics. Such improved properties were shown to result from the grain orientation, anisotropy of single crystal properties, and degree of texture of the sintered ceramics. A quantitative model was presented for predicting the maximum spontaneous polarization, P_S, of randomly oriented and textured SBT ceramics as a function of the degree of texture, using a texture analysis accomplished via the orientation distribution of large anisometric grains. The March-Dollase equation was selected to fit the measured orientation distribution, and the spatial distribution of polarization vector in platelet grains of BLSF materials was discussed. The results were applied to the case of textured SBT ceramics, and the predicted P_S values as a function of the degree of texture were compared with those measured from the hysteresis loops.

A mi esposa Eva

A mis padres,
Gladys y Nelson

A mi hermano Harold

TABLE OF CONTENTS

5. GENERAL CONCLUSIONS AND FUTURE WORK

CHAPTER 1

CHAPTER 2

CHAPTER 3

CHAPTER 4

CHAPTER 1

CHAPTER 3

CHAPTER 4

D_i	Electric Displacement
E_j	Electric Field
ε_{ij}	Dielectric Permittivity
$\varepsilon_{r\,ij}$	Relative Dielectric Permittivity
ε_o	Dielectric Permittivity of the Vacuum (8.85×10^{-12} F/m)
P_i	Polarization Vector
$\tan\delta$	Dielectric Loss
ε''	Imaginary Part of the Permittivity
ε'	Real Part of the Permittivity
T_{jk}	Applied Stress
d_{ijk} (= d_{kij})	Piezoelectric Coefficients
S_{ij}	Strain
a, b, c	Unit Cell Parameters
T_C	Curie Temperature
T_{CW}	Curie-Weiss Temperature
P_S	Spontaneous Polarization
P_r	Remanent Polarization
E_d	Depolarizing Field
E_C	Coercive Field
T_{CW}	Curie-Weiss Temperature
G	Gibbs free energy
T_m	Transition Temperature
W_{dw}	Domain Wall Energy

W_e	Elastic Energy
α	Tilt Angle from the *c*-axis of the BO_6 Octahedra in SBT
α_x	Rotation Angle in the *ac*-plane of the BO_6 Octahedra in SBT
α_y	Rotation Angle in the *bc*-plane of the BO_6 Octahedra in SBT
m_i	Site Multiplicity
Δx_i	Atomic Displacement along the *a*-axis in SBT
Q_i	Ionic Charge
V	Volume of the Unit Cell
t	Tolerance Factor
T_1	Liquidus Temperature
T_n	Temperature of Spontaneous–Three-Dimensional–Nucleation
Q_m	Mechanical Quality Factor
k_{ij}	Electromechanical Coupling Coefficient
λ	Wavelength
hkl	Miller Indexes
d_{hkl}	Spacing between Atomic Planes
θ_{hkl}	Bragg Angle
C_p	Capacitance of a Parallel Plane Capacitor
R	Parallel Resistance
ω	Frequency
C_o	Linear Capacitor (~ 1 μF)
C_x	Ferroelectric Material Capacitor
V_Y	Voltage Across the Linear Capacitor C_O
A	Area of the Electrodes
E_P	Poling Electric Field

V_{ac}	*ac* Voltage
E_{ac}	*ac* Electric Field
f	Lotgering Factor
$I_{(hkl)}$	XRD Peak Intensities of all the (*hkl*) Plane Reflections
$P_{(00l)}$	Percentage of (00*l*) Orientation in the XRD Pattern
P_o	$P_{(00l)}$ for the Randomly Oriented Powder
β	Azimuthal Angle for Axisymmetric Texture
ω	Platelet Orientation Angle
f_v	Volume Fraction
F_{Max}	Major Feret Lengths
F_{Min}	Minor Feret Lengths
r	Texture Factor
S_o	Spontaneous Strain
Q	Structural Order Parameter
d^*	Equilibrium Domain Width
γ_{90}	Energy per Unit Area of the 90º Domain Wall
G	Effective Shear Modulus of the Crystal
Q_o	Structural Order Parameter in the Equilibrium
m	Number of BO_6 Octahedral Layers in BLSF Materials
P_S^a	Spontaneous Polarization along Polar *a*-axis
ρ_r	Relative Density
ρ	Density
ρ_{Th}	Theoretical Density of SBT (8.78 g/cm^3)
L	Length of the Large Anisometric Grains
T	Thickness of the Large Anisometric Grains

N	Number of Templates in 1 cm^3
V_T	Average Volume of a Single Template Particle
R_t	Average Template Radii at Time t
R_o	Average Template Radii at Time Zero
K_m	Growth Kinetic Constant
t_s	Sintering Time
K_m^L	Length Growth Kinetic Constant
F	Probability Distribution Function
F^N	Normalized Probability Distribution Function
E_m	Maximum Applied Electric Field
ε^E	Permittivity for High Electric Fields
P_o	Spontaneous Polarization of the Single Crystal
θ	Angle between the Major Face of the Platelet Grain and the Electric Field Direction
φ	Angle between P_o and the Projection of the Applied Electric Field (z-axis) in the Major Face Plane of the Platelet Grain
Φ	Upper Limit of the Integration for the φ Angle
P^{Theor}	Maximum Expected Polarization
$\langle P \rangle_{random}$	Predicted Polarization for Randomly Oriented Materials
$\langle P \rangle_{fully\ textured}$	Predicted Polarization for Fully Textured Materials

FeRAMs	Ferroelectric Random Access Memories
PZT	Lead Zirconate Titanate
BLSF	Bi-Layer Structured Ferroelectrics
dc	Direct Current
ac	Alternating Current
SBT	$SrBi_2Ta_2O_9$
SBN	$SrBi_2Nb_2O_9$
XRD	X-Ray Diffraction
PFM	Piezoelectric Force Microscopy
PZN-PT	$Pb(Zn_{1/3}Nb_{2/3})O_3$-$PbTiO_3$
NBT-BT	$Na_{1/2}Bi_{1/2}TiO_3$-$BaTiO_3$
TGG	Templated Grain Growth
P-E	Polarization-Electric Field
S-E	Strain-Electric Field
KDP	Potassium Dihydrogen Phosphate
MPB	Morphotropic Phase Boundary
GASH	Guanidine Aluminum Sulphate Hexahydrate
HTS	High-Temperature Solution
RTGG	Reactive Templated Grain Growth
TD	Theoretical Density
EEPROM	Electrically Erasable Programmable Read-Only Memory
SRAM	Static Random Access Memory
IC	Integrated Circuit

CMOS	Complementary Metal Oxide Semiconductor
BLT	$(Bi,La)_4Ti_3O_{12}$
WEEE	Waste from Electrical and Electronic Equipment
RoHS	Restriction of Hazardous Substances
ELV	End-of-Life Vehicles
TP	Thermal Profile
SBT5T	$SrBi_2Ta_2O_9$ with 5 wt% templates
SBT3Bi	$SrBi_2Ta_2O_9$ with 3 wt% Bi_2O_3 excess
SBT3Bi5T	$SrBi_2Ta_2O_9$ with 3 wt% Bi_2O_3 excess and 5 wt% templates
WSR	Wide Scanning Range
SFM	Scanning Force Microscopy
RD	Rolling Direction
TD	Transverse Direction
MRD	Multiple of a Random Distribution
SEM	Scanning Electron Microscopy
//P	Cross-Sections Parallel to the Pressing Direction
⊥P	Cross-Sections Perpendicular to the Pressing Direction
FWHM	Full Width at the Half-Maximum
ODF	Orientation Distribution Function
E//P	Electric Field Parallel to the Pressing Direction
E⊥P	Electric Field Perpendicular to the Pressing Direction
AR	Aspect Ratio
RT	Room Temperature
DWS	Domain Wall Switching
MD	March-Dollase

Introduction

Nowadays, the terms *smart materials* and *functional materials* have become common within the materials science and engineering community. Smart materials are those materials which undergo transformations (*e.g.*, changes in the shape, size, etc.) throughout physical interactions, sensing a change in its environment and adapting to correct such change through the use of a feedback system, whereas functional materials cover a broader range of materials whose physical and chemical properties are sensitive to changes in the environment, such as temperature, pressure, electric field, magnetic field, etc., having the ability of performing a certain "function" under a determined stimulus.[1] Ferroelectric and piezoelectric materials are examples of functional materials whose sensing and actuating capabilities account for a large number of applications that span most industrial sectors.[2]

Ferroelectric materials can be used as bulk ceramics or films depending on the relative ease with which they can be adapted to the requirement of the application, thus making reliable devices.[3] Although there always will be a large demand for bulk devices, mainly in piezoelectric and electrostrictive applications, there is also an increasing trend today for the device miniaturization, which is accompanied by a growing demand of functional thick and thin film devices.

Ferroelectric thin film capacitors have been combined with Si integrated circuits to provide, probably, the most important application of ferroelectric thin films: non-volatile *ferroelectric random access memories* (FeRAMs), which are currently being considered as a strong alternative to other types of memories, *e.g.*, non-volatile semiconductor *Flash* memory. The most popular ferroelectric material and primary candidate for non-volatile FeRAMs is *lead zirconate titanate* (PZT), which has been investigated for that purpose since the middle 80s.[4] However, besides lead toxicity issues, PZT memories with platinum (Pt) electrodes suffer from aging, retention, imprint and, most importantly, fatigue, which makes the switchable polarization to decline after ~ 10^8 read/write cycles.[5]

The interest in *Bi-layer structured ferroelectrics* (BLSF) for substituting PZT in non-volatile FeRAMs appeared in the middle 90s, when it was understood that, along with the high switching polarization, low *dc* leakage currents, and sufficiently low coercive field, some BLSF materials, namely $SrBi_2Ta_2O_9$ (SBT) and $SrBi_2Nb_2O_9$ (SBN), are immune to

ferroelectric fatigue on Pt electrodes (at least up to 10^{12} cycles at saturation).[6-8] Since then, a large amount of work has been focused on thin films, where dramatic improvement of the ferroelectric properties has been achieved using modern deposition techniques. However, these achievements have not been followed by the corresponding understanding of the fundamental properties of these compounds that are obviously obscured by the texture, insufficient quality, polycrystallinity and interface problems of the investigated films.[9]

For thin film technology, the knowledge of the *single crystal* fundamental properties, such as the high dielectric, ferroelectric and piezoelectric anisotropy, is prerequisite for the understanding of the distinct effects observed to date. Besides, from the fundamental science point of view, single crystal data are also required for the thermodynamic analysis of the phase transitions in these technologically important materials, where many important physical, chemical and structural properties remain to be further investigated.

In the end of the 60s, Cummins and Cross could demonstrate for the first time highly anisotropic optical and electrical properties in one of the most popular BLSF compositions, $Bi_4Ti_3O_{12}$.[10] In the last decade, Miyayama *et al*. have renewed the interest for the growth and characterization of BLSF materials in a single crystal form with the ultimate goal of comparing their properties with those of polycrystalline materials of identical composition, and studied the anisotropy of the ferroelectric and dielectric properties.[11-15] To perform such measurements, large single crystals of sufficiently high quality should be grown with a single domain state or at least a controlled domain configuration.

Although SBT has been a key material for FeRAMs,[16] a detailed study of its intrinsic ferroelectricity, dielectric anisotropy, domain structure and phase transitions has not been achieved in single crystal form, due mainly to the low quality of the SBT crystals obtained so far.[17-19] Only recently, Sih *et al*. have successfully grown large SBT crystals using the *high-temperature self-flux solution* method using a B_2O_3 modified Bi_2O_3 flux, but the dielectric and ferroelectric properties could not be successfully measured.[20] On the other hand, to the best of our knowledge, the SBN intrinsic properties have not been reported yet in the scientific literature, due also to the lack of SBN single crystals, contrary to SBT and SBN ceramics and thin films which have been extensively studied for a long time.

In addition, to improve the thin films functionality and accelerate SBT-FeRAMs device development, a detailed investigation of the domain configuration in single crystals is desirable. Several papers on the presence of domains in SBT thin films and ceramics have been published, but the direct observation of domains in single-crystalline SBT has been studied only by optical and transmission electron microscopy.[21,22]

Therefore, the first general objective of the present work is to study the optimization of the processing conditions for growing large and high-quality $SrBi_2Ta_2O_9$ and $SrBi_2Nb_2O_9$ single crystals via high-temperature self-flux solution method.

For this purpose some specific goals will be pursued:

- To study the effects of the processing parameters on the morphology and quality of the SBT and SBN grown crystals and to evaluate the crystallographic quality via the x-ray diffraction (XRD) and x-ray topography analyses.

- To investigate the domain configuration of the high-quality SBT single crystals using XRD and piezoelectric force microscopy (PFM) studies.

- To investigate the anisotropy in the dielectric, ferroelectric and piezoelectric properties of the high-quality SBT and SBN single crystals, and to correlate them with the crystallographic orientations.

On the other hand, in response to the improved piezoelectric properties reported for several relaxor-based ferroelectric single crystals, especially in perovskite systems such as: $Pb(Zn_{1/3}Nb_{2/3})O_3$-$PbTiO_3$ (PZN-PT)[23] or lead free $Na_{1/2}Bi_{1/2}TiO_3$-$BaTiO_3$ (NBT-BT),[24] several research groups in this area are attempting to lower the costs of growing such single crystals by flux techniques. Actually, the piezoelectric and electromechanical coupling coefficients of these crystals are significantly greater than those of randomly oriented ceramics. However, these routes of crystal growth require a long period of time at high temperature and a careful control of the growth process, thus the cost of ferroelectric single crystals for piezoelectric applications remains high and the geometries that can be achieved are limited.

The development of texture in ferroelectric ceramics is an alternative strategy for increasing the piezoelectric response of these materials due to the inherent anisotropy in the material properties. Such approach has allowed achieving properties lying between those of single crystals and those of randomly oriented ceramics. The intensity of the enhanced response depends on the material crystallographic orientation, and thus can not be fully exploited in randomly oriented polycrystalline materials. Consequently, textured ceramics of piezoelectric materials are being considered of a special scientific and commercial interest.[25]

Following the current trend of developing lead-free piezoelectric components, BLSF materials have also emerged as promising candidates for high-temperature piezoelectric applications due mainly to its high Curie temperatures.[26] However, it is difficult to achieve high piezoelectric response in randomly oriented BLSF polycrystalline materials because of the two-dimensional character of the ferroelectric switching. Therefore, the study of textured BLSF ceramics is of fundamental importance for tailoring their piezoelectric, ferroelectric and dielectric properties, thus improving the sensing and actuating capabilities of various devices.

One of the promising routes for the controlled texture development is the *templated grain growth* (TGG).[27] Briefly, this process consists of the ceramic sintering mediated by a small amount of well-oriented anisometric template particles distributed in a fine-grained matrix. The template particles grow at the expense of the fine randomly oriented powder ensuring a large volume fraction of highly oriented grains. Being based on a standard powder processing and sintering, TGG achieves texture at a significantly lower cost as compared to other techniques used for texturing like hot forging or hot pressing.

Highly textured ferroelectric ceramics, including some BLSFs such as $Bi_4Ti_3O_{12}$,[28] have been fabricated by TGG with piezoelectric properties similar to those of single crystals in the texture direction.[27] An obstacle to the low-cost processing of TGG-derived materials is the difficulty of producing large amounts of template particles with controlled particle size and aspect ratio, *e.g.*, the anisotropic seeds that control texture development. Because of the complexity of SBT single crystal synthesis, to the best of our knowledge, this technique has not been used for SBT so far.

Therefore, the second general objective of the present work is to study the production of textured $SrBi_2Ta_2O_9$ ceramics with improved performances by TGG using anisometric SBT template particles (the grown SBT single crystals previously referred). Some specific goals included in this study are:

- To study the effects of the initial processing parameters (*e.g.*, Bi_2O_3 excess, amount of templates, uniaxial pressure and sintering conditions) on the microstructure evolution and texture development.

- To study and evaluate the effects of the degree of texture on the anisotropy of the dielectric and ferroelectric properties.

- To model the spatial distribution of the polarization in BLSF materials and to predict the theoretical spontaneous polarization of randomly oriented and partially textured SBT ceramics as a function of the degree of texture.

The present thesis is organized in four chapters. Chapter 1 is dedicated to literature revision aiming at to update the reader with the state of the art regarding the following issues: the fundaments of the ferroelectric and piezoelectric phenomena, description of the BLSF materials, especially SBT and SBN, methods for growing single crystals (high-temperature self-flux solution method) and processing textured ceramics (templated grain growth), and finally the advantages, disadvantages and current functionality of BLSF materials on memory and piezoelectric applications.

In Chapter 2, the experimental procedures used for growing SBT and SBN single crystals, for processing SBT textured ceramics, and for characterizing the single crystals and the textured ceramics are detailed.

The obtained results are presented, analyzed and discussed in the next two chapters. In Chapter 3, the results regarding the study of the processing conditions for growing large and high-quality SBT single crystals and their application to the growth of SBN single crystals are discussed. In both cases, the crystal morphology is analyzed based on their crystalline structure. Structural, dielectric, ferroelectric and piezoelectric characterization data are used to describe the intrinsic anisotropy of both SBT and SBN single crystals.

Chapter 4 discusses the effects of the processing parameters on the microstructure and degree of texture of both seeded and unseeded SBT ceramics. The microstructure evolution is analyzed and correlated with the processing parameters via a stereological analysis. The anisotropy of the dielectric and ferroelectric behaviors of the textured samples and its dependence on the degree of texture is demonstrated. Finally, a quantitative model relying on the texture analysis is put forward for predicting the spontaneous polarization of SBT ceramics as a function of the degree of texture.

The last chapter of this thesis is used for presenting the general conclusions of the present work and to outline some future work for complementing it.

References

[1] Z. L. Wang and Z. C. Kang, "Functional and Smart Materials: Structural Evolution and Structure Analysis". Plenum Publ. Corp., New York (1998).

[2] P. M. Vilarinho, "Functional Materials: Properties, Processing and Applications", in *Scanning Probe Microscopy: Characterization, Nanofabrication and Device Application of Functional Materials*. Kluwer Academic Publ., *NATO Sci. Series II.* **186** (2005) 3-33.

[3] G. H. Haertling, "Ferroelectric Ceramics: History and Technology". *J. Am. Ceram. Soc.* **82** [4] (1999) 797-818.

[4] J. F. Scott and C. A. Paz de Araujo, "Ferroelectric Memories". *Science* **246** (1989) 1400-1405.

[5] O. Auciello, J. F. Scott and R. Ramesh, "The Physics of Ferroelectric Memories". *Phys. Today* **51** [7] (1998) 22-27.

[6] K. Amanuma, T. Hase and Y. Miyasaka, "Preparation and Ferroelectric properties of $SrBi_2Ta_2O_9$ Thin-Films". *Appl. Phys. Lett.* **66** [2] (1995) 221-223.

[7] R. Dat, J. K. Lee, O. Auciello, A. I. Kingon, "Pulsed-Laser Ablation Synthesis and Characterization of Layered $Pt/SrBi_2Ta_2O_9/Pt$ Ferroelectric Capacitors with Practically no Polarization Fatigue". *Appl. Phys. Lett.* **67** [4] (1995) 572-574.

[8] C. A. Paz de Araujo, J. D. Cuchiaro, L. D. McMillan, M. C. Scott, J. F. Scott, "Fatigue-Free Ferroelectric Capacitors with Platinum-Electrodes". *Nature* **374** (1995) 627-629.

[9] J. F. Scott, "Ferroelectric Random Access Memories - Fundamental and Applications - Overview". *Topics Appl. Phys.* **93** (2004) 3-17.

[10] S. E. Cummins and L. E. Cross, "Electrical and Optical Properties of Ferroelectric $Bi_4Ti_3O_{12}$ Single Crystals". *J. Appl. Phys.* **39** [5] (1968) 2268-2273.

[11] S. K. Kim, M. Miyayama and H. Yanagida, "Electrical Anisotropy of $BaBi_4Ti_4O_{15}$ Single-Crystal". *J. Ceram. Soc. Jpn.* **102** [8] (1994) 722-726.

[12] M. Miyayama and I.-S. Yi, "Electrical Anisotropy in Single Crystals of Bi-Layer Structured Ferroelectrics". *Ceram. Int.* **26** [5] (2000) 529-533.

[13] H. Irie, M. Miyayama and T. Kudo, "Structure Dependence of Ferroelectric Properties of Bismuth Layer-Structured Ferroelectric Single Crystals". *J. Appl. Phys.* **90** [8] (2001) 4089-4094.

[14] H. Irie and M. Miyayama, "Dielectric and Ferroelectric Properties of $SrBi_4Ti_4O_{15}$ Single Crystals". *Appl. Phys. Lett.* **79** [2] (2001) 251-253.

[15] T. Kobayashi, Y. Noguchi and M. Miyayama, "Enhanced Spontaneous Polarization in Superlattice - Structured $Bi_4Ti_3O_{12}$ - $BaBi_4Ti_4O_{15}$ Single Crystals". *Appl. Phys. Lett.* **86** [1] (2005) 012907.

[16] J. F. Scott, F. M. Ross, C. A. Paz de Araujo, M. C. Scott and M. Huffman, "Structure and Device Characteristic of $SrBi_2Ta_2O_9$-Based Nonvolatile Random-Access Memories". *Mater. Res. Soc. Bull.* **21** [7] (1996) 33-39.

[17] M. Suzuki, N. Nagasawa, A. Machida and T. Ami, "Preparation of Layered Ferroelectric $Bi_2SrTa_2O_9$ Single-Crystal Platelets". *Jpn. J. Appl. Phys.* **35** [5A] (1996) L564-L567.

[18] A. Machida, N. Nagasawa, T. Ami and M Suzuki, "Ferroelectricity of $Bi_2SrTa_2O_9$ Single Crystals Grown by the Self-Flux method". *Jpn. J. Appl. Phys.* **36** [12A] (1997) 7267-7271.

[19] A. Machida, N. Nagasawa, T. Ami and M Suzuki, "Domain Motion of ferroelectricity of $Bi_2SrTa_2O_9$ Single Crystals Under an *ac*-Voltage Electric Field". *Jpn. J. Appl. Phys.* **37** [2A] (1999) 795-799.

[20] B. Sih, J. Tang, M. Dong and Z.-G. Ye, "Ferroelectric $SrBi_2Ta_2O_9$ Single-Crystal Growth and Characterization". *J. Mater. Res.* **16** [6] (2001) 1726-1733.

[21] X. H. Zhu, J. M. Zhu, S. H. Zhou, Q. Li, Z. G. Liu and N. B. Ming, "Domain Structures and Planar Defects in $SrBi_2Ta_2O_9$ Single Crystals Observed by Transmission Electron Microscopy". *Appl. Phys. Lett.* **78** [6] (2001) 799-801.

[22] S. Kamba, J. Pokorny, V. Porokhonsky, J. Petzelt, M. P. Moret, A. Garg, Z. H. Barber and R. Zallen, "Ferroelastic Phase in $SrBi_2Ta_2O_9$ and Study of the Ferroelectric Phase-Transition Dynamics". *Appl. Phys. Lett.* **81** [6] (2002) 1056-1058.

[23] S. E. Park and T. R. Shrout, "Ultrahigh Strain and Piezoelectric Behavior in Relaxor Based Ferroelectric Single Crystals". *J. Appl. Phys.* **82** [4] (1997) 1804-1811.

[24] Y. M. Chiang, G. W. Farrey and A. N. Soukhojak, "Lead-Free High-Strain Single-Crystal Piezoelectrics in the Alkaline-Bismuth-Titanate Perovskite Family". *Appl. Phys. Lett.* **73** [25] (1998) 3683-3685.

[25] S. Trolier-McKinstry, E. M. Sabolsky, S. Kwon, J. H. Yoshimura, J. H. Park, G. Zhang and G. L. Messing, "Oriented Films and Ceramics of Relaxor-Ferroelectric-$PbTiO_3$ Solid Solutions", in *Piezoelectric Materials in Devices*. Ed. N. Setter, Publ. Ceramics Laboratory, EPFL, Lausanne, Switzerland (2002) 497-518.

[26] D. Damjanovic, "Materials for High Temperature Piezoelectric Transducers". *Current Opinion in Sol. State Mater. Sci.* **3** [5] (1998) 469-473.

[27] G. L. Messing, S. Trolier-McKinstry, E. M. Sabolsky, C. Duran, S. Kwon, B. Brahmaroutu, P. Park, H. Yilmaz, P. W. Rehrig, K. B. Eitel, E. Suvaci, M. M. Seabaugh and K. S. Oh, "Templated Grain Growth of Textured Piezoelectric Ceramics". *Crit. Rev. Solid State Mater. Sci.* **29** [2] (2004) 45-96.

[28] J. A. Horn, S. C. Zhang, U. Selvaraj, G. L. Messing and S. Trolier-McKinstry, "Templated Grain Growth of Textured Bismuth Titanate". *J. Am. Ceram. Soc.* **82** [4] (1999) 921-926.

Chapter 1

Background on Ferroelectric Materials and Applications

1.1. Introduction

It is the purpose of this chapter to provide a brief description of the ferroelectric and piezoelectric phenomena in ferroelectrics and related materials for electronic and memory applications. Firstly, the fundamental issues associated with the ferroelectric phenomena such as phase transitions, appearance of domains and switching of polarization vector will be outlined, followed by a brief description of the basic physical properties and structures of common ferroelectric materials with special attention to the Aurivillius family.

Single crystals of ferroelectric materials are being received a great attention today, mainly due to their elevated ferroelectric, piezoelectric, and dielectric properties. Thus, in the following section, several methods for growing ferroelectric crystals, in particular, the high-temperature self-flux solution method will be introduced. On the other hand, lead-free piezoelectric components, such as bismuth layer structured ferroelectrics, are becoming increasingly important for the substitution of lead-based materials for high-temperature piezoelectric applications. Therefore, different methods for obtaining textured piezoelectric ceramics, in particular, the templated grain growth method will be also described.

Finally, the basic operation of a memory device and some characteristics of piezoelectric components will be provided as briefly as possible, with special focus to the functionality of lead-free ferroelectric materials.

1.2. Ferroelectricity and Piezoelectricity: Basic Definitions

1.2.1. Ferroelectric phenomena and spontaneous polarization

Ferroelectricity is a phenomenon that was discovered by Joseph Valasek in 1921 during his studies of single crystals of Rochelle salt ($NaKC_4H_4O_6 \cdot 4H_2O$).[1] Since then, many ferroelectric materials have been discovered and several essential features of the phenomenon (accompanied with a number of phenomenological theories) were studied and described in several books.[2-6] Chronological information on the early study of ferroelectric materials with different structure and their relevant properties are presented in Table 1.1.

Table 1.1 Chronological list and relevant properties of early ferroelectric crystals.[4,5]

Name and chemical formula	Curie Temperature T_C (ºC)	Spontaneous Polarization P_S (μC/cm^2)	Structural family	Year of first report
Rochelle Salt $NaKC_4H_4O_6{\cdot}4H_2O$	23	0.25	Hydrogen Bonds	1920
Potassium Dihydrogen Phosphate KH_2PO_4 (KDP)	-150	4.8	Hydrogen Bonds	1935
Barium Titanate $BaTiO_3$	120	26	Perovskite	1945
Lead Titanate $PbTiO_3$	490	57	Perovskite	1950
Lead Zirconate Titanate * $Pb(Zr_xTi_{1-x})O_3$ (PZT)	~ 375	> 40	Perovskite	1952
Strontium Barium Niobate $(Sr_{0.5}Ba_{0.5})Nb_2O_6$	120	30	Tungsten Bronze	1960
Bismuth Titanate $Bi_4Ti_3O_{12}$	675	50	Aurivillius	1961

* Polycrystalline ceramics near the morphotropic phase boundary (MPB).

Ferroelectric materials are characterized by a *spontaneous polarization* (P_S) that can be reoriented by the application of an electric field over some temperature range. This spontaneous polarization (dipole moment per unit volume) typically arises from the small displacements of some of the ions off their centro-symmetric position in the unit cell of their crystallographic structure. Some other ordering processes (*e.g.*, order-disorder) can also result in a reversible dipole moment. Figure 1.1 illustrates the unit cell of the ABO_3 perovskite-type structure for the $BaTiO_3$ showing the corresponding ionic displacements. Since electrical properties are strongly related to the crystal structure, the orientation of spontaneous polarization usually coincides with crystallographic axes. Most ferroelectric materials posses a transition temperature (*Curie point*, T_C), below which they are polar (non-centro-symmetric) and above which they present a centro-symmetric structure and, then, lose the spontaneous polarization. In this state the material is termed *paraelectric*.

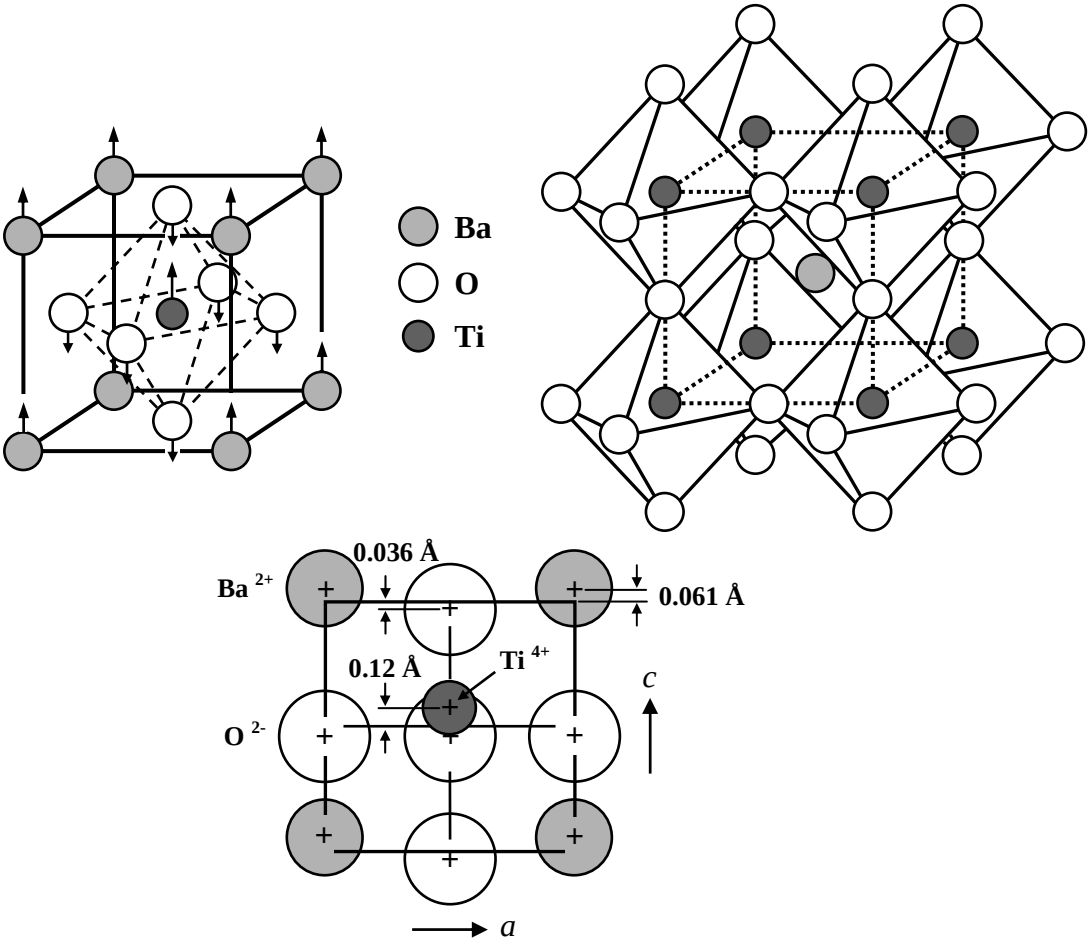

Figure 1.1 Several views of the unit cell of the ABO_3-type perovskite structure for $BaTiO_3$.[4-6] Above T_C the cell is cubic, while below T_C the structure is tetragonal with Ba^{2+} and Ti^{4+} ions displaced relative to the O^{2-} ions.

The electric displacement (D_i) in a dielectric material is related to the applied electric field (E_j) by the relation,[7]

$$D_i = \varepsilon_{ij} E_j \tag{1.1}$$

where ε_{ij} (F/m) is the *dielectric permittivity* of the material. The *relative* dielectric permittivity, $\varepsilon_{r\,ij}$, is defined as,

$$\varepsilon_{ij} = \varepsilon_o \varepsilon_{r\,ij} \tag{1.2}$$

where ε_o is the dielectric permittivity of the vacuum (8.85×10^{-12} F/m).

The expression (1.1) can be written also as,

$$D_i = \varepsilon_o E_i + P_i \tag{1.3}$$

where P_i is the polarization of the material, which includes both the spontaneous (if any) and induced contributions. Generally, the dielectric permittivity is obtained from the capacitance of the material at a frequency well below mechanical resonances (*e.g.*, 1 kHz). The *dielectric loss* is defined as the tangent of the loss angle, tanδ, *e.g.*, the ratio of the imaginary part ε'' to the real part ε' of the permittivity,[8]

$$\tan\delta = \frac{\varepsilon''}{\varepsilon'} \tag{1.4}$$

The dielectric permittivity and the loss factor of a ferroelectric material are important electrical parameters of the device that often have a peak at T_C, while the spontaneous polarization vanishes at this point (*i.e.*, see Fig. 1.4 for typical 1st and 2nd order phase transitions in ferroelectric crystals).

1.2.2. Piezoelectric coefficients and related properties

The *piezoelectric* effect was discovered by Jacques and Pierre Curie in 1880 during their study of the effects of pressure on the generation of electrical charge on crystals such as quartz, tourmaline and Rochelle salt.[9-11] They found that, if certain crystals are subjected to a mechanical force, they become electrically polarized and the degree of polarization is proportional (*i.e.*, linear) to the applied stress. Piezoelectric materials also show the inverse effect, where a geometric strain (deformation) is produced by the application of an electric field. For a crystal to exhibit the piezoelectric effect, its crystal structure should also be non-centrosymmetric as in the case ferroelectrics. In fact, all ferroelectric materials have to be piezoelectrics (see Fig. 1.2 for crystal classification scheme).

Piezoelectricity is a 3rd rank tensor effect, where the direct and inverse effects can be expressed in tensor notation as,[7]

$$P_i = d_{ijk} T_{jk} \qquad \text{(Direct piezoelectric effect)} \tag{1.5}$$

$$S_{ij} = d_{kij} E_k \qquad \text{(Inverse piezoelectric effect)} \tag{1.6}$$

where P_i is the polarization produced along the *i*-axis in response to the applied stress T_{jk}, and d_{ijk} (= d_{kij}) is the piezoelectric coefficient. For the inverse effect, S_{ij} is the strain generated along a specific orientation of the crystal in response to the applied electric field E_k along the *k*-axis. The units of the *d* coefficient are (C/N) or (m/V).

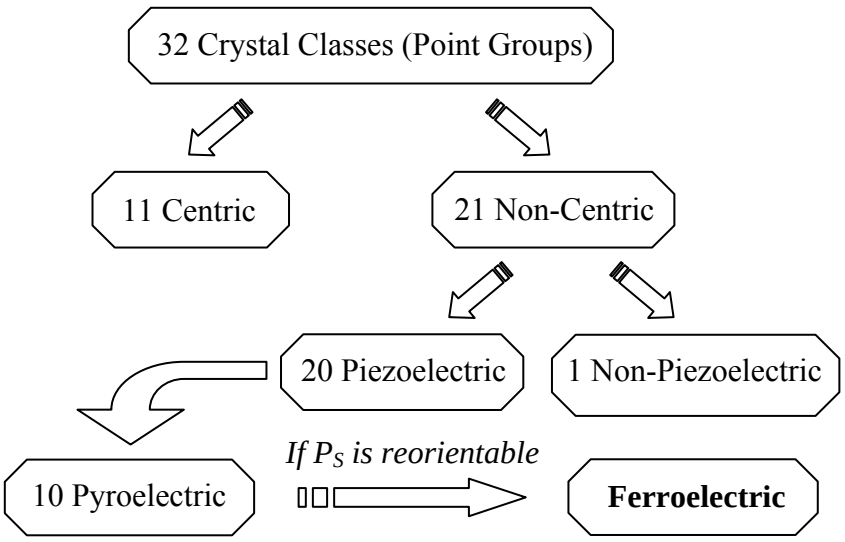

Figure 1.2 The crystal classification scheme for 32 point groups.[5]

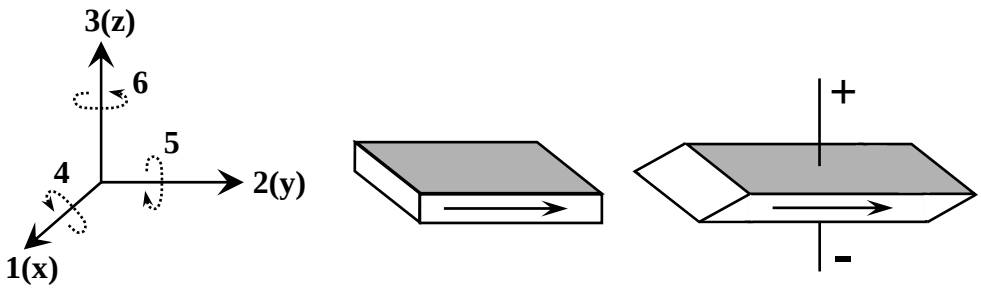

Figure 1.3 Directions X, Y and Z and illustration of the shear mode.[7,11]

Since piezoelectric materials are anisotropic, their physical constants must depend on both the orientation of the applied stress or electric field. Consequently, each constant generally has two subscript indices that refer to the directions of the two related quantities (*i.e.*, strain and electric field for piezoelectricity, or electric displacement and electric field for permittivity). The direction of positive polarization is agreed to coincide with the Z-axis of a rectangular system of X, Y and Z axes (see Fig. 1.3). Directions X, Y and Z are represented by the subscripts 1, 2 and 3, respectively, and the shear displacements about these axes are represented by the subscripts 4, 5 and 6, depending on the orientation of

shear plane. Definitions for permittivity and piezoelectric coefficient (the most used parameters in this work) are presented in Table 1.2.

Table 1.2 Definitions of some constants used in this work, dielectric permittivity (ε) and piezoelectric coefficient (d).[11]

Constant	Definition
ε_{11}	Permittivity for D and E in direction 1 (perpendicular to P_S)
ε_{33}	Permittivity for D and E in direction 3 (parallel to P_S)
d_{33}	Induced polarization in direction 3 (parallel to P_S) per unit stress applied in direction 3 *or* induced strain in direction 3 per unit electric field applied in direction 3.
d_{31}	Induced polarization in direction 3 (parallel to P_S) per unit stress applied in direction 1 (perpendicular to P_S) *or* induced strain in direction 1 per unit electric field applied in direction 3.
d_{15}	Induced polarization in direction 1 (perpendicular to P_S) per unit shear stress applied about direction 2 (2^{nd} direction perpendicular to P_S) *or* induced shear strain about direction 2 per unit electric field applied in direction 1 (see Fig. 1.3).

1.2.3. Ferroelectric phase transitions

Early research work on ferroelectric phase transitions is summarized in several articles by R. E. Nettleton.[12] When the temperature decreases through the Curie point, a ferroelectric crystal undergoes a structural phase transformation from the paraelectric state to the ferroelectric one. If there are two or more ferroelectric phases in a crystal, the Curie point only specifies the upper temperature at which the paraelectric-ferroelectric phase transition occurs.[5] Some ferroelectric crystals, such as GASH (guanidine aluminum sulphate hexahydrate), $LiH_3(SeO_3)_2$ and the $BaCoF_4$ family, do not possess Curie points owing to the fact that they remain ferroelectric up to their decomposition temperature.[13-15]

The most important progress in the modern theory of ferroelectric phase transitions is the concept of a *soft mode*, which was proposed on the basis of lattice dynamics by W. Cochran in the end of the 1950´s.[16] According to the concept of a soft mode, ferroelectric order stems from the instability of a transverse vibrational mode, referred to as a soft mode or a ferroelectric mode. Detailed lattice dynamic calculations for several ferroelectric crystals and more rigorous mathematical treatments of the soft mode in ferroelectrics have been reported by Blinc and Zeks.[17] Near T_C the crystalline lattice is also "soft" and can be polarized strongly with a relatively small coercive field. Therefore, the dielectric permittivity of many of useful ferroelectrics is very high in the vicinity of T_C, and can reach 10,000-80,000 at this point. This phenomenon is usually called *dielectric anomaly*. The "softness" of the lattice at temperatures near T_C makes dielectric properties and other related properties such as elastic, optical and thermal constants, to be temperature dependent in a wide range of temperatures around T_C.[5] In most ferroelectrics, the temperature dependence of the dielectric permittivity above T_C (in the paraelectric phase) can be described by a simple law called the *Curie-Weiss law*,[4,5]

$$\varepsilon = \varepsilon_o + \frac{C}{T - T_{cw}} \tag{1.7}$$

which is originated from the temperature dependence of the first coefficient in the phenomenological expression for Gibbs free energy in Landau theory.[4] In this case, C is the Curie-Weiss constant and T_{CW} is the Curie-Weiss temperature, which is generally somewhat lower than T_C in the case of a first-order phase transition, while for a second-order phase transition $T_{CW} = T_C$.

The transition from the paraelectric to the ferroelectric state occurs differently in different types of ferroelectric materials. These transitions may be of the first or second order in classical proper ferroelectrics.[4] The order of the phase transition is defined by the discontinuity in partial derivatives of the Gibbs free energy, **G**, at the phase transition temperature.[18] By the definition, for an n^{th}-order phase transition, the n^{th}-order derivative of **G** is a discontinuous function at the transition temperature. Thus, spontaneous polarization and strain change continuously at T_C for a ferroelectric with 2^{nd}-order phase transition, and are discontinuous at T_C for a ferroelectric with 1^{st}-order phase transition. It should be

mentioned that the slope of the reciprocal permittivity versus temperature curve below T_C is negative and twice that above T_C for a 2nd-order phase transition, while the ratio of these slopes immediately below T_C to that above T_C is -8 for a 1st-order phase transition.[4,18] Phenomenological theories (sometimes called thermodynamic theories) are based on *Landau-Ginsburg-Devonshire* models,[19] and have been also reviewed in the literature.[2-5] Figure 1.4 summarizes, schematically, the temperature dependence of the dielectric permittivity and the spontaneous polarization for different ferroelectric phase transitions.[18]

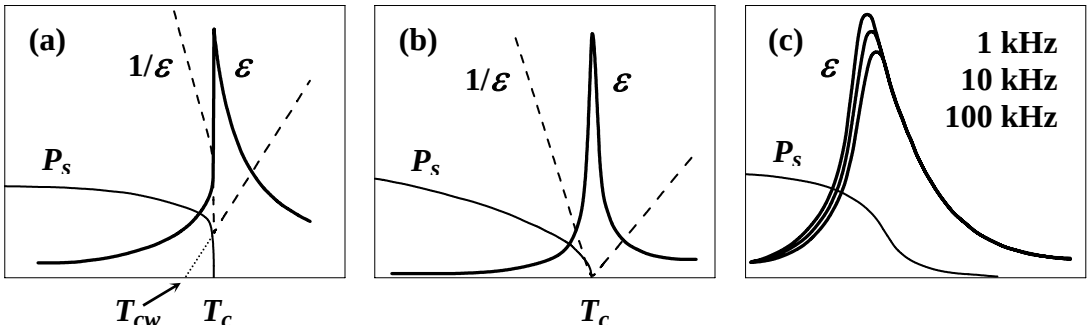

Figure 1.4 Schematic representations of ferroelectric phase transitions via temperature dependences of the dielectric permittivity ε and the spontaneous polarization P_S, for (a) first- (b) second-order ferroelectric, and (c) a relaxor ferroelectric.[18]

Other ferroelectric materials called *relaxors*, as exemplified by several perovskite-type compounds [*e.g.*, $Pb(Mg_{1/3}Nb_{2/3})O_3$] and tungsten-bronze-type compounds [*e.g.*, $(Sr_{1-x}Ba_x)Nb_2O_6$], can be distinguished from normal ferroelectrics such as $BaTiO_3$ and PZT, by the presence of a broad, diffused and dispersive dielectric peaks on cooling over the so-called transition temperature, T_m, at which the permittivity is maximum [see Fig. 1.4(c)].[20] In relaxor ferroelectrics, the Curie-Weiss law is not completely obeyed close to T_m.

1.2.4. Ferroelectric and ferroelastic domains

Once the ferroelectric crystal is cooled down across the Curie point, an electrical polarization develops. If it develops uniformly throughout the crystal, a depolarizing field (E_d) will appear as shown in Fig. 1.5(a).[8] To minimize the electrostatic energy associated with the polarization interaction with depolarizing field, uniform alignment of electric dipoles only occurs in certain regions of the crystal, while in other regions polarization may be oriented oppositely, as shown in Fig. 1.5(b). Such regions with uniform

polarization value are called *ferroelectric domains*, and the interface between two adjacent domains (with thickness typically of the order of 10-100 Å) is called the *domain wall*.[5] Ferroelectric domains were first demonstrated in a study of spontaneous birefringence in barium titanate single crystals.[21] Domain walls that separate different orientations of the spontaneous polarization vector are *ferroelectric domain walls*, while those which separate different orientations of the spontaneous strain (associated with mechanical *twinning*) are *ferroelastic domain walls*. Inside the domain wall the dipole/strain orientation changes gradually from one domain orientation to another.

The configuration of ferroelectric domains depends on the crystal structure. The spontaneous polarization in an ideal ferroelectric crystal can be distributed with equal probability among several crystallographic directions of the centro-symmetric prototype structure (paraelectric phase). In a tetragonal phase, for example, the spontaneous polarization can be oriented only along three mutually perpendicular crystallographic directions, giving rise to two types of domain walls [see Fig. 1.5(c)]: the walls that separate domains with oppositely oriented polarization (called 180°-walls), and those which separate domains with mutually perpendicular polarization (called 90°-walls). The 90°-walls are both ferroelectric and ferroelastic domain walls, because they separate regions with different orientation of the polarization and strain. Since the formation of the domain walls requires some energy, there is a certain amount of energy (domain wall energy, W_{dw}) associated with them, in addition to the elastic energy (W_e) due to 90º domains.[22] The switching of polarization by 180º does not involve elastic deformation, while the switching of 90º does involve elastic deformation, and the energy of both should be different. From energy considerations, in real crystals, domain patterns depend on many factors, including the defect type and concentration, stress and electric history, temperature range relative to T_C, boundary conditions, and even the history of the crystal growth.[4]

From a phenomenological point of view, the multidomain state is not energetically favorable if the system is free from other constraints.[23] However, in reality, other forces (electrical and/or elastic) are always present during crystal growth and preparation. The external forces, in addition to the existence of multiple nucleation sites during phase transition, prevent the ferroelectric system from reaching a single domain state. The presence of a large mechanical stress in a crystal results in the development of non-180º

domains wall configured to minimize the strain.[22] Thus, the natural state of a ferroelectric crystal is generally multidomain configuration rather than single domain. Nevertheless, this multidomain state can usually be transformed into a single domain by applying an electric field parallel to one of the polar directions.

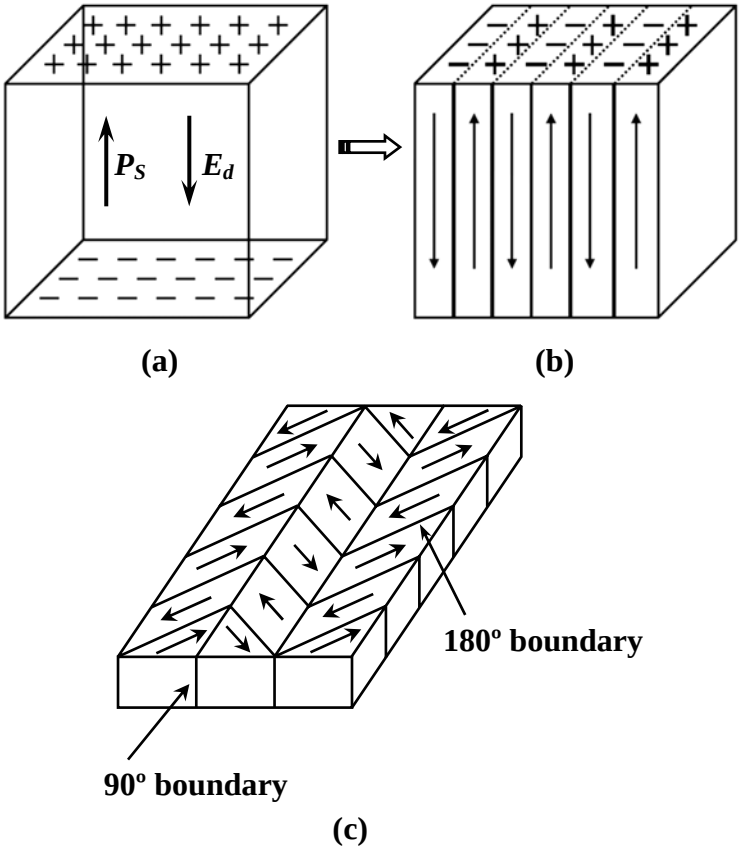

Figure 1.5 (a) Surface charge and depolarizing field (E_d) associated with spontaneous polarization (P_S). (b) Formation of 180º domains to minimize the electrostatic energy. (c) Schematic representation of 180º and 90º domain walls.[7,8]

Ferroelectric properties of any ferroelectric material are largely determined by its static domain structure, together with nucleation of new domains and domain wall mobility. The way in which the material splits up into domains upon the transition from the paraelectric to the ferroelectric phase depends strongly on the mechanical and electrical boundary conditions imposed on the sample, as well as on the nature of the sample itself.

1.2.5. Polarization switching and hysteresis loop

As described above, ferroelectric crystal is likely in a polydomain state when it has just been grown and cooled down across its Curie point. However, each individual domain can be reoriented upon application of the external electric field of high enough strength. This dynamic process of domain reversal is called *domain* (or *polarization*) *switching*.[5] The parameters of ferroelectric domains switching are anisotropic and depend on the temperature and the strength of the applied electric field.[21,24] When the direction of the applied electric field is opposite to the polarization direction of a domain, a new domain may appear inside the old one by means of *nucleation* and *growth*. The motion of the domain wall depends not only on extrinsic physical mechanisms but also on the stress distribution, space charges and defects in the crystal.[5]

When an alternative field of sufficiently high amplitude is applied to a ferroelectric material below T_C, the polarization shows a hysteretic behavior with the applied electric field, as illustrated in Fig. 1.6(a).[4,5,9] The observation of the *polarization-electric field* (*P-E*) *hysteresis loop* is often used for the identification of ferroelectrics. For a typical ferroelectric material, the first term in Eq. 1.3 is negligible, and a *D-E* loop and *P-E* loop become equivalent. Application of a weak electric field generates a linear P(E) relationship because the field is not large enough to disturb or switch any domain and the crystal will behave as a normal dielectric material (paraelectric), which can be described as,

$$P_i = \varepsilon_{r\,ij}\,\varepsilon_o\,E_j \tag{1.8}$$

At low and at very high electric fields a ferroelectric behaves like an ordinary dielectric with a high dielectric constant, but on approaching to the *coercive field* (E_C) the domain walls can move from their equilibrium position and domains that are oriented favorably with respect to the direction of the electric field grow rapidly at the expense of domains with opposite polarization direction, producing a switching of net polarization and a large *P-E* non-linearity. Once most of domains are switched, the material is said to reach its *saturation polarization*, where almost single domain state is attained. If the applied electric field is then removed, some of the domains will remain aligned and the crystal will have a *remanent polarization* (P_r). The extrapolation of the high field linear segment of the hysteresis loop back to the polarization axis represents the value of the spontaneous

polarization (P_S), *e.g.*, the polarization of a single domain in the absence of electric field. Following the *P-E* loop, the value of the negative electric field required to return the net polarization to zero is again the (negative) coercive field. Further increase of the field in negative direction will cause an alignment of the dipoles in this direction and the cycle can be completed by reversing the field direction once again. Thus, the relation between *P* and *E* is represented by the hysteresis loop as shown in Fig. 1.6(a).[4,5,9]

In addition to the *P-E* hysteresis loop, polarization switching by an external electric field leads to a strain-electric field (*S-E*) hysteresis in ferroelectric materials, as shown in Fig. 1.6(b).[2-5,8,9] The shape resembles that of a butterfly, and thus it is often referred to as the *butterfly loop*. At low electric fields, only a linear strain vs. electric field relationship is obtained due to the converse piezoelectric effect. The slope of the S(E) curve near the zero electric field represents the piezoelectric modulus (d_{33} for the longitudinal strain). As the field is increased, the strain is no longer linear with the field due to domain switching.[2]

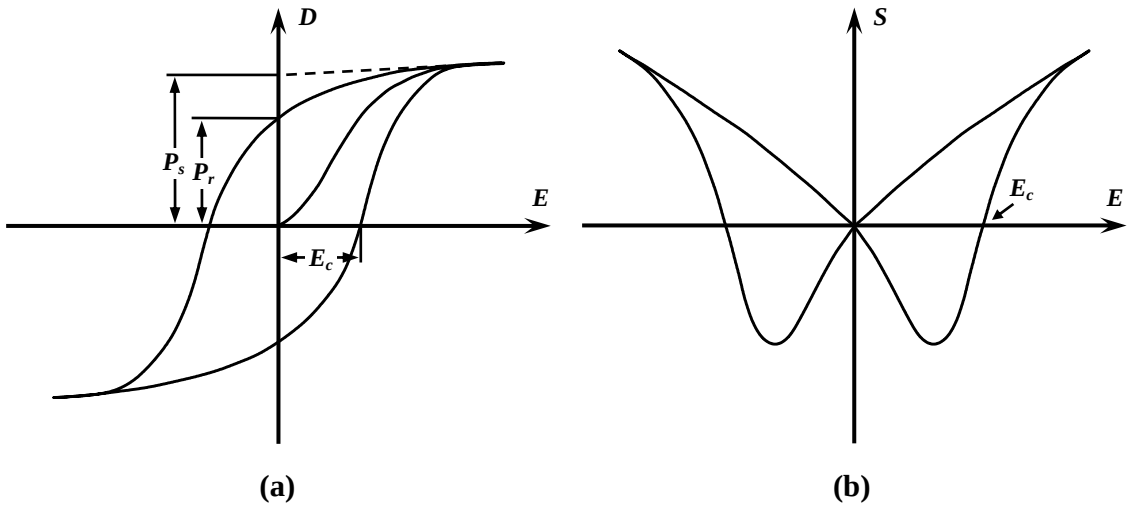

Figure 1.6 (a) *P-E* hysteresis and (b) *S-E* butterfly loops.[4,5,9]

1.3. Some Common Ferroelectric Materials

1.3.1. Ferroelectric perovskites family

Ferroelectric properties of ABO_3 perovskites were first discovered in barium titanate by Wul and Goldman in 1945.[25] $BaTiO_3$ was considered not only as a model system for ferroelectricity, but also as a main material for practical applications. Shortly after that, the

whole class of ferroelectric perovskites was discovered by several groups.[26-28] Perovskite is the mineral name of calcium titanate (see Fig. 1.1 for ABO_3 crystal structure). Its simplest structure is *cubic* (space symmetry *Pm*3*m*), which is the high temperature form for most ABO_3 oxides, but transforms to a *pseudocubic* (tetragonal, rhombohedral or orthorhombic) when the temperature decreases below the Curie point.[5] For simple perovskites such as $BaTiO_3$, the polarization is attributed mainly to the displacement of *B*-site ion (titanium in this case) from the center of BO_6 octahedra.

The most commercially available ferroelectric materials belong to the perovskite family, which includes $BaTiO_3$, lead titanate ($PbTiO_3$), potassium niobate ($KNbO_3$) and many compositions in the PZT system: lead zirconate-lead titanate ($PbZr_xTi_{1-x}O_3$). In fact, PZT compositions are now the most widely exploited of all piezoelectric ceramics both in research and industry; however, this system is very difficult to obtain in the form of high-quality single crystals.[29,30] ABO_3 structure is very tolerant to cation substitution of both *A* and *B* lattice sites, and hence may lead to more complex compounds, such as $Pb(Mg_{1/3}Nb_{2/3})O_3$, $Pb(Zn_{1/3}Nb_{2/3})O_3$, $(K_{1/2}Bi_{1/2})TiO_3$, $Pb(Fe_{1/2}Ta_{1/2})O_3$, $Pb(Co_{1/4}Mn_{1/4}W_{1/2})O_3$ and, in many cases, to the solid solutions between some of them. The substitution of alkaline-earth ions at the perovskite *A* site by Pb ions induces another soft mode, in which the *A*-site ions contribute to the spontaneous polarization, resulting in an enhancement of the ferroelectric polarization.[31] On the other hand, Yamashita *et al.*[32,33] have reported a detailed study of the effect of the molecular mass of *B*-site ions in the electromechanical coupling factors of lead-based perovskite piezoelectric materials.

1.3.2. Bi-layer structured ferroelectrics (BLSF)

Ferroelectric materials belonging to the Aurivillius family owe their name to Bengt Aurivillius, who found in 1949 a new phase ($Bi_4Ti_3O_{12}$) with a laminar structure when studying the phase diagram of the bismuth oxide-titanium oxide.[34] However, it was not until 1959, when Smolensky *et al.* discovered ferroelectric properties in the $PbBi_2Nb_2O_9$ system,[35] a representative compound of a large family of *Bi-layer structured ferroelectrics* (BLSF). Later on, the same authors and E. C. Subbarao have confirmed ferroelectric properties in a large number of BLSF materials.[36-39] The crystal structure of BLSF

materials consists of layers of pseudo-perovskite blocks, infinite in two dimensions, interleaved with bismuth oxide layers (see Fig. 1.7), having general formula,[36-38]

$$(Bi_2O_2)^{2+}(A_{m-1}B_mO_{3m+1})^{2-},\ (m = 1, 2, \ldots, 5)$$

where m denotes the number of BO_6 octahedral layers in the perovskite block interleaved between two (Bi_2O_2) layers, A can be mono-, di-, or trivalent ions (Na^{1+}, K^{1+}, Sr^{2+}, Ba^{2+}, Ca^{2+}, Pb^{2+}, Bi^{3+}, rare-earth elements) and B represents small ions with high charge such as Ti^{4+}, Nb^{5+}, Ta^{5+} W^{6+} or some combination of them. Most of these compounds have been assumed to be proper ferroelectrics at room temperature with a ferrodistortive paraelectric-ferroelectric phase transition in the range of 300-700 ºC. Typical examples of the prototype structure as a function of the value of m are shown in Fig. 1.7.[40] For simplification, only half of the unit cell is shown for each case.

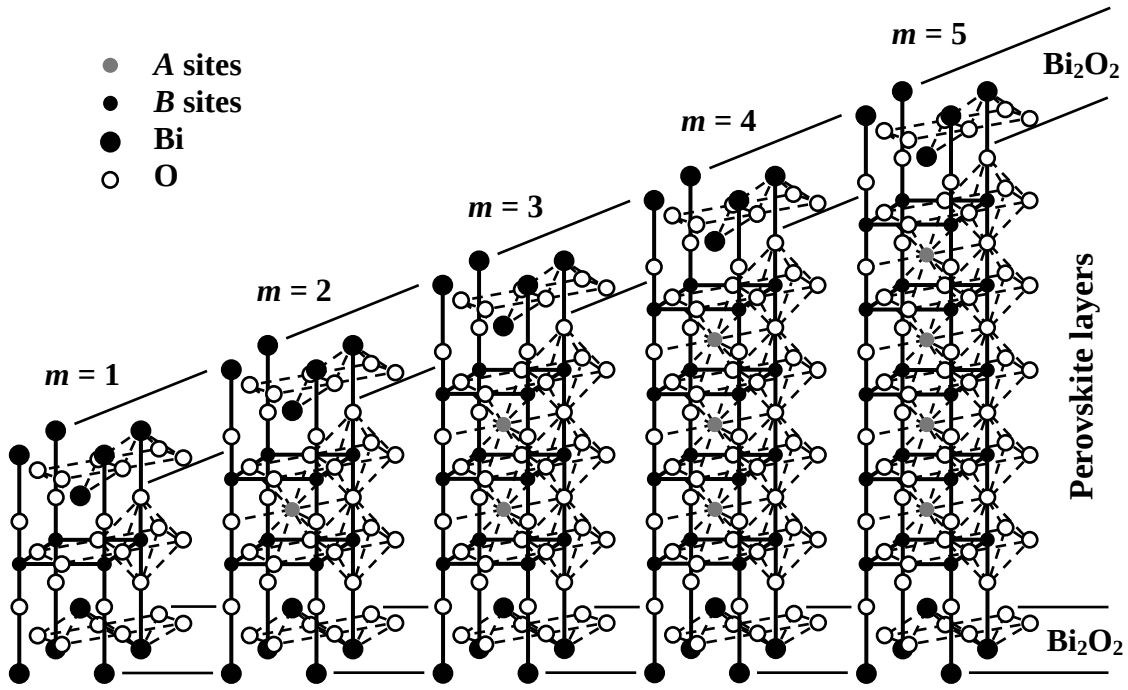

Figure 1.7 Aurivillius prototype structures as a function of m.[40]

In general, BLSF compounds have been reported to be pseudotetragonal at room-temperature, with a tetragonal high-symmetry (space group $I4/mmm$) in the paraelectric state transforming to an orthorhombic symmetry in the ferroelectric state.[5] As in other orthorhombic structures, the a and b-axes are rotated by 45º with respect to the parent tetragonal phase (see Fig. 1.8).

From the very beginning it was understood that the layered structure of BLSF should lead to a high dielectric, ferro-, and piezoelectric anisotropy due to predominantly 2D character of ferroelectric switching. But it was only in the end of the 60s, when Cummins and Cross could demonstrate highly anisotropic optical and electrical properties of one of the most popular BLSF compositions, $Bi_4Ti_3O_{12}$.[41] In BLSF, the dielectric and ferroelectric anisotropy originates from the two-dimensional perovskite-type structure and depends on the value of *m* (mainly on whether *m* is even or odd).[42] The most studied examples of BLSF compounds where *m* is odd are: Bi_2WO_6 (*m* = 1), where the *A*-site does not exist, and the above mentioned $Bi_4Ti_3O_{12}$ (*m* = 3). On the other hand, the most studied BLSF compounds where *m* is even are: $SrBi_2Ta_2O_9$ (SBT), $SrBi_2Nb_2O_9$ (SBN), Bi_3TiNbO_9 (*m* = 2), and $Bi_5FeTi_3O_{15}$, $(Ca,Ba,Sr)Bi_4Ti_4O_{15}$ (*m* = 4). There are, however, more complex structures corresponding to the intergrowth of perovskite blocks with different sizes, *i.e.* $Bi_7Ti_4NbO_{21}$, where perovskite blocks with *m* = 2 and 3 intercalate and are separated by the (Bi_2O_2) layers, or $SrBi_8Ti_7O_{27}$, where *m* intercalates between 3 and 4.[43-45]

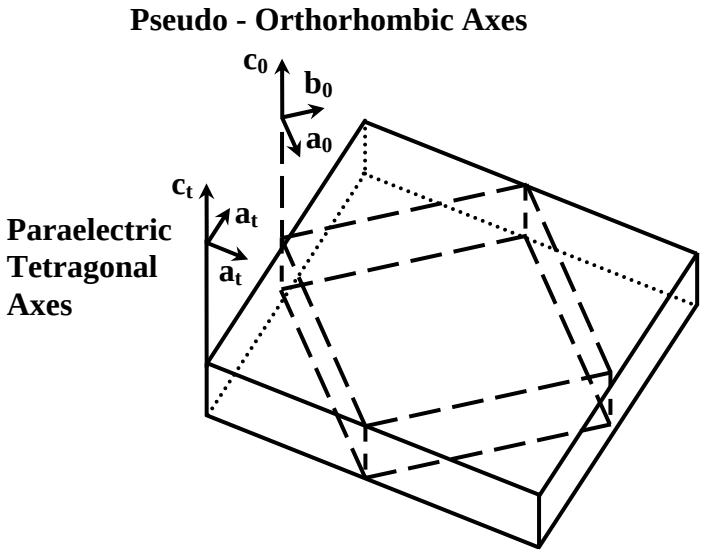

Figure 1.8 Illustration of the crystal axes in prototype tetragonal and ferroelectric orthorhombic structures.[41]

In his original work Aurivillius noted an orthorhombic distortion in this type of materials, but failed to observe any weak superstructure reflections and, therefore, described the structure with an incorrect space group *Fmmm*. Subsequently, Newnham *et al*. proposed for the first time that the room-temperature crystal structure of the $(Sr,Ba)Bi_2Ta_2O_9$ system is better described in the orthorhombic space group $A2_1am$.[46] The

room-temperature crystal structure of some BLSF single crystals (with m = 1, 2 and 3) was studied by Newnham *et al*. at the beginning of the 70s, when it was also established that the spontaneous polarization vector of these materials lies in the *ab*-plane of the pseudo-perovskite blocks.[42,46-48] These works were re-refined by Rae *et al*. at the beginning of the 90s by introducing new symmetry elements in single-crystal x-ray diffraction studies.[49-51] In the case of $Bi_4Ti_3O_{12}$ (m = 3) system, where m is odd, the small component of P_S along the *c*-axis was also explained from a crystallographic point of view.[50] The ferroelectric state is a result of a monoclinic distortion (space group $B1a1$) rather than of an orthorhombic one, and the polarization direction is inclined at a small angle (~ 4.5º) from the *a*-axis in the *ac*-plane, which can be resolved into two reversible components: a large one of ~ 50 μC/cm^2 along the *a*-axis and a small one of ~ 4 μC/cm^2 along the *c*-axis.[41]

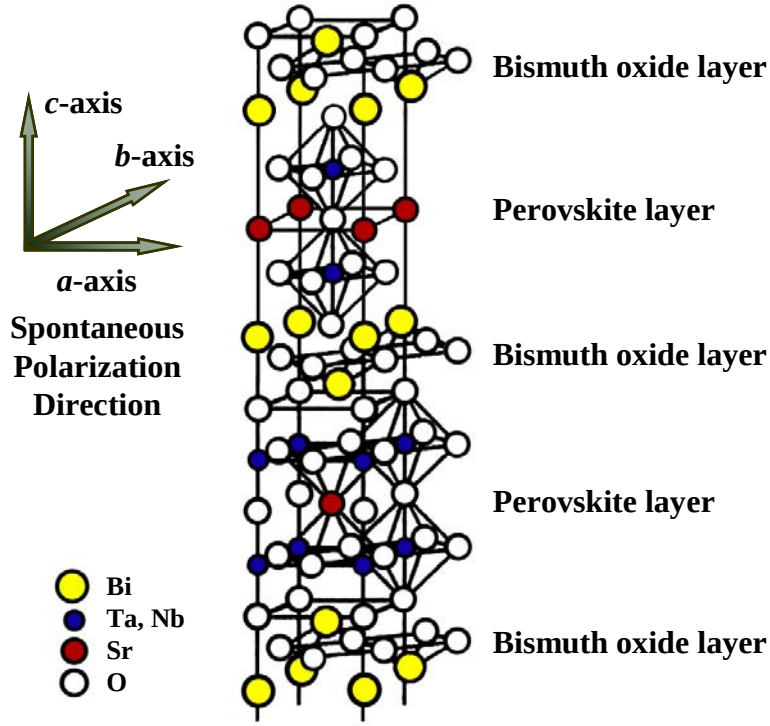

Figure 1.9 Crystal structure of $SrBi_2(Ta,Nb)_2O_9$ in the tetragonal prototype phase.[53]

As many other BLSF compounds with m = 2 or 4 (even-layers), SBT and SBN represent an orthorhombic distortion in the ferroelectric state (space group $A2_1am$) of the high-symmetry body-centered tetragonal prototype structure (space group $I4/mmm$) due to the consequence of changes in both the bismuth oxide and perovskite layer.[51,52] In the prototype structure, Sr is coordinated by 12 oxygen atoms, bismuth is bound by 4 oxygen

atoms in a square pyramidal geometry, while tantalum (niobium) occupies the typical 6-fold BO_6 position in the perovskite layer (see Fig. 1.9 for the body-centered tetragonal prototype phase).[53] The continuous O–Nb–O chains expected in a simple perovskite-type structure are interrupted along the *c*-axis not only by the (Bi_2O_2) layers but also by translation of the perovskite plane perpendicular to the *c*-axis relative to the neighboring perovskite planes. On the other hand, unbroken O–Nb–O chains are present in the plane perpendicular to the *c*-axis.

In this system, Bi_2O_2 layers are proposed to largely control the electronic response (band gap, effective masses, etc.),[54] while the dielectric and ferroelectric anisotropy originates from the two-dimensional perovskite-like structure, where pseudo-perovskite blocks $(SrB_2O_7)^{2-}$ (with *B* = Ta, Nb) are composed of double BO_6 octahedra with Sr at the *A* sites. In ferroelectric SBT (or SBN), there exist three displacive-type *soft* modes:[51,55,56] the $\Gamma(B_{3u})$ mode, which is the displacive mode of the Sr–Ta(Nb)–O layers relative to Bi–O layers along the *a*-axis in the *ac*-plane; the $X_x(B_{2u})$ mode, which is due to rotation of the Ta(Nb)O_6 octahedra in the *bc*-plane; and the $X_x(B_{1g})$ mod, which is due to rotation of the Ta(Nb)O_6 octahedra in the *ab*-plane. The only mode that contributes to the spontaneous polarization is the $\Gamma(B_{3u})$ mode.[51] First principle calculations of the electronic structure have demonstrated that most of the contribution to the macroscopic spontaneous polarization in SBT is due to the displacements of the *quasiparaelectric* Sr–Ta–O layers relative to Bi–O layers along the *a*-axis in the *ac*-plane from their corresponding positions in the parent tetragonal structure.[56,57] Shimakawa *et al*.[58] have confirmed this result from the x-ray diffraction Rietveld analysis, where the largest atomic displacements were obtained for the Bi^{3+} on the (Bi_2O_2) layer and the O^{2-} in the BO_6 octahedron in opposite directions, playing a transcendental role in the spontaneous polarization of SBT. On the other hand, in SBN the Sr–Nb–O layers are not *quasiparaelectric* and the displacements of the six oxygen atoms in the NbO_6 octahedra relative to the Bi–O layers also contribute to the total spontaneous polarization.[56]

Schematic representations of BO_6 octahedral distortions in perovskite blocks of $SrBi_2(Ta,Nb)_2O_9$ are shown in Fig. 1.10, where the tilting and rotation of the octahedra as projections in the *ac*- and *ab*-plane, respectively, can be observed.[58-61] For stoichiometric SBT, the tilt angle from the *c*-axis which is defined as α [see Fig. 1.10(a)] is reported to be

≈ 8º [O(2)–O(1)–O(2) bond angle: 164º], while the components along the *a*- and *b*-axes, *i.e.*, in the *ac*-plane (α_x) and *bc*-plane (α_y), are ≈ 0.4º and 7.9º, respectively.[59] On the other hand, the BO_6 octahedra predominantly rotate in the *ab*-plane accompanied with the whole shift of the octahedra along the *a*-axis, as schematically illustrated in Fig. 1.10(b). The average octahedral rotation angle (β) is reported to be ≈ 4.3º.[59,61] The spontaneous polarization vector, however, lies entirely along the orthorhombic *a*-axis (polar axis), since dipole moments caused by ionic displacements along *b*- and *c*-axes, in contrast, are cancelled out due to the presence of glide and mirror planes perpendicular to their axes, respectively.[51,58] This spontaneous polarization can be calculated from the equation,[58-60]

$$P_s = \sum_i \frac{m_i \times Q_i \times \Delta x_i}{V} \tag{1.9}$$

where m_i is the site multiplicity, Δx_i is the atomic displacement along the *a*-axis of the corresponding position in the parent tetragonal (*I*4/*mmm*) structure, Q_i represents the ionic charge for the i^{th} constituent ion, and *V* is the volume of the unit cell. Using this formula and the Rietveld refined structure; Rae *et al.*,[51] Shimakawa *et al.*,[58,60] and Noguchi *et al.*[59,61] have independently calculated the spontaneous polarization for the stoichiometric SBT and obtained P_S ≈ 14, 18 and 16 μC/cm^2, respectively. For SBN, on the other hand, the spontaneous polarization was estimated as P_S ≈ 20 μC/cm^2 by Shimakawa *et al.*[62]

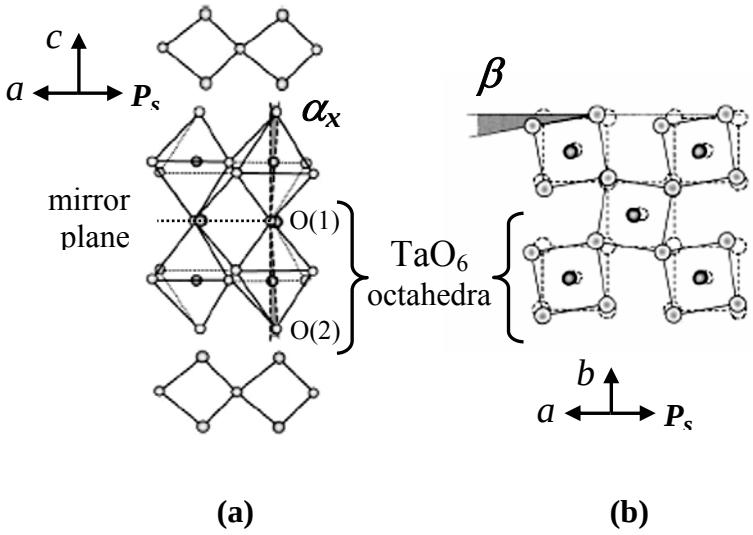

Figure 1.10 Schematic representation of the TaO_6 octahedral distortions in perovskite blocks of $SrBi_2(Ta,Nb)_2O_9$.[59,61]

For a long time, an intermediate phase between the high-symmetry tetragonal (*I*4/*mmm*) and the ferroelectric orthorhombic ($A2_1am$) phases has been suggested for some BLSF compounds, in particular, for the cases with even *m* value.[42,46] Recently, Onodera *et al.* have proposed the existence of an intermediate phase in SBT based on the anomalous change observed in the lattice parameters vs. temperature.[63,64] Hervoches *et al*. suggested the *Amam* space group for this intermediate orthorhombic phase between prototypes (*I*4/*mmm*) and ferroelectric ($A2_1am$) phases in the SBT system.[65] This intermediate phase has been shown to be ferroelastic and to occur between $T_C \approx 300$ ºC (ferroelectric-paraelectric phase transition) and ~ 550 ºC (ferroelastic-paraelastic phase transition).[65-69] The centrosymmetric space group *Amam* is obtained from *I*4/*mmm* by tilting the BO_6 octahedra around 110-type axes, however, such tilting alone is not sufficient to induce ferroelectricity.[70] The difference between the $A2_1am$ (ferroelectric) and the *Amam* (paraelectric-ferroelastic) orthorhombic structures is that the displacive mode along the polar axis (*a*-axis) and the rotational mode of the TaO_6 octahedra, around de *c*-axis, of the perovskite unit are both freezing out in the *Amam* space group.

Even though this intermediate phase (*Amam*) has been observed in other BLSF compounds with even *m* value, *e.g.*, $SrBi_4Ti_4O_{15}$, it has not been observed in all BLSF compounds with even *m* value and its symmetry is still under discussion.[70-73] For instance, $SrBi_2Nb_2O_9$ exhibit just one phase transition from ferroelectric (orthorhombic, $A2_1am$) to paraelectric (tetragonal, *I*4/*mmm*) at $T_C \approx 440$ ºC with no evidence of any intermediate phase.[72,74] In both cases, the transition temperatures are only approximate and can vary strongly with slight variations of the composition, *e.g.*, in Sr-deficient and Bi-excess compositions, which is rather flexible in these compounds.[58,59,75]

The stability of the perovskite-type unit of $Sr(Ta,Nb)_2O_7$, which may explain the structural distortion in terms of a lattice mismatch between BO_6 and Sr-O planes, can be determined by considering the geometrical *tolerance factor* (*t*) introduced by V. M. Goldschmidt for perovskite structures, which is also valid for Aurivillius-type structures,[39]

$$t = \frac{(r_A + r_O)}{\sqrt{2}\,(r_B + r_O)} \tag{1.10}$$

where r_A, r_B and r_O are the ionic radii of the *A*-site, *B*-site and oxygen ions, respectively. The following ionic radii: Sr^{2+} (CN = 12) = 1.44 Å for the *A*-site cation, Ta^{5+} and Nb^{5+} (CN = 6) = 0.64 Å for the *B*-site cation, and O^{2-} (CN = 6) = 1.40 Å, were used.[76] The great stability of the perovskite-type unit in both SBT and SBN is obtained from $t = 0.98$, which is less than 1 but very close to unity (ideal perovskite lattice). This also means that in the orthorhombically distorted structure the BO_2 plane is under compressive stress, while the Sr–O plane is under tensile stress.[60] Nevertheless, contrary to other BLSF compositions such as $ABi_2Ta_2O_9$ (*A* = Ba, Ca, Sr),[60] the tolerance factor is not applicable to explain the difference in the ferroelectric properties between SBN and SBT.

1.4. Single Crystals Growth

1.4.1. Methods for growing single crystals

For a long time a term "*crystal*" was identified with a *quartz* (meaning rock crystal), which was first used by G. Agricola in sixteenth century.[77] Nevertheless, it was only several hundred years later that the general term *crystal* was used in a broad sense. *Crystal growth* is a relatively small but important area of modern materials science and many useful books dealing with this topic are found in the literature.[78-80] The preparation of single crystals is more difficult than the preparation of polycrystalline materials. However, in polycrystalline materials, boundaries between individual grains are inevitably present, which may affect the material properties.

The preparation of novel materials has contributed to important advances in research on lasers, magnetism, semiconductors, ferro- and piezoelectrics, etc. The current interest in various single crystals for device applications and fundamental studies has stimulated the development of many techniques, in most cases distinguished only by rough boundaries. There are a number of methods for crystal growth and their use depends largely on the quality of the crystals to be grown and nature of the materials.[79] Table 1.3 summarizes shortly details, advantages and disadvantages of the most used crystal growth techniques.

There are not strict rules for the choice of the growth method that might be particularly suitable for a given material. However, the universality of a method, its ability to produce large and high-quality crystals, requirements for specific equipment, and cost,

time and need of previous experience, are some of the criteria that determine its suitability. Particular attention has to be paid to the techniques that are relatively simple, easy to control, which produce reasonably perfect crystals, and are suitable to a wide range of materials to be grown. The optimum method has to be described as a sequence of steps including: preparation of raw materials, effective growth and post-growth treatments of crystals, etc., which leads to crystals with the required structural and compositional quality. Besides, it is also important to know all the possible thermodynamical and thermophysical information concerning the material to be grown.

1.4.2. The high-temperature solution growth method

As many other ferroelectric systems, $BaTiO_3$ undergoes a structural transition at a temperature below its melting point, and because of this the crystal could not be grown from the pure melt. The needs of the single crystals of ferroelectrics like $BaTiO_3$ for studying intrinsic properties and the nature of the phase transition of such materials has lead to the development of various methods for crystal growth, such as *high-temperature solution* (*HTS*) crystal growth. In recent years, HTS crystal growth has been successfully used to grow high-quality, pure and large single crystals for a wide range of materials for electronic devices and physical measurement purposes.

There are several techniques included in HTS crystal growth that are often considered separately.[78-80] The best known of these related techniques is the *flux growth*, where the solvent is a molten salt or oxide. When the flux contains only the constituents of the crystal, the method is called *self-flux solution growth*. M. Gaudin was the first to use the *fluxed melt growth* to crystallize corundum from silicate fluxes, potassium sulphide and sulphate.[81] J. P. Remeika successfully employed the *fluxed melt* technique to grow for the first time large platy $BaTiO_3$ crystals from solutions of potassium fluoride.[82] It is worth to mention that it is rather difficult to define the terms *high-temperature* exactly. Although there are not strict values for the temperature limits, the growth temperatures are typically higher than the boiling point of water and lower than 2000º C.

Table 1.3 Most used techniques for crystal growth.[78-80]

Technique	Details	Advantages / Disadvantages
Growth from pure melt	The most important commercial method of crystal growth, where the pure material is first fused and then resolidified to yield crystals. Addition of seed crystals to the system substantially increases the power of the method.	High-quality crystals, where no impurities are introduced except possible contamination from the crucible. Growth rate is higher than that achieved by other methods. Several materials cannot be crystallised by this method because of theirs particular properties. The high viscosity lowers significantly the diffusion.
Growth from solvents	Single crystals are crystallized from supersaturated solutions: aqueous or ionising solvents such as NH_3, H_2S, HF, etc.	A large number of organic and inorganic salts, including piezo- and ferroelectric materials, are crystallized from aqueous or organic solutions. Probably the oldest and simplest method to produce highly structural perfect crystals. There are many materials which are either chemically unstable or do not have an appropriate solubility. This technique is not suitable for growing large crystals.
Growth from solid state	Few crystallites in a polycrystalline solid are allowed to grow preferentially with the elimination of theirs neighbors within the material.	This is an easy process known as recrystallisation and may be carried out by normal sintering or straining and subsequent annealing of the material. Recrystallisation is only possible in the case of materials that are stable at the temperature where significant diffusion takes place. Small crystals are generally obtained with low quality.

Growth from vapour phase	Widely used for the commercial preparation of thin film crystals in the semiconductor industry. A reversible reaction is utilised to carry the material to be crystallised as a volatile substance (vapour) to the region of crystallization.	Suitable for the materials that are stable only over a narrow temperature range in a given flux, thus compromising the applicability of slow cooling. Molecular beam technique offers an easy control of the growth conditions by this method. Main problems are to find out a suitable agent for transporting the material to be crystallised and the inability to produce large crystals because of the involved multinucleation.
Vapour-liquid-solid growth	In multi-component growth, more than two phases may be involved, in this case, vapour-liquid-solid. The vapour phase reaction does not directly originate the crystal, but a liquid solution from which the crystal grows.	Many semiconductor materials have been grown by this method; it is also suitable for other systems such as: γ-Al_2O_3, SiC, etc. Crystals are generally dislocation-free. The size of the crystal is not large.
High-temperature solution growth	The material gets dissolved at high temperature in a suitable solvent and crystallization is allowed during the cooling, which makes the solution critically supersaturated.	Enable crystals to grow well below their melting points, being particularly suitable for materials which: (a) have incongruent melting points, (b) undergo phase transition resulting in strain or fracture, (c) have very volatile constituents whose composition may change, and (d) are highly refractory. Low growth rates are observed and final small sized crystals are obtained.

Although HTS method for crystal growth have not found applications on an industry scale, they have been used by many groups to prepare ferroelectric crystals suitable for the study of fundamental physical properties, such as dielectric and piezoelectric anisotropy, domains configuration, structural phase transitions, etc. Table 1.4 summarizes some of the most frequently grown and studied ferroelectric perovskite single crystals.

The following properties are prerequisite for the HTS and the flux:[83]

(1) The material to be grown as a single crystal must be the only stable solid phase under the growth conditions.
(2) The solubility of the crystal and its components in the flux should be high and should decrease with temperature.
(3) The flux should have a low melting point and a low vapour pressure.
(4) The viscosity of the solution should be low.
(5) The solution should not attack the growth crucible.
(6) The residual melt should be easily separated from the crystals.

Table 1.4 List of recently grown ferroelectric perovskite crystals (with references).

Chemical Formula	Crystal size	Habit	References
ABO_3 family (A = Ba, Sr, Na, K and B = Ti, Nb, Ta)	> 25 mm	Cubic	84 - 86
$Na_{1/2}Bi_{1/2}TiO_3$ family	< 10 mm	Cubic	87, 88
$Pb(B_{1/3}Nb_{2/3})O_3$ (B = Zn, Mg)	> 10 mm	Cubic	89, 90
$Pb(B_{1/3}Nb_{2/3})O_3$-$PbTiO_3$ (B = Zn, Mg)	~ 20 mm	Cubic	91 - 96
$Pb(B_{1/2}Nb_{1/2})O_3$-$PbTiO_3$ (B = In, Sc, Yb)	~ 10 mm	Cubic	97, 98

In the growth of crystals from HTS, the material to be crystallized and the flux are put inside a platinum (Pt) crucible sealed with a Pt lid, and crystallization takes place when the high temperature solution is allowed to become critically supersaturated by cooling.[78-80] The most commonly used fluxes are basic oxides or fluorides like: PbO, PbF_2, Bi_2O_3, B_2O_3, Na_2O, or KF, which choice depends on the composition of the crystal to be grown. Supersaturation and supercooling are defined by the phase diagram. Figure 1.11 shows

schematically a pseudo-binary system of the flux and the solute, where the three ways to achieve the required supersaturation for crystal growth are represented,[83]

(1) Crystal growth by *slow cooling* when the temperature is decreased from *A* to *B* and growth occurs along the arrow to *C* at varying growth temperature.

(2) Crystal growth by *flux evaporation* when the solvent or a part of it is evaporating and the solute concentration increases from *D* to *E* at constant growth temperature. This method is frequently used for aqueous and organic solutions.

(3) Crystal growth by *vertical temperature gradient transport* when the crystal grows in a colder region *G* of the furnace, while the crystallized material is continuously replaced at the furnace hotter region *F*, generally by dissolution of the polycrystalline nutrient. Since the growth temperature in each region of the furnace is constant, this steady state method is particularly suitable for the growth of solid solutions.

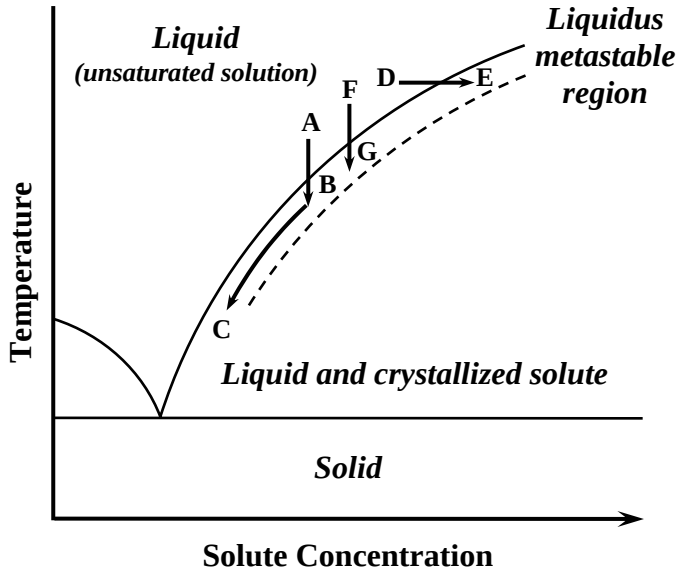

Figure 1.11 Scheme of a pseudo-binary system of flux and solute.[83]

The *slow cooling* is the most commonly applied method, where the required supersaturation for crystal growth is created by cooling the melt from the point *A* slowly below the liquidus temperature (T_l) into the metastable region (Ostwald-Miers region), as demonstrated in Fig. 1.11.[83] To reach the temperature of spontaneous – three-dimensional – nucleation (T_n) at point *B*, a larger supersaturation or supercooling ($\Delta T = T_l - T_n$) than

that required for the growth of a nucleus is necessary. Crystals grow at the lowest temperature, which is determined by the unavoidable temperature gradients, whether at the bottom of the crucible or near the surface of the melt. The crucible is placed in a muffle furnace, then, the temperature is increased well above the liquidus temperature of the flux and kept there for a while (soaking time) to achieve complete dissolution of all components. The temperature is then lowered just above the liquidus temperature very slowly to create the supersaturation for nucleation. In some cases, the temperature is increased again somewhat to reduce the number of nuclei (cycling). Heterogeneous nucleation is usually obtained at the wall of the platinum crucible which can be reduced by a long soak period above the liquids temperature.[99] Growth should be terminated at least before the solution solidifies, usually performed by a faster cooling. The crystals must be separated from the solidified melt as far as possible mechanically, *i.e.*, crystals can be separated from the flux at high temperature by inverting the crucible within the furnace, using a crucible with a volume twice as large as that of the melt.[100,101]

The main advantages of this method is that it can be applied successfully to materials which: (a) melt incongruently, *i.e.*, which decompose before melting; (b) undergo a phase transition resulting in a severe strain or even fracture; (c) have a very high vapor pressure at the melting point; (d) have very volatile components whose composition may change when heated at a temperature close to the melting point; and (e) are highly refractory.[79] In such cases it is desirable to grow crystals at temperatures well below their melting points. The advantages of solution growth also include unconstrained growth conditions, no steep temperature gradient, low growth temperature, etc. Crystals grown at low temperatures compared to the melting point of the solute often have a better quality with respect to point defects, dislocation density, etc., than crystals grown directly from their own melt. However, HTS growth leads, in general, to substitution or interstitial inclusion of solvent ions into the crystal structure, microscopic incorporation of impurities, slow growth rates, etc. Thus, crystals obtained from the flux are in general of small size. For industrial production, the facetted form of the crystals grown from HTS is a severe disadvantage compared to the round boule obtained by pulling a seed crystal from the melt as allowed by the well-known Czochralski technique.

Nevertheless, the growing interest in the use of ferroelectric and ferromagnetic crystals increased the application of the HTS methods, providing a convenient and powerful method for obtaining samples for research and technological applications. In general, crystal growth from the melt is preferable whenever is possible. However, since only small crystals are often needed for basic investigation or measurements, the effort to grow these from HTS is not as strong as that from melt techniques. Furthermore, with some experience and with the choice of a suitable flux composition and growth methods, the disadvantages of the HTS growth can be minimized.

1.5. Fabrication of Textured Ceramics

1.5.1. Processing of ferroelectric ceramics and their properties

The fabrication of most bulk ferroelectric ceramics starts with powder preparation (mixing and firing process). The powder is then pressed to the required shape and size, and the *green sample* is thermally processed for their densification and mechanical integrity. The most important steps that influence the product characteristics and properties are powder preparation, shaping and sintering. Specific information on the preparation and properties of ferro- and piezoelectric ceramics can be found in Jaffe *et al*.[9] and Moulson *et al*.,[8] among others. There has been a great deal of development in powder processing, shaping and sintering that has resulted in further expanding the application of piezoelectric ceramics.[6-9] Some processing methods that have been traditionally used to fabricate electroceramics for piezoelectric applications are: extrusion, die pressing, slip casting, injection molding, tape casting, etc. In general, ceramics are formed by randomly oriented micrometric *grains*, which may vary in crystalline structure, composition, size, shape, and in term of internal stress to which they are subjected. The interfaces between grains, known as *grain boundaries*, are regions where changes in lattice orientation, composition and/or electrical behavior usually occur. The materials properties are basically controlled by the grain and/or grain boundary compositions, but will also be affected by the grain size and porosity of the sintered sample.

In ferroelectric ceramics, such grains typically present an initial multidomain configuration, as shown in Fig. 1.12(a).[5,7,8] Thus, these ceramics which are composed of a

random domain orientations are piezoelectrically inactive, *i.e.*, the effects from the individual grains cancel each other and no noticeable piezoelectricity is observed. *Poling* is the commonly used method to orient the domains by polarizing the ceramics through the application of a static electric field in a specific direction at room or higher temperatures depending on the material [see Fig. 1.12(b)]. Even when some monodomain grains are obtained, the result will never be the full orientation of all the domains, and thus, the polycrystalline ceramic exhibits a remanent polarization lower than that of a single crystal. The oriented domain structure is fairly permanent unless the temperature exceeds the phase transition temperature or mechanical stress limits, or both.

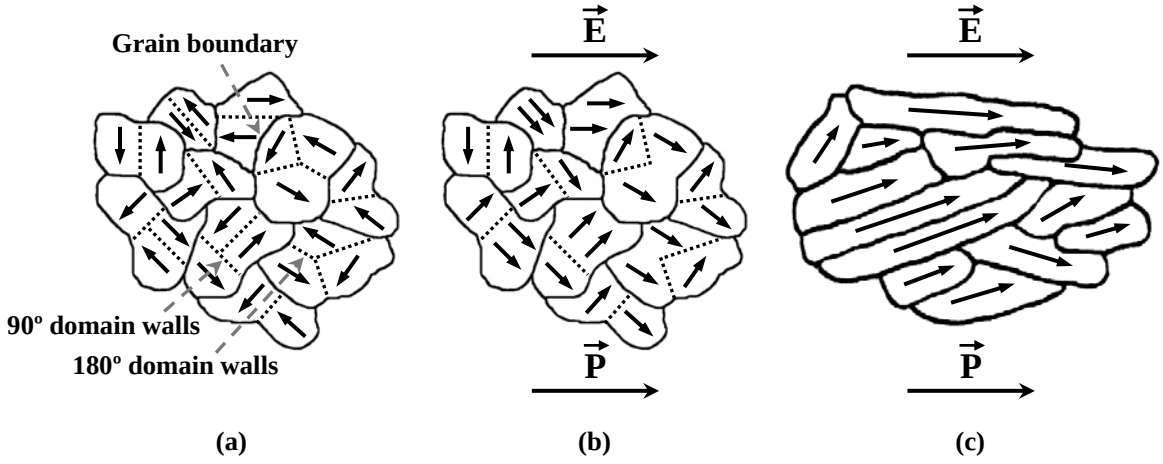

Figure 1.12 Domain configurations and poling process (b) in a ferroelectric ceramic and (c) in a textured ceramic.

The development of texture in piezoelectric materials offers different routes for increasing the available piezoelectric response. In uniaxial ferroelectrics, or in materials where the spontaneous polarization is confined to a plane, texturing enables a more efficient alignment of the polar vector, increasing in this way the poling efficiency and thus the response.[102] This is clearly seen if a uniaxial ferroelectric is considered, such as a member of the tungsten bronze structural family, in which two antiparallel domain states are allowed. In this case, it is very difficult to obtain a high degree of polarization during the poling process, as some grains will not have domains states that are possible to align with the electric field. Such grains may be completely unable to switch, and may thus constrain the switching of adjacent, better-aligned grains.[103] In such materials, the measured remanent polarization may be substantially lower than the calculated value based

on an ensemble of single crystals with the same orientation distribution. A comparable situation, but less pronounced, appears in BLSF materials, where the spontaneous polarization is confined to a plane.

In general, the controlled development of texture in electroceramic polycrystalline materials is a topic of recent interest in ceramic processing, since it allows improved tailoring of physical properties such as: piezoelectric, electrical or mechanical properties, approaching them to those of single crystals and enhancing in this way the sensing and actuating capabilities of the various devices. In certain materials the grains grow in an anisotropic form (whisker, needle or platelet shape) allowing the fabrication of grain-oriented materials by using special forming techniques such as hot-forging or hot-pressing to induce orientation of the anisometric grains by shear-induced plastic deformation of grains, coupled with subsequent sintering.[102,104-106] In addition, poling the ceramics in a preferential direction may also be easier in a textured ceramic, because the axes of the crystals are already aligned, as shown in Fig. 1.12(c). One of the most promising routes for controlled crystallographic and morphologic texture developments in polycrystalline ceramic bodies is the *templated grain growth* (*TGG*) process.[107]

1.5.2. The templated grain growth (TGG) process

Early works on TGG include several patents for producing single crystals from polycrystalline precursors as well as textured ceramics.[108-110] TGG process can be applied either to the growth of a large single crystal or a small amount of anisotropically shaped particles (*e.g.*, templates) distributed and oriented in a fine-grained matrix.[107] In most cases, single crystals or textured ceramics are obtained by a *homoepitaxial* TGG process, where the matrix powder has the same composition and crystal structure as the template material. In this case, both the crystal layer and the matrix grow by a simple Ostwald ripening-type process (*i.e.*, the large grains grow at the expense of the finer matrix grains).[111] Alternatively, the TGG method is *heteroepitaxial* when the template material has a different composition, but the same crystal structure or the lattice matches with the matrix material, *e.g.*, TGG of $Pb(Mg_{1/3}Nb_{2/3})O_3$-$PbTiO_3$ or $BaTiO_3$ single crystals from a $SrTiO_3$ template.[112,113] The lattice match ensures that the nucleation of the growing phase

to occur on the templates surface, and then further heating drives densification and subsequently grain growth in the same way as in the homoepitaxial case.

To fabricate textured materials by TGG a small amount of anisotropic templates is dispersed in a matrix of relatively fine and equiaxed particles. Initially, the template particles may be randomly oriented, but become then aligned by a shear gradient imposed during forming (*e.g.*, tape-casting, extrusion or uniaxial pressing); after that they are finally sintered to produce a dense textured ceramic.[107] The template particle must have a high aspect ratio morphology (like a whisker or platelet), so that it can be mechanically oriented under the applied shear force during green forming. Depending on how the orientation axes are controlled, it is possible to obtain either fiber or biaxial (sheet) texture.

The synthesis of the anisometric template particles and their necessary thermal stability during the TGG process are special challenges to the TGG process. The amount of grown material depends on the concentration, size, and distribution of the templates, while the resulting texture quality (*e.g.*, degree of texture and orientation) depends on the initial alignment of the template particles.[114] The template particles must have a good lattice match with the desired final composition, sufficient stability, and an appropriate driving force for growth. For instance, if the purpose of the texturing is to access physical properties that are correlated to crystallographic orientation (*e.g.*, thermal conductivity, dielectric permittivity, piezoelectricity, etc.), it is preferable that the template axis matches the desired crystallographic orientation.[107]

On the other hand, the matrix powder particles are of equal importance for successful TGG as the templates. In the homoepitaxial case, the matrix powder is already in the final phase form, and it is important that its size has to be finer than the template particles after densification and it must be sintered to high density (*e.g.*, > 95% theoretical density).[115] When the matrix is a precursor to the final ceramic phase, the template particles can act as nucleation sites and control the phase transformation of the matrix. This process is referred in the literature to as reactive TGG (RTGG) because the dual role of the templates.[116-118] In this case, the templates must react with the matrix to obtain the desired final phase, which takes the morphological form of the templates.

In general, the TGG process occurs in three stages:[119-121] densification, rapid radial growth of individual template particles until template impingement, and slower growth by template thickening, as schematically shown in Fig. 1.13.[107] Because the pores restrain the boundary motion, a significant template growth can not occur during densification, being generally limited until the matrix density is ≥ 90% theoretical density (TD) as observed by Messing *et al.*[121-123] and Watanabe *et al.*[124] in Al_2O_3 and $Bi_4Ti_3O_{12}$ ceramics, respectively. During heating, the anisotropic template particles grow at the expense of the fine randomly oriented powder particles increasing the volumetric fraction of highly oriented material with a specific crystallographic orientation. The thermodynamic driving force for the migration of the template boundary into the polycrystalline matrix during the thermal processing appears from the difference in surface free energies between the advancing crystal plane and the matrix grains.[107] A large matrix grain growth during sintering can reduce the thermodynamic driving force enough so that template growth stops. Therefore, the finer the matrix grain size, the higher the driven force for TGG.

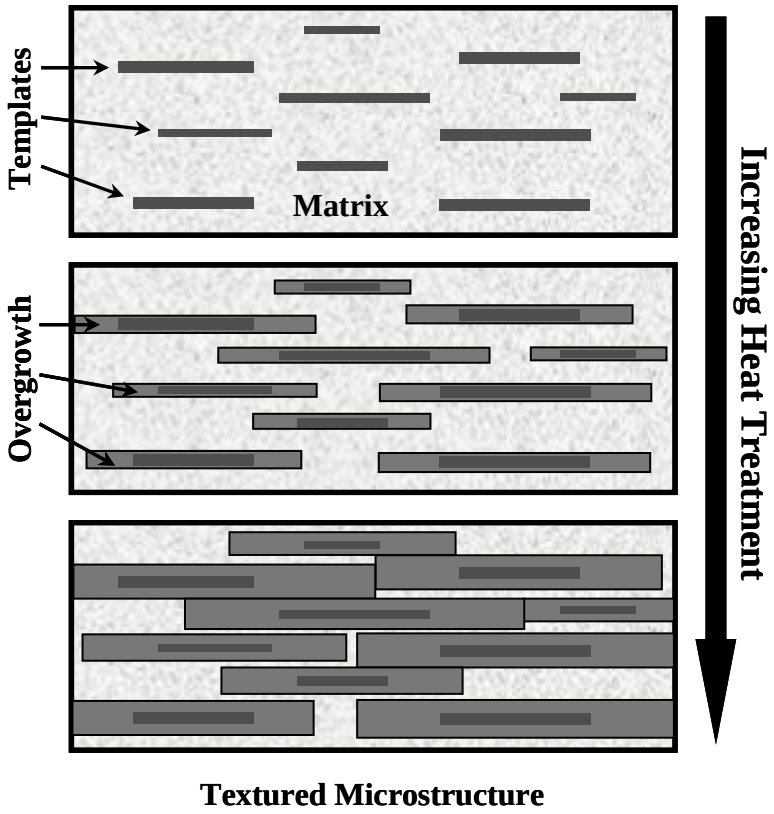

Figure 1.13 Schematic of the stages for the TGG process.[119]

On the other hand, the large area of low-energy faces on each template provides a common surface and influences the rotation of other small grains further from the template interface.[125] In addition, secondary nucleation of new elongated grains from the matrix grains is also possible due to the cooperative arrangement of the matrix grains, resulting in a higher degree of texture.[119] In almost all the cases of TGG, the kinetics of boundary migration is increased by intentionally introducing a liquid phase at the grain boundaries to reduce the stress around the templates, thus facilitating the densification and grain growth.[107,115] Because a small amount of liquid is present during growth, template growth occurs by dissolution of the polycrystalline matrix grains and deposition on the lowest energy surface in the system, that is the template major face.

In summary, TGG offers significant opportunities for reducing the cost of single-crystal-like materials to produce large samples with simple or complex geometries.[107] Being based on a conventional powder processing and sintering, highly oriented ceramics can be achieved at a significantly lower cost as compared to other techniques including hot-forging and hot-pressing of anisotropically shaped particles, which are too expensive to be commercially viable.

1.5.3. BLSF textured ceramics: Microstructure and properties

In the last decade a variety of materials have been produced by TGG to yield highly oriented textured ceramics or produce single crystals with interesting properties, such as: Al_2O_3[114,115,120-122] and Mullite,[119,123] with higher fracture toughness perpendicular to the basal surface; Si_3N_4[126,127] and SiC,[128] with interesting fracture characteristics and thermal conductivity; and a variety of ferroelectric materials with piezoelectric properties similar to those of single crystals, *e.g.*, $Pb(Mg_{1/3}Nb_{2/3})O_3$-$PbTiO_3$,[129-131] $Sr_{0.53}Ba_{0.47}Nb_2O_6$,[103,132] $(Na_{1/2}Bi_{1/2})TiO_3$,[117,118] $BaTiO_3$,[133,134] and some BLSF, such as $Bi_4Ti_3O_{12}$,[124,125,135,136] and $CaBi_4Ti_4O_{15}$.[116,137] Recently, the interest in the study of BLSF textured ceramics has increased as a way to optimize their piezoelectric properties, approaching them to those of single crystals. The increase in the piezoelectric response of textured ceramics appears to be more significant in systems with fewer possible orientations for the spontaneous polarization.[107] Thus, ferroelectrics where the polarization is confined to an axis (*e.g.*, $Sr_{1-x}Ba_xNb_2O_6$) or to a plane (*e.g.*, BLSF materials) show larger property improvements on

fiber texturing than do the 3-dimensional ferroelectrics such as perovskites. In systems where there are few possible directions for the spontaneous polarization, misaligned grains may constrain switching of surrounding material, thus greatly reducing the remanent polarization and piezoelectric response from values calculated assuming a similar distribution of grain orientations, but where each grain is able to switch freely.[103] In these cases, a critical level of connectivity of the oriented grains for efficient poling is required.

In BLSF materials, the grains grow in anisometric form showing platelet morphology by reproducing their crystalline structure, *i.e.*, the major face of the platelet grains is parallel to the *ab*-plane and perpendicular to the *c*-axis of the material structure.[125] Platelet-shaped single crystals can be oriented along the *c*-axis, face-to-face, by an appropriate process, *e.g.*, tape-casting. Thus, BLSF ceramics obtained by TGG show anisotropic properties because of most of the platelet grains are arranged face-to-face, in such a way that the non-ferroelectric *c*-axis lies perpendicular to the texture direction (non-favorable direction of polarization), while the highest piezoelectric and ferroelectric properties are achieved on samples cut perpendicular to the texture direction with the *ab*-plane arranged in parallel to the thickness, *t*, of the sample, as shown in Fig. 1.14.

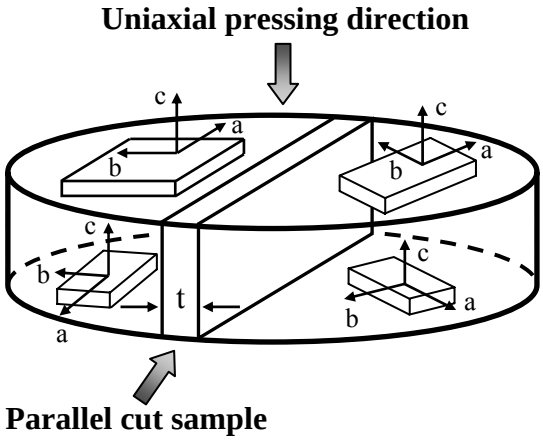

Figure 1.14 Ideal orientations of platelet grains during TGG.[138]

The anisotropy in the dielectric ferro- and piezo-electric properties has been reported in $Bi_4Ti_3O_{12}$ and other BLSF ceramics, where a degree of orientation higher than 0.95 have been reached by TGG (for an ideal textured ceramic a degree of orientation of 1.0 is expected).[116,135] The main advantage of this kind of processing is the higher values of piezoelectric coefficients (*e.g.*, two times higher d_{33}) achieved in textured ceramics with

respect to the randomly oriented sample. The arrangement of the grains does not avoid the necessity of the poling process, but it allows reaching higher values of remanent polarization, and thus, increasing the piezoelectric activity. Nevertheless, due to the high electrical conductivity in the *ab*-plane of BLSF materials, poling of these textured ceramics still being a difficult task. This is maybe the main disadvantage today for the applicability of textured BLSF materials.

1.6. Microelectronic and Piezoelectric Applications for BLSF

1.6.1. Introduction

The concept of reversible spontaneous polarization as a *memory state* was one of the greatest motivations since the early days of ferroelectric research.[139] With the advances in thin film technology over the past 20 years, ferroelectric films with improved properties have been receiving renewed attention for memory applications.[140] The major device type under investigation is the *nonvolatile ferroelectric random access memory* (*FeRAM*), which utilizes the spontaneous (reorientable) polarization of a ferroelectric thin film as a memory state.[140-150] FeRAM has evolved from a concept on a paper to a memory product that is used in a variety of consumer products and industrial applications, such as smart cards, power meters, printers and video games, etc.[144,145,150,151] The advantage of using FeRAM instead of other types of nonvolatile memory, such as *electrically erasable programmable read-only memory* (*EEPROM*) and battery-backed *static random access memory* (*SRAM*), varies according to the application. FeRAM exhibits a unique combination of performance features, including low power consumption, high read/write endurance, a fast read/write access time, long-term retention, and a low-cost embedded memory solution that can be scaled to high densities.

Ferroelectric crystals and ceramics have been studied for a long time in the search of new microelectronic and mechatronic devices due to their excellent piezoelectric, pyroelectric, ferroelectric and dielectric properties.[4-6,9-11] P. Langevin[152] was the first who developed a piezoelectric ultrasonic transducer during World War I and their success opened up new opportunities for piezoelectric materials in underwater applications as well as a host of other applications such as ultrasonic transducers, actuators and sensors, etc.,

which include hydrophones, sonar, accelerometers, power supplies, ultrasonic motors, transformers, filters, robotic muscles, and medical ultrasound. In the following two sections, a brief description of the basic operation of a FeRAM device and some characteristics of piezoelectric devices are provided. Finally, the advantages, disadvantages and present functionality of BLSF and other lead-free ferroelectric materials are discussed.

1.6.2. Non-volatile ferroelectric random access memories (FeRAMs)

The memory application of ferroelectric materials is based on the hysteretic behavior of the spontaneous polarization with electric field, as shown in Fig. 1.6(a).[140-150] At zero applied electric field there are two states of remanent polarization which are equally stable, $\pm P_r$. Either of these two polarization sates could be encoded as a "1" or a "0" (the bases of digital computing) and since no external field is required to maintain these states once reached, the memory device is nonvolatile. Clearly, to switch the state of the device from "1" to "0" or vice versa, a threshold field greater than the coercive field is required. Additionally, in order to reduce the required applied voltage (to within a 5 V limit) for a given E_C, the ferroelectric materials need to be processed in the form of thin films.

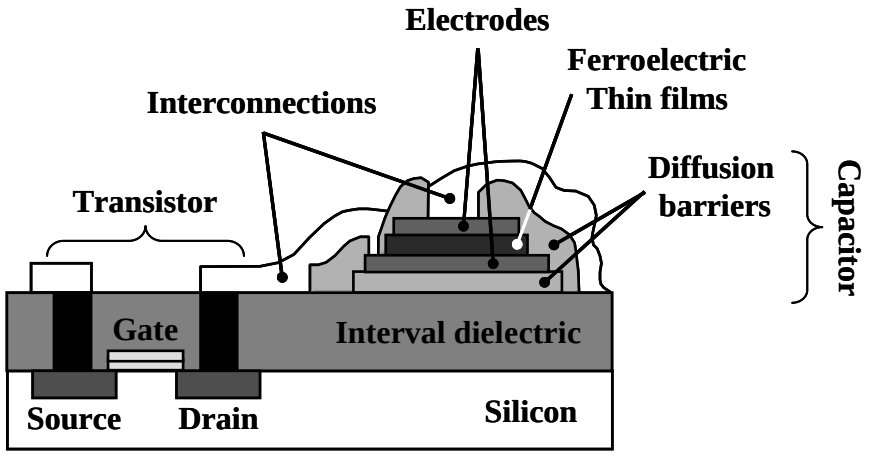

Figure 1.15 Schematic diagrams of high density architecture for non-volatile FeRAMs as example of 1T-1C design for use as computer memory. This configuration helps to prevent crosstalk between adjacent cells.[144]

From a digital point of view, if a voltage is applied to a ferroelectric capacitor in a direction opposite of the previous application, the remanent domains will switch, requiring compensating charge to flow onto the capacitor plates.[153] If the field is applied in the

direction of the previously applied field, no switching takes place, and only a linear nonswitching response is measured in the form of a voltage across a 10-50 Ohm resistor. This property can be used to read the state or write a desired state into the capacitor. A sense amplifier and other associated circuitry are used in a FeRAM device to compare these responses with that of a reference cell, and thereby, read the state of the device.[144]

In general, the basic structure of such high-density memory includes a thin film ferroelectric capacitor sandwiched between two chemically stable metal electrodes, integrated on a top of semiconductor *IC* (*integrated circuit*) fabricated using existing *CMOS* (*complementary metal oxide semiconductor*) technology, as shown in Fig. 1.15.[144] The design consists of a square matrix array of memory elements and transistors, where each memory cell capacitor is isolated from its neighbors by means of a pass-gate transistor. Since it has one transistor and one capacitor per bit, this FeRAM architecture is called 1T-1C. The need for this transistor arises from the fact that ferroelectrics do not exhibit well defined coercive fields or switching voltages, thus creating the so called *half-select disturb-pulse*, *i.e.*, the possibility of unintentional switching of cells adjacent to the ones being addressed in a large array of memory elements. The selected transistor provides electrical isolation to each memory cell, allowing the circuit to select which capacitor is to be switched and creating individually addressable bits.

FeRAM was first demonstrated in 1988 using $PbZr_xTi_{1-x}O_3$ (PZT) as the ferroelectric material for data storage.[154] Since then, many ferroelectric materials have been investigated for thin-films FeRAM, but only two families of ferroelectric materials are known to be the most important for memory applications: perovskite PZT[155-160] compositions and BLSFs, namely $SrBi_2Ta_2O_9$ (SBT),[53,161-170] and $(Bi,La)_4Ti_3O_{12}$ (BLT).[171-175] Their thin-film characteristics are summarized in Table 1.5.[148] Generally, the following characteristics are desired for a ferroelectric thin film to be used as a FeRAM:[147]

(1) The remanent polarization should be large, so that a relatively high polarization reversal current can be derived from a small-area capacitor.
(2) The dielectric constant should be sufficiently low, because a high dielectric constant material produces a large displacement current (linear response) and hinders detection of the polarization reversal current.

(3) The coercive field should be as low as possible for low-voltage operation of the FeRAM device.

(4) The Curie temperature should be high, much higher than the storage and operating temperature range of the device.

Table 1.5 Main properties of typical ferroelectric thin-films used for FeRAMs.[148]

Materials	P_r (μC/cm^2)	E_C (kV/cm)	Crystallization Temperature (ºC)
$Pb(Zr,Ti)O_3$ (PZT)	25	60	600
$SrBi_2Ta_2O_9$ (SBT)	10	40	750
$(Bi,La)_4Ti_3O_{12}$ (BLT)	15	80	700

The reliability of a ferroelectric memory is characterized by three main effects: *fatigue*, *imprint* and *retention*.[176] *Fatigue* is a term describing the fact that the remanent polarization becomes small when a ferroelectric film experiences a large number of polarization reversals. Regular US specification, derived from magnetic memory parameters, is that the film is fatigue-free for switching over 10^{15} cycles when a 10-yr operation is assumed.[148] However, in the present FeRAM technology the actual test cycles are about 10^{12}. This number seems to be determined by limited test time as well as an expectation that a single cell is not used continuously in the normal use of a memory, but various cells are used randomly. The *retention time*, that is, the time period for which a ferroelectric film can retain the polarization sign and magnitude after the write operation, must be longer than 10 years. *Imprint* is a degradation effect, in which the polarization of a ferroelectric film and its response to applied voltages of opposite polarity are not symmetric. This effect should be as small as possible. It depends upon the prior switching history and results in an asymmetry of switching times and incomplete polarity reversal.

Some of the largest problems with PZT for FeRAMs were fatigue and imprint, which were conspicuous with Pt electrodes. Studies on the integration of Pt into ferroelectric capacitors yielded devices with FeRAMs-compatible properties, such as large values of remanent polarization, film resistivity values higher than 10^{10} Ωcm and sufficient retention characteristics.[177,178] Furthermore, the crystallization temperature of PZT films is lower than 650 ºC, which is suitable for implementing PZT capacitors on *CMOS* logic circuits.

However, Pt does not prevent oxygen diffusion to the poly-Si plug,[179] and these films suffered from fatigue and imprint.[180] These problems have almost been solved at present by the use of oxide electrodes such as IrO_2, RuO_2 and $SrRuO_3$.[157-159,181,182] On the other hand, one of the largest advantages of SBT films over PZT is that SBT does not show the fatigue phenomenon up to 10^{13} switching cycles, even if Pt electrodes are used.[161-164,144,165] The imprint and retention characteristics at high temperatures are also known to be superior to those of PZT.[162-163] On the contrary, the main disadvantages of SBT are the low values of remanent polarization and Curie temperature in comparison with PZT thin-films (see Table 1.5). In addition, the high crystallization temperatures, generally higher than 700 ºC, make them incompatible with conventional FeRAM technologies. In some cases Nb doping of SBT or SBT-Bi_3TaTiO_9 (BTT) solid solution have been suggested to increase remanent polarization and Curie temperature, while maintaining fatigue-free properties.[164,183-185] Today, serial 4-256 kbit FeRAM based on PZT with read/write endurance ~10^{12} cycles and retention time longer than 10 yrs are available in the market.[186]

1.6.3. High-temperature piezoelectric applications

Piezoelectric materials convert electrical energy into mechanical one and vice verse. The range of commercial piezoelectric materials, including single crystals and ceramics is extensive as needed for the fabrication of various devices such as transducers, actuators, surface acoustic wave devices, frequency control devices, sensors, and so on.[6,8,11] For high-performance actuators, the piezoelectric materials must show high strain, high thermal stability, low mechanical loss, and weak hysteresis in the strain-field response.[6,11,187,188] Piezoelectric materials for sensors applications should possess high d_{ij} and g_{ij} coefficients, as well as low conductivity. In some applications a high *mechanical quality factor* (Q_m) is required. In high-performance transducer applications, ***e.g.***, medical, a high *electro-mechanical coupling coefficient* (k_{ij}) is also required since k_{ij} dictates the usable bandwidth of the transducer.[6,11] The next generation of actuators and transducers requires a significant increase in some or all of the typical figure of merit coefficients (d_{ij}, k_{ij}, Q_m).

Currently, piezoelectric ceramics are the mostly widely used in electromechanical conversion devices, since they show the highest generative forces, precise displacements, and best high frequency capabilities. The advantages of ferroelectric ceramics over other

piezoelectric materials lie in the highest coupling coefficients and in the possibility to control, by compositional modifications, various mechanisms which contribute to the electromechanical response. There are a great number of ferroelectric materials that are potential candidates for high-temperature applications.[189] The most important family are: firstly, BLSF compositions with transition temperature above 600 ºC (*e.g.*, $Bi_4Ti_3O_{12}$, T_C = 685 ºC or Bi_3TiNbO_9, T_C = 940 ºC); secondly, the strontium niobate family (represented by $Sr_2Nb_2O_7$, $T_C > T_{melting}$ = 1700 ºC); thirdly, lead metaniobate, $PbNb_2O_6$ with T_C = 560 ºC; and finally, lead titanate, $PbTiO_3$, and its modifications ($T_C \leq$ 490 ºC). The main disadvantage of ferroelectric ceramics is the high conductivity at elevated temperatures.[18] Depoling pyroelectric effects, temperature dependence of materials parameters, and phase transitions represent additional problems for high-temperature applications of many ferroelectric ceramics.

1.6.4. Functionality of BLSF and other lead-free ferroelectric materials

PZT-based materials near the MPB are the most widely used ferroelectric materials today in room-temperature piezoelectric as well as in memory applications, since no other material displays better ferroelectric and piezoelectric properties than the PZT.[5-9,11,190] Under application of a strong electric field during the poling process, the large number of thermodynamically equivalent states and field-induced phase transitions allow a high-degree of alignment of ferroelectric dipoles, resulting in a dramatic enhancement of ferroelectric and piezoelectric properties.[191] Because of the lead toxicity, however, it was forbidden by EU to use lead-based materials in consumer products such as cars, various kinds of smart systems and sound generators, for environmental protection. The legislation will be enforced in the EU as draft directives on *Waste from Electrical and Electronic Equipment* (*WEEE*), *Restriction of Hazardous Substances* (*RoHS*) and *End-of-Life Vehicles* (*ELV*).[192] Therefore, at present, a research interest related to this environmental problem is the developing piezoelectric materials that are environmentally friendly. Another impetus for seeking alternatives to lead-based compositions is the need of piezoelectric materials for operation at high temperatures and having high-temperature stability.

An application of a piezoelectric material at high temperatures (above 300 ºC) presents many challenges. The most fundamental limitations are phase transitions, which in general, lead to instability of the materials properties with temperature and, under high load, may even be responsible for the switching into non piezoelectric phase. Quartz, SiO_2, is the best known and the most widely used piezoelectric material in a single crystal form, due to its excellent stability with electromechanical properties that only weakly depend on temperature.[193] However, the main disadvantages of this material include low electro-mechanical and piezoelectric coefficients, and limitation to high-temperature applications due to mechanical twinning and a phase transition at 573 ºC that leads to instability in the material properties. Other often used piezoelectric crystals are ferroelectric lithium niobate, $LiNbO_3$, and lithium tantalate, $LiTaO_3$, which exhibit very interesting properties at room temperature, but both materials suffer from high conductivity and strong pyroelectric effects at high temperature. Nevertheless, single crystal quartz, lithium niobate and lithium tantalate are extensively used in industrial applications as a result of their temperature stability, wide operating temperature range, and ease of growing large, defect-free single crystals. In recent years, lithium tetraborate, $Li_2B_4O_7$, langasite, $La_3Ga_5SiO_{14}$, gallium phosphate, $GaPO_4$, and aluminum nitride, AlN, has been proposed as new alternative high temperature piezoelectric materials.[193]

Table 1.6 Room temperature piezoelectric and electromechanical properties of selected lead-free materials with different structure. T_C is the Curie temperature, ε is the permittivity for poled samples, d is the piezoelectric strain constant, k is the electromechanical coupling coefficient and Q_m is the mechanical quality factor.[107]

Material	Structure	T_C (ºC)	ε (1 kHz)	d_{33} d_{15} (pC/N)	k_{33} k_{15}	Q_m
$BaTiO_3$	Perovskite	120	1500	190 270	0.49 0.48	100
$(Na_{1/2}Bi_{1/2})TiO_3$	Perovskite	335 (FE-AFE)	500	74 19	0.42 0.11	225
SiO_2 (single crystal)	α-Quartz (Non-FE)	573 (α-β)	4.5 (ε_{11})	2 – (d_{11})	– –	100,000
$LiNbO_3$ (single crystal)	Corundum	1150	27.8	6 ~70	0.23 0.60	10,000
$Na_{0.5}Bi_{4.5}Ti_4O_{15}$	Aurivillius	~ 600	140	18 –	0.15 –	100

Table 1.6 summarizes the room temperature piezoelectric properties of mostly used lead-free piezoelectric materials with different crystal structure. These materials exhibit transition temperatures of up to 1000 ºC, however, they generally have low permittivity (< 500) and small piezoelectric coefficients (d_{33} < 200 pC/N).[194] $BaTiO_3$ and $(Na_{1/2}Bi_{1/2})TiO_3$ are lead-free piezoelectric materials that show relatively large piezoelectric coefficients for this class of materials, thus, they are expected for actuator and high power applications.[194-196] However, these materials have some problems such as low T_C, difficulties in poling treatment and/or low densities.

Another important lead-free piezoelectrics are based on the bismuth layered structure. BLSF materials are characterized by their low dielectric constant, relatively high T_C, and large anisotropy in the electromechanical and piezoelectric coefficients, and, as such, have been described as promising candidates for lead-free ferroelectric materials to reduce environmental damages.[193,189,194,196] Pure $Bi_3Ti_4O_{12}$ for example, has a high *p*-type conductivity, and despite the large piezoelectric coefficient (ten times larger than in quartz) and a high transition temperature, it can not be used at elevated temperatures. Doping with small concentration of Nb reduces the conductivity of this system by three orders of magnitude.[197] Thus, Nb-doped $Bi_4Ti_3O_{12}$ is a potential candidate for piezoelectric applications at temperatures up to 400 ºC. Other BLSF materials of interest for the same temperature range are: $SrBi_4Ti_4O_{15}$, $SrBi_2Ta_2O_9$-Bi_3TiTaO_9, and $Na_{0.5}Bi_{4.5}Ti_4O_{15}$.[193,194,196] However, the wide use of BLSF family in piezoelectric and memory applications is hampered by the limited knowledge of their fundamental characteristics, such as: anisotropy, phase transition and domain structure.

1.7. References

[1] J. Valasek, "Piezoelectric and Allied Phenomena in Rochelle Salt". *Phys. Rev.* **15** [6] (1920) 537-538; *ibid*. **17** [4] (1921) 475-481.

[2] F. Jona and G. Shirane, "Ferroelectric Crystals". Pergamon Press, Oxford (1962).

[3] E. Fatuzzo and W. J. Merz, "Ferroelectricity". North-Holland Publ., Amsterdam (1967).

[4] M. E. Lines and A. M. Glass, "Principles and Applications of Ferroelectrics and Related Materials". Clarendon Press, Oxford (1977).

[5] Y. Xu, "Ferroelectric Materials and their Applications". North-Holland Elsevier Sci. Publ., Amsterdam (1991).

[6] K. Uchino, "Ferroelectric Devices". Marcel Dekker, Inc., New York (2000).

[7] N. Setter, "ABC of Piezoelectricity and Piezoelectric Materials", in *Piezoelectric Materials in Devices*. Ed. N. Setter, Publ. Ceramics Laboratory, EPFL, Lausanne, Switzerland (2002) 1-27.

[8] A. J. Moulson and J. M. Herbert, "Electroceramics". Chapman and Hall, London (1990).

[9] B. Jaffe, W. R. Cook and H. Jaffe, "Piezoelectric Ceramics". Academic Press, London and New York (1971).

[10] T. Ikeda, "Fundamentals of piezoelectricity". Oxford University Press, New York (1990).

[11] J. W. Waanders, "Piezoelectric Ceramics: Properties and Applications". Philips Components, Eindhoven-The Netherlands (1991).

[12] R. E. Nettleton, "Ferroelectric Phase Transitions: A Review of Theories and Experiment". *Ferroelectrics* **1** (1970) 3, 87, 93, 111, 121, 127, 207, 221; *ibid*. **2** (1971) 5, 77, 93.

[13] A. N. Holden, B. T Matthias, W. J. Merz and J. P. Remeika, "New Class of Ferroelectrics". *Phys. Rev.* **98** [2] (1955) 546.

[14] R. Pepinsky and K. Vedam, "$LiH_3(SeO_3)_2$: New Room-Temperature Ferroelectric". *Phys. Rev.* **114** [5] (1959) 1217-1218.

[15] M. Eibschutz and H. J. Guggenheim, "Antiferromagnetic-Piezoelectric Crystals - $BaMe_4$ (Me = Mn, Fe, Co and Ni)". *Solid State Commun.* **6** [10] (1968) 737-740.

[16] W. Cochran, "Crystal Stability and the Theory of Ferroelectricity". *Phys. Rev. Lett.* **3** [9] (1959) 412-414; ***ibid***. *Adv. Phys.* **9** [36] (1960) 387-423; **10** [40] (1961) 401-420.

[17] R. Blinc and B. Zeks, "Soft Modes in Ferroelectric and Antiferroelectrics". Elsevier, New York (1974).

[18] D. Damjanovic, "Ferroelectric, Dielectric and Piezoelectric Properties of Ferroelectric Thin Films and Ceramics". *Rep. Prog. Phys.* **61** [9] (1998) 1267-1324.

[19] A. F. Devonshire, "Theory of Barium Titanate". *Philos. Mag.* **40** [309] (1949) 1040-1063; *ibid*. **42** [333] (1951) 1065-1079.

[20] L. E. Cross, "Relaxor Ferroelectrics". *Ferroelectrics* **76** [3-4] (1987) 241-267.

[21] B. T. Batthias and A. Von Hippel, "Domain Structure and Dielectric Response of Barium Titanate Single Crystals". *Phys. Rev.* **73** [11] (1948) 1378-1384.

[22] G. Arlt, "Twinning in Ferroelectric and Ferroelastic Ceramics: Stress Relief". *J. Mater. Sci.* **25** [6] (1990) 2655-2666.

[23] W. Cao, "Phenomenological Theories of Ferroelectric Phase Transitions". *Brit. Ceram. Trans.* **103** [2] (2004) 71-75.

[24] W. J. Merz, "Switching Time in Ferroelectric $BaTiO_3$ and its Dependence on Crystal Thickness". *J. Appl. Phys.* **27** [8] (1956) 938-943.

[25] B. Wul and I. M. Goldman, *C. R. Acad. Sci. URSS* **46** (1945) 139; *ibid*. **49** (1945) 177; *ibid*. **51** (1946) 21.

[26] B. T. Matthias, "New Ferroelectric Crystals". *Phys. Rev.* **75** [11] (1949) 1771.

[27] G. Shirane, S. Hoshino and K. Suzuki, "X-Ray Study of the Phase Transition in Lead Titanate". *Phys. Rev.* **80** [6] (1950) 1105-1106.

[28] G. Shirane, "Phase Transitions in Solid Solutions Containing $PbZrO_3$". *Phys. Rev.* **84** [4] (1951) 854-855.

[29] R. Clarke and R. W. Whatmore, "Growth and Characterization of $PbZr_xTi_{1-x}O_3$ Single Crystals". *J. Cryst. Growth* **33** [1] (1976) 29-38.

[30] T. Hatanaka and H. Hasegawa, "Dielectric Properties of $Pb(Zr_xTi_{1-x})O_3$ Single Crystals Including Monoclinic Zirconia". *Jpn. J. Appl. Phys.* **34** [9B] (1995) 5446-5448.

[31] R. E. Cohen, "Origin of Ferroelectricity in Perovskite Oxides". *Nature* **358** [6382] (1992) 136-138.

[32] Y. Yamashita, K. Harada, Y. Hosono, S. Natsume and N. Ichinose, "Effect of B-site Ions on the Electromechanical Coupling Factors of $Pb(B'B'')O_3$-$PbTiO_3$ Piezoelectric Materials". *Jpn. J. Appl. Phys.* **37** [9B] (1998) 5288-5291.

[33] Y. Yamashita, Y. Hosono, K. Harada and N. Ichinose, "Effect of Molecular Mass of B-site Ions on the Electromechanical Coupling Factors of Lead-Based Perovskite Piezoelectric Materials". *Jpn. J. Appl. Phys.* **39** [9B] (2000) 5593-5596.

[34] B. Aurivillius, "Mixed Bismuth Oxides with Layer Lattices". *Arkiv Kemi* **1** [5] (1950) 463-480; *ibid*. **1** [6] (1950) 499-512; *ibid*. **2** [6] (1950) 519-527.

[35] G. A. Smolensky, V. A. Isupov and A. I. Agranovskaya, "A New Group of Ferroelectrics–(with Layered Structure)". *Soviet Phys.-Solid State* **1** [1] (1959) 149-150.

[36] G. A. Smolensky, V. A. Isupov and A. I. Agranovskaya, "Ferroelectrics of the Oxygen–Octahedral Type with Layered Structure". *Soviet Phys.-Solid State* **3** [3] (1961) 651-655.

[37] E. C. Subbarao, "Ferroelectricity in Mixed Bismuth Oxides with Layer-Type Structure". *J. Chem. Phys.* **34** [2] (1961) 695-696.

[38] E. C. Subbarao, "A Family of Ferroelectric Bismuth Compounds". *J. Phys. Chem. Solids* **23** (1962) 665-676.

[39] E. C. Subbarao, "Crystal Chemistry of Mixed Bismuth Oxides with Layer-Type Structure". *J. Am. Ceram. Soc.* **45** [4] (1962) 166-169.

[40] S. T. Zhang, Y. F. Chen, H. P. Sun, X. Q. Pan, W. S. Tan, Z. G. Liu and N. B. Ming, "Structural and Electrical Properties of *c*-axis Epitaxial Homologous $Sr_{m-3}Bi_4Ti_mO_{3m+3}$ (m = 3, 4, 5 and 6) Thin-Films". *J. Appl. Phys.* **94** [1] (2003) 544-550.

[41] S. E. Cummins and L. E. Cross, "Electrical and Optical Properties of Ferroelectric $Bi_4Ti_3O_{12}$ Single Crystals". *J. Appl. Phys.* **39** [5] (1968) 2268-2273.

[42] R. E. Newnham, R. W. Wolfe and J. F. Dorrian, "Structural Basis of Ferroelectricity in the Bismuth Titanate Family". *Mater. Res. Bull.* **6** [10] (1971) 1029-1040.

[43] B. Frit and J. P. Mercurio, "The Crystal-Chemistry and Dielectric-Properties of the Aurivillius Family of Complex Bismuth Oxides with Perovskite-Like Layered Structures". *J. Alloys Compd.* **188** [1-2] (1992) 27-35.

[44] Y. Noguchi, M. Miyayama and T. Kudo, "Ferroelectric Properties of Intergrowth $Bi_4Ti_3O_{12}$-$SrBi_4Ti_4O_{15}$ Ceramics". *Appl. Phys. Lett.* **77** [22] (2000) 3639-3641.

[45] P. Boullay, G. Trolliard and D. Mercurio, "Toward a Unified Approach to the Crystal Chemistry of Aurivillius-Type Compounds II. $Bi_7Ti_4NbO_{21}$, a Case Study". *J. Solid State Chem.* **164** [2] (2002) 261-271.

[46] R. E. Newnham, R. W. Wolfe, R. S. Horsey, F. A. Diazcolo and M. I. Kay and, "Crystal-Structure of $(Sr,Ba)Bi_2Ta_2O_9$". *Mater. Res. Bull.* **8** [10] (1973) 1183-1195.

[47] R. W. Wolfe and R. E. Newnham, "Crystal Structure of Bi_2WO_6". *Solid State Commun.* **7** [24] (1969) 1797-1802.

[48] J. F. Dorrian, R. E. Newnham, M. I. Kay and D. K. Smith, "Crystal-Structure of $Bi_4Ti_3O_{12}$". *Ferroelectrics* **3** [1] (1971) 17-28.

[49] A. D. Rae, J. G. Thompson and R. L. Withers, "Structure Refinement of Commensurately Modulated Bismuth Tungstate, Bi_2WO_6". *Acta Crystallogr., Sect. B: Struct. Sci.* **47** [6] (1991) 870-881.

[50] A. D. Rae, J. G. Thompson, R. L. Withers and A. C. Willis, "Structure Refinement of Commensurately Modulated Bismuth Titanate, $Bi_4Ti_3O_{12}$". *Acta Crystallogr., Sect. B: Struct. Sci.* **46** [4] (1990) 474-487.

[51] A. D. Rae, J. G. Thompson and R. L. Withers, "Structure Refinement of Commensurately Modulated Bismuth Strontium Tantalate, $Bi_2SrTa_2O_9$". *Acta Crystallogr., Sect. B: Struct. Sci.* **48** [4] (1992) 418-428.

[52] Ismunandar, B. J. Kennedy, Gunawan and Marsongkohadi, "Structure of $ABi_2Nb_2O_9$ (A = Sr, Ba): Refinement of Powder Neutron Diffraction Data". *J. Solid State Chem.* **126** [1] (1996) 135-141.

[53] C. A. Paz de Araujo, J. D. Cuchiaro, L. D. McMillan, M. C. Scott, J. F. Scott, "Fatigue-Free Ferroelectric Capacitors with Platinum-Electrodes". *Nature* **374** [6523] (1995) 627-629.

[54] J. Robertson, C. W. Chen, W. L. Warren and C. D. Gutleben, "Electronic Structure of the Ferroelectric Layered Perovskite $SrBi_2Ta_2O_9$". *Appl. Phys. Lett.* **69** [12] (1996) 1704-1706.

[55] K. Miura and M. Tanaka, "The Effect of Bi Ions Substituting at the Sr Site in $SrBi_2Ta_2O_9$". *Jpn. J. Appl. Phys.* **37** [5A] (1998) 2554-2558.

[56] K. Miura, "Electronic Properties of Ferroelectric $SrBi_2Ta_2O_9$, $SrBi_2Nb_2O_9$, and $PbBi_2Nb_2O_9$ with Optimized Structures". *Appl. Phys. Lett.* **80** [16] (2002) 2967-2969.

[57] M. G. Stachiotti, C. O. Rodriguez, C. Ambrosch-Draxl and N. E. Christensen, "Electronic Structure and Ferroelectricity in $SrBi_2Ta_2O_9$". *Phys. Rev. B* **61** [21] (2000) 14434-14439.

[58] Y. Shimakawa, Y. Kubo, Y. Nakagawa, T. Kamiyama, H. Asano and F. Izumi, "Crystal Structure and Ferroelectric Properties of $SrBi_2Ta_2O_9$ and $Sr_{0.8}Bi_{2.2}Ta_2O_9$". *Appl. Phys. Lett.* **74** [13] (1999) 1904-1906.

[59] Y. Noguchi, M. Miyayama and T. Kudo, "Direct Evidence of *A*-Site-Deficient Strontium Barium Tantalate and its Enhanced Ferroelectric Properties". *Phys. Rev. B* **63** [21] (2001) 214102.

[60] Y. Shimakawa, Y. Kubo, Y. Nakagawa, S. Goto, T. Kamiyama, H. Asano and F. Izumi, "Crystal Structure and Ferroelectric Properties of $ABi_2Ta_2O_9$ (A = Ca, Sr and Ba)". *Phys. Rev. B* **61** [10] (2000) 6559-6564.

[61] Y. Noguchi, M. Miyayama, K. Oikawa and T. Kamiyama, "Cation-Vacancy-Induced Low Coercive Field in La-Modified $SrBi_2Ta_2O_9$". *J. Appl. Phys.* **95** [8] (2004) 4261-4266.

[62] Y. Shimakawa, Y. Kubo, Y. Tauchi, T. Kamiyama, H. Asano and F. Izumi, "Structural Distortion and Ferroelectric Properties of $SrBi_2(Ta_{1-x}Nb_x)_2O_9$". *Appl. Phys. Lett.* **77** [17] (2000) 2749-2751.

[63] A. Onodera, K. Yoshio, C. C. Myint, S. Kojima, H. Yamashita and T. Takama, "Thermal and Structural Studies of Phase Transitions in Layered Perovskite $SrBi_2Ta_2O_9$". *Jpn. J. Appl. Phys.* **38** [9B] (1999) 5683-5685.

[64] A. Onodera, T. Kubo, K. Yoshio, S. Kojima, H. Yamashita and T. Takama, "Crystal Structure of High-Temperature Paraelectric Phase in Bi-Layered Perovskite $Sr_{0.85}Bi_{2.1}Ta_2O_9$". *Jpn. J. Appl. Phys.* **39** [9B] (2000) 5711-5715.

[65] C. H. Hervoches, J. T. S. Irvine and P. Lightfoot, "Two High-Temperature Paraelectric Phases in $Sr_{0.85}Bi_{2.1}Ta_2O_9$". *Phys. Rev. B* **64** [10] (2001) 100102.

[66] R. Macquart, B. J. Kennedy, B. A. Hunter, C. J. Howard and Y. Shimakawa, "Structural Phase Transitions in the Ferroelectric Oxides $SrBi_2Ta_2O_9$". *Integr. Ferroelectr.* **44** (2002) 101-112.

[67] S. Kamba, J. Pokorny, V. Porokhonsky, J. Petzelt, M. P. Moret, A. Garg, Z. H. Barber and R. Zallen, "Ferroelastic Phase in $SrBi_2Ta_2O_9$ and Study of the Ferroelectric Phase-Transition Dynamics". *Appl. Phys. Lett.* **81** [6] (2002) 1056-1058.

[68] K. Yoshio, I. Matsubara, A. Yamada, A. Onodera, A. Sakai and H. Yamashita, "Phase Transition in Ferroelectric $SrBi_2Ta_2O_9$ Single Crystal". *J. Korean Phys. Soc.* **42** (2003) S1034-S1037.

[69] A. Onodera, K. Yoshio and H. Yamashita, "Structural Study of Intermediate Phase in Layered Perovskite $SrBi_2Ta_2O_9$ Single Crystal". *Jpn. J. Appl. Phys.* **42** [9B] (2003) 6218-6221.

[70] R. Macquart, B. J. Kennedy, T. Vogt and C. J. Howard, "Phase Transition in $BaBi_2Nb_2O_9$: Implications for Layered Ferroelectrics". *Phys. Rev. B* **66** [21] (2002) 212102.

[71] C. H. Hervoches, A. Snedden, R. Riggs, S. H. Kilcoyne, P. Manuel and P. Lightfoot, "Structural Behavior of the Four-Layer Aurivillius-Phase Ferroelectrics $SrBi_4Ti_4O_{15}$ and $Bi_5Ti_3FeO_{15}$". *J. Solid State Chem.* **164** [2] (2002) 280-291; *ibid*. **166** [2] (2002) 449.

[72] A. Snedden, C. H. Hervoches and P. Lightfoot, "Ferroelectric Phase Transitions in $SrBi_2Nb_2O_9$ and $Bi_5Ti_3FeO_{15}$: A Powder Neutron Diffraction Study". *Phys. Rev. B* **67** [9] (2003) 092102.

[73] R. Macquart, B. J. Kennedy, T. Kamiyama and F. Izumi, "Structural Phase Transitions in the Ferroelectric Oxides $Ba_{1-x}Pb_xBi_2Nb_2O_9$ (x = 0.375, 0.625)". *J. Phys.: Condens. Matter* **16** [30] (2004) 5443-5442.

[74] Y. Shimakawa, H. Imai, H. Kimura, Y. Kubo, E. Nishibori, M. Takata, M. Sakata, K. Kato and Z. Hiroi, "Orbital Hybridization and Covalency in Paraelectric and Ferroelectric $SrBi_2Nb_2O_9$". *Phys. Rev. B* **66** [14] (2002) 144110.

[75] T. Noguchi, T. Hase and Y. Miyasaka, "Analysis of the Dependence of Ferroelectric Properties of Strontium Bismuth Tantalate (SBT) Thin Films on the Composition and Process Temperature". *Jpn. J. Appl. Phys.* **35** [9B] (1996) 4900-4904.

[76] R. D. Shannon, "Revised Effective Ionic-Radii and Systematic Studies of Interatomic Distances in Halides and Chalcogenides". *Acta Crystallogr., Sect. A: Cryst. Phys. Diffr., Theor. Gen. Crystallogr.* **32** (1976) 751-767.

[77] G. Agricola, "Bermannus, sive De re Metallica". Basle (1530).

[78] D. Elwell and H. J. Scheel, "Crystal Growth from High Temperature Solution". Academic Press, London (1975).

[79] B. N. Roy, "Crystal Growth from Melts". John Wiley & Sons, England (1992).

[80] D. T. Hurle, "Handbook of Crystal Growth 2: Basic Techniques". Elsevier Science, North Holland (1994).

[81] M. A. Gaudin, *C. R. Acad. Sci. Paris* **69** (1869) 1342.

[82] J. P. Remeika, "A Method for Growing Barium Titanate Single Crystals". *J. Am. Chem. Soc.* **76** [3] (1954) 940-941.

[83] W. Tolksdorf, "Flux Growth", in *Handbook of Crystal Growth 2: Basic Techniques*. Ed. D. T. Hurle, Elsevier Science, North Holland (1994) 563-611.

[84] K. Bethe and F. Welz, "Preparation and Properties of (Ba,Sr)TiO_3 Single Crystals". *Mater. Res. Bull.* **6** [4] (1971) 209-218.

[85] D. Rytz and H. J. Scheel, "Crystal Growth of $KTa_{1-x}Nb_xO_3$ ($0 < x \leq 0.04$) Solid Solutions by a Slow-Cooling Method". *J. Cryst. Growth* **59** [3] (1982) 468-484.

[86] D. Rytz, B. A. Wechsler, C. C. Nelson and K. W. Kirby, "Top Seeded Solution Growth of $BaTiO_3$, $KNbO_3$, $SrTiO_3$, $Bi_{12}TiO_{20}$ and $La_{2-x}Ba_xCuO_4$". *J. Cryst. Growth* **99** [1-4] (1990) 864-868.

[87] S. E. Park, S. J. Chung and I. T. Kim, "Ferroic Phase Transitions in $(Na_{1/2}Bi_{1/2})TiO_3$ Crystals". *J. Am. Ceram. Soc.* **79** [5] (1996) 1290-1296.

[88] Y.-M. Chiang, G. W. Farrey and A. N. Soukhojak, "Lead-Free High-Strain Single-Crystal Piezoelectrics in the Alkaline-Bismuth-Titanate Perovskite Family". *Appl. Phys. Lett.* **73** [25] (1998) 3683-3685.

[89] N. Setter and L. E. Cross, "Flux Growth of Lead Scandium Tantalate $Pb(Sc_{0.5}Ta_{0.5})O_3$ and Lead Magnesium Niobate $Pb(Mg_{1/3}Nb_{2/3})O_3$ Single Crystals". *J. Cryst. Growth* **50** [2] (1980) 555-556.

[90] S.-E. Park, M. L. Mulvihill, G. Risch and T. R. Shrout, "The Effect of Growth Conditions on the Dielectric Properties of $Pb(Zn_{1/3}Nb_{2/3})O_3$ Single Crystals". *Jpn. J. Appl. Phys.* **36** [3A] (1997) 1154-1158.

[91] J. Kuwata, K. Uchino and S. Nomura, "Dielectric and Piezoelectric Properties of $0.91Pb(Zn_{1/3}Nb_{2/3}) - 0.09PbTiO_3$ Single-Crystals". *Jpn. J. Appl. Phys.* **21** [9] (1982) 1298-1302.

[92] M. L. Mulvihill, S.-E. Park, G. Risch, Z. Li, K. Uchino and T. R. Shrout, "The Role of Processing Variables in the Flux Growth of Lead Zinc Niobate - Lead Titanate Relaxor Ferroelectric Single Crystals". *Jpn. J. Appl. Phys.* **35** [7] (1996) 3984-3990.

[93] T. Kobayashi, S. Shimanuki, S. Saitoh and Y. Yamashita, "Improved Growth of Large Lead Zinc Niobate Titanate Piezoelectric Single Crystals for Medical Ultrasonic Transducers". *Jpn. J. Appl. Phys.* **36** [9B] (1997) 6035-6038.

[94] M. Dong and Z.-G. Ye, "High-Temperature Solution Growth and Characterization of the Piezo-/Ferroelectric $(1 - x)$ $Pb(Mg_{1/3}Nb_{2/3})O_3 - x$ $PbTiO_3$ [PMNT] Single Crystals". *J. Cryst. Growth* **209** [1] (2000) 81-90.

[95] S. Gentil, G. Robert, N. Setter, P. Tissot and J.-P. Rivera, "Growth and Properties of Transparent $Pb(Zn_{1/3}Nb_{2/3})O_3 - PbTiO_3$ Single Crystals with Cubic Habitus". *Jpn. J. Appl. Phys.* **39** [5A] (2000) 2732-2735.

[96] K. Harada, S. Shimanuki, T. Kobayashi, Y. Yamashita and S. Saitoh, "Growth of High-Quality $Pb((Zn_{1/3}Nb_{2/3})_{0.91}Ti_{0.09})O_3$ Single Crystals by Excess ZnO Addition". *J. Am. Ceram. Soc.* **85** [1] (2002) 145-149.

[97] Y. Yamashita and K. Harada, "Crystal Growth and Electrical Properties of Lead Scandium Niobate - Lead Titanate Binary Single Crystals". *Jpn. J. Appl. Phys.* **36** [9B] (1997) 6039-6042.

[98] S. J. Zhang, P. W. Rehrig, C. Randall and T. R. Shrout, "Crystal Growth and Electrical Properties of $Pb(Yb_{1/2}Nb_{1/2})O_3 - PbTiO_3$ Perovskite Single Crystals". *J. Cryst. Growth* **234** [2-3] (2002) 415-420.

[99] B. M. Wanklyn and B. E. Watts, "Nucleation Sites on Platinum Surfaces in Flux Growth". *Mater. Res. Bull.* **19** [6] (1984) 711-716.

[100] G. H. Bennett, "Seeded Growth of Garnet from Molten Salts". *J. Cryst. Growth* **3-4** (1968) 458-462.

[101] W. Tolksdorf, "Growth of Yttrium Iron Garnet Single Crystals". *J. Cryst. Growth* **3-4** (1968) 463-466.

[102] T. Takenaka and K. Sakata, "Grain-Orientation and Electrical-Properties of Hot-Forged $Bi_4Ti_3O_{12}$ Ceramics". *Jpn. J. Appl. Phys.* **19** [1] (1980) 31-39.

[103] C. Duran, S. Trolier-McKinstry and G. L. Messing, "Dielectric and Piezoelectric Properties of Textured $Sr_{0.53}Ba_{0.47}Nb_2O_6$ Ceramics Prepared by Templated Grain Growth". *J. Mater. Res.* **17** [9] (2002) 2399-2409; *erratum* **18** [1] (2003) 228-238.

[104] K. Nagata, Y. Yamamoto, H. Igarashi and K. Okazaki, "Properties of the Hot-Pressed Strontium Barium Niobate Ceramics". *Ferroelectrics* **38** [1-4] (1981) 853-856.

[105] T. Kimura, T. Yoshimoto, N. Iida, Y. Fujita and T. Yamaguchi, "Mechanism of Grain-Orientation during Hot-Pressing of Bismuth Titanate". *J. Am. Ceram. Soc.* **72** [1] (1989) 85-89.

[106] Z. Zhang, H. X. Yan, P. H. Xiang, X. L. Dong and Y. L. Wang, "Grain Orientation Effects on the Properties of a Bismuth Layer-Structured Ferroelectric (BLSF) Bi_3NbTiO_9 Solid Solution". *J. Am. Ceram. Soc.* **87** [4] (2004) 602-605.

[107] G. L. Messing, S. Trolier-McKinstry, E. M. Sabolsky, C. Duran, S. Kwon, B. Brahmaroutu, P. Park, H. Yilmaz, P. W. Rehrig, K. B. Eitel, E. Suvaci, M. M. Seabaugh and K. S. Oh, "Templated Grain Growth of Textured Piezoelectric Ceramics". *Crit. Rev. Solid State Mater. Sci.* **29** [2] (2004) 45-96.

[108] K. Kugimiya, K. Hirota and K. Matsuyama, "Process for Producing Single-Crystal Ceramics". *U.S. Patent* **4,900,393** (1990).

[109] M. P. Harmer, H. M. Chan, H.-Y. Lee, A. M. Scotch, T. Li, F. Meschke and A. Khan, "Method for Growing Single Crystals from Polycrystalline Precursors". *U.S. Patent* **6,048,394** (2000).

[110] G. L. Messing and E. Suvaci, "Method for Fabricating Textured Ceramics". *U.S. Patent* **6,251,335** (2001).

[111] M. Kitayama, K. Hirao, M. Toriyama and S. Kanzaki, "Modeling and simulation of grain growth in Si_3N_4 - I. Anisotropic Ostwald ripening". *Acta Mater.* **46** [18] (1998) 6541-6550.

[112] T. Li, S. X. Wu, A. Khan, A. M. Scotch, H. M. Chan and M. P. Harmer, "Heteroepitaxial Growth of Bulk Single-Crystal $Pb(Mg_{1/3}Nb_{2/3})O_3$ – 32 mol% $PbTiO_3$ from (111) $SrTiO_3$". *J. Mater. Res.* **14** [8] (1999) 3189-3191.

[113] P. W. Rehrig, "Templated Grain Growth of $BaTiO_3$-Based Perovskite Single Crystals". Ph.D. thesis at The Pennsylvania State University, Pennsylvania (1999).

[114] M. M. Seabaugh, G. L. Messing and M. D. Vaudin, "Texture Development and Microstructure Evolution in Liquid-Phase-Sintered Alpha-Alumina Ceramics Prepared by Templated Grain Growth". *J. Am. Ceram. Soc.* **83** [12] (2000) 3109-3116.

[115] M. M. Seabaugh, I. H. Kerscht and G. L. Messing, "Texture Development by Templated Grain Growth in Liquid-Phase-Sintered Alpha-Alumina". *J. Am. Ceram. Soc.* **80** [5] (1997) 1181-1188.

[116] T. Takeuchi, T. Tani and Y. Saito, "Piezoelectric Properties of Bismuth Layer-Structured Ferroelectric Ceramics with a Preferred Orientation Processed by the Reactive Templated Grain Growth Method". *Jpn. J. Appl. Phys.* **38** [9B] (1999) 5553-5556.

[117] H. Yilmaz, G. L. Messing and S. Trolier-McKinstry, "(Reactive) Templated Grain Growth of Textured Sodium Bismuth Titanate ($Na_{1/2}Bi_{1/2}TiO_3$ - $BaTiO_3$) Ceramics - I processing". *J. Electroceram.* **11** [3] (2003) 207-215.

[118] D. L. West and D. A. Payne, "Reactive - Templated Grain Growth of $Bi_{1/2}(Na,K)_{1/2}TiO_3$: Effects of Formulation on Texture Development". *J. Am. Ceram. Soc.* **86** [7] (2003) 1132-1137.

[119] S. H. Hong and G. L. Messing, "Development of Textured Mullite by Templated Grain Growth". *J. Am. Ceram. Soc.* **82** [4] (1999) 867-872.

[120] E. Suvaci, M. M. Seabaugh and G. L. Messing, "Reaction-Based Processing of Textured Alumina by Templated Grain Growth". *J. Eur. Ceram. Soc.* **19** [13-14] (1999) 2465-2474.

[121] E. Suvaci and G. L. Messing, "Critical Factors in the Templated Grain Growth of Textured Reaction-Bonded Alumina". *J. Am. Ceram. Soc.* **83** [8] (2000) 2041-2048.

[122] E. Suvaci, K.-S. Oh and G. L. Messing, "Kinetics of Template Growth in Alumina during the Process of Templated Grain Growth (TGG)". *Acta Mater.* **49** [11] (2001) 2075-2081.

[123] S. H. Hong and G. L. Messing, "Anisotropic Grain Growth in Diphasic-Gel-Derived Titania-Doped Mullite". *J. Am. Ceram. Soc.* **81** [5] (1998) 1269-1277.

[124] H. Watanabe, T. Kimura and T. Yamaguchi, "Sintering of Plate-Like Bismuth Titanate Powder Compacts with Preferred Orientation". *J. Am. Ceram. Soc.* **74** [1] (1991) 139-147.

[125] J. A. Horn, S. C. Zhang, U. Selvaraj, G. L. Messing and S. Trolier-McKinstry, "Templated Grain Growth of Textured Bismuth Titanate". *J. Am. Ceram. Soc.* **82** [4] (1999) 921-926.

[126] K. Hirao, T. Nagaoka, M. E. Brito and S. Kanzaki, "Microstructure Control of Silicon-Nitride by Seeding with Rodlike Beta-Silicon Nitride Particles". *J. Am. Ceram. Soc.* **77** [7] (1994) 1857-1862.

[127] K. Hirao, M. Ohashi, M. E. Brito and S. Kanzaki, "Processing Strategy for Producing Highly Anisotropic Silicon-Nitride". *J. Am. Ceram. Soc.* **78** [6] (1995) 1687-1690.

[128] M. D. Sacks, G. W. Scheiffele and G. A. Staab, "Fabrication of Textured Silicon Carbide via Seeded Anisotropic Grain Growth". *J. Am. Ceram. Soc.* **79** [6] (1996) 1611-1616.

[129] T. Li, A. M. Scotch, H. M. Chan, M. P. Harmer, S. E. Park, T. R. Shrout and J. R. Michael, "Single Crystals of $Pb(Mg_{1/3}Nb_{2/3})O_3$ – 35 mol% $PbTiO_3$ from Polycrystalline Precursors". *J. Am. Ceram. Soc.* **81** [1] (1998) 244-248.

[130] A. Khan, F. A. Meschke, T. Li, A. M. Scotch, H. M. Chan and M. P. Harmer, "Growth of $Pb(Mg_{1/3}Nb_{2/3})O_3$ – 35 mol% $PbTiO_3$ Single Crystals from (111) Substrates by Seeded Polycrystal Conversion". *J. Am. Ceram. Soc.* **82** [11] (1999) 2958-2962.

[131] E. M. Sabolsky, G. L. Messing and S. Trolier-McKinstry, "Kinetics of Templated Grain Growth of $0.65Pb(Mg_{1/3}Nb_{2/3})O_3 – 0.35PbTiO_3$". *J. Am. Ceram. Soc.* **84** [11] (2001) 2507-2513.

[132] C. Duran, S. Trolier-McKinstry and G. L. Messing, "Fabrication and Electrical Properties of Textured $Sr_{0.53}Ba_{0.47}Nb_2O_6$ Ceramics by Templated Grain Growth". *J. Am. Ceram. Soc.* **83** [9] (2000) 2203-2213.

[133] P. W. Rehrig, S. E. Park, S. Trolier-McKinstry, G. L. Messing, B. Jones and T. R. Shrout, "Piezoelectric Properties of Zirconium-Doped Barium Titanate Single Crystals Grown by Templated Grain Growth". *J. Appl. Phys.* **86** [3] (1999) 1657-1661.

[134] P. W. Rehrig, G. L. Messing and S. Trolier-McKinstry, "Templated Grain Growth of Barium Titanate Single Crystals". *J. Am. Ceram. Soc.* **83** [11] (2000) 2654-2660.

[135] S. H. Hong, S. Trolier-McKinstry and G. L. Messing, "Dielectric and Electro mechanical Properties of Textured Niobium-Doped Bismuth Titanate Ceramics". *J. Am. Ceram. Soc.* **83** [1] (2000) 113-118.

[136] Y. M. Kan, P. L. Wang, Y. X. Li, Y. B. Cheng and D. S. Yan, "Fabrication of Textured Bismuth Titanate by Templated Grain Growth using Aqueous Tape Casting". *J. Eur. Ceram. Soc.* **23** [12] (2003) 2163-2169.

[137] H. Ogawa, M. Kimura, A. Ando and Y. Sakabe, "Temperature Dependence of Piezoelectric Properties of Grain-Oriented $CaBi_4Ti_4O_{15}$ Ceramics". *Jpn. J. Appl. Phys.* **40** [9B] (2001) 5715-5718.

[138] A. Moure, A. Castro and L. Pardo, "Improvement by Recrystallization of Aurivillius-Type Structure Piezoceramics from Mechanically Activated Precursors". *Acta Mater.* **52** [4] (2004) 945-957.

[139] W. J. Merz, "Domain Formation and Domain Wall Motions in Ferroelectric $BaTiO_3$ Single Crystals". *Phys. Rev.* **95** [3] (1954) 690-698.

[140] J. F. Scott and C. A. Paz de Araujo, "Ferroelectric Memories". *Science* **246** [4936] (1989) 1400-1405.

[141] P. K. Larsen, R. Cuppens and G. A. Spierings, "Ferroelectric Memories". *Ferroelectrics* **128** [1-4] (1992) 265-292.

[142] R. E. Jones, P. D. Maniar, R. Moazzami, P. Zurcher, J. Z. Witowski, Y. T. Lii, P. Chu and S. J. Gillespie, "Ferroelectric Non-Volatile Memories for Low-Voltage, Low-Power Applications". *Thin Solid Films* **270** [1-2] (1995) 584-588.

[143] J. F. Scott, "Ferroelectric Memories". *Phys. World* **8** [2] (1995) 46-50.

[144] O. Auciello, J. F. Scott and R. Ramesh, "The Physics of Ferroelectric Memories". *Phys. Today* **51** [7] (1998) 22-27.

[145] H. Takasu, "The Ferroelectric Memory and its Applications". *J. Electroceram.* **4** [2-3] (2000) 327-338.

[146] T. Mikolajick, C. Dehm, W. Hartner, I. Kasko, M. J. Kastner, N. Nagel, M. Moert and C. Mazure, "FeRAM Technology for High Density Applications". *Microelectron. Reliab.* **41** [7] (2001) 947-950.

[147] R. Ramesh, S. Aggarwal and O. Auciello, "Science and Technology of Ferroelectric Films and Heterostructures for Non-Volatile Ferroelectric Memories". *Mater. Sci. Eng. R* **32** [6] (2001) 191-236.

[148] J. F. Scott, "Ferroelectric Random Access Memories - Fundamental and Applications - Overview". *Topics Appl. Phys.* **93** (2004) 3-16.

[149] G. R. Fox, R. Bailey, W. B. Kraus, F. Chu, S. Sun and T. Davenport, "The Current Status of FeRAM". *Topics Appl. Phys.* **93** (2004) 139-148.

[150] S. Masui, S. Fueki, K. Masutani, A. Inoue, T. Teramoto, T. Suzuki and S. Kawashima, "The Application of FeRAM to Future Information Technology World". *Topics Appl. Phys.* **93** (2004) 271-283.

[151] Y. Shimada, K. Arita, E. Fujii, T. Nasu, Y. Nagano, A. Noma, Y. Izutsu, K. Nakao, K. Tanaka, T. Yamada, Y. Uemoto, K. Asari, G. Nakane, A. Inoue, T. Sumi, T. Nakakuma, S. Chaya, H. Hirano, Y. Judai, Y. Sasai, T. Otsuki, "Advanced LSI Embedded with FeRAM for Contactless IC Cards and its Manufacturing Technology". *Integr. Ferroelectr.* **27** [1-4] (1999) 1335-1358.

[152] P. Langevin, "Oeuvres Scientifiques de Paul Langevin". Centre National de la Recherche Scientifique, Paris (1950).

[153] J. T. Evans and R. Womack, "An Experimental 512-bit Nonvolatile Memory with Ferroelectric Storage Cell". *IEEE J. Solid-State Circuits* **23** [5] (1988) 1171-1175.

[154] S. S. Eaton, D. B. Butler, M. Parris, D. Wilson and H. McNeillie, "A Ferroelectric Nonvolatile Memory". *Proc. IEEE Int. Solid-State Conf.* (1988) 130-131.

[155] S. K. Dey and R. Zuleeg, "Integrated Sol-Gel PZT Thin-Films on Pt, Si, and Gaas for Nonvolatile Memory Applications". *Ferroelectrics* **108** (1990) 37-46.

[156] R. Ramesh, W. K. Chan, B. Wilkens, H. Gilchrist, T. Sands, J. M. Tarascon, V. G. Keramidas, D. K. Fork, J. Lee and A. Safari, "Fatigue and Retention in Ferroelectric Y-Ba-Cu-O / Pb-Zr-Ti-O / Y-Ba-Cu-O Heterostructures". *Appl. Phys. Lett.* **61** [13] (1992) 1537-1539.

[157] T. Nakamura, Y. Nakao, A. Kamisawa and H. Takasu, "Preparation of $Pb(Zr,Ti)O_3$ Thin-Films on Electrodes Including IrO_2". *Appl. Phys. Lett.* **65** [12] (1994) 1522-1524.

[158] J. J. Lee, C. L. Thio and S. B. Desu, "Electrode Contacts on Ferroelectric $Pb(Zr_xTi_{1-x})O_3$ and $SrBi_2Ta_2O_9$ Thin-Films and their Influence on Fatigue Properties". *J. Appl. Phys.* **78** [8] (1995) 5073-5078.

[159] C. Guerrero, J. Roldan, C. Ferrater, M. V. Garcia-Cuenca, F. Sanchez and M. T. Varela, "Growth and Characterization of Epitaxial Ferroelectric $PbZr_xTi_{1-x}O_3$ Thin-Film Capacitors with $SrRuO_3$ Electrodes for Non-Volatile Memory Applications". *Solid-State Electron.* **45** [8] (2001) 1433-1440.

[160] N. Inoue, T. Takeuchi and Y. Hayashi, "Compositional Design of $Pb(Zr,Ti)O_3$ for Highly Reliable Ferroelectric Memories". *IEEE Trans. Electron Devices* **49** [9] (2002) 1572-1579.

[161] K. Amanuma, T. Hase and Y. Miyasaka, "Preparation and Ferroelectric properties of $SrBi_2Ta_2O_9$ Thin-Films". *Appl. Phys. Lett.* **66** [2] (1995) 221-223.

[162] R. Dat, J. K. Lee, O. Auciello, A. I. Kingon, "Pulsed-Laser Ablation Synthesis and Characterization of Layered $Pt/SrBi_2Ta_2O_9/Pt$ Ferroelectric Capacitors with Practically no Polarization Fatigue". *Appl. Phys. Lett.* **67** [4] (1995) 572-574.

[163] T. Mihara, H. Yoshimori, H. Watanabe and C. A. Paz de Araujo, "Characteristic of Bismuth Layered $SrBi_2Ta_2O_9$ Thin-Films Capacitors and Comparison with $Pb(Zr,Ti)O_3$". *Jpn. J. Appl. Phys.* **34** [9B] (1995) 5233-5239.

[164] H. Watanabe, T. Mihara, H. Yoshimori and C. A. Paz de Araujo, "Preparation of Ferroelectric Thin-Films of Bismuth Layer Structured Compounds". *Jpn. J. Appl. Phys.* **34** [9B] (1995) 5240-5244.

[165] J. F. Scott, F. M. Ross, C. A. Paz de Araujo, M. C. Scott and M. Huffman, "Structure and Device Characteristics of $SrBi_2Ta_2O_9$-Based Nonvolatile Random-Access Memories". *Mater. Res. Soc. Bull.* **21** [7] (1996) 33-39.

[166] D. J. Taylor, R. E. Jones, P. Zurcher, P. Chu, Y. T. Lii, B. Jiang, S. J. Gillespie, "Electrical Properties of $SrBi_2Ta_2O_9$ Thin-Films and their Temperature Dependence for Ferroelectric Nonvolatile Memory Applications". *Appl. Phys. Lett.* **68** [16] (1996) 2300-2302.

[167] J. P. Han and T. P. Ma, "$SrBi_2Ta_2O_9$ Memory Capacitor on Si with a Silicon Nitride Buffer". *Appl. Phys. Lett.* **72** [10] (1998) 1185-1186.

[168] Y. Igarashi, K. Tani, M. Kasai, K. Ashikaga and T. Ito, "Submicron Ferroelectric Capacitors Fabricated by Chemical Mechanical Polishing Process for High-Density Ferroelectric Memories". *Jpn. J. Appl. Phys.* **39** [4B] (2000) 2083-2086.

[169] J. Kawahara, T. Matsuki, Y. Y. Hayashi, K. Igarashi, M. Tani, K. Kasai, "Analysis of Processing Damage on a Ferroelectric $SrBi_2Ta_2O_9$ Capacitor for Ferroelectric Random Access Memory Device Fabrication". *Jpn. J. Appl. Phys.* **40** [4A] (2001) 2341-2347.

[170] K. H. Kim, J. P. Han, S. W. Jung and T. P. Ma, "Ferroelectric DRAM (FEDRAM) FET with metal/$SrBi_2Ta_2O_9$/SiN/Si Gate Structure". *IEEE Electron Device Lett.* **23** [2] (2002) 82-84.

[171] R. Ramesh, A. Inam, W. K. Chan, B. Wilkens, K. Myers, K. Remschnig, D. L. Hart and J. M. Tarascon, "Epitaxial Cuprate Superconductor Ferroelectric Heterostructures". *Science* **252** [5008] (1991) 944-946.

[172] T. Kijima, S. Satoh, H. Matsunaga and M. Koba, "Ultra-Thin Fatigue-Free $Bi_4Ti_3O_{12}$ Films for Nonvolatile Ferroelectric Memories". *Jpn. J. Appl. Phys.* **35** [2B] (1996) 1246-1250.

[173] B. H. Park, B. S. Kang, S. D. Bu, T. W. Noh, J. Lee and W. Jo, "Lanthanum-Substituted Bismuth Titanate for use in Non-Volatile Memories". *Nature* **401** [6754] (1999) 682-684.

[174] U. Chon, H. M. Jang, M. G. Kim and C. H. Chang, "Layered Perovskites with Giant Spontaneous Polarizations for Nonvolatile Memories". *Phys. Rev. Lett.* **89** [8] (2002) 087601.

[175] H. N. Lee, D. Hesse, N. Zakharov and U. Gosele, "Ferroelectric $Bi_{3.25}La_{0.75}Ti_3O_{12}$ Films of Uniform *a*-axis Orientation on Silicon Substrates". *Science* **296** [5575] (2002) 2006-2009.

[176] Y. Shimada, "Testing and Reliability". *Topics Appl. Phys.* **93** (2004) 177-194.

[177] J. M. Benedetto, R. A. Moore and F. B. McLean, "Effects of Operating-Conditions on the Fast-Decay Component of the Retained Polarization in Lead-Zirconate-Titanate Thin-Films". *J. Appl. Phys.* **75** [1] (1994) 460-466.

[178] J. J. Lee, C. L. Thio and S. B. Desu, "Retention and Imprint Properties of Ferroelectric Thin-Films". *Phys. Status Solidi A* **151** [1] (1995) 171-182.

[179] J. O. Olowolafe, R. E. Jones, A. C. Campbell, R. I. Hegde, C. J. Mogab and R. B. Gregory, "Effects of Anneal Ambients and Pt Thickness on Pt/Ti and Pt/Ti/TiN Interfacial Reactions". *J. Appl. Phys.* **73** [4] (1993) 1764-1772.

[180] J. Lee, L. Johnson, A. Safari, R. Ramesh, T. Sands, H. Gilchrist and V. G. Keramidas, "Effects of Crystalline Quality and Electrode Material on Fatigue in $Pb(Zr,Ti)O_3$ Thin-Film Capacitors". *Appl. Phys. Lett.* **63** [1] (1993) 27-29.

[181] H. N. AlShareef, A. I. Kingon, X. Chen, K. R. Bellur and O. Auciello, "Contribution of Electrodes and Microstructures to the Electrical-Properties of $Pb(Zr_{0.53}Ti_{0.47})O_3$ Thin-Film Capacitors". *J. Mater. Res.* **9** [11] (1994) 2968-2975.

[182] C. M. Foster, G. R. Bai, R. Csencsits, J. Vetrone, R. Jammy, L. A. Wills, E. Carr and J. Amano, "Single-Crystal $Pb(Zr_xTi_{1-x})O_3$ Thin-Films Prepared by Metal-Organic Chemical Vapor Deposition: Systematic Compositional Variation of Electronic and Optical Properties". *J. Appl. Phys.* **81** [5] (1997) 2349-2357.

[183] Y. Shimada, K. Nakao, A. Inoue, M. Azuma, Y. Uemoto, E. Fujii and T. Otsuki, "Temperature Effects on Charge Retention Characteristics of Integrated $SrBi_2(Ta,Nb)_2O_9$ Capacitors". *Appl. Phys. Lett.* **71** [17] (1997) 2538-2540.

[184] S. O. Ryu, P. C. Joshi and S. B. Desu, "Low Temperature Processed $0.7SrBi_2Ta_2O_9$-$0.3Bi_3TaTiO_9$ Thin-Films Fabricated on Multilayer Electrode-Barrier Structure for High-Density Ferroelectric Memories". *Appl. Phys. Lett.* **75** [14] (1999) 2126-2128.

[185] M. Mitsuya, N. Nukaga, T. Watanabe, H. Funakubo, K. Saito and M. Osada, "Low Leakage Current and Good Ferroelectric Properties of $SrBi_2(Ta_{0.7}Nb_{0.3})_2O_9$-$Bi_3TiTaO_9$ Solid Solution Thin-Film". *Appl. Phys. Lett.* **79** [13] (2001) 2067-2069.

[186] G. R. Fox, F. Chu and T. Davenport, "Current and Future Ferroelectric Nonvolatile Memory Technology". *J. Vac. Sci. Technol. B* **19** [5] (2001) 1967-1971.

[187] S. E. Park and T. R. Shrout, "Ultrahigh Strain and Piezoelectric Behavior in Relaxor Based Ferroelectric Single Crystals". *J. Appl. Phys.* **82** [4] (1997) 1804-1811.

[188] S. E. Park and T. R. Shrout, "Characteristics of Relaxor-Based Piezoelectric Single Crystals for Ultrasonic Transducers". *IEEE Trans. Ultrason. Ferroelectr. Freq. Control* **44** [5] (1997) 1140-1147.

[189] R. C. Turner, P. A. Fuierer, R. E. Newnham and T. R. Shrout, "Materials for High-Temperature Acoustic and Vibration Sensors - A Review". *Appl. Acoustics* **41** [4] (1994) 299-324.

[190] G. H. Haertling, "Ferroelectric Ceramics: History and Technology". *J. Am. Ceram. Soc.* **82** [4] (1999) 797-818.

[191] R. Guo, L. E. Cross, S. E. Park, B. Noheda, D. E. Cox and G. Shirane, "Origin of the High Piezoelectric Response in $PbZr_{1-x}Ti_xO_3$". *Phys. Rev. Lett.* **84** [23] (2000) 5423-5426.

[192] See the following web pages:
http://www.europa.eu.int/comm/environment/waste/;
http://www.environment-agency.gov.uk/business/444217/444663/;
http://www.defra.gov.uk/environment/waste/index.htm;
http://www.icer.org.uk/legislation.htm; http://www.plastics-in-elv.org

[193] D. Damjanovic, "Materials for High Temperature Piezoelectric Transducers". *Curr. Opin. Solid State Mater. Sci.* **3** [5] (1998) 469-473.

[194] T. Takenaka and H. Nagata, "Current Status and Prospects of Lead-Free Piezoelectric Ceramics". *J. Eur. Ceram. Soc.* **25** [12] (2005) 2693-2700.

[195] T. Takenaka, K. Maruyama and K. Sakata, "$(Bi_{1/2}Na_{1/2})TiO_3$-$BaTiO_3$ System for Lead-Free Piezoelectric Ceramics". *Jpn. J. Appl. Phys.* **30** [9B] (1991) 2236-2239.

[196] Y. Saito, H. Takao, T. Tani, T. Nonoyama, K. Takatori, T. Homma, T. Nagaya and M. Nakamura, "Lead-Free Piezoceramics". *Nature* **432** [7013] (2004) 84-87.

[197] H. S. Shulman, M. Testorf, D. Damjanovic and N. Setter, "Microstructure, Electrical Conductivity, and Piezoelectric Properties of Bismuth Titanate". *J. Am. Ceram. Soc.* **79** [12] (1996) 3124-3128.

Chapter 2

Materials Processing and Experimental Techniques

2.1. Introduction

SBT and SBN single crystals were grown using the high-temperature self-flux solution method described elsewhere.[1-3] As mentioned in Chapter 1, during this process the material to be crystallized is dissolved at a high temperature in a suitable solvent inside a platinum crucible and crystallization is achieved by a controlled cooling, *i.e.*, by making the solution critically supersaturated. This chapter is partially devoted to the details of the experiment, which include the processing for SBT and SBN single crystals growth, and details about the methods used to orient, cut, polish, and electrode the single crystals. Besides, detailed descriptions of the experimental techniques for characterizing structurally and electrically both single crystals are also included.

In addition, textured SBT ceramics were produced by templated grain growth using the grown SBT single crystals as templates. As described in Chapter 1 (section 1.5.2), to fabricate textured materials by TGG a small amount of anisotropic templates has to be dispersed and oriented in a matrix of relatively fine and equiaxed particles (polycrystalline material), and finally sintered to produce dense textured ceramics.[4] The second part of this chapter is devoted to the details of the processing of textured SBT ceramics. Texture can be evaluated by a number of techniques including relative peaks heights (*Lotgering factor*), pole figures, and stereology. Each texture measurement technique has its strengths and weaknesses, which affect the quality of the analysis. All these techniques are used for the determination of the texture degree in SBT ceramics and, as such, are described here.

2.2. $SrBi_2M_2O_9$ (M = Ta, Nb) Single Crystal Growth

2.2.1. Solid state reaction of precursors

The polycrystalline SBT and SBN powders were independently synthesized via solid-state reaction using commercial grade $SrCO_3$ (> 99%, *Merck*), Bi_2O_3 (> 99.5%, *Riedel-de Haën*), Ta_2O_5 (99.8%, *ABCR*), and Nb_2O_5 (99.9% *Alfa Aesar*) reagents. Each compound (SBT or SBN) was prepared by mixing their corresponding reagents in stoichiometric amounts for 2 hours in ethanol, dried at 120 ºC in air, and then placed in a

~ 15 ml platinum crucible tightly sealed with a platinum lid. The platinum crucible was then inserted in a larger alumina crucible sealed with alumina cement to minimize the evaporation of bismuth oxide, and then placed in a programmable furnace equipped with an automatic temperature controller [see Fig. 2.1(a)].

Stoichiometric SBT and SBN powders were obtained independently after heating up to 950 ºC at 300 ºC/h, soaking at this temperature for 2 hours in air, and finally cooled down to room temperature at 300 ºC/h. After the firing process the weight losses were evaluated in both cases, representing the amount of CO_2 evaporated during the reaction. The weight losses were calculated as 4.46 wt% and 5.24 wt% for SBT and SBN, respectively, in a good agreement with the theoretical values (4.2 wt% and 5.0 wt% for SBT and SBN, respectively) calculated from each reaction equation,

$$SrCO_3 + Bi_2O_3 + Ta(Nb)_2O_5 \Rightarrow SrBi_2Ta(Nb)_2O_9 + CO_2 \qquad (2.1)$$

The powders were ball milled separately in ethanol for 8 hours using zirconia balls in polyethylene jars and then mixed with the flux using a molar ratio of 60/40 of SBT(or SBN) to flux. The flux used in both cases was a mixture of 35 wt% of Bi_2O_3 (> 99.5%, *Riedel-de Haën*), which has a melting point of 825 ºC, and of 5 wt% of B_2O_3 (> 99.9%, *Merck*), with a melting point of 450 ºC. Such flux based on Bi_2O_3 at high temperature is advantageous, because bismuth is also a part of the desired final composition and, therefore, the incorporation of foreign ions into the lattice of the grown crystals is avoided. Moreover, the melting point may be conveniently reduced by adding other component to the flux, *e.g.*, B_2O_3, resulting in a more stable flux with crystals nucleating in an optimum homogeneous and viscous medium.[5]

2.2.2. Experimental growth runs and processing variables

An amount of ~ 40 gs of the ground SBT(or SBN)/flux homogeneous mixture was placed into a 15 ml platinum crucible (base diameter of 2 cm) tightly sealed with a platinum lid. The crucible was never filled till the top, to avoid the overpressure inside the crucible during heating, thus, the mentioned amount of powder only occupied about ¾ vol. parts of the crucible. Figure 2.1(b) shows the crucible design used for the growth of SBT and SBN single crystals. The Pt/Al_2O_3 double crucible sealed with alumina cement was

used to prevent the evaporation of the flux at high temperatures, due to the high volatility of the Bi_2O_3, thus avoiding possible damages to the electric furnace. A furnace with a very small vertical temperature gradient of ~ 2 ºC between the top and the bottom of the platinum crucible and equipped with a thermocouple located on the top of the crucible was used, as schematically illustrated in Fig. 2.1(a).

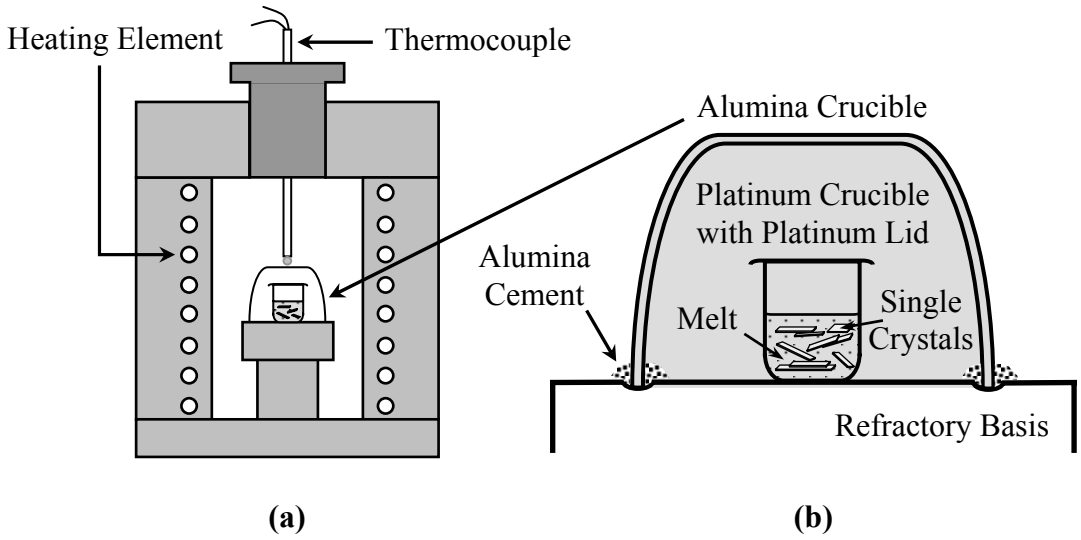

Figure 2.1 (a) Schematic diagram of the furnace setup used for the growth of SBT and SBN single crystals and (b) the double crucible arrangements used to prevent the evaporation of the flux at high temperatures.

First, a premelting was done at 950 ºC for 2 h, followed by the melting, soaking and cooling stages using three different temperature profiles, as shown in Fig. 2.2. Each crystal batch was performed in an independent run with the crucible placed in the middle of the furnace chamber. All these profiles include heating up from room temperature to 1350 ºC and soaking at this temperature for 10 hours. After this, a *gradually accelerated slow cooling process* is introduced in order to create the required supersaturation for crystals nucleation and growth,[6] following one of the three different paths, hereafter TP1, TP2 and TP3. These changes in the slow cooling rates enable the study of the effect of different supersaturation conditions on the crystal morphology and size. The two first profiles, TP1 and TP2, lasted ~ 4 days, being faster than TP3, a longer profile that allowed for slow cooling for more than a week. This last profile, TP3, was similar to that used by Sih *et al*.[5]

The TP1 profile included a soaking at 1350 ºC for 10 hours, slow cooling at 5 ºC/h down to 1200 ºC, which was then changed to 10 ºC/h down to 1000 ºC, then to 20 ºC/h

down to 800 ºC, and finally to 100 ºC/h down to room temperature. The only and very important difference appearing in the TP2 profile with respect to the TP1 profile is the inclusion of an initial slow cooling rate of 2 ºC/h, after the soaking at 1350 ºC for 10 hours, from 1350 ºC down to 1300 ºC. After this, the cooling rate was increased to 5 ºC/h, following a parallel path to the TP1 profile. In case of the TP3 profile, an initial slow cooling rate as low as 2 ºC/h following the soaking stage is prolonged down to 1100 ºC, changing to 10 ºC/h down to 1000 ºC, then to 20 ºC/h down to 800 ºC, and finally to 100 ºC/h down to room temperature. As mentioned before, this last profile (TP3) was two times slower than the two first profiles. After cooling to room temperature the platinum crucible was weighed to evaluate the weight loss of contents during heat treatment.

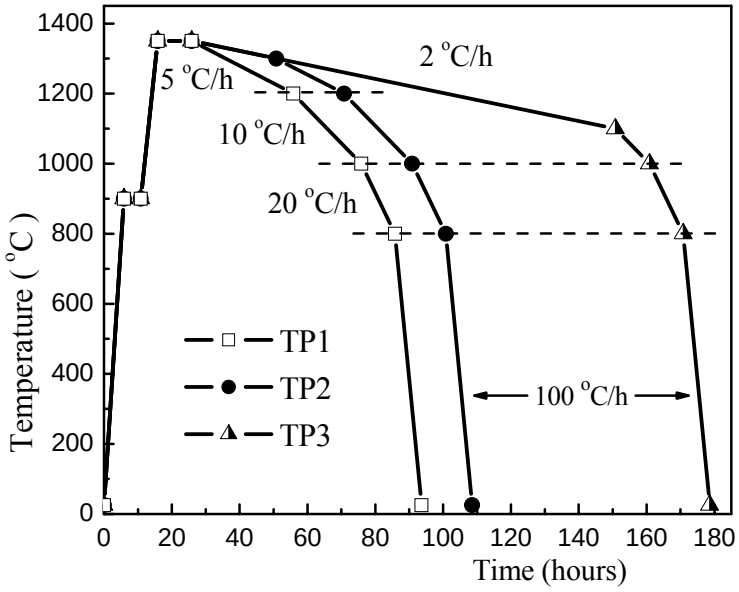

Figure 2.2 Illustration of the furnace thermal profiles with several slow cooling rates used for the growth of SBT and SBN single crystals.

These three different thermal profiles were tested for the case of the SBT system in an attempt to achieve single crystals having no second phases, being stoichiometric, with size greater than 1 × 1 mm^2, and of the high optical and crystalline quality. After the various growth runs the weight losses were evaluated. In all cases, the weight losses fluctuated between 15% and 20% of the initial powder amount (flux plus SBT). Since the initial amount of flux was 40 wt% of the total powder, the losses are believed to be associated with the flux evaporation out from the platinum crucible during the thermal treatment. This fact was also confirmed by the analysis of the alumina crucible after the

various growth runs, where some yellowish coloration in the inner side of the alumina crucible was observed. However, neither the outer side of the alumina crucible nor the alumina cement were found to be visibly colored with yellowish contaminant. In case of the SBN system, TP2 profile was only employed, since it resulted in the largest crystals as will be stated in the next chapter.

2.2.3. Separation of grown crystals from the residual flux

Although flux growth seems to be the most appropriate growth technique for several classes of materials, the separation of the crystals from the residual solution is problematic. The crystals must be separated from the crucible and the solidified melt as long as possible mechanically, *i.e.*, crystals can be separated from the flux at elevated temperature by inverting the crucible within the furnace, using a volume of the crucible twice as large as that of the melt.[7] In our case, the grown SBT and SBN single crystals were separated from the flux using a two-step process. First, attempts were made to separate the crystals from the platinum crucible by inverting it over a porous ceramic at 1000 ºC (above the flux melting point). The flux did not soaked into the ceramics as expected, but the crystals and the residual flux were taken off from the crucible as a solidified mass, and then, the crystals were separated by leaching in hot HNO_3 to dissolve the residual flux while the crystals remain intact. This process was too slow and took a few days to completely remove the existing flux between the platelet single crystals and to separate them from the others. Finally, SBT crystals were leached in a hot water for several hours to dissolve the nitric salt and then annealed at 750 ºC for 10 hours.

2.3. $SrBi_2Ta_2O_9$ Textured Ceramic Processing

2.3.1. Solid state reaction of precursors and template preparation

To produce textured SBT ceramics by templated grain growth (TGG) for the present investigation, polycrystalline SBT powder was firstly synthesized via solid-state reaction using identical method and reagents similar to those previously described in section 2.2.1. That is, ~ 40 gs of SBT powder was prepared by mixing in stoichiometric amounts for 2 h in ethanol, then, placed in a Pt/Al_2O_3 double crucible sealed with alumina cement to

prevent the evaporation of bismuth oxide [see Fig. 2.1(a)], and finally placed in a programmable furnace equipped with an automatic temperature controller. Stoichiometric SBT crystalline powder was obtained after heating up to 950 ºC at 300 ºC/h, soaking at this temperature for 2 hours, and finally cooled down to room temperature at 300 ºC/h. After the firing process the weight losses were calculated as 4.4 wt%, in a good agreement with the expected theoretical value of 4.2 wt% for SBT. Subsequently, the powder was vigorously ball milled in ethanol for 12 hours using a combination of zirconia balls of 4.5 and 10 mm diameter in a polyethylene jar, until a fine-grained powder with an average particle size of ~ 0.2 μm and a specific surface area of ~ 20 m^2/g was reached. The milled SBT powder was dried in an oven at ~ 120 ºC for several hours, being thus considered ready to be used as a matrix for TGG.

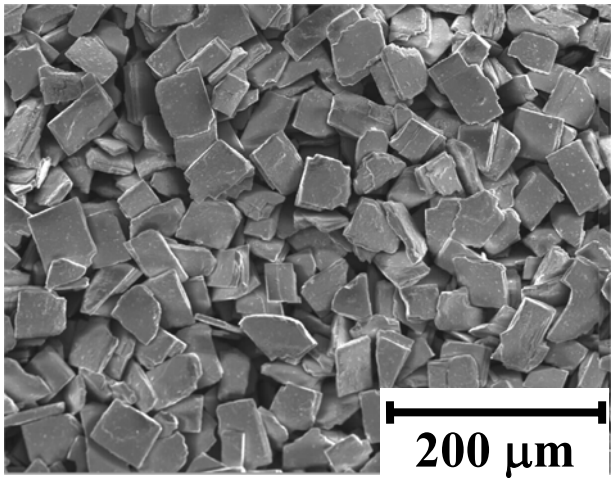

Figure 2.3 SEM micrographs of SBT template particles used as seeds for TGG.

The processing and completion of the template particles is of special interest since the degree of texture of the sintered bodies strongly depends on the number, size and distribution of the templates.[4] In our case, the plate-like SBT crystals, previously obtained by high-temperature self-flux solution method, were prepared to be used as seeds for homoepitaxial TGG of SBT ceramics. Several big crystals with rectangular shape and the [001] direction (*c*-axis) perpendicular to the major face were crushed in a mortar to pass through a 325-mesh sieve (45 μm of nominal aperture size), and then cleaned by leaching first in a hot HNO_3 and then in a hot water for several hours to dissolve the nitric salt. The platelet were separated and washed three more times. Figure 2.3 shows the anisometric

template particles thus obtained with a plate-like morphology and average size of ~ 40 × 40 × 8 μm^3, which conserve the platelet morphology after crushing and sieving.

After the matrix powder and templates preparation, different amounts of Bi_2O_3 excess (up to 5 wt%) as a liquid phase former were added to the starting SBT powder to evaluate the influence of the liquid phase during densification and grain growth in the TGG process. Moreover, 3 or 5 wt% of the prepared templates were also added to the SBT powder with different amounts of Bi_2O_3 excess, and then, the powder-template mixtures were stirred in ethanol for 2 h until the mixture was homogeneous, and subsequently dried in air at 120 ºC. Hereafter the notation for the samples is SBT*x*Bi*y*T, where *x* is the amount of Bi_2O_3 excess and *y* is the amount of templates, both in wt%, in the initial powder mixture. The growth of template particles during TGG was investigated as a function of the sintering time and sintering temperature for the following compositions: SBT5T (seeded sample without liquid phase) and SBT3Bi5T samples. For comparison, unseeded SBT ceramics having 3 wt% of Bi_2O_3 excess were also prepared under similar conditions and denoted as SBT3Bi.

2.3.2. Compaction and sintering

For the compaction of the green samples, one drop of distilled water per pellet of ~ 0.5 gs of powder was used and the pellets were obtained using two different uniaxial pressures: 150 and 300 MPa, to highly orient the template particles, followed by cold isostatical pressing at ~ 200 MPa for homogenous compaction of the pellets before the thermal treatment. In both cases, the samples were maintained at the selected pressure for 1 min before starting to decrease the pressure very slowly to avoid the abrupt expansion accompanied with the consequent fracture of the samples. Two different values of uniaxial pressure were used to evaluate the pressure effects on the texture development. Finally, the pellets with dimensions of ~ 10 mm in diameter and ~ 1 mm in thickness were dried in an oven at ~ 120 ºC for several hours and the green density was determined by measuring their volume and weighing them.

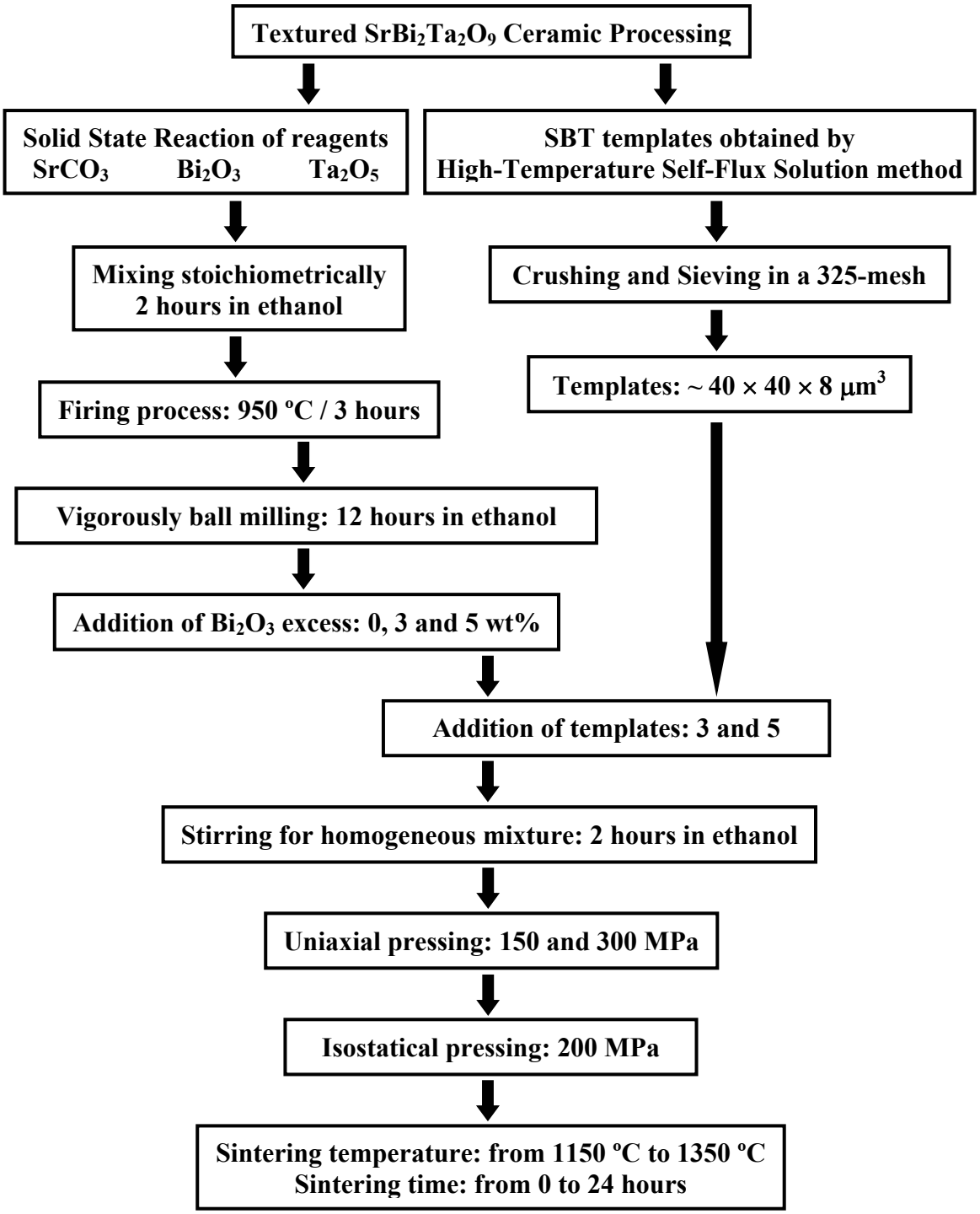

Figure 2.4 Processing steps for the fabrication of textured SBT ceramics by TGG.

After pressing, the samples were covered with SBT powder inside an alumina crucible sealed with an alumina lid to minimize the bismuth evaporation and placed in a programmable furnace equipped with an automatic temperature controller. Then, the samples were heated at 5 ºC/min to the selected sintering temperature, which varied from

1150 to 1350 ºC, held for different sintering time from 0 up to 48 hours, and finally cooled down to room temperature at 5 ºC/min. All heat treatments were performed in air. Figure 2.4 shows the flow chart used in this work for the processing of SBT ceramics. After the sintering process, the density of the sintered samples was calculated by measuring their volume and weighing them.

2.4. Experimental Techniques for Single Crystals

2.4.1. X-ray diffraction analysis

The crystallographic structure, orientation and quality of both SBT and SBN single crystals were first examined by *x-rays diffraction* (XRD) analysis. Diffraction from a perfect crystal may occur either in Bragg (reflection) or Laue (transmission) geometries as presented in Fig. 2.5. In both cases, diffraction depends on spacing between lattice planes and wavelength (λ) of incident monochromatic x-ray radiation. For a given set of lattice planes [see Fig. 2.5(a)], the Bragg's law relates the spacing between the planes, d_{hkl}, to the particular Bragg angle, θ_{hkl}, at which reflections from these planes are observed,[8-10]

$$n\lambda = 2d_{hkl}\sin\theta_{hkl} \tag{2.2}$$

where n is always taken as unity and hkl are the Miller indexes. Bragg's law indicates that diffraction is only observed when a set of planes makes a very specific angle (*Bragg angle*) with the incoming x-ray beam. This angle depends on the inter-plane spacing d_{hkl}, which itself depends on the size of the molecules/ions that make up the structure.

A characteristic pattern for each compound in a powdery form is produced by plotting the angular positions and intensities of the resultant diffracted peaks. However, with standard diffraction geometries, such as the Bragg geometry, lattice planes that are parallel to the sample surface are only measured, thus, this method can not be applied for the accurate determination of the crystallographic orientation in a single crystal.

The XRD measurements were performed in crystals with natural rectangular platelet morphology and dimensions of ~ 2 × 1 × 0.1 mm^3, using a *SIEMENS D500* diffractometer and CuK_α radiation (λ = 1.5418 Å) at room temperature. Single crystals were cut and

scanned using both reflection and transmission geometries [similar to that shown in Fig. 2.5(b,c)], in the 2θ range from 4º to 130º with a step length of 0.02º, while the rocking curve was recorded for the (00<u>18</u>) plane reflection.

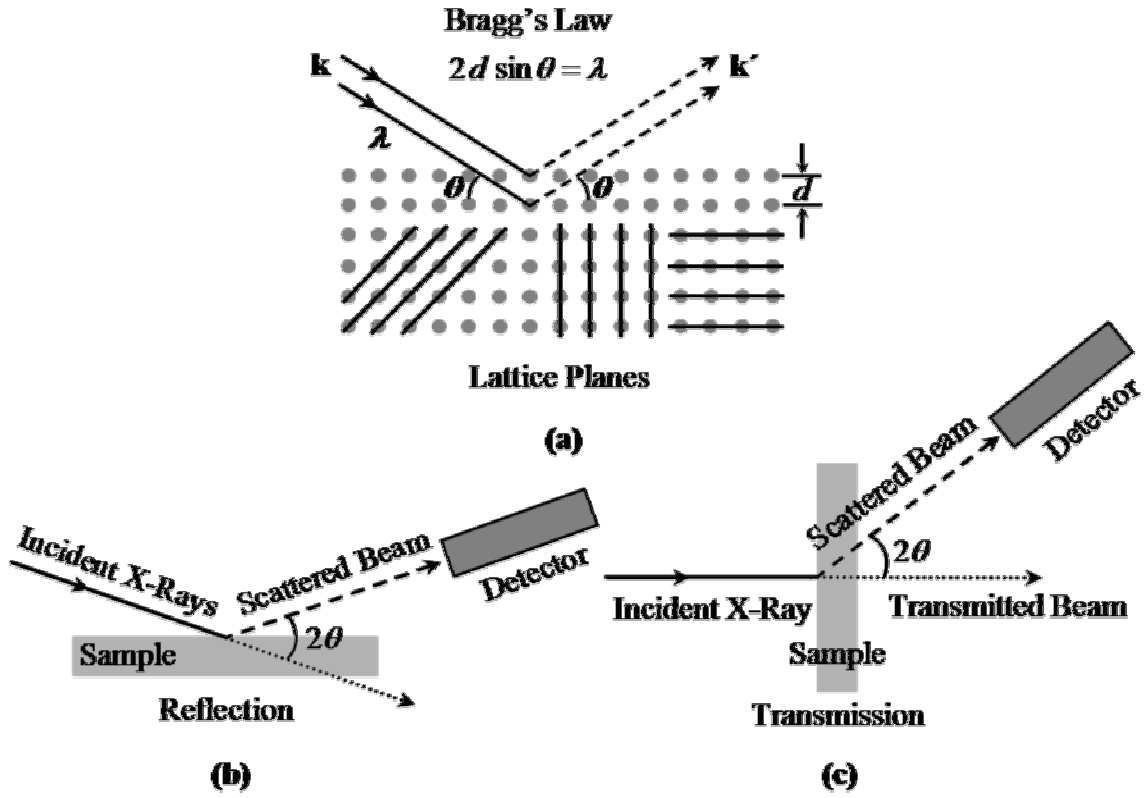

Figure 2.5 (a) Diffraction condition for a given set of lattice planes. *d* is the spacing between atomic planes and **k** and **k′** are the wave vectors of the incident and diffracted beams, respectively.[8-10] Diffraction in (b) Bragg reflection and (c) Laue transmission geometries.

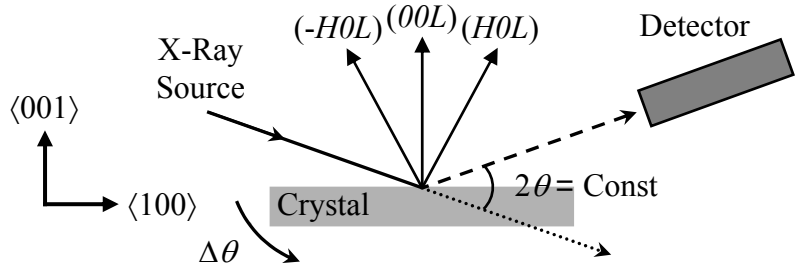

Figure 2.6 Schematic illustration of the wide scanning range (WSR) method. The (*H0L*) and (*-H0L*) plane reflections are obtained by rotating the crystal about the [010] direction for a fixed 2θ.

Furthermore, in order to establish the possibility of twinning planes in SBT single crystals, related to the exchange between *a*- and *b*-axes along the *ab*-plane, the extinction rules for the space group $A2_1am$ were investigated using the rocking curves in a *wide scanning range* (WSR) of the (20$\underline{18}$), (02$\underline{18}$), (10$\underline{15}$) and (01$\underline{15}$) plane reflections at room temperature, as schematically presented in Fig. 2.6. In this case, the x-ray source and detector are initially positioned to satisfy the diffraction condition for a given set of planes [*e.g.*, (*H0L*)] in Bragg reflection geometry, and then the crystal is rotated about the [010] direction in this case, while keeping fixed 2θ, to obtain the diffraction condition for both the (*H0L*) and the reciprocal planes (-*H0L*).

2.4.2. X-ray angular θ-2θ and θ-scanning topography methods

X-ray diffraction topography is an imaging technique based on a Bragg diffraction widely used for the verification of the quality of single crystals. In this technique, the detector is replaced by a photographic film, which provides a two-dimensional intensity mapping of the beam diffracted by the crystal, as schematically represented in Fig. 2.7(a).[10] This technique gives information about crystal defects (impurities, dislocations, twins, etc.), lattice misorientation, change of parameters, and the crystallographic orientation of the crystal edges. The evaluation of the structural quality of the grown single crystals was performed by x-ray angular θ-2θ and θ scanning topography methods on a standard *DRON-2* diffractometer (CuK_α radiation) at room temperature, and using the (00$\underline{18}$) reflection for θ-2θ scanning in reflection geometry and the (110) and (200) reflections for θ scanning in transmission geometry, as schematically represented in Fig. 2.7(c,d).[11]

In these methods, the platelet sample is rotated at an angular rate ω and the photographic film, placed directly in front of the x-ray detector and perpendicular to the diffracted beam, is rotated at an angular rate 2ω for θ-2θ scanning topography or kept fixed for θ scanning topography [see Fig. 2.7(c,d)]. Both methods can be applied either in reflection or transmission geometries. The θ-2θ scanning topography method is sensitive to misorientation between adjacent section of the crystal, and the misorientation angles are related to the angular interval of rotation [see Fig. 2.7(b)]. It allows us to produce images from the chosen reflection of all the crystal sections with misorientation less than the scan interval. On the other hand, the θ scanning topography does not display the misorientation

of the crystallites in the direction of scanning, and only records reflections with different parameters of unit cell. Thus, we can determine if the crystal platelet is composed by one single crystal or it is a block of several single crystals with different lattice parameters, thus confirming the quality of the crystals to be used for domain structure observation and ferroelectric measurements. In both cases, θ-2θ and θ scanning topography methods, the misorientation between crystal sections around the direction perpendicular to the rotation axis of the goniometer is manifested along the vertical direction on the topographs.

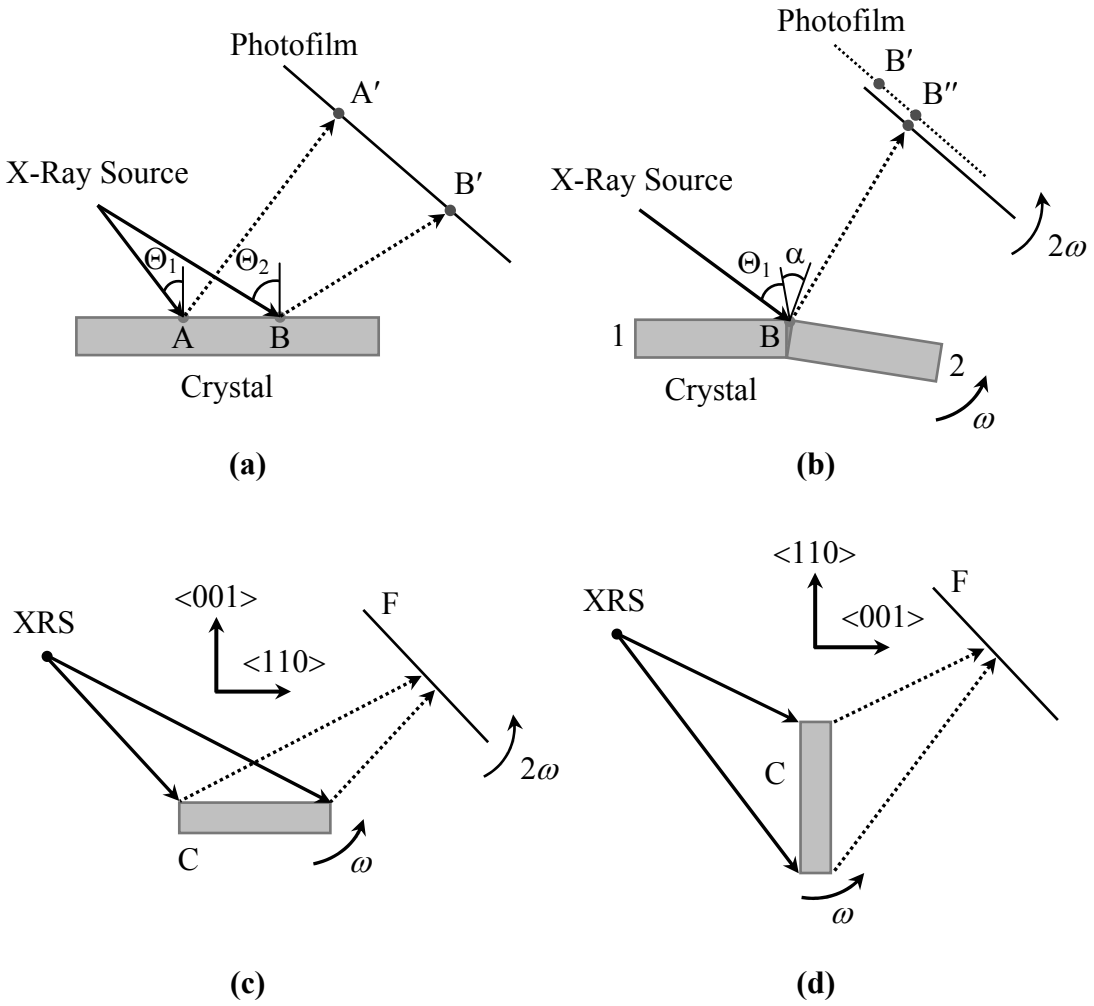

Figure 2.7 Basic principle of x-ray topography for (a) a perfect single crystal and for (b) an imperfect crystal with some misorientation. Schematic illustrations of the (c) θ-2θ and (d) θ scanning topography methods in transmission and reflection geometry, respectively.[10,11]

2.4.3. Electroding and surface preparation for domain observation and ferroelectric characterization

For electrical characterization, naturally rectangular shaped SBT and SBN single crystals were polished flat in two directions: parallel to the *ab*-plane for measurements along the [001] direction (*c*-axis direction), and perpendicular to the *ab*-plane for measurements along the [110] direction, as schematically illustrated in Fig. 2.8. The oriented crystals were polished to the desired thicknesses by using several abrasives in the following order: a) silicon carbide paper, b) diamond paste (15 μm, 6 μm, 3 μm, 1 μm and 0.25 μm), and c) colloidal-silica aqueous suspension (~ 0.05 μm). Submicron polish was performed only when required by certain experiments, such as domain studies. The final surface area of the polished crystals used in this study varied from 3 × 3 mm^2 for measurements along *c*-axis to 3 × 0.2 mm^2 for measurements along *ab*-plane, while the final thicknesses were about 100 μm to 200 μm in both cases. Following the polishing steps, samples were cleaned in ethanol and dried in air. Gold electrodes were then sputtered onto the whole area of the parallel polished facets using a *Polaron E5000* vacuum sputtering system working with argon partial pressure of 0.2 mtorr, acceleration voltage of 1.2 kV, and emission current of 12 mA.

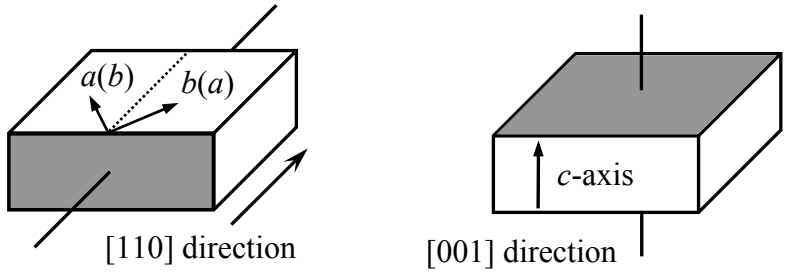

Figure 2.8 Schematic representations of the crystal configurations for electrical measurements along the (a) [001] and (b) [110] directions.

For domain observation via piezoelectric force microscopy, only one facet (upper facet) of the single crystals was polished similarly to the method previously described, that is, until colloidal-silica aqueous suspension (~ 0.05 μm) was used. Prior to electroding the bottom face of the crystals, the samples were annealed at 750 ºC for 10 hours to eliminate stresses and domain deformation on the crystal surface during sample preparation steps. Then, the whole area of the bottom facet of the crystals was electroded by sputtering a gold layer using the *Polaron E5000* vacuum sputtering system.

2.4.4. Piezoelectric force microscopy (PFM) measurements

Several *scanning force microscopy* (SFM) modes are capable to image domain patterns at the surface of ferroelectric single crystals, thin films or even ceramics materials.[12] In this thesis, the examination of the domain structure was carried out via *piezoresponse force microscopy* (PFM), which is a modification of contact SFM specially adapted for local piezoelectric measurements. Detailed description of the PFM mode could be found elsewhere.[12-14] Briefly, PFM mode is based on the detection of local electro mechanical vibrations of a cantilever induced by a probing *ac* electric signal applied between the conductive tip of the SFM and the bottom electrode of a ferroelectric sample, as schematically illustrated in Fig. 2.9.[12] The interaction between the tip and the sample can be estimated plotting the cantilever deflection against the elevation above the surface of the Z scanner, the so-called *force distance curve*. The cantilever vibrations are converted into an electrical signal by the position sensitive detector of the SFM and extracted from the global deflection signal using a standard lock-in technique.

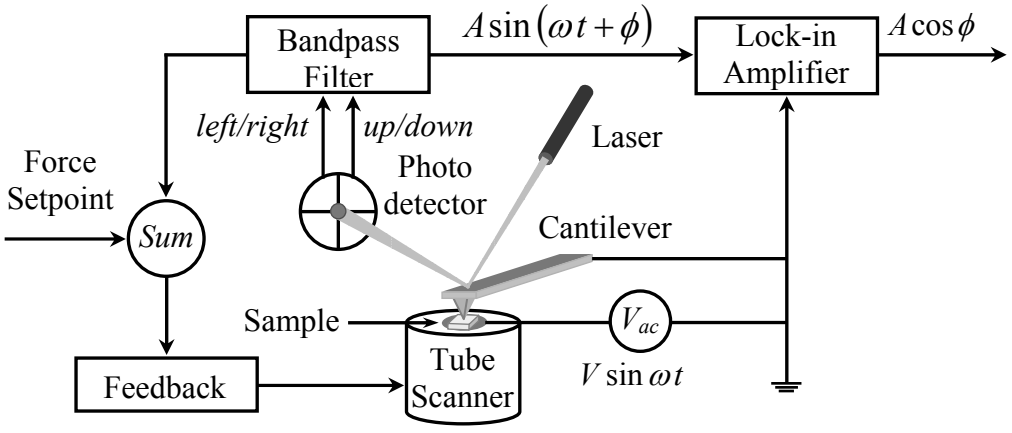

Figure 2.9 Experimental setup used for piezoresponse force microscopy measurements operating in contact mode. The tip is brought into contact with the crystal surface and the cantilever deformation is measured by the laser deflection onto a four quadrant detector. The up/down deflection of the cantilever is fed into a feedback adjusting the static force.

PFM is capable of detecting not only out-of-plane domains, where the spontaneous polarization direction is normal to the crystal plane and which induce vertical vibrations of the cantilever [see Fig. 2.10(a)], but also in-plane domains, where the spontaneous polarization lies within the plane of the crystal, and where the shear strain induces lateral oscillations detected via friction by the torsion of the cantilever [see Fig. 2.10(b)].[15] The

amplitude of these local vibrations is a function of the local piezoelectric coefficient and its phase depends on the orientation of the local polarization relative to the applied electric field, which allows us to distinguish between different domains as illustrated in Fig. 2.10.

Figure 2.9 shows the experimental setup used for PFM measurements in the SBT single crystals. The vertical and lateral vibrations due to the longitudinal (d_{33}) and the shear (d_{15}) piezoelectric effects, respectively, were detected by using a commercial *Multimode* AFM setup (*Digital Instruments Nanoscope IIIa*) equipped with a standard doped silicon conductive tip-cantilever system (FMR, *Nanosensors*, spring constant about 3 N/m and a resonance frequency of 80 kHz). To induce the piezoelectric deformation an external ac voltage signal (with amplitude of 10 - 20 V and frequency of 3 kHz) was applied using a functional generator (Model FG120, *Yokogawa*) and an amplifier (Model 7602, *Kronh-Hite Wideband*) both connected to the SFM. The amplitude and phase of the induced deflection of the cantilever was detected using a lock-in amplifier (SR830, *Stanford Research System*). Finally, the topography and domain images were processed using the WSxMbeta6_0 software (*Nanotec*-2002).

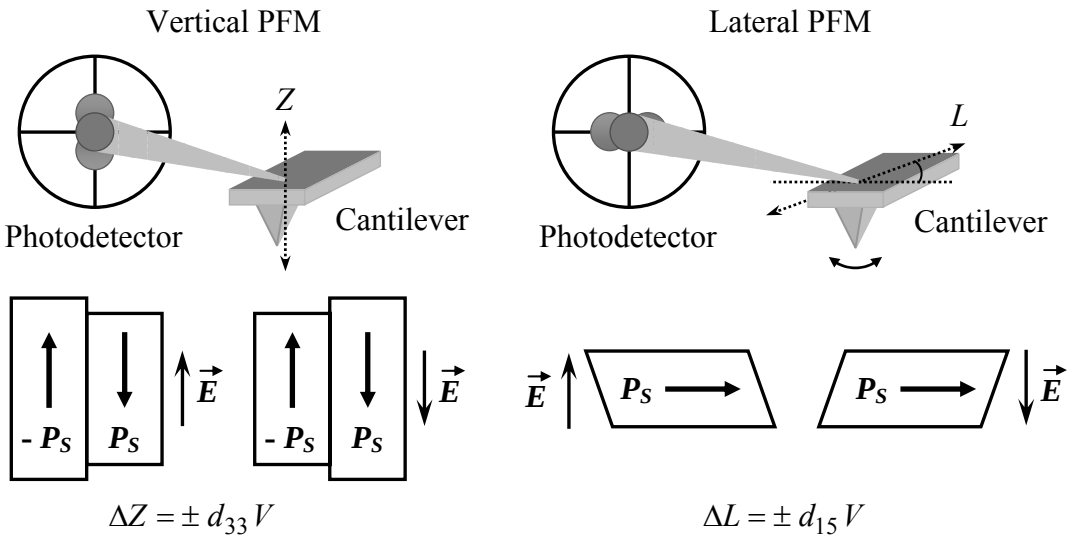

Figure 2.10 Piezoelectric deformations in ferroelectric materials (a) due to d_{33} for the spontaneous polarization aligned parallel to the electric field and (b) due to d_{15} for the spontaneous polarization in the plane of the crystal perpendicularly to the electric field. In both cases, the deformation is reversed if the electric field is reversed.

2.4.5. Dielectric characterization

For most applications of ferroelectric materials, dielectric properties, *e.g.*, *dielectric permittivity* (ε) and *dielectric loss* (tan δ), are important practical parameters which provides a great deal of information for understanding the polarization mechanism in ferroelectric materials.[16-18] In the practice, the dielectric permittivity or dielectric constant is obtained from the capacitance measurements under an *ac* electric field and is a function of frequency. Generally, this measurement is performed in the frequency range from several Hertz to hundred megahertz or even gigahertz. Thus, assuming that the sample is a parallel plane capacitor filled with a dielectric medium (the ferroelectric sample), the *relative permittivity* (ε_r) can be obtained taking into account the sample thickness (t) and the area of the electrodes (A), using the following expression,

$$\varepsilon_r = \frac{C_p\ t}{\varepsilon_o\ A} \tag{2.3}$$

where C_p is the capacitance of the parallel plane capacitor and ε_o is the dielectric permittivity of the vacuum (8.85×10^{-12} F/m). On the other hand, dielectric losses are obtained from the ratio of the imaginary part (ε'') to the real part ($\varepsilon' = \varepsilon_r$) of the permittivity as expressed in Eq. 1.4, being ε'' obtained from,

$$\varepsilon'' = \omega R C_p \tag{2.4}$$

where ω is the frequency and R is the parallel resistance. This information is useful to verify the quality of the sample and the electrodes. Typically, a $\tan\delta < 0.02$ is considered to indicate high quality of the sample in terms of loss factor.

Dielectric properties were measured from room temperature up to 500 ºC at 2 ºC/min using a *Hewlett-Packard* precision LCR Meter (Model HP4284A) connected to a PC via a GPIB card and working in the frequency range from 1 kHz to 1 MHz. The temperature was controlled using an *Eurotherm* 2404 controller and a thermocouple positioned very close to the sample without touching it, reaching a temperature control with a precision of ± 0.5 ºC. Prior each measurement, a correction for the stray capacitance of the sample holder and

connecting wires was performed in the LCR Meter which is necessary to separate the capacitance of the sample.

2.4.6. Ferroelectric hysteresis measurements

To confirm the anisotropy in the ferroelectric properties of the studied single crystals, the *polarization-electric field* (P-E) hysteresis loops were measured at room temperature both along *c*-axis and in the *ab*-plane (parallel to [110] direction) using a modified Sawyer-Tower circuit (see Fig. 2.11).[16] An alternating voltage is applied across the electrodes on the ferroelectric sample (C_x) connected to the horizontal plates of an oscilloscope, hence the quantity plotted on the horizontal axis of the oscilloscope (V_X) is proportional to the electric field across the sample (E), which can be calculated considering the sample thickness (t) and the following expression,

$$E = \frac{V}{t} \tag{2.5}$$

C_O is a linear capacitor with a large capacitance of ~ 1 μF that is connected in series with the ferroelectric material C_x in such a way that most of the voltage drops across the sample. The voltage across the linear capacitor C_O (V_Y) is therefore proportional to the polarization (P) of the ferroelectric material, which is calculated taking into account the area of the electrodes (A), using the following expression,[16]

$$P = \frac{C_o\, V_Y}{A} \tag{2.6}$$

A typical loop for a ferroelectric material is shown in Fig. 1.6(a).The observation of the *P-E* hysteresis loop is still frequently used for the identification of ferroelectrics as well as for the determination of the spontaneous (P_S) and remanent (P_r) polarizations and the coercive field (E_C) of the studied material. All these parameters can be computed from the recorded hysteresis loop as well as the value of the relative permittivity (ε_r) calculated from the slope of the P-E linear behavior on saturation,

$$P = \varepsilon_r\, \varepsilon_o\, E \tag{2.7}$$

Electric fields as high as ~ 100 kV/cm were applied to the samples at the frequency of 50 Hz. During P-E hysteresis measurements, the samples were submerged in silicon oil, an insulating liquid, to prevent arcing. The hysteresis loop was visualized and recorded using a digital oscilloscope (*LeCroy* LT322) and the acquired data was saved on a floppy disk. Once again, because of the small transverse size of the samples, a correction for the stray capacitance of the sample holder and connecting wires was necessary to separate the P-E hysteresis loop of the sample from the linear contribution due to stray capacitance.

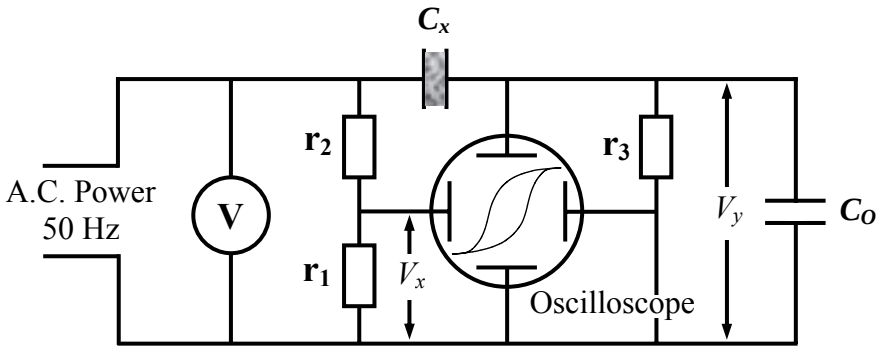

Figure 2.11 Modified Sawyer-Tower circuit used for the P-E hysteresis loop measurements in single crystals and ceramics.[16]

2.4.7. Piezoelectric characterization

For piezoelectric applications of ferroelectric materials, several properties such as the piezoelectric coefficients, the elastic constant and the electromechanical coupling factor are all important to give optimized response for external vibrations, but, probably, the most important property of a piezoelectric crystal is determined by their piezoelectric coefficients (see section 1.2.2 and Table 1.2 for definitions). A number of techniques are used to evaluate the piezoelectric properties of ferroelectric materials at frequencies much lower than the fundamental resonance frequency of the sample (which is in the order of the hundreds kHz for the most important vibration modes, *e.g.*, length, radial or thickness shear modes). In this work, piezoelectric measurements of the *ac* electric field induced strain (converse piezoelectric effect) at low frequencies (from 500 Hz to 5 kHz) were performed using an interferometric technique described elsewhere.[19] The longitudinal piezoelectric coefficient d_{33} was calculated from the slope of the straight line between the strain and the electric field (see Eq. 1.6).

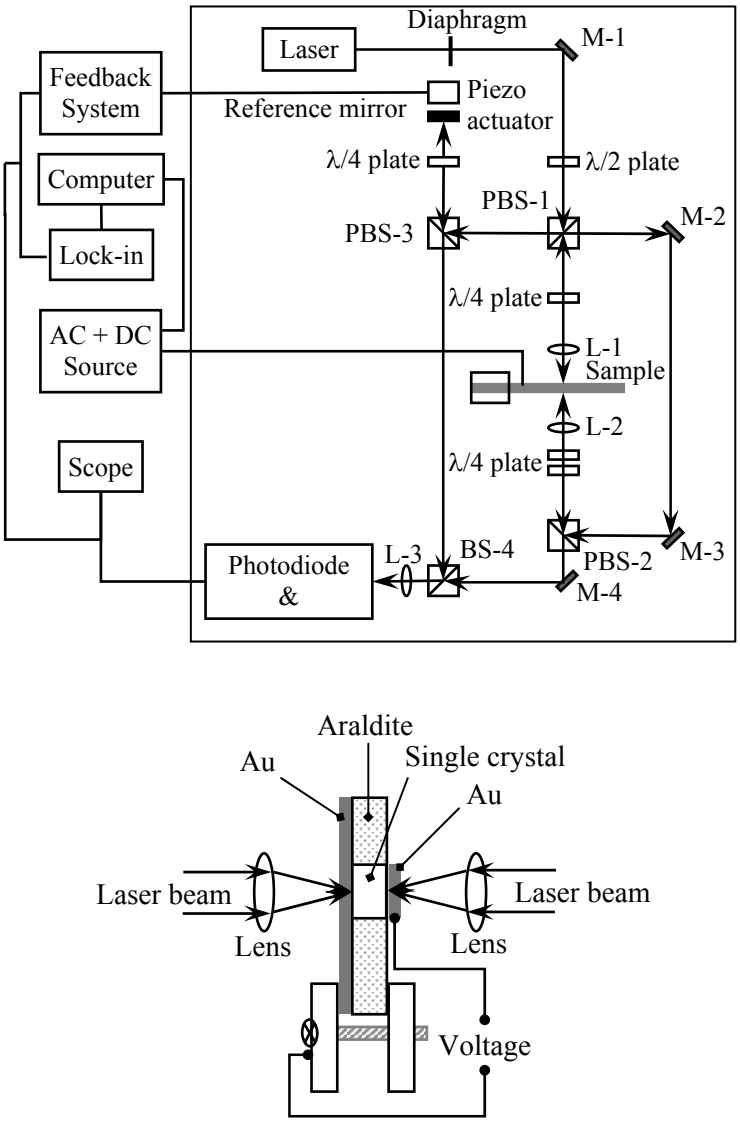

Figure 2.12 Schematic of the (a) optical table with the double-beam laser interferometer used for piezoelectric measurements and (b) setup for the assembly single crystal-araldite holder used for the elimination of bending motion in the single crystals.[19]

A double-beam (Mach-Zender) laser interferometer with an active stabilization of the working point was used to measure the d_{33} coefficient of the grown single crystals along different crystallographic directions, that is, parallel to [100], [110] and [001] directions. In this case, the probing beam reflects from both the front and back faces of the sample and the bending contribution to the measured vibrational piezoelectric response is automatically eliminated by the optical arrangement.[19] The sensitivity of the used interferometer was about 3×10^{-4} Å, which has been considerably improved as compared to the previous analogous setups, due to the better thermal and acoustical isolation of the

active component. Figure 2.12 shows the schematic diagram of the optical arrangement of the used double-beam laser interferometer, where L, M and BS are the lens, mirrors and beam splitters, respectively. Details of the experimental setup for the interferometric measurements were previously reported elsewhere.[19] Briefly, the *ac* electric field induced strain in the single crystal is determined by measuring the change in the light intensity on the photodetector, which is associated with the optical path-length difference of the laser, and is finally sensed using a lock-in amplifier.

For piezoelectric measurements, the crystals were previously embedded in araldite (due to the small thickness) and polished to optical quality in both the front and back faces. Gold electrodes were sputtered onto the whole area of the parallel polished facets resulting in mirror-like reflection, and the crystals were poled at room temperature with an electric field of E_P = 60 kV/cm for piezoelectric characterization. The frequency dependence of the d_{33} coefficient and phase of the poled crystals was measured at room temperature using an *ac* voltage of V_{ac} = 100 V ($E_{ac} \approx$ 3 kV/cm) in the frequency range from 500 Hz to 5 kHz.

The behavior of the d_{33} coefficient for different *dc* poling fields was also measured at room temperature as follows: first, a *dc* poling field is applied to the crystal during 1 min, and then the poling field is removed and a weak *ac* voltage (V_{ac} = 100 V) is applied for piezoelectric deformation, which is measured using a lock-in amplifier (Perkin-Elmer 7265). This process is repeated increasing (and decreasing) the *dc* poling field in steps of ~ 3 kV/cm in both senses for each direction.

2.5. Experimental Techniques for Textured Ceramics

2.5.1. X-ray diffraction analysis and Lotgering factor

Powder x-ray diffraction analysis is perhaps the most widely used XRD technique for characterizing materials.[8] As the name suggests, the sample to be studied is usually in a *powdery* form, consisting of randomly oriented fine grains (or crystallites). Therefore, when a 2D diffraction pattern is recorded, it shows scattering peaks corresponding to the various *d* spacing in the crystal lattice. The positions and the intensities of the peaks are used for identifying the underlying structure (or phase) of the studied material. Basic details of the XRD technique were previously described in section 2.4.1.

This technique is also widely used for studying polycrystalline solids (bulk or thin film materials) with standard diffraction geometries such as the Bragg reflection geometry [see Fig. 2.5(a)]. When the bulk material is composed of randomly oriented grains, the XRD pattern obtained is quite similar to that of the powder material. On the other hand, when the polycrystalline solid present a crystallographic texture, the relative intensity of all the peaks in the XRD patterns changes significantly with respect to the pattern obtained for the randomly oriented material in such a way that the most intense peaks are those associated with lattice planes, *hkl*, perpendicular to the bisectrix between incident and diffracted beam, *i.e.*, planes similar to that illustrated in Fig. 2.5(a).

The degree of orientation of some polycrystalline materials can be determined from the XRD pattern by estimating the ⟨001⟩-texture fraction in terms of the *Lotgering factor* (*f*), which is a comparison of the relative intensities of (00*l*) reflections to all reflections observed in a powder XRD pattern,[20] that is,

$$f_{(00l)} = \frac{P_{(00l)} - P_o}{1 - P_o} \tag{2.8}$$

where

$$P_{(00l)} = \frac{\sum I_{(00l)}}{\sum I_{(hkl)}} \tag{2.9}$$

$\sum I_{(00l)}$ is the summation of the XRD peak intensities of all the (00*l*) peaks (*e.g.*, 002, 004… for SBT ceramics) in the textured sample pattern, $\sum I_{(hkl)}$ is the summation of the peak intensities of all (*hkl*) peaks that appear in the XRD pattern, and $P_o = P_{(00l)}$ for the randomly oriented powder. P_o was measured in the randomly oriented powder, because the processing of randomly oriented BLSF ceramics is very difficult because the (00*l*) texture naturally forms parallel to the pressing direction in the sintered ceramics. The calculated f describes the *degree of texture* defined by the surface area, which was characterized by XRD and ranges from 0 to 100%.

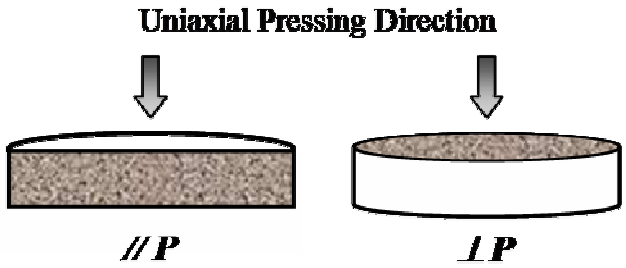

Figure 2.13 Schematic design of the samples cut for bulk XRD and SEM analysis. Cross-sections parallel (//P) and perpendicular (⊥P) to the uniaxial pressing direction.

The crystallographic texture analysis of the sintered samples was first examined by XRD using a conventional *Rikagu/New* x-ray diffractometer (CuK_α radiation) equipped with the MDI *data_scan*3.2 controller software and analyzed using the MDI *Jade*6.1 software. The textured SBT ceramics were scanned on the polished cross-sections parallel (//P) and perpendicular (⊥P) to the pressing direction, as illustrated in Fig. 2.13. The *f* factor was calculated using the Eq. 2.8 for the (00*l*) plane reflections in the 2θ scan between 4º and 80º in samples scanned ⊥P, using a step length of 0.02º.

2.5.2. Pole figure measurements with XRD technique

The most common method of texture evaluation is a *pole figure* measurement, which measures the intensity of a given XRD peak as the sample rotates about two orthogonal axes, thus collecting the sum of the lattice plane reflection signals from a large number of crystallites in a polycrystalline material.[21] The principle is simple, in order to determine the orientation of a given lattice plane, *hkl*, the detector is first set to the proper Bragg angle, 2θ, of the diffraction peak of interest and then the sample is rotated in a goniometer until the lattice plane *hkl* is in the reflection condition (*i.e.*, the normal to the lattice plane is the bisectrix between incident and diffracted beam). Pole figures are characterized by the angles ω and β, where ω radial range vary from 0º at the center to 90º at the edge, and β azimuthal range vary from 0º to 360º, as illustrated in Fig. 2.14 for the reflection geometry.

The pole figure is a stereographic projection showing the orientation distribution of a certain direction (pole) within the crystallites of the specimen. In polycrystalline materials, the intensity recorded at a certain sample orientation is proportional to the volume fraction of crystallites with their lattice planes in reflection geometry. A material with randomly

oriented crystallites will give a pole figure with a uniform pole density whereas crystallites with a preferred orientation will make the pole density non-uniform, and show their projections in clusters [see Fig. 2.15(a)]. A common symmetry encountered in materials is uniaxial or *fiber* symmetry, where only one sample direction (the symmetry axis) is of interest. Figure 2.15(b) shows the pole figure projection of concentric rings usually obtained in materials with *fiber* texture. The texture plot can be also slices of pole figures representing intensity versus ω at fixed β.

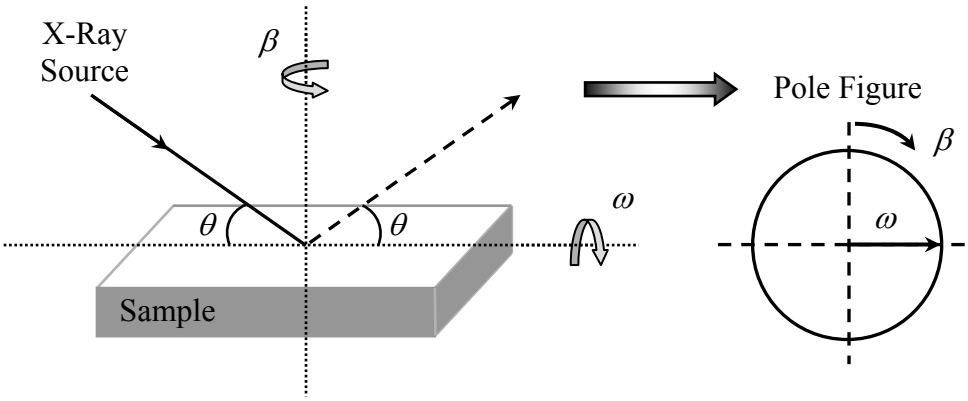

Figure 2.14 Scheme of the experimental setup for pole figure measurements in reflection geometry, showing the sample position and its rotation about ω and β.[22]

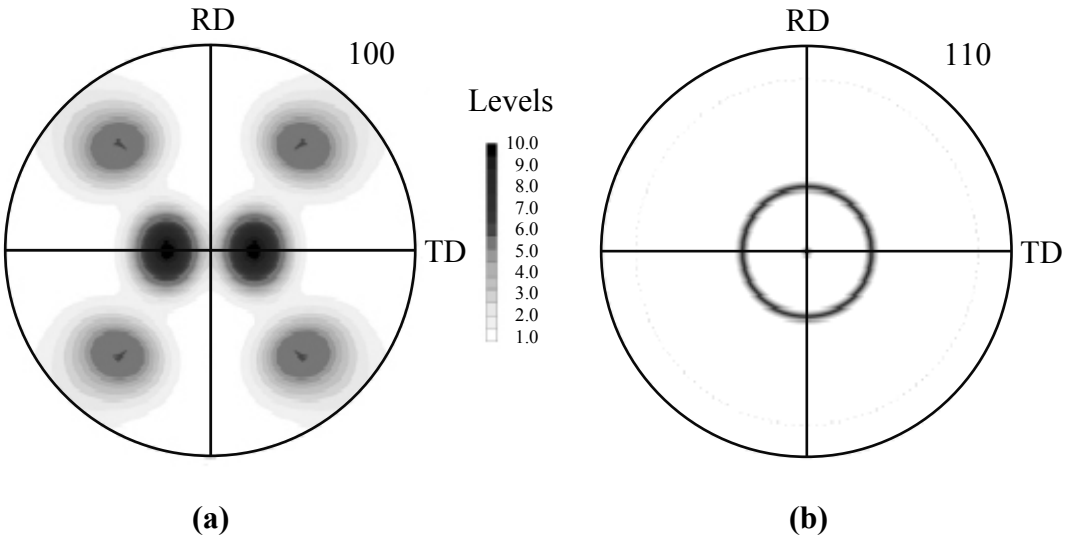

Figure 2.15 Schematic pole figures of specimens with (a) orthorhombic symmetry and preferred orientation (projections in clusters) and (b) axial symmetry (axisymmetric texture). RD and TD indicate the rolling and transverse directions, respectively.[21]

Pole figure measurements were performed on the polished cross-section ⊥P using a four-circle *X'Pert* MPD diffractometer (CuK_α radiation). The samples were mounted with the polished cross-section parallel to the Bragg plane, while the (00$\underline{1}$0), (200) and (115) pole figures were achieved with a continuous azimuthal (β) scan in the range $0º \leq \beta \leq 360º$ at various tilt angles in steps of $\Delta\omega = 0.25º$ and with a scan step time of 3 min/point in the range of $0º \leq \omega \leq 90º$. The ω step was relatively small and the azimuthal scan was continuous because the specimens typically displayed high level of axisymmetric texture (*fiber* symmetry). An incident area of ~ 1 × 1 mm^2 in the specimen was used. Since the specimens displayed axisymmetric texture with the (00*l*) poles preferentially oriented toward the symmetry axis, *i.e.*, the crystallographic *c*-axis is rather oriented parallel to the pressing direction, then, the data were averaged over β to produce a distribution of average intensity versus ω in the range of $-90º \leq \omega \leq 90º$. The measured intensity distribution for the (00$\underline{1}$0) reflection in the textured samples was divided by the measured intensity distribution of the same reflection at equivalent angles in the randomly oriented sample to correct for changes in illumination area with tilt angle, x-ray absorption and defocusing of the beam, and acquire a multiple of a random distribution (MRD).

2.5.3. Scanning electron microscopy (SEM) measurements

Scanning electron microscopy (SEM) is a micro-analytical technique, which is able to *image* or *analyze* materials that cannot generally be observed with the resolution offered by optical techniques, thus allowing a detailed analysis of the grain growth and morphology of the studied material. During SEM inspection, a fine beam of electrons, also referred to as *primary* electrons, is formed by the source and scanned across the specimen surface. The electrons dislodged from the interaction of the primary electron with the specimen, also known as *secondary* electrons, are then collected and displayed on a monitor as a function of the position. Magnification is increased by reducing the size of the scan area on the sample surface.

The microstructure of the textured samples was examined by SEM on the cross-sections parallel (//P) and perpendicular (⊥P) to the pressing direction, as schematically shown in Fig. 2.13. In order to measure the grain sizes and grain orientation distributions, the ceramics were first cut and polished to a highly quality. The polished process is very

important in order to avoid several adversities such as the pull-out of softer regions of the material, which is mainly produced by abrasives of particle sizes of the order of the grain size, and makes the results false. The ceramics were first inserted in araldite and then polished by using several abrasives in the following order: a) silicon carbide paper and then b) diamond paste (15 μm, 6 μm, 3 μm, 1 μm and 0.25 μm). Following the polishing steps, samples were taken off from the araldite, cleaned in ethanol and dried in air.

Several thermal treatments on the polished samples were tested in order to reveal the grain boundary and grain morphology for SEM observation. The thermal treatments were done at high temperatures between 1100 ºC and 1250 ºC for different times from 1 to 30 min, including quenching from 1200 ºC to room temperature. In all cases, a glassy phase deposited over the polished surface during thermal etchings makes difficult the observation of the grain morphology in the polished and thermally etched samples. It is assumed that this glassy phase appears due to diffusion of Bi_2O_3 from the bulk to the polished surface during thermal etching. Thus, the polished ceramics were chemically etched successfully by using a mixture of 50 vol.% of hydrofluoric acid (HF 5% in water) and 50 vol.% of hydrochloric acid (HCl 37% in water) for different etching times from 1 to 60 min, which depend on the sintering condition, *i.e.*, the higher the sintering temperature or time, the higher the chemical etching time in order to reveal the grain boundaries.

For SEM measurements the polished and etched samples were pasted in a special sample holder using a conductive carbon paste and dried for 24 hours in an oven at 120 ºC. Then, the samples were covered with a thin layer of carbon in order to improve the quality of the image. The carbon deposition process was performed using an *Emitech* K950 carbon deposition chamber equipped with a turbo pump. SEM measurements were performed using a field emission scanning electron microscope *Hitachi* S4100 and the images were obtained using an electron acceleration field of 25 kV and a filament emission current of 10 μA, and recorded using a variable magnification.

2.5.4. Stereological analysis and processing of the SEM images

Most of the microstructural studies in a large number of materials deals with the grain size and pore distributions as well as with the vol.% of second phases. However, there are few works using automatic image analysis methods.[23] Automatic image analysis

of grain size is an alternative method to the manual stereological methods, which can provide far more and statistically improved stereological information. In this work, a stereological analysis was performed by a semi-automatic method using image analysis software (*analySIS* 3.2).[24] At least ~ 300 large grains in each specimen were analyzed by taken several micrographs of the cross-sections //P in each sample. The semi-automatic method basically consist of a transformation of a digital image with several gray levels obtained from SEM measurement, that is, for each point or pixel it is defined a value of gray color between zero (black) and 255 (white), into a digital binary image, that is, black and white image, which defines and delimits the measured objects. In this case, the measured objects are the anisotropically shaped large grains which grew inside the matrix smaller grains, *i.e.*, see Fig. 2.16(a) for the sample SBT3Bi5T sintered at 1250 ºC for 2 h. The criterion used to separate the large grains or templates from the matrix grains was to select those grains which are greater than the initial size of the templates, that is, greater than 40 μm in length. Figure 2.16 shows an example of the initial digital image with level of gray and the final binary image with only the studied large grains in black.

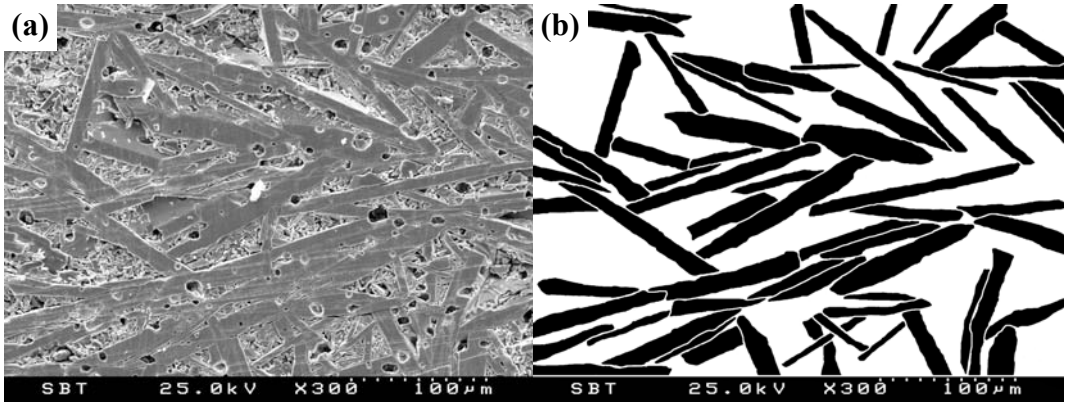

Figure 2.16 (a) Initial digital image obtained from the SEM measurement on the cross-section //P in the sample SBT3Bi5T sintered at 1250 ºC / 2 h, showing levels of gray, and (b) the corresponding binary image used in the image analysis software to measure the grain sizes, aspect ratio and grain orientation distributions as well as the volume fraction of textured material in SBT ceramics.

The advantages of using this semi-automatic method for image analysis are: first, the reduction of the human error in the treatment of the images, where several suppositions are often taken in the human criteria making fictitious the results in many cases; and, second, a large quantity of objects (or grains in this case) can be thus analyzed in a more precise and

faster way than that used by manual treatment of images, which makes possible a much more trustworthy statistical treatment of the images in the semi-automatic method.

In BLSF materials, the grains grow in anisotropic form showing platelet morphology, contrary to *circular* grains usually studied in isotropic materials, thus, in order to perform the stereological analysis of textured SBT ceramics, the chosen characteristic parameters related with the grain morphology and platelet orientation have to be defined. Figure 2.17 shows a typical grain with platelet morphology where some characteristic parameters are defined, namely the major and minor *Feret lengths* termed from now on grain length and thickness, respectively.[25] The aspect ratio for each platelet grain was also calculated as the length/thickness ratio, while the angle between the major *Feret* length of each platelet and the horizontal axis of the micrograph, which is perpendicular to the pressing direction, was chosen as the platelet grain orientation angle, as shown in Fig. 2.17. The volume fraction, f_v, of oriented material was determined by measuring the total area fraction of platelet grains, multiplied by the appropriate stereological correction factor.

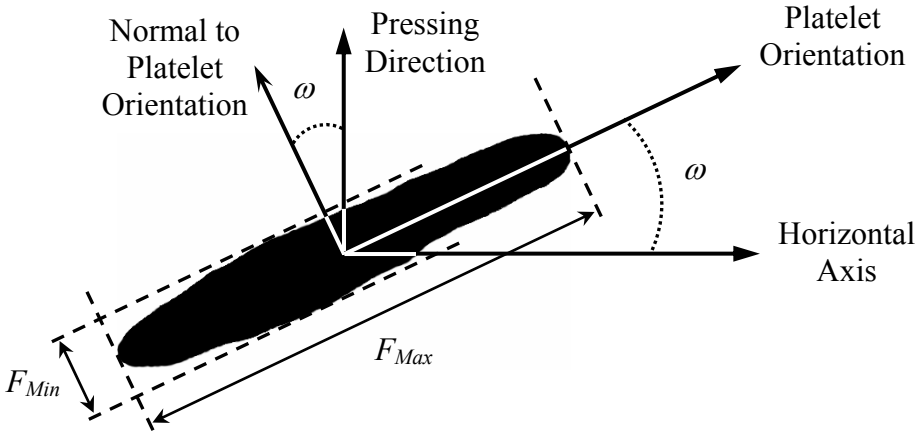

Figure 2.17 A typical grain with platelet morphology with schematic definitions of the major (F_{Max}) and minor (F_{Min}) *Feret lengths*, as well as the platelet orientation angle, ω.

Once the corresponding distributions of the grain length, thickness and aspect ratio have been measured, it is necessary to make a statistical analysis of the measured values to obtain a quantitative characterization of the sample morphology. In order to quantify each parameter, the average value and standard deviation of the corresponding distribution were obtained from the normal distribution that better adjust the experimental values plotted in histogram graphs. Figure 2.18 shows an example of the histogram graphs obtained for the

length, thickness and aspect ratio parameters with their corresponding normal distributions in the sample SBT3Bi5T sintered at 1250 ºC during 2 hours. The *full width at half-maximum* (*FWHM*), which is commonly used to compare the broadness of different distributions, was also determined for the aspect ratio distributions. On the other hand, the measured orientation distribution was used for the evaluation of the degree of texture, as described in the next section.

2.5.5. Orientation distribution function

The texture analysis using the simplest technique (*Lotgering factor*) does not provide enough information about the distribution of platelet orientations in the material, which can be fundamental in understanding processing-texture relationships.[26] The most complete descriptions of texture quantify the probability of given crystalline orientations with respect to the reference sample coordinate axes, the so-called orientation distribution function (ODF).[21] The value of the ODF for a given orientation is the probability of finding a crystallite of similar orientation. Based on the evaluation of texture analysis approaches described in the literature,[27] the XRD pole figure technique and a stereological method have been chosen in this work to measure the crystallographic and morphological texture in partly textured SBT ceramics. The *crystallographic texture*, obtained from the pole figure technique, reflects the preferred orientation of the crystal lattice in the material, while the *morphological texture* is a measure of the preferred orientation of grains with anisotropic morphology and is measured stereologically.

By fitting the data obtained from pole figure and stereological measurements to a suitable model function, properties such as *textured fraction* and *degree of texture* can be thus evaluated. Fitting ODF to stereological data of plate-like grains was first discussed by Sandlin *et al*.[28] using an elliptically symmetric *Gaussian* distribution function. Later, Messing *et al*.[4,27] have proposed the *March-Dollase* function (Eq. 2.10) as the model equation to fit and to quantify the measured texture distributions of platelet grains, because its fitting parameters are related to experimentally measurable stereological values,[29]

$$F(f_v, r, \omega) = f_v \left(r^2 \cos^2 \omega + \frac{\sin^2 \omega}{r} \right)^{-\frac{3}{2}} + (1 - f_v) \qquad (2.10)$$

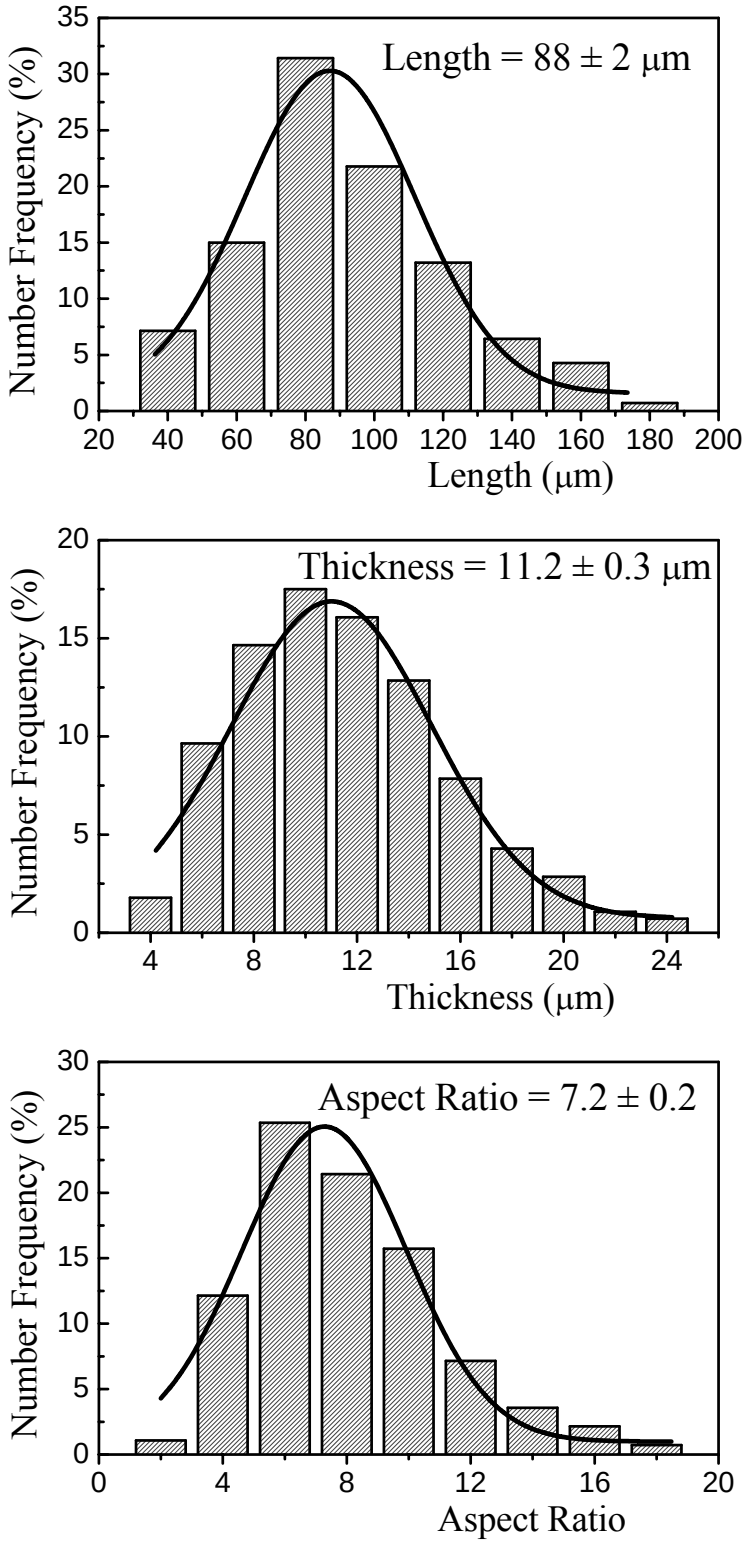

Figure 2.18 Example of histogram graphs for the length, thickness and aspect ratio parameters with their corresponding Gaussian distributions obtained in the sample SBT3Bi5T sintered at 1250 ºC for 2 hours.

The *r* parameter (*texture factor*) characterizes the width of the texture (orientation) distribution, taking values in the range $0 \leq r \leq 1$, while f_v is the *volume fraction* of oriented material. Small *r* indicates a narrow distribution of platelet normal orientations about the sample normal; *r* is 1 for a random oriented sample and tends to 0 for a perfectly textured sample. The definition of *r* and f_v remain consistent for both techniques, but the definition of ω changes. For pole figure measurements, ω is that defined in section 2.5.2, *i.e.*, the angle between the specimen normal (texture axis) and the scattering vector, while for stereological measurements, ω is that defined in section 2.5.4, *i.e.*, the angle between the specimen normal and the normal to the major facet of the platelets in the cross-section //P, as illustrated in Fig. 2.17.

The March function obtained by setting $f_v = 1$ in Eq. 2.10 was first proposed as a probability distribution function to describe the orientation of anisotropically shaped particles (platelets or rods) in a compact formed by uniaxial pressing. Dollase chose the March equation, among several possible solutions, to adjust for preferred orientation in Rietveld refinements, and then extended it to account for microstructures with differently textured components, thus producing the March-Dollase equation.[29] In the present work, two populations of grains in the SBT specimens were studied: one textured (large grains or templates) with volume fraction f_v and texture factor *r* and one random (matrix small grains). The *r* value for templates is obtained by fitting the orientation distribution with the March-Dollase equation (Eq. 2.10) with f_v set equal to 1. Since *r* and f_v can be measured using both stereological observations and pole figure measurements, it will allows correlations between the fitting parameters obtained from both techniques.

2.5.6. Dielectric characterization

Dielectric properties of the textured SBT ceramics were measured from room temperature up to 400 ºC at 2 ºC/min using setups and methods previously described in section 2.4.5. For dielectric measurements, the specimens were cut and polished in two plates: parallel (//P) and perpendicular (⊥P) to the pressing direction. Gold electrodes were then sputtered onto the whole area of the polished //P and ⊥P facets in the same way described in section 2.4.3 for measuring electrical properties.

2.5.7. Ferroelectric hysteresis measurements

To study the anisotropy in the ferroelectric properties of the textured SBT ceramics, the P-E hysteresis loops were measured at room temperature both parallel (//P) and perpendicular (⊥P) to the pressing direction using a modified Sawyer-Tower circuit and setup described in section 2.4.6. For P-E hysteresis measurements the samples were first polished to the final thicknesses of ~ 200 μm and surface area around 3×1 mm^2. Electric field as high as 150 kV/cm was applied to the samples at the frequency of 50 Hz.

2.6. References

[1] D. Elwell and H. J. Scheel, "Crystal Growth from High Temperature Solution". Academic Press, London (1975).

[2] B. N. Roy, "Crystal Growth from Melts". John Wiley & Sons, England (1992).

[3] W. Tolksdorf, "Flux Growth", in *Handbook of Crystal Growth 2: Basic Techniques*. Ed. D. T. Hurle, Elsevier Science, North Holland (1994) 563-611.

[4] G. L. Messing, S. Trolier-McKinstry, E. M. Sabolsky, C. Duran, S. Kwon, B. Brahmaroutu, P. Park, H. Yilmaz, P. W. Rehrig, K. B. Eitel, E. Suvaci, M. M. Seabaugh and K. S. Oh, "Templated Grain Growth of Textured Piezoelectric Ceramics". *Crit. Rev. Solid State Mater. Sci.* **29** [2] (2004) 45-96.

[5] B. Sih, J. Tang, M. Dong and Z.-G. Ye, "Ferroelectric $SrBi_2Ta_2O_9$ Single-Crystal Growth and Characterization". *J. Mater. Res.* **16** [6] (2001) 1726-1733.

[6] M. Dong and Z.-G. Ye, "High-Temperature Solution Growth and Characterization of the Piezo-/Ferroelectric (1 - x) $Pb(Mg_{1/3}Nb_{2/3})O_3 - x$ $PbTiO_3$ [PMNT] Single Crystals". *J. Cryst. Growth* **209** [1] (2000) 81-90.

[7] W. Tolksdorf, "Growth of Yttrium Iron Garnet Single Crystals". *J. Cryst. Growth* **3-4** (1968) 463-466.

[8] B. D. Cullity, "Elements of X-ray Diffraction". 2nd Ed., Addison-Wesley, London (1978).

[9] J. Als-Nielsen and D. McMorrow, "Elements of Modern X-ray Physics". John Wiley & Sons Ltd., England (2001).

[10] D. K. Bowen and B. K. Tanner, "High Resolution X-ray Diffractometry and Topography". Taylor & Francis Ltd., London (1998).

[11] I. K. Bdikin, I. M. Shmytko, A. M. Balbashov and A. V. Kazansky, "Twinning of $LaGaO_3$ Single-Crystals". *J. Appl. Crystallogr.* **26** (1993) 71-76.

[12] M. Alexe and A. Gruverman, "Nanoscale Characterization of Ferroelectric Materials: Scanning Probe Microscopy Approach". Springer-Verlag, Berlin (2004).

[13] R. Luthi, H. Haefke, K. P. Meyer, E. Meyer, L. Howald and H. J. Guntherodt, "Surface and Domain-Structures of Ferroelectric-Crystals Studied with Scanning Force Microscopy". *J. Appl. Phys.* **74** [12] (1993) 7461-7471.

[14] A. Gruverman, O. Auciello and H. Tokumoto, "Imaging and Control of Domain Structures in Ferroelectric Thin Films via Scanning Force Microscopy". *Annu. Rev. Mater. Sci.* **28** (1998) 101-123.

[15] M. Abplanalp, L. M. Eng and P. Gunter, "Mapping the Domain Distribution at Ferroelectric Surfaces by Scanning Force Microscopy". *Appl. Phys. A: Mater. Sci. Process.* **66** (1998) S231-S234.

[16] B. Jaffe, W. R. Cook and H. Jaffe, "Piezoelectric Ceramics". Academic Press, London and New York (1971).

[17] M. E. Lines and A. M. Glass, "Principles and Applications of Ferroelectrics and Related Materials". Clarendon Press, Oxford (1977).

[18] Y. Xu, "Ferroelectric Materials and their Applications". North-Holland Elsevier Sci. Publ., Amsterdam (1991).

[19] A. L. Kholkin, C. Wutchrich, D. V. Taylor and N. Setter, "Interferometric Measurements of Electric Field-Induced Displacements in Piezoelectric Thin Films". *Rev. Sci. Instrum.* **67** [5] (1996) 1935-1941.

[20] F. K. Lotgering, "Topotactical Reactions with Ferrimagnetic Oxides having Hexagonal Crystal Structures - I". *J. Inorg. Nucl. Chem.* **9** [2] (1959) 113-123.

[21] U. F. Kocks, C. N. Tomé and H.-R. Wenk, "Texture and Anisotropy: Preferred Orientations in Polycrystals and their Effect on Material Properties". Cambridge University Press, UK (2000) 126-177.

[22] J. Ricote and D. Chateigner, "Quantitative Texture Analysis Applied to the Study of Preferential Orientations in Ferroelectric Thin Films". *Bol. Soc. Esp. Ceram. Vidrio* **38** [6] (1999) 587-591.

[23] R. Chinn, "Grain Sizes of Ceramics by Automatic Image-Analysis". *J. Am. Ceram. Soc.* **77** [2] (1994) 589-592.

[24] Software AnalySIS 3.2, Soft Imaging System, Olympus Company (2004). See web page: http://www.soft-imaging.com

[25] T. Allen, "Particle Size, Shape, and Distribution", in *Particle Size Measurement*. Ed. B. Scarlett, Chapman and Hall Inc, New York (1990) 124-189.

[26] J. L. Jones, E. B. Slamovich and K. J. Bowman, "Critical Evaluation of the Lotgering Degree of Orientation Texture Indicator". *J. Mater. Res.* **19** [11] (2004) 3414-3422.

[27] M. M. Seabaugh, M. D. Vaudin, J.P. Cline and G. L. Messing, "Comparison of Texture Analysis Techniques for Highly Oriented α-Al_2O_3". *J. Am. Ceram. Soc.* **83** [8] (2000) 2049-2054.

[28] M. S. Sandlin, C. R. Peterson and K. J. Bowman, "Texture Measurement on Materials Containing Platelets Using Stereology". *J. Am. Ceram. Soc.* **77** [8] (1994) 2127-2131.

[29] W. A. Dollase, "Correction of Intensities for Preferred Orientation in Powder Diffractometry: Application of the March Model". *J. Appl. Crystallogr.* **19** [4] (1986) 267-272.

Chapter 3

Growth and Characterization of $SrBi_2Ta_2O_9$ and $SrBi_2Nb_2O_9$ Single Crystals

3.1. Introduction

This chapter is focused on the results describing the optimization of the processing parameters for growing high-quality $SrBi_2Ta_2O_9$ (SBT) and $SrBi_2Nb_2O_9$ (SBN) single crystals, as well as on the study of the intrinsic properties of the grown crystals including the anisotropy of the dielectric, ferroelectric and piezoelectric properties. Both crystals were grown by a high-temperature self-flux solution method using a B_2O_3 modified Bi_2O_3 flux, as described in Chapter 2 (section 2.2). The processing conditions were firstly optimized to increase the size and to improve the quality of the SBT single crystals. Then, they were applied for the growth of SBN single crystals. The manipulated variables were essentially related to the temperature profiles used during growth runs, *e.g.*, cooling rates and soaking times, while maintaining fixed the flux composition and concentration.

The experimental results regarding SBT and SBN single crystals are discussed in separate sections of this chapter. Each section is further divided into several subsections where the crystals quality is first described based on the x-ray diffraction and topography analyses. In the following subsection, a detailed study of the domain configuration is reported in the case of SBT single crystals, and discussed based on the presence of separate ferroelastic and ferroelectric phase transitions in SBT. Lastly, a separate subsection focuses on the evaluation of dielectric, ferroelectric and piezoelectric properties along different crystallographic directions, demonstrating the large anisotropy in the intrinsic properties of both SBT and SBN single crystals.

3.2. $SrBi_2Ta_2O_9$ Single Crystals

3.2.1. Single crystal growth with optimized processing conditions

It has been already reported that large SBT single crystals can be obtained by the self-flux solution method adding a low amount of B_2O_3 (boron oxide) to the Bi_2O_3 (bismuth oxide) flux.[1] Without B_2O_3 addition, the SBT powder does not melt thoroughly at 1350 ºC due to the high and incongruent melting point of the SBT phase, resulting in small crystals (smaller than 1 mm) of different phases including SBT, $SrTa_4O_{11}$ and $Sr_2Ta_2O_7$,[2-4]

some of them being formed around the Pt lid in the vapor phase region. The addition of a small amount of B_2O_3 (5 wt% in this case) to the flux improves the crystallization by promoting powder melting and leading to a more viscous and stable medium for SBT nucleation and growth.[1]

Therefore, SBT single crystals were grown using a 60/40 molar ratio of SBT to flux (35 wt% Bi_2O_3 and 5 wt% B_2O_3), following the results obtained by Sih *et al.*[1] and using three different thermal profiles, as described in section 2.2.2. Figure 3.1 shows a top view of the solidified mass inside the Pt crucible composed of SBT crystals and flux, obtained after the growth experiment using thermal profile TP3. The crystals were stuck together in different directions denoting multiple nucleations and the lack of space in the Pt crucible, and exhibited an outside yellowish coloration due to the Bi_2O_3 flux. A similar appearance of the solidified mass was observed after the growth experiments using thermal profiles TP1 and TP2, except the size of the crystals which seemed to be the first major difference.

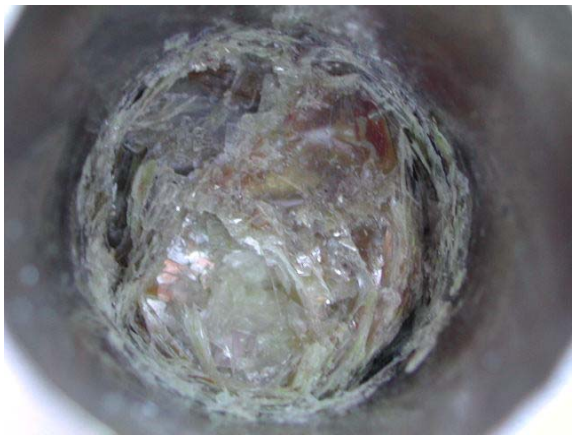

Figure 3.1 Solidified mass of $SrBi_2Ta_2O_9$ crystals and flux inside the Pt crucible (2 cm base diameter) after the growth experiment using thermal profile TP3.

Figure 3.2 shows two micrographs of the typical as-grown and acid cleaned SBT crystals obtained using thermal profiles TP2 and TP3. As observed, large and transparent SBT single crystals with a layered habit and faceted surfaces were obtained with the boron-modified flux. The obtained crystal dimensions for the three thermal profiles (TP1, TP2 and TP3) and a SBT/flux ratio of 60/40 are summarized in Table 3.1. The sizes of the crystals are seen to depend on the used temperature profile. For the first profile (TP1), small crystals were obtained with major face size smaller than 1×1 mm^2. In contrast, for

the other two profiles (TP2 and TP3), the crystal sizes varied between $5 \times 3 \times 0.1$ mm^3 for the thermal profile TP3 (dimensions similar to those reported by Sih *et al.*[1] when using a 2 cm base diameter Pt crucible and the same profile) and $7 \times 5 \times 0.2$ mm^3 for the thermal profile TP2.

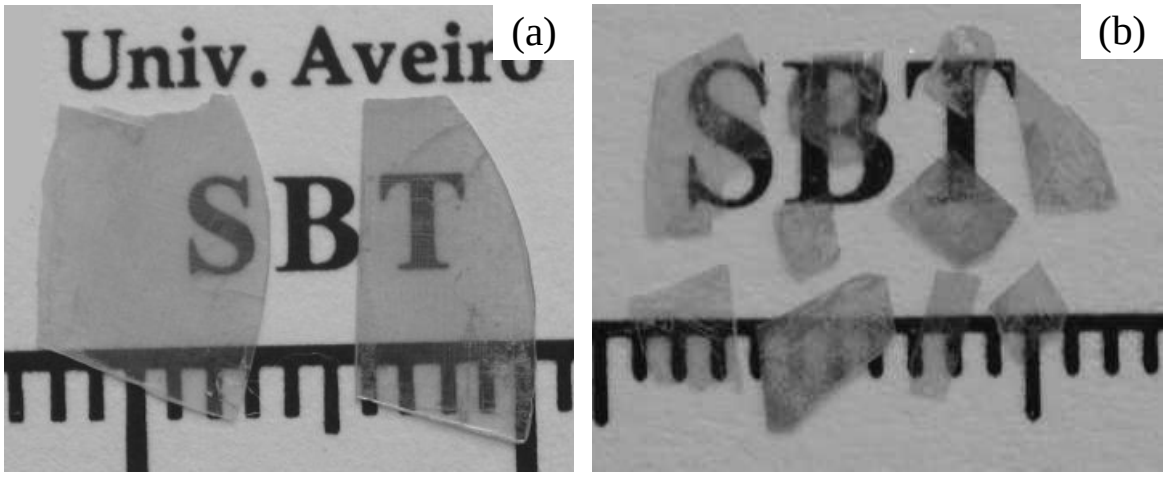

Figure 3.2 Top views of the as-grown and acid cleaned $SrBi_2Ta_2O_9$ crystals with platelet morphology, grown using thermal profiles: (a) TP2 and (b) TP3 (1 division = 1 mm).

Table 3.1 Dimensions of $SrBi_2Ta_2O_9$ crystals for different thermal profiles.

Flux composition (wt%) Bi_2O_3	B_2O_3	Thermal profile	Maximum size (mm^3)
35	5	TP1	$1 \times 1 \times 0.02$
35	5	TP2	$7 \times 5 \times 0.2$
35	5	TP3	$5 \times 3 \times 0.1$

It is noteworthy to mention that the biggest crystals were not obtained with the longer profile (TP3) having the slowest cooling process, but with rather short thermal profile TP2 [see Fig. 3.2(a)]. The thickest crystals (~ 200 μm in most cases) were also obtained with thermal profile TP2. This was a very important achievement in view of the later ferroelectric characterization along the *ab*-plane. Nevertheless, the single crystals of the highest quality (with perfectly rectangular shape, transparent and free of cracks) were somewhat smaller, typically ~ $2 \times 2 \times 0.1$ mm^3, being preferred for crystallographic and ferroelectric characterization.

Crystal growth and morphology

During the cooling process, supersaturation was created and two distinct phenomena took place: crystal nucleation and crystal growth. For a fixed amount of starting solution, the higher is the number of nuclei, the smaller is the size of the final crystals. For the present system, the dependence of the nucleation and growth rates on cooling procedure has not been reported so far. The obtained results are likely to result from the competition between these two phenomena. The used combination of temperature and time (profile TP2) is believed to provide adequate conditions for SBT crystal nucleation and growth, since large SBT crystals were indeed obtained.

If the initial cooling is speed up (as in TP1 profile), smaller resulting crystals are obtained. This behavior may be understood assuming that in this case the initial supersaturation is higher and thus enhances the nucleation rate, giving rise to a larger number of critical nuclei as compared to that formed during TP2 thermal process. Since both profiles run in parallel after 1300 ºC, present results also suggest that the temperature range 1300-1350 ºC is critical for SBT nucleation. As for TP3 profile, which produced less developed SBT crystals as compared to TP2 profile, its early stage of crystallization is identical to that of TP2 profile and so the number of nuclei should be similar in both cases. The cooling below 1300 ºC distinguishes TP2 and TP3 processes, being faster in TP2 and thus promoting in this case a higher initial growth rate of the nucleated crystals.[5] The slower cooling rate during thermal profile TP3, while allowing a slower crystal growth, is prone to the secondary nucleation events which also contribute to the decrease of supersaturation of the system, thus limiting crystal growth. To avoid the effect of secondary nucleation, temperature cycling has been proposed as an effective procedure to dissolve smaller crystals.[6]

The growth morphology of a single crystal is the end result of different kinds of phenomena:[7] (a) external processes operating in the bulk solution (*e.g.*, mass transport, chemical reactions, heat transport, etc.), (b) processes occurring at the crystal surface (*e.g.*, adsorption and surface migration of growth units followed by integration), and (c) system tendency for an equilibrium shape corresponding to a minimum Gibbs energy.

The equilibrium shape generally implies that the face with smallest specific surface energy is the largest. In the present case, the interplay of the above referred phenomena originated a platelet shaped SBT crystal which morphology is largely dominated by [001] faces, parallel to the crystallographic *ab*-plane (see next section 3.2.2 for the details of crystallographic study). These macroscopic flat faces which were observed for all the used growing conditions are suggested to be those of lowest surface energy. In other comparable layered system like $YBa_2Cu_3O_{7-\delta}$ (a CuO_2 layered oxygen-deficient perovskite), single crystals having well developed dominant [001] faces and similar growth rate anisotropy have been experimentally confirmed, which correspond to the lowest surface energy faces.[7]

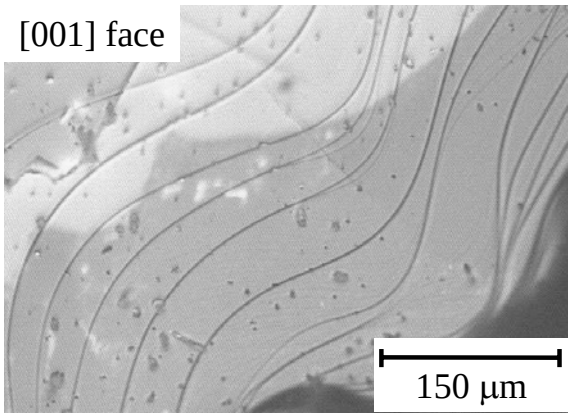

Figure 3.3 Micro-morphology of the $SrBi_2Ta_2O_9$ single crystal major face near the crystal edge, showing layered growth steps aligning perpendicular to the [001] direction.

Figure 3.3 shows the surface micro-photograph of the SBT single crystal major face (parallel to [001] plane) near the crystal edge, revealing growth steps aligned perpendicular to the [001] direction and suggesting a dominant layer growth mechanism in that face. Further studies have to be carried out, aiming at the clarification of the role of the different growth parameters (*i.e.*, effects of the supersaturation and/or of the undercooling on the interfacial kinetics and on the solute diffusion) for determining the final morphology.

3.2.2. X-ray diffraction and x-ray topography analysis

The obtained SBT crystals were characterized by x-ray diffraction (XRD) and x-ray topography techniques at room temperature. XRD measurements were firstly performed in reflection geometry perpendicular to the major face of platelet-like SBT crystals obtained using thermal profile TP3 (see section 2.4.1 and Fig. 2.5 for better understanding).

Although diffractions from the {00*l*} planes of the SBT structure clearly dominate the XRD pattern, as shown in Fig. 3.4(a), most of the crystals were not perfectly *c*-axis oriented, since some small reflections of non-(00*l*) peaks can be also observed in this pattern. For comparison, the XRD pattern of the pure SBT powder calcined at 950 ºC for 3 hours is also included in Fig. 3.4(b). Therefore, these platelets may contain small regions with orientations other than (00*l*), which are probably due to strong bending of the single crystal or the blending of two single crystals inside the Pt crucible during growth.

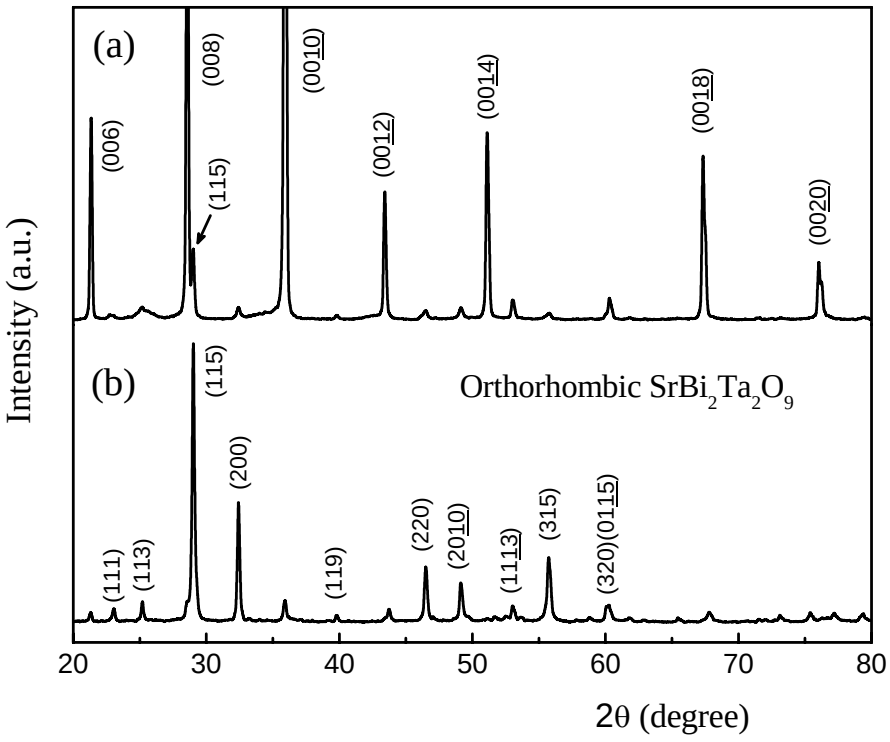

Figure 3.4 X-ray diffraction patterns for (a) non-perfectly *c*-axis oriented $SrBi_2Ta_2O_9$ crystal platelets scanned in reflection geometry perpendicular to the crystal major face and obtained using thermal profile TP3, where some small reflections of non-(00*l*) peaks are observed, and (b) pure SBT powder calcined at 950 ºC for 3 hours for comparison. The Miller indexes for the orthorhombic SBT phase are included.

Figure 3.5 shows transverse sections by optical microscopy of non-perfectly *c*-axis oriented SBT crystal obtained using thermal profile TP3. As can be seen in Fig. 3.5(a), several layers oriented parallel to the major face can be distinguished in the cross-section. These layers are possibly associated with several crystals which nucleate over the surface of another crystal and thus are stuck together parallel to the *ab*-plane during growth. On the other hand, Figure 3.5(b) shows several layers that are lying at some angle relative to the

plane of the crystal face, interfacing with the parallel layers. This seems to be related with the blending of two crystals and may be the reason for the XRD results showing some reflections other than (00*l*). Based on the above arguments, these imperfect SBT crystals were not considered for domain structure, dielectric and ferroelectric measurements.

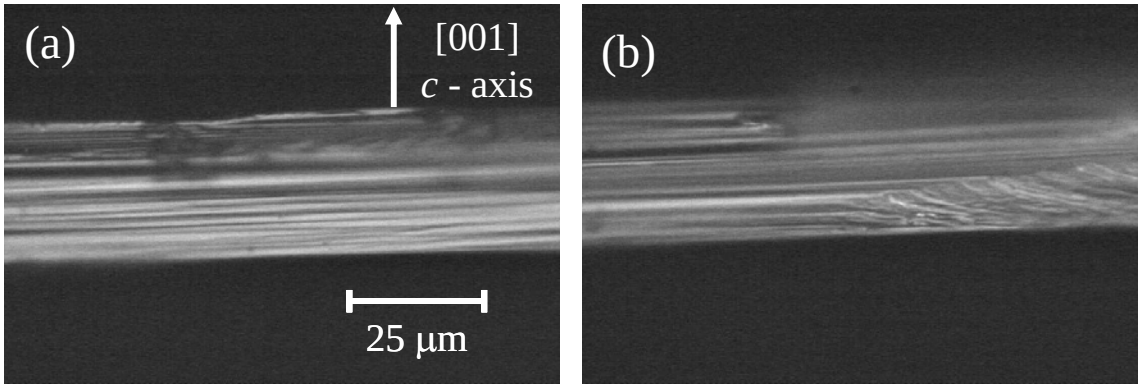

Figure 3.5 Cross-section of a $SrBi_2Ta_2O_9$ crystal obtained using thermal profile TP3, showing several layers lying at some angle relative to crystal major face interfacing with layers stuck parallel to the *ab*-plane.

On the other hand, the XRD spectra in reflection and transmission geometries for a rectangular SBT crystal platelet obtained using thermal profile TP2 is shown in Fig. 3.6(a,b), where only (*h*00) and (00*l*) plane reflections are observed in the directions parallel and perpendicular to the major face, respectively. In this way, highly oriented SBT single crystal platelets (with *c*-axis perpendicular to the major face) were successfully produced using thermal profile TP2.

Pseudo-tetragonal lattice parameters were estimated using the orthorhombic space group $A2_1am$ and the reflections (600) and (00$\underline{28}$), where the Cu $K_{\alpha1}$ can be completely separated from the Cu $K_{\alpha2}$, as shown in Fig. 3.7. The results obtained [$a,b \approx 5.508(1)$ Å and $c \approx 25.01(1)$ Å] are in a good agreement with the reported data.[8,9]

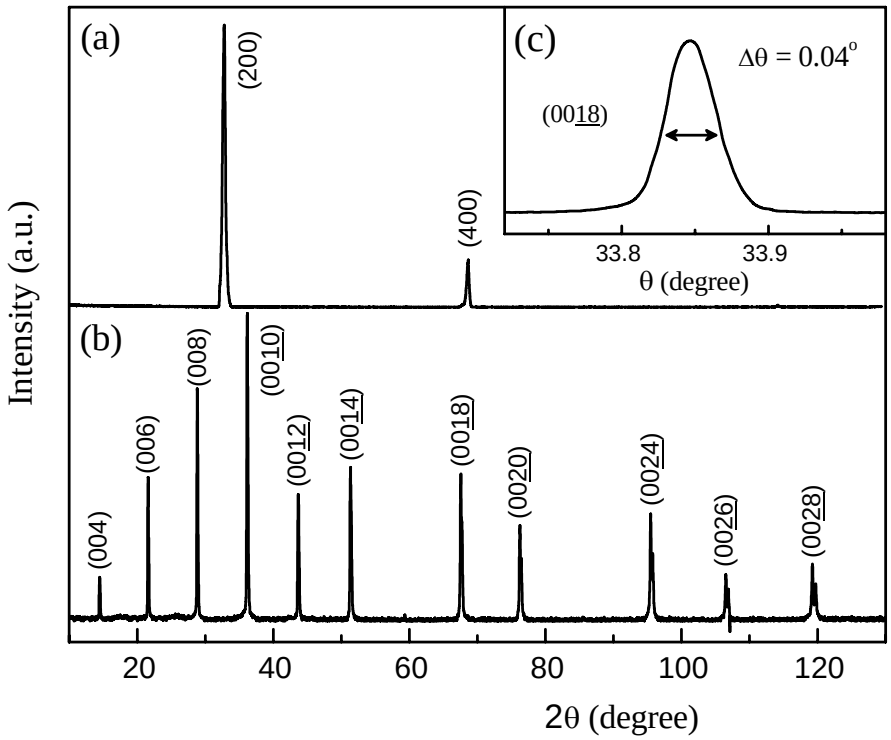

Figure 3.6 X-ray diffraction spectra along the (a) [100] and (b) [001] directions for a perfectly *c*-axis oriented $SrBi_2Ta_2O_9$ single crystal platelet obtained using thermal profile TP2. (c) Rocking curve of the (00$\underline{1}$8) reflection, where Δθ is the Full-Width at the Half-Maximum (FWHM). The Miller indexes for the orthorhombic SBT phase are included.

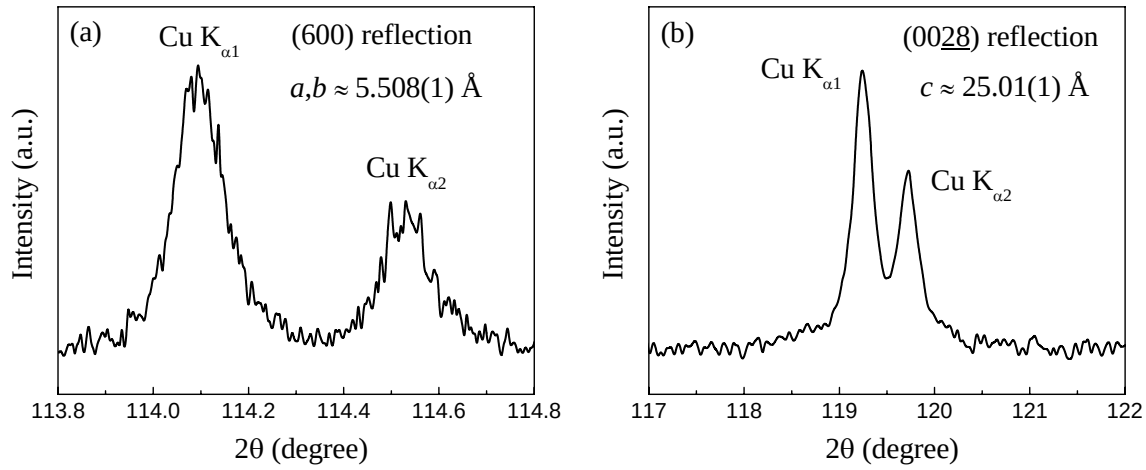

Figure 3.7 X-ray diffraction profiles of the reflections (a) (600) and (b) (00$\underline{2}$8). Pseudo-tetragonal lattice parameters were estimated and are included in the graphs.

X-ray topography measurements were performed on a small and rectangular shaped SBT single crystal obtained using thermal profile TP2 with the size of ~ 2 × 1 × 0.02 mm^3. The x-ray θ- and θ-2θ-angular scanning topographies are represented in Fig. 3.8(a) and (b),

respectively. The θ-angular scanning topograph in Fig. 3.8(a) was obtained using the (110) reflection. The uniform contrast was observed over all the surface of the sample confirming its perfect orientation. The intensity of this image depends on the thickness of the sample and extinction (defect) crystal conditions. Figure 3.8(b) represents the diffraction image for θ-2θ-angular scanning topographs using the (00$\underline{18}$) reflection. For an ideal crystal this image should correspond to the shape of the sample with a linear transformation governed by the geometry of the experimental setup.[10,11] For the present case, the small deviation of the diffraction image in Fig. 3.8(b) from the real shape [see θ-angular scanning topograph in Fig. 3.8(a)] can be due to small bending of the crystal surface along its major face. Indeed, this deviation is determined by the magnitude of the misorientation, being smaller than 1º for this crystal.

In addition, the crystal quality is better demonstrated through the rocking curves [see Fig. 3.6(c)], where the Full-Width at the Half-Maximum (FWHM) of the rocking curve for the (00$\underline{18}$) reflection was $\Delta\theta = 0.04^{o}$, indicating very high quality of the crystals.

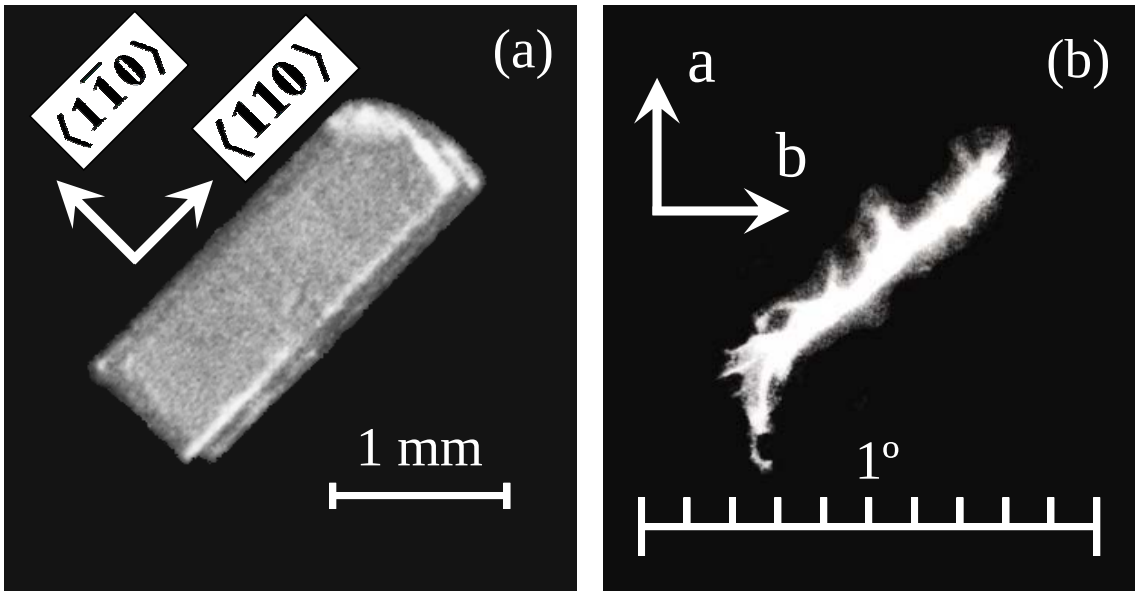

Figure 3.8 X-ray (a) θ-scanning and (b) θ-2θ-angular scanning topographies, using the (110) and (00$\underline{18}$) reflections, respectively, for a small ($2 \times 1 \times 0.02$ mm^3), rectangular shaped and perfect $SrBi_2Ta_2O_9$ single crystal obtained using thermal profile TP2.

The crystallographic orientation of the SBT single crystal facets can also be deduced from x-ray topography. Figure 3.8(a) illustrates the directions of the main crystallographic axes, where the narrow sides of the rectangular shaped crystals are oriented along the [110]

and $[1\bar{1}0]$ directions with the [001] direction (*c*-axis) lying perpendicular to the major face. As a matter of fact, the shape of the crystals should be determined by the high-symmetry tetragonal phase (space group $I4/mmm$, $a = b \cong 3.85$ Å),[8] since they were grown at high temperature (far above 1000 ºC). It is believed that, when cooled down to room temperature, the symmetry of the single crystal transforms from tetragonal into orthorhombic one (space group $A2_1am$) but its original shape formed at high temperature is retained. Apparently, during this transformation, *a*- and *b*-axes rotate by 45º relative to tetragonal axis and [100] direction in the tetragonal phase becomes [110] direction in the orthorhombic phase. It can be thus concluded that the edges of our crystals (directed along [110] and $[1\bar{1}0]$ directions at room temperature) originate from the high-symmetry [100] and [010] directions of the parent tetragonal structure.

3.2.3. Ferroelectric domains and twinning

On cooling from high temperatures, SBT first experiences an improper ferroelastic phase transition at $T_{C1} \approx 550$ ºC from the parent tetragonal phase ($I4/mmm$) to the intermediate orthorhombic phase (*Amam*), and then at $T_{C2} \approx 350$ ºC undergoes the proper ferroelectric transition to the low-temperature orthorhombic phase ($A2_1am$),[12] as previously described in section 1.3.2. The structure of the intermediate orthorhombic phase (*Amam*) permits the formation of ferroelastic domains or twins.[13] Below the Curie temperature T_{C2}, both ferroelastic/ferroelectric 90º domains and purely ferroelectric 180º domains can exist. In this section, the first reliable measurements of the domain structure in high-quality SBT crystals using PFM are reported.

Rocking curves in a wide scanning range

Ferroelastic domains (twins) in SBT single crystals are related to the interchange of the crystallographic *a*- and *b*-axes in the *ab*-plane. In order to prove the existence of these twins, the extinction rules for the space group $A2_1am$ were investigated using the XRD profiles at room temperature for a couple of parent reflections, *e.g.*, (20$\underline{1}$8), (02$\underline{1}$8), (01$\underline{1}$5) and (10$\underline{1}$5) reflections.

For this space group, the extinction rules of possible reflections are,[14]

$k + l = 2n$ (n is an integer) for the (h, k, l) reflections,

and

$h = 2n$, $l = 2n$ for the (h, 0, l) reflections,

which are the same rules as those for the intermediate orthorhombic phase *Amam*.

Accordingly, if the SBT single crystal is free of twinning in the *ab*-plane, it can be positioned and rotated in such a way that reflections from the (20$\underline{1}$8), (02$\underline{1}$8) and (01$\underline{1}$5) planes are possible, but the (10$\underline{1}$5) plane reflection is not possible since it is forbidden for this space group (see Fig. 2.6 in section 2.4.1 for a better understanding of the measuring technique). Hence the occurrence of the (10$\underline{1}$5) reflections by rotating the crystal by 90º about the *c*-axis from the position where the (01$\underline{1}$5) reflections are obtained must indicate the presence of multiple twins in the SBT single crystal.

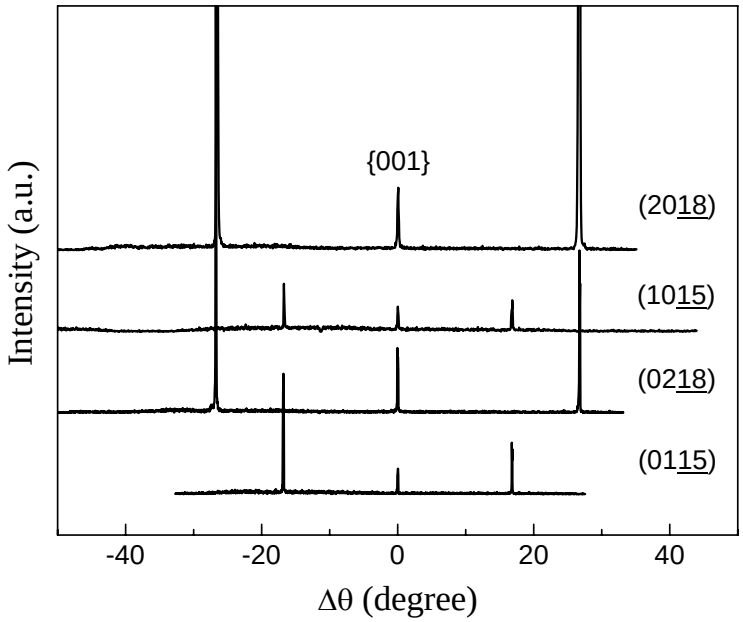

Figure 3.9 Rocking curves in a wide scanning range (θ-scanning) for the (20$\underline{1}$8), (02$\underline{1}$8), (01$\underline{1}$5) and (10$\underline{1}$5) reflections obtained by rotating the crystal about the [010] direction.

Figure 3.9 displays the rocking curves in a wide scanning range (θ-scanning) for the above mentioned reflections obtained when the crystal is rotated about the [010] direction

(see Fig. 2.6 in section 2.4.1 for a better understanding), and considering that reflections (20$\underline{1}$8) and (10$\underline{1}$5) can be obtained by rotating the single crystal by 90º about the *c*-axis from the position where the reflections (02$\underline{1}$8) and (01$\underline{1}$5), respectively, were obtained. The same peaks were observed in both pairs of parent reflections after the 90º rotation of the crystal about the *c*-axis. Thus, the presence of the pair of (01$\underline{1}$5) and (10$\underline{1}$5) reflections in both cases, before and after 90º rotation, indicates that in the studied SBT single crystal the *a*- and *b*-axes alternate along two possible directions corresponding to the diagonals of the (001)-oriented face of the unit cell in the parent tetragonal phase (*I*4/*mmm*). Therefore, twin walls separating ferroelastic 90º domains should exist in this crystal. However, the orientation and density of twin walls cannot be determined from the XRD experiment.

Piezoelectric force microscopy: 180º domains

Piezoelectric force microscopy (PFM) measurements were firstly performed onto several small areas of the as-grown and acid cleaned SBT single crystal obtained using thermal profile TP2. In this case, two different configurations were used to visualize 180º domains, *i.e.*, when the cantilever is parallel to *ab*-plane (major face) of the single crystal and when it is positioned normal to *ab*-plane. In the first case, the in-plane component of polarization vector was observed following the *lateral* deflection of the cantilever, as described in section 2.4.4. Since only the in-plane component orthogonal to the cantilever contributes to the measured signal (see Fig. 2.10), the cantilever was positioned parallel to one of the crystal edges ⟨110⟩ and the crystal surface was scanned by moving the tip at a small rate of 1 μm/s.

Figures 3.10(a) and 3.10(b) show simultaneously acquired topography and piezoresponse images, respectively, using the first configuration (cantilever parallel to the *ab*-plane). The straight lines in the topography image are scratches appearing onto the crystal surface due to the submicron polish using a colloidal-silica aqueous suspension (particle size ~ 0.05 μm). Although, crystal surfaces with the roughness smaller than that achieved in this case at this submicron scale is very difficult to obtain, the domain patterns are not greatly influenced by these scratches and can be clearly visualized in the piezoresponse image. The bright and dark stripes observed in the piezoresponse image correspond to ferroelectric 180º domains. These domains are visualized as antiparallel

stripes with a periodicity of about 350 nm. As expected, the polarization is oriented along the [100] direction (*a*-axis direction), that is, inclined at 45º from the crystal edges ⟨110⟩ (the crystal edges ⟨110⟩ match with the vertical and horizontal sides of these images).

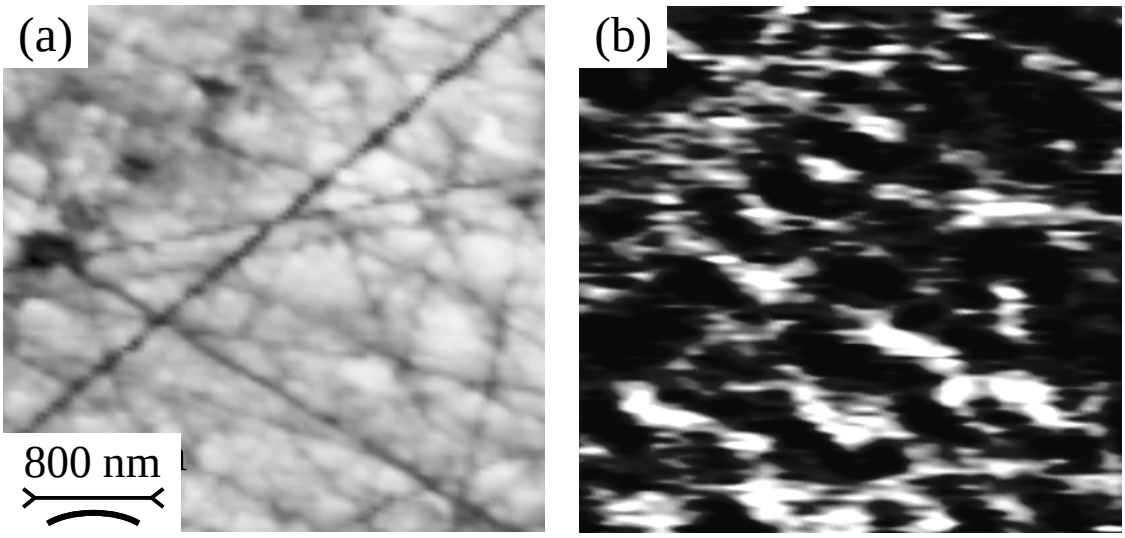

Figure 3.10 PFM images on the [001] face of a $SrBi_2Ta_2O_9$ single crystal obtained using thermal profile TP2: (a) topography and (b) *lateral* piezoresponse images simultaneously obtained using the first configuration, that is, the cantilever is *parallel* to *ab*-plane.

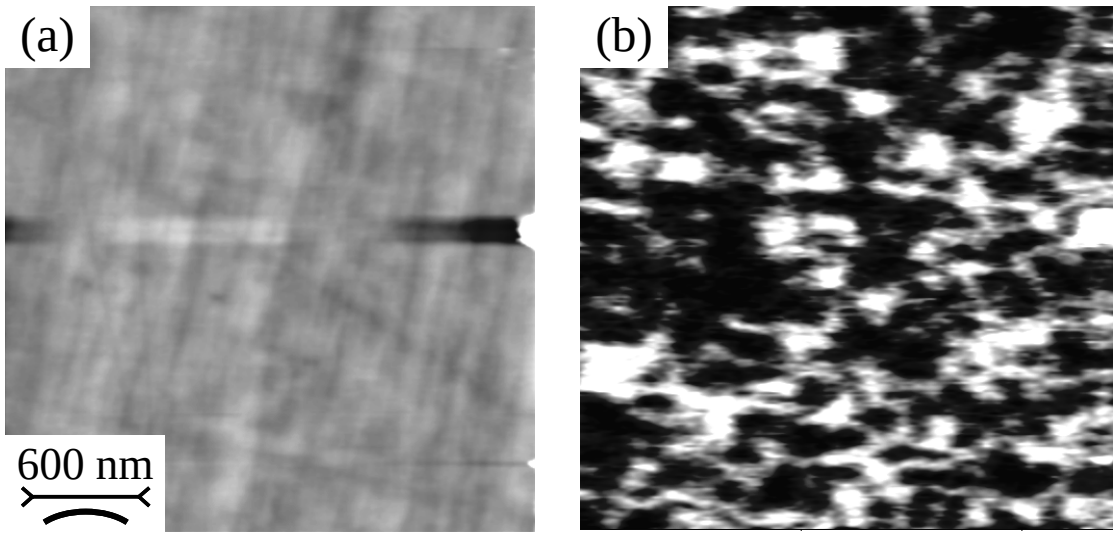

Figure 3.11 PFM images on the [100] face of a $SrBi_2Ta_2O_9$ single crystal obtained using thermal profile TP2: (a) topography and (b) *vertical* piezoresponse images simultaneously obtained using the second configuration, that is, the cantilever is *normal* to *ab*-plane.

Figures 3.11(a) and 3.11(b) show simultaneously acquired topography and piezoresponse images, respectively, using the second configuration (cantilever normal to

the *ab*-plane). In this case, the measured signal corresponds to the *vertical* deflection of the cantilever and reflects the distribution of out-of-plane component of polarization. Bright and dark contrast corresponds to opposite polarization vectors oriented parallel to the *a*-axis. The observed domain pattern is much less regular in this view than in the first configuration. It is understood that these 180º domains correspond to the domain structure presented in the Fig. 3.10(b) but seen from the *bc*-plane.

From this first examination of ferroelectric 180º domains by PFM, it is believed that a 3D domain image should consist of rod-like shaped 180º domains oriented along *a*-axis, as schematically shown in Fig. 3.12.

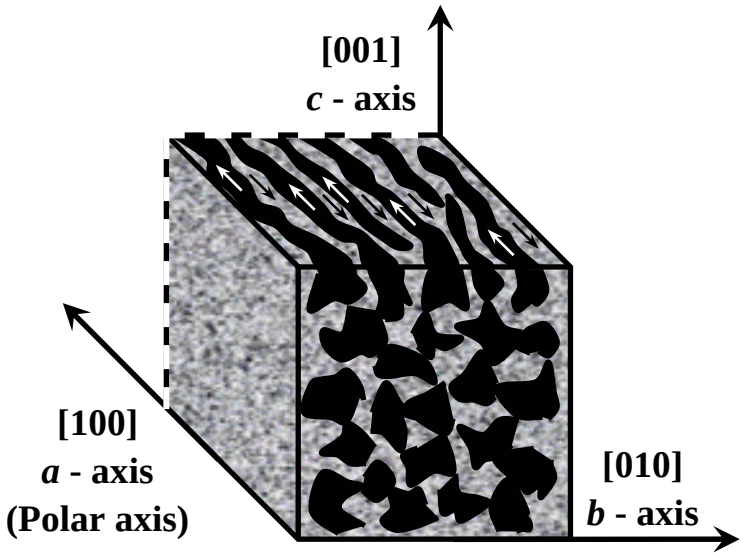

Figure 3.12 Schematic illustration of the 3D arrangement of 180º domains suggested by the PFM measurements in a typical *c*-axis oriented $SrBi_2Ta_2O_9$ single crystal.

Piezoelectric force microscopy: 90º domains

In order to further investigate the possibility of 90º domain walls, corresponding to twinning planes, together with the above observed 180º domains, the same SBT single crystal was annealed at 750 ºC for 10 hours, that is, above both ferroelastic and ferroelectric phase transitions, and then was cooled down very slowly to room temperature at ~ 60 ºC/h. Subsequently, a greater area of the crystal surface was scanned following the first configuration, *i.e.*, the cantilever was positioned parallel to both one of the crystal edges ⟨110⟩ and the crystal major face. The PFM measurements were performed at room

temperature to directly image the domain walls in SBT crystals via determination of local polarization directions in the ferroelectric phase.

Simultaneously acquired topography and piezoresponse images are shown in Figs. 3.13(a) and 3.13(b), respectively. On the piezoresponse image, the regions with bright and dark contrast correspond to ferroelectric domains with the in-plane polarization having upward and downward vertical component, respectively. To fully ascertain the polarization orientation inside domains, the sample was rotated by 90º about the *c*-axis and then scanned again. The images of similar domains obtained at the initial position of the sample [Fig. 3.14(a)] and after its rotation by 90º [Fig. 3.14(b)] are complementary. This observation shows that the vertical and horizontal components of the spontaneous polarization are comparable in magnitude, which agrees with the expected orientation of the polarization, that is, inclined at 45º from the crystal edges ⟨110⟩. Therefore, the extended vertical domain boundaries seen in Fig. 3.13(b) may be attributed to 90º domain walls separating domains with orthogonal directions of the polar axis.

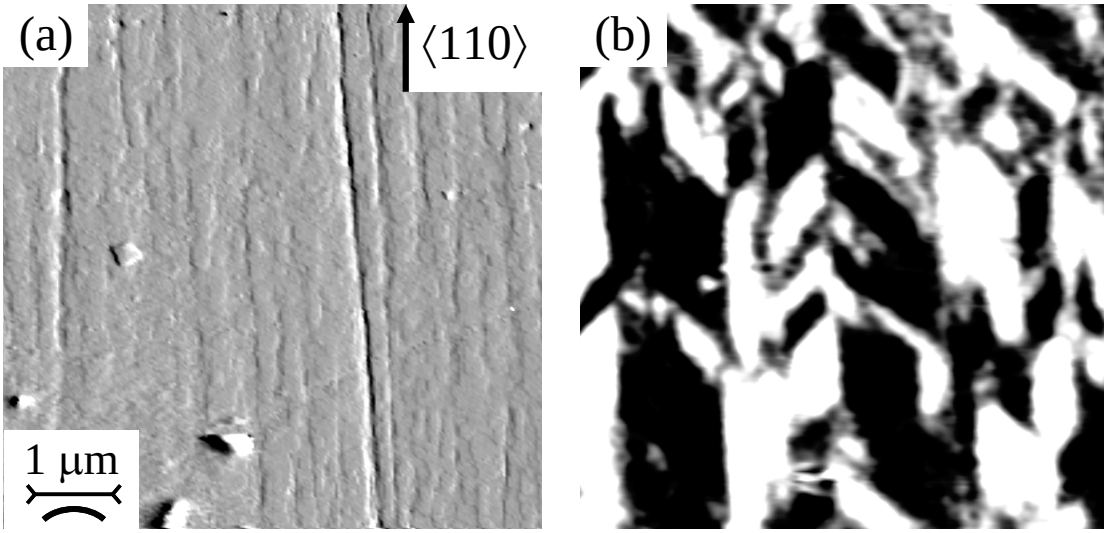

Figure 3.13 PFM images on the (001) face of $SrBi_2Ta_2O_9$ single crystal: (a) topography and (b) *lateral* piezoresponse images simultaneously obtained using the first configuration.

Such ferroelastic/ferroelectric walls tend to be parallel to the (100) or (010) plane of the parent tetragonal phase (*I*4/*mmm*), which agrees with the observed preferential orientation. The twin boundaries are slightly inclined due to a small angle between the crystal edge and the scanning direction. By analyzing several images taken at different locations, we found that the widths of 90º domains (twins) forming laminar structures lie in

the range of 0.7 - 1.5 μm. Alternating bright and dark stripes inside these twins correspond to the ferroelectric 180º domains with the boundaries parallel to the *a*-axis, as mentioned above. The width of these 180º domains varies from 250 to 500 nm. It should be noted that individual 90º domains were also observed inside some laminar twins. The comparison with previous observation of the *ac*(*bc*)-plane of the SBT crystal (see Figs. 3.10 and 3.11) allows us confirming that 180º domain walls have rod-like shape parallel to *a*-axis.

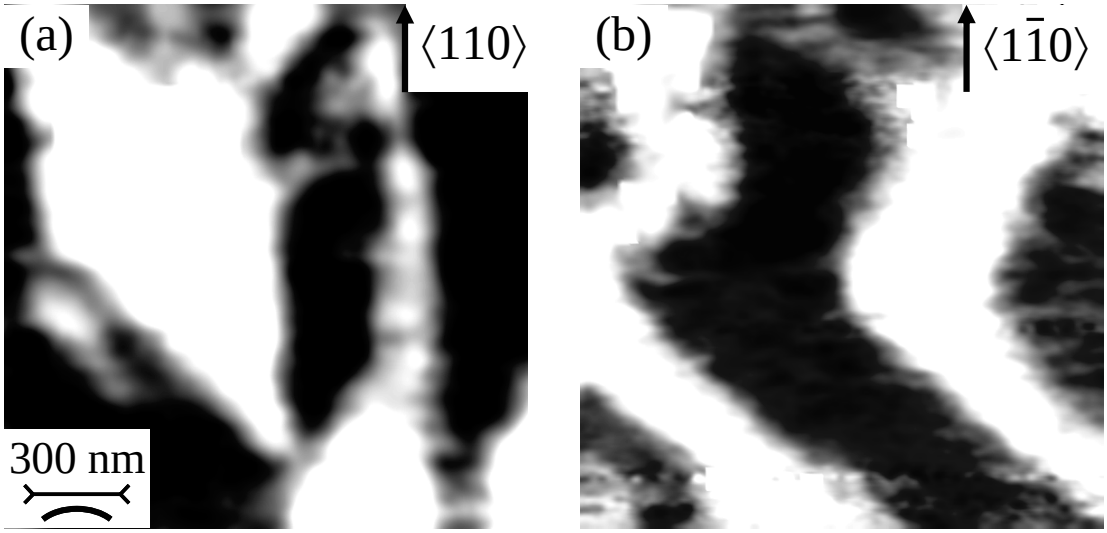

Figure 3.14 *Lateral* piezoresponse images on the (001) face of $SrBi_2Ta_2O_9$ crystal. The image (b) was acquired after rotating the sample by 90º relative to the initial position in (a).

Remarkably, the coexisting domains of two types form a well-defined *herringbone* structure (see Fig. 3.15 for the schematic illustration). In contrast to the previous reported observations of irregular 90º domain patterns with curved boundaries,[15-17] the 90º walls were found to be mostly flat in the studied SBT crystals. This is an unexpected result, because the bending of ferroelastic walls should be easy in SBT due to a very small spontaneous strain $S_o = b/a - 1$ (about 7×10^{-4} at room temperature, calculated from Rae *et al.*[8]). Indeed, the energy associated with the wall bending is proportional to S_o^2.[18] Accordingly, this energy must be much smaller in SBT that in conventional perovskite ferroelectrics (by a factor of 100 as compared with $BaTiO_3$). This feature explains the earlier observations[15-17] of highly curved 90º walls but apparently excludes the existence of flat walls. However, the wall bending produces elastic fields of very long range in the surrounding material since it leads to the appearance of effective *disclinations* with a density directly proportional to the wall curvature.[18] Therefore, even $S_o \sim 10^{-3}$ may be

sufficient to stabilize flat walls in high-quality SBT crystals (in contrast to ceramics, films and imperfect crystals).

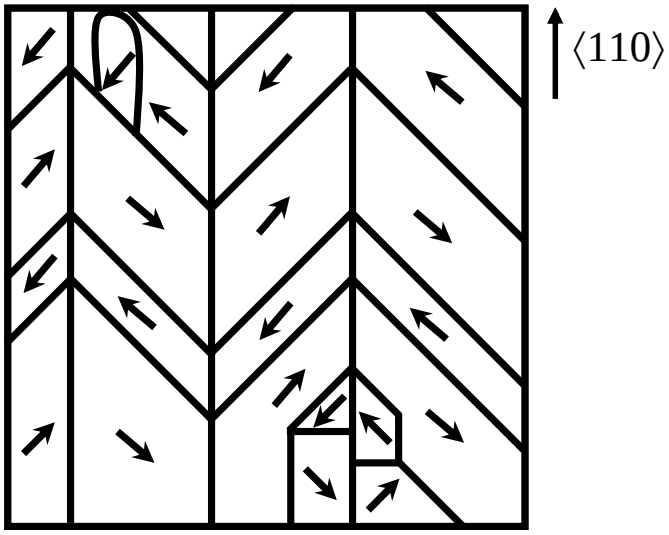

Figure 3.15 Reconstructed domain structure of the $SrBi_2Ta_2O_9$ single crystal. The cross-section of domain pattern in the *ab*-plane is depicted. Arrows show polarization directions.

The *herringbone* domain pattern observed at room temperature is believed to be formed in the following way. First, a laminar twin structure appears during the ferroelastic phase transition occurring at $T_{C1} \approx 550$ ºC.[13] The twinning of the ferroelastic phase is driven by the resulting decrease of the elastic energy associated with the clamping of the spontaneous strains.[19] These strains are coupled to the structural order parameter $\boldsymbol{Q}$ of the improper ferroelastic transition, which is related to the tilting of the oxygen octahedra.[20] Additional ferroelectric 180º domain structure appears in the twinned crystal below the ferroelectric transition temperature $T_{C2} \approx 350$ ºC.[21] Formation of 180º domains is driven by the reduction of the electric energy associated with the presence of polarization charges $\rho = -$ div $\boldsymbol{P}$.[22] Since 180º walls are formed in the twinned crystal lattice, they acquire a zigzag shape, tending to be parallel to the spontaneous polarization $\boldsymbol{P}$ inside each 90º domain to minimize the electric energy.

The equilibrium width d^* of the 90º domains (twins) forming a laminar structure can be calculated from the formula,[23]

$$d^* = \sqrt{\frac{\pi^3 \gamma_{90}}{G S_o^2} L} \tag{3.1}$$

where γ_{90} is the energy per unit area of the 90º domain wall, G is the effective shear modulus of the crystal, and L is the thickness of a plate-like nucleus of the ferroelastic phase clamped by the surrounding parent phase. In crystals experiencing a second-order phase transition, the domain-wall energy scales as $\gamma_{90} \sim Q_o^3$ with the equilibrium value Q_o of the order parameter.[24] At the same time, the coupling between the symmetry-breaking strain and the order parameter should be linear-quadratic in improper ferroelastics like SBT. Hence for the spontaneous strain is $S_o \sim Q_o^2$. Substituting the above relations into the Eq. 3.1, it is obtained that the domain width d^* varies as,

$$d^* \sim Q_o^{-\frac{1}{2}} \sim S_o^{-\frac{1}{4}} \tag{3.2}$$

for a fixed size L. This relationship predicts that smaller values of the spontaneous strain S_o favor larger twin widths in improper ferroelastics like SBT, in contrast to the pseudo-proper ferroelastics where the coupling between the strain and the order parameter is bilinear, so that $S_o \sim Q_o$. Thus, since in this case $\gamma_{90} \sim S_o^3$,[24] the Eq. 3.1 gives $d^* \sim S_o^{\frac{1}{2}}$.

In addition, the width d^* is expected to decrease during the cooling due to the increase of S_o. This prediction agrees with the temperature dependence of the twin width observed in the ferroelectric phase of SBT crystals by Kamba *et al.*[13] In the presence of two frozen order parameters (***Q*** and ***P***) in the ferroelectric phase, the spontaneous strain S_o is a sum of two contributions, with the second contribution being caused by the electrostrictive coupling between strain and polarization. Since the electrostriction in SBT is relatively strong, see reports of Kholkin *et al.*,[25] the strain S_o may change considerably on cooling from T_{C2} to room temperature, owing to the increase of the ferroelectric polarization. The fact that the twin-wall density at room temperature is considerably larger than near T_{C2} also demonstrates the ability of 90º domains to nucleate at temperatures much lower than the ferroelastic transition temperature T_{C1}. This unusual phenomenon may be explained by a very small domain-wall energy $\gamma_{90} \sim S_o^{\frac{3}{2}}$ in SBT.

3.2.4. Dielectric, ferroelectric and piezoelectric properties

Dielectric characterization

Dielectric, ferroelectric and piezoelectric characterizations were performed in SBT single crystals obtained using thermal profiles TP2, since they exhibit the highest structural quality. Figures 3.16(a) and 3.16(b) show the temperature dependence of the dielectric permittivity upon cooling at several frequencies (from 1 kHz to 1 MHz) measured in the *ab*-plane (along the [110] direction) and along the *c*-axis (the [001] direction), respectively (see section 2.4.3 and Fig. 2.8 for a better understanding of the crystal configurations for electrical measurements). In both cases, the maximum of dielectric permittivity corresponding to the ferroelectric-paraelectric phase transition is clearly observed at $T_C \approx 355$ ºC (Curie temperature), in a good agreement with previous reports using other techniques on SBT crystals.[13,14,26] It is worth noting that the T_C's reported for SBT ceramics (~ 300 ºC,[27,28] see also results in section 4.4.1) are somewhat lower than that obtained for single crystals. Besides, neither a frequency dispersion of the transition temperature nor thermal hysteresis upon heating and cooling were observed in the permittivity curves along both directions.

The anisotropy in the temperature dependence of the dielectric permittivity along the [110] and the [001] directions can clearly be observed by plotting together both curves at the frequency of 10 kHz, as shown in Fig. 3.17. The maximum permittivity for SBT in the *ab*-plane (~ 1500) was about an order of magnitude greater than that along *c*-axis (~ 135) in line with results reported in other BLSF single crystals.[29,30] Besides, the values of the permittivity in the *ab*-plane exceed significantly those of bulk ceramics (~ 600 at T_C).[27,28]

It should be noted that the present measurements in the *ab*-plane were performed along the [110] direction. As such, this corresponds to a dielectric permittivity averaged for both *a*- (ferroelectric polarization direction) and *b*-axes (non-polar direction), *e.g.*,

$$\varepsilon_{[110]} = \frac{(\varepsilon_a + \varepsilon_b)}{2} \tag{3.3}$$

The in-plane anisotropy (ε_a and ε_b) could not be measured due to the ferroelastic twinning observed in the entire ferroelectric phase, as discussed in section 3.2.3.

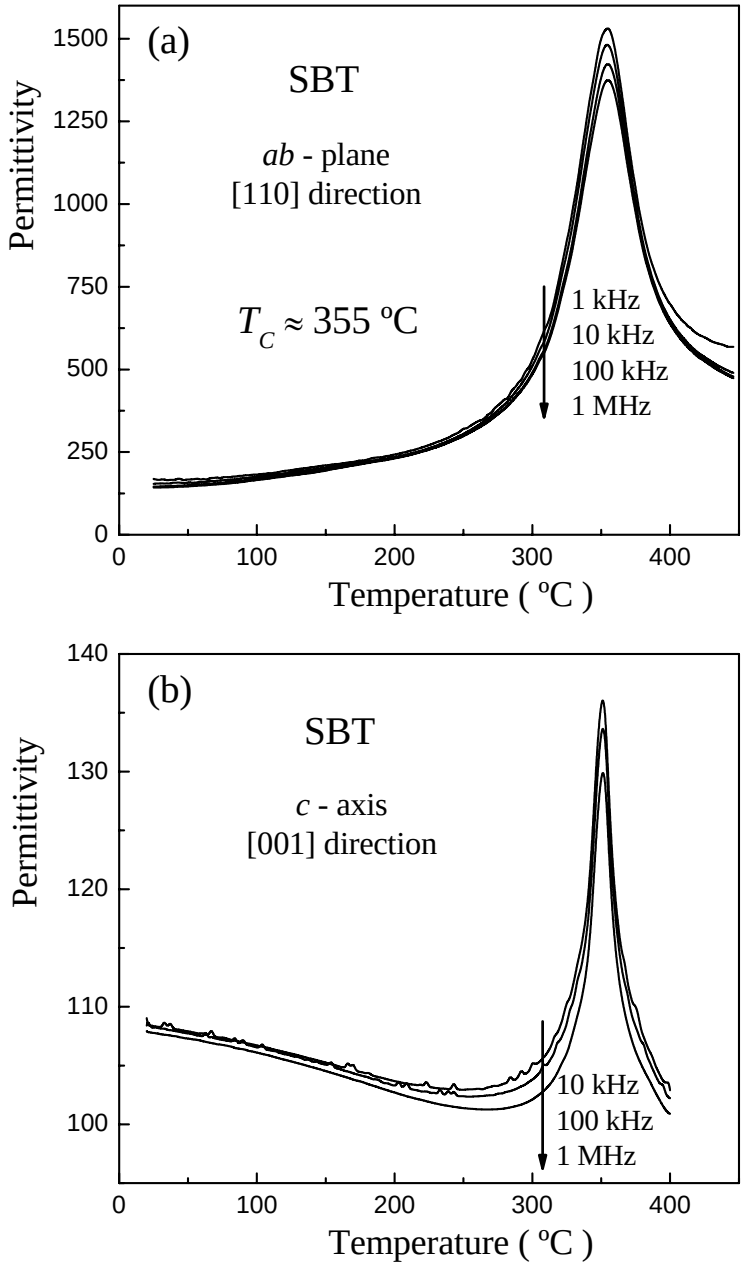

Figure 3.16 Temperature dependence of the dielectric permittivity upon cooling at several frequencies (from 1 kHz to 1 MHz in the sequence indicating by the arrows) along the (a) [110] (*ab*-plane) and the (b) [001] (*c*-axis) directions in the $SrBi_2Ta_2O_9$ single crystal.

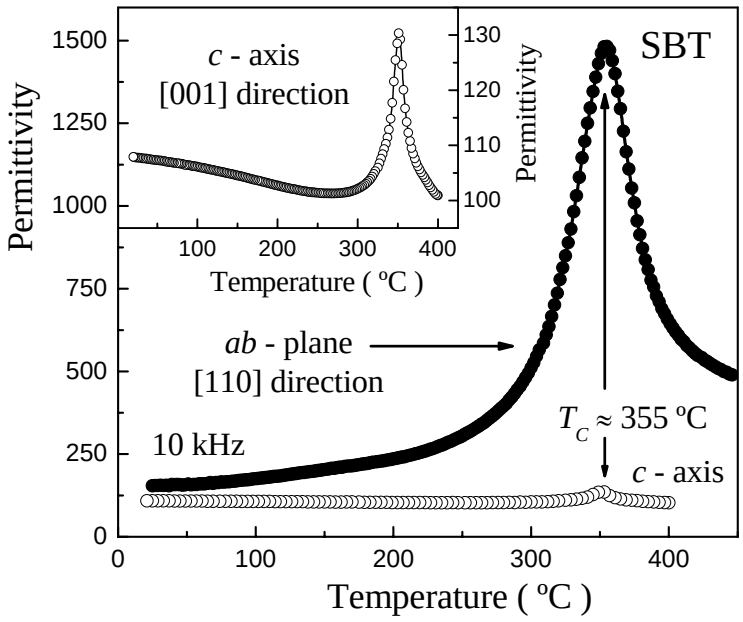

Figure 3.17 Temperature dependence of the dielectric permittivity upon cooling at 10 kHz along the [110] (*ab*-plane) and the [001] (*c*-axis) directions in the $SrBi_2Ta_2O_9$ single crystal.

Figure 3.18 compares the temperature behavior of the dielectric losses ($\tan\delta$) upon cooling at 1 MHz in the *ab*-plane and along *c*-axis in SBT single crystal. The temperature of $\tan\delta$ peak is also observed at $T_C \approx 350$ ºC, close to the value corresponding to the permittivity peak. The losses at low temperatures are essentially higher in the *ab*-plane, indicating that there exists large contribution from the domain wall motion in SBT materials. The loss factor could be measured both below and above T_C thus suggesting that the *dc* conductivity that typically disturbs the high-temperature dielectric measurements in BLSF is negligible in the present crystals. The low values of $\tan\delta$ (< 0.04 both above and below T_C) confirm low defect concentration and high quality of the SBT single crystals.

From the crystallographic point of view for SBT there should be no coupling between the order parameter lying in the *ab*-plane and the out-of-plane (along *c*-axis) dielectric displacement. The dielectric behavior along *c*-axis should be mainly determined by the paraelectric bismuth oxide layers and the small peak observed around T_C is of the extrinsic character due to, probably, a slight inclination from the [001] direction during the crystal preparation for electrical characterization.

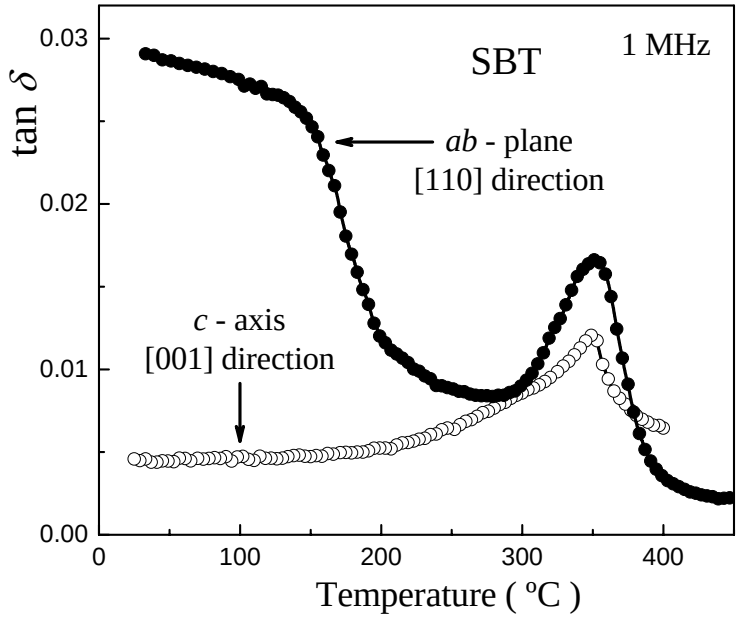

Figure 3.18 Temperature dependence of the dielectric losses (tanδ) upon cooling at 1 MHz along the [110] (*ab*-plane) and the [001] (*c*-axis) directions in the $SrBi_2Ta_2O_9$ single crystal.

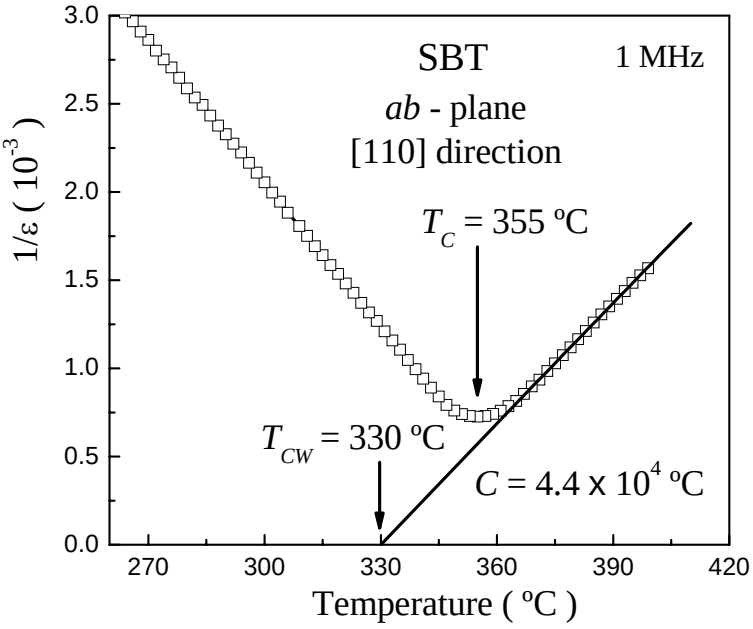

Figure 3.19 Linear relationship between inverse permittivity and temperature near T_C in $SrBi_2Ta_2O_9$ single crystal along the [110] direction at 1 MHz. C is the Curie constant, T_C is the Curie temperature and T_{CW} is the Curie-Weiss temperature.

Figure 3.19 shows a linear relationship between inverse permittivity and temperature, both above and below T_C, for the curve measured in the *ab*-plane at 1 MHz in the SBT single crystal. This linear relationship in the proximity of T_C is well-known as the Curie-

Weiss law previously described in section 1.2.3 (Eq. 1.7), which should be satisfied in most (non-relaxor) ferroelectrics. The Curie constant was determined from the slope of the straight line above T_C ($C = 4.4 \times 10^4$ ºC) and T_{CW} was 330 ºC approximately. It is worth noting that the C value is slightly lower than that typically reported for displacive-type ferroelectric materials, including several BLSFs.[27] The slope of $1/\varepsilon(T)$ dependence below T_C is approximately two times greater than that above T_C, which is characteristic of the 2nd-order phase transition. However, we cannot exclude a possibility of the 1st-order transition in this material due to the significant difference between T_{CW} and T_C (~ 25 ºC). More data are obviously needed to determine the type of the ferroelectric phase transition in SBT.

Ferroelectric characterization

To confirm the anisotropy in the ferroelectric properties of the SBT single crystal, the room temperature P-E hysteresis loop was measured both along *c*-axis ([001] direction) and in the *ab*-plane (parallel to [110] direction), in the same way that the permittivity measurements. Anisotropy in the P-E hysteresis loops can be clearly observed by comparing the two plots. Well-saturated hysteresis loop was observed in the *ab*-plane (solid circles in Fig. 3.20), from which the values of the spontaneous polarization (P_S) and the coercive field (E_C) were estimated as ≈ 14 μC/cm^2 and ≈ 22 kV/cm, respectively. On the other hand, only a linear P-E behavior with vanishing spontaneous polarization and coercive field was obtained for the measurements along the [001] direction (open circles in Fig. 3.20). These results confirm that the P_S vector in the SBT structure lies entirely in the *ab*-plane and no polarization is obtained perpendicular to the bismuth oxide layers. This finding is consistent with that expected for BLSF materials with even number (m) of BO_6 octahedra, where the dipole moments caused by ionic displacements along *c*-axis are cancelled out due to the presence of a mirror plane perpendicular to it (see section 1.3.2).[31]

For the SBT crystal the macroscopic spontaneous polarization, which is directed along the *a*-axis, was predicted to be ≈ 18 μC/cm^2 from ionic displacements.[28] In our crystals, the hysteresis loop was measured along the [110] direction, *i.e.*, the spontaneous polarization vector is oriented at 45º with respect to the measuring direction (see Fig. 2.8 in section 2.4.3). The existence of a combination of ferroelastic twins filled with 180º domains was also confirmed from piezoelectric force microscopy measurements.

Thus, the spontaneous polarization along polar *a*-axis could be determined as $P_S^a = P_S \cos(45^o)$, considering that all 180º domains are switched under saturation. In this way, the spontaneous polarization along the polar direction was estimated to be ≈ 20 μC/cm^2, in a good agreement with the above mentioned calculations.[28]

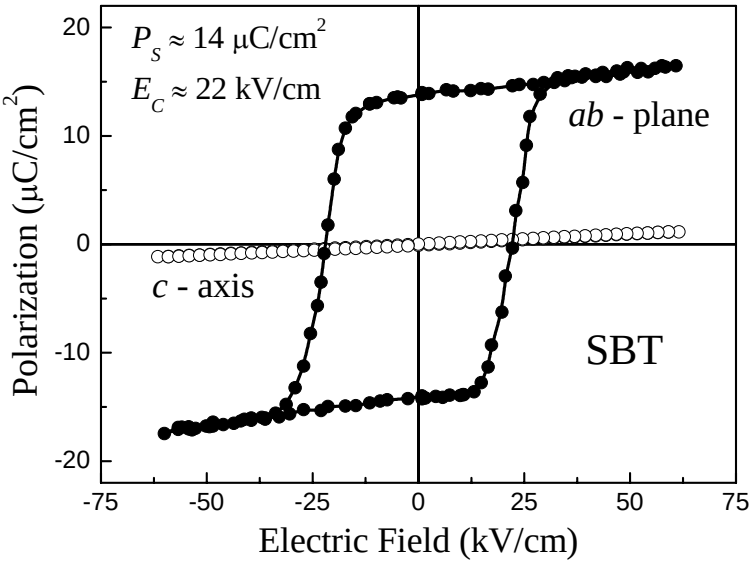

Figure 3.20 Room temperature P-E hysteresis loops measured along the [110] (*ab*-plane) and the [001] (*c*-axis) directions in the $SrBi_2Ta_2O_9$ single crystal. The values for the spontaneous polarization (P_S) and the coercive field (E_C) are indicated.

Piezoelectric characterization

Piezoelectric characterization of SBT crystals was performed along two directions in the *ab*-plane, that is, along the [110] and the [100] directions, as well as along the *c*-axis (the [001] direction), to confirm the anisotropy in the longitudinal piezoelectric coefficient (d_{33}) along different crystallographic orientations. SBT crystals were previously embedded in araldite and poled at E_P = 60 kV/cm, as described in section 2.4.7. Figures 3.21(a) and 3.21(b) show the frequency (*f*) dependences of the d_{33} coefficient and phase using an *ac* voltage of V_{ac} = 100 V ($E_{ac} \approx 3$ kV/cm) in the frequency range from 500 Hz to 5 kHz, and measured along the [110] direction of the SBT single crystal.

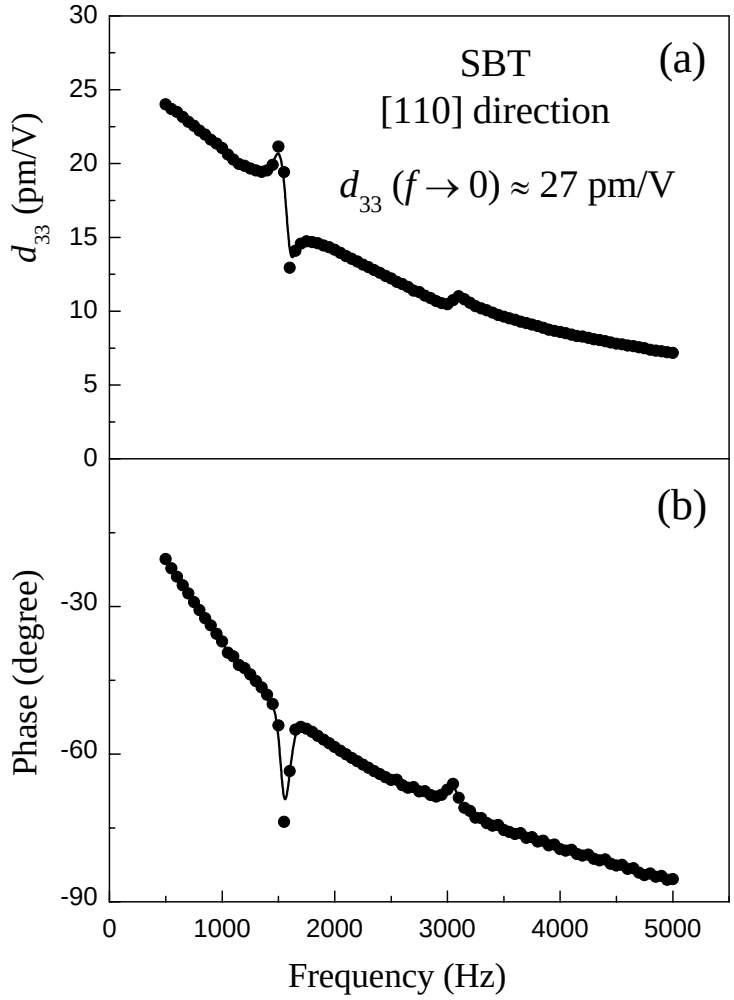

Figure 3.21 Frequency dependence of the (a) piezoelectric coefficient d_{33} and (b) phase measured along the [110] direction of the $SrBi_2Ta_2O_9$ single crystal and using an *ac* voltage of V_{ac} = 100 V (E_{ac} ≈ 3 kV/cm). The value estimated for low-frequency d_{33} is indicated.

A strong frequency dispersion of the d_{33} is observed in this frequency range with two clear mechanical resonances at 1.5 and 3 kHz (probably consecutive harmonics). The observed resonances cannot be associated with common vibration modes appearing in a piezoelectric resonator, *e.g.*, length, radial, thickness or shear modes. These should occur at much higher frequencies (> 50 kHz). Thus, it is believed that the resonances as well as the strong frequency dispersion observed in our experiments can be of extrinsic character due to, probably, clamping of the small SBT crystal by the soft araldite used for the piezoelectric measurements (see section 2.4.7 and Fig. 2.12(b) for better understanding). The SBT crystal together with araldite constitutes a piezoelectric composite which total impedance depends on the individual parameters of both materials. This may result in a

different equivalent circuit where mechanical resonance may occur at lower frequencies (probably, flexural vibrations). In fact, this idea was corroborated by the various resonance frequency shifts induced by the different positioning of the SBT crystal - araldite assembly on the sample holder.

Based on the above arguments, the value of d_{33} coefficient when the measuring frequency extrapolates to zero ($f \rightarrow 0$) was estimated to be $d_{33} \approx 27$ pm/V for SBT crystals along the [110] direction, being the d_{33} coefficient in a *dc* mode. Figure 3.22 shows the linear relationships between the strain and the amplitude of the applied *ac* voltage at several frequencies, which is expected in piezoelectric crystals when the applied electric field is lower than the crystal coercive field. The value of d_{33} coefficient for each frequency is calculated from the slope of the straight line and included in the figure.

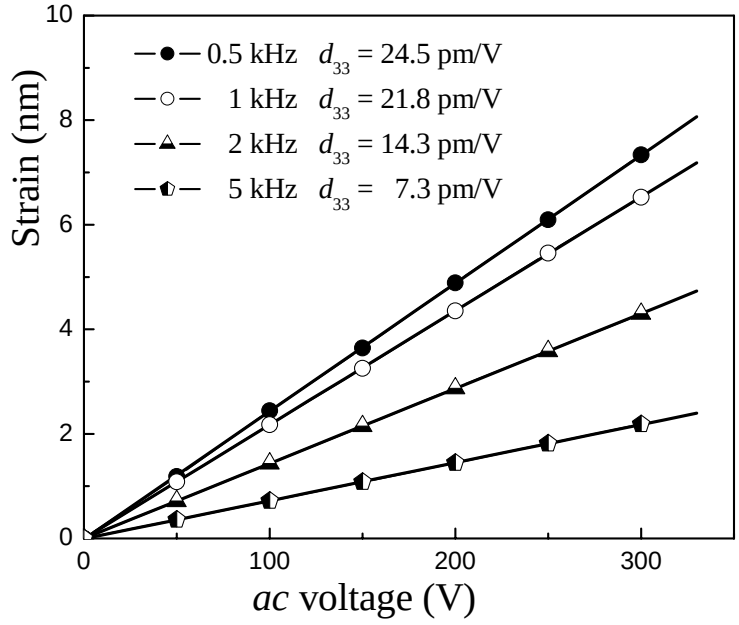

Figure 3.22 Linear relationships between the strain and the amplitude of the *ac* voltage at different frequencies (0.5, 1, 2 and 5 kHz), measured along the [110] direction in $SrBi_2Ta_2O_9$ crystals. The calculated d_{33} coefficients for different frequencies are indicated.

Figure 3.23 shows the behavior of the d_{33} coefficient after different applied *dc* poling field (piezoelectric hysteresis loop), which is obtained by poling the SBT crystal along the [110] direction and then measuring the d_{33} coefficient using a low *ac* voltage V_{ac} = 100 V at 1 kHz, as described in section 2.4.7. The hysteretic behavior of the calculated d_{33} coefficient with the *dc* poling field is confirmed, and the electric field value at which d_{33}

vanishes should be close to the conventional coercive field, because approximately at this point half of the ferroelectric domains that were previously oriented along the poling field direction have switched back from their original states (180º domains) due to the poling in the opposite direction. Therefore, the net polarization of the crystal tends to zero and the crystal is piezoelectrically inactive, *i.e.*, the effects from the individual domains cancel each other and no piezoelectricity is observed. The coercive field was then estimated from this experiment as $E_C \approx 20$ kV/cm, in a good agreement with the result of the P-E hysteresis measurements along the [110] direction (see Fig. 3.20).

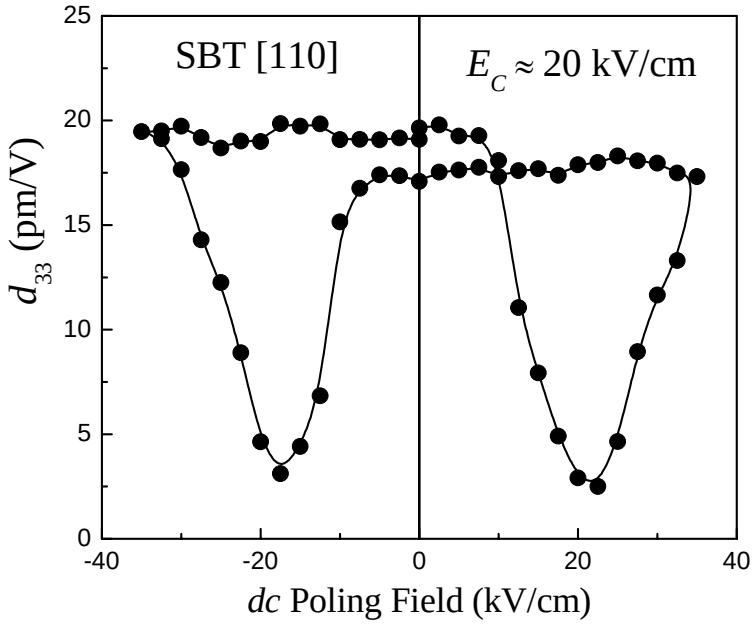

Figure 3.23 Dependence of the piezoelectric coefficient d_{33} measured at 1 kHz with the *dc* poling field along the [110] direction in $SrBi_2Ta_2O_9$ crystals. The estimated crystal coercive field (E_C) is also indicated.

As referred above, a similar strong frequency dispersion of the d_{33} coefficient, including mechanical resonances, was observed in SBT crystals measured along the [100] direction in the same frequency range from 500 Hz to 5 kHz, which were also dependent on the positioning of the assembly SBT crystal - araldite on the sample holder. Figure 3.24 shows the relationships between the d_{33} coefficient and the *dc* poling field measured along the [100] (loop with solid circles) and the [001] (loop with open circles) directions, using an *ac* voltage V_{ac} = 100 V at 1 kHz. In both cases, the hysteretic behavior of the d_{33} coefficient with the *dc* poling field is also observed, and the value of poling field at which d_{33} vanishes along the [100] direction was also estimated as $E_C \approx 20$ kV/cm.

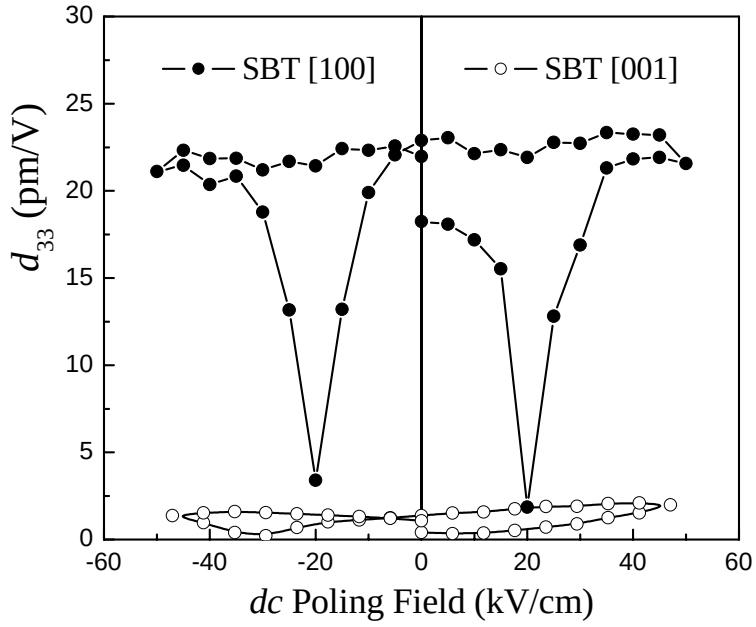

Figure 3.24 Dependence of the piezoelectric coefficient d_{33} measured at 1 kHz with the *dc* poling field along the (●) [100] and the (○) [001] directions in $SrBi_2Ta_2O_9$ crystals.

The value for d_{33} when the measuring frequency extrapolates to zero ($f \rightarrow 0$) was estimated to be $d_{33} \approx 30$ pm/V along the [100] direction, which is very close to the value previously obtained along the [110] direction. At first view, this result suggests a negligible anisotropy of the d_{33} coefficient when the [100] and the [110] directions are being compared, contrary to that expected in BLSF single crystals, where the spontaneous polarization vector is oriented along the [100] direction (*a*-axis), and thus, at 45º with respect to the [110] direction. Harnagea *et al.*[32] have proposed a plausible d_{zz} surface for BLSF materials, where the maximum d_{zz} is obtained along the [100] direction (*a*-axis) and the minimum along the [010] direction (*b*-axis). As a result, the d_{33} coefficient along the [110] direction is expected to be somewhat smaller than that along the [100] direction (ferroelectric polarization direction).

It should be noted, that the ferroelastic twinning observed in the ferroelectric phase is not considered to be a problem in our measurements along the [100] direction, since for high poling fields (*e.g.*, $E_P \sim 2E_C$) it is believed that both kinds of domains (corresponding to 180º and 90º domain walls) are fully switched in the direction of the poling field, and the maximum expected spontaneous polarization is reached.

A possible explanation of this result may be found on the experimental set up used for the piezoelectric measurements (see section 2.4.7). The SBT crystals were rigidly embedded in an araldite, and thus, they were not free to expand or contract in the direction perpendicular to the applied *ac* voltage, specifically, in the [010] direction (non-polar direction) for the crystals measured along the [100] direction. As a result, the measured d_{33} coefficient is smaller than the real value for the crystal free of any stress, due to the effect of the lateral stress induced in the crystal by the rigid araldite. In other words, the clamping of the piezoelectric coefficient d_{31}, *i.e.*, the induced strain in the [010] direction per unit electric field applied in the [100] direction, modifies the true d_{33} coefficient of the unclamped crystal (see Ref. 33 for a better understanding). A correction factor should be introduced to obtain the true d_{33} coefficient of SBT crystals (*i.e.*, this correction factor has been reported to be about a 10% of the measured clamped d_{33} in piezoelectric $LiNbO_3$ and $LiTaO_3$ crystals).[33] Unfortunately, this factor is unknown for SBT crystals.

On the other hand, a significant anisotropy in the d_{33} coefficient is clearly observed between the [100] and the [001] directions of the SBT crystal. In the second case, very small values of d_{33} coefficient were obtained for all the poling fields (see open circles in Fig. 3.24), thus confirming that the P_S vector in the SBT structure lies in the *ab*-plane and neither polarization, nor piezoelectric activity, are obtained along the *c*-axis (perpendicular to the bismuth oxide layers), as previously discussed in the P-E hysteresis measurements.

As mentioned in the dielectric behavior of the SBT crystals, the small values of d_{33} coefficient obtained along the [001] direction (*c*-axis) should be of the extrinsic character due to, probably, slight inclination of the crystal from the [001] direction during the crystal preparation for piezoelectric characterization.

3.3. $SrBi_2Nb_2O_9$ Single Crystals

3.3.1. Single crystal growth with the optimized processing condition

It was confirmed in this chapter that large and high-quality SBT single crystals can be grown by the self-flux solution method adding a low amount of B_2O_3 to the Bi_2O_3 flux and using a *gradually accelerated slow cooling process* (thermal profile TP2), where the combination of temperature and time creates proper conditions for crystal nucleation and

growth. Therefore, equivalent experimental conditions were used for growing $SrBi_2Nb_2O_9$ (SBN) single crystals, including a 60/40 molar ratio of SBN to flux (35 wt% Bi_2O_3 and 5 wt% B_2O_3) and the thermal profile TP2.

Figure 3.25(a) shows the top view of the solidified mass inside the Pt crucible composed of the SBN crystals and flux obtained after the growth experiment using thermal profile TP2. The crystals exhibit a uniform multilayered array inside the Pt crucible, different from that of SBT crystals, but with a similar outside yellowish coloration associated with the Bi_2O_3 flux.

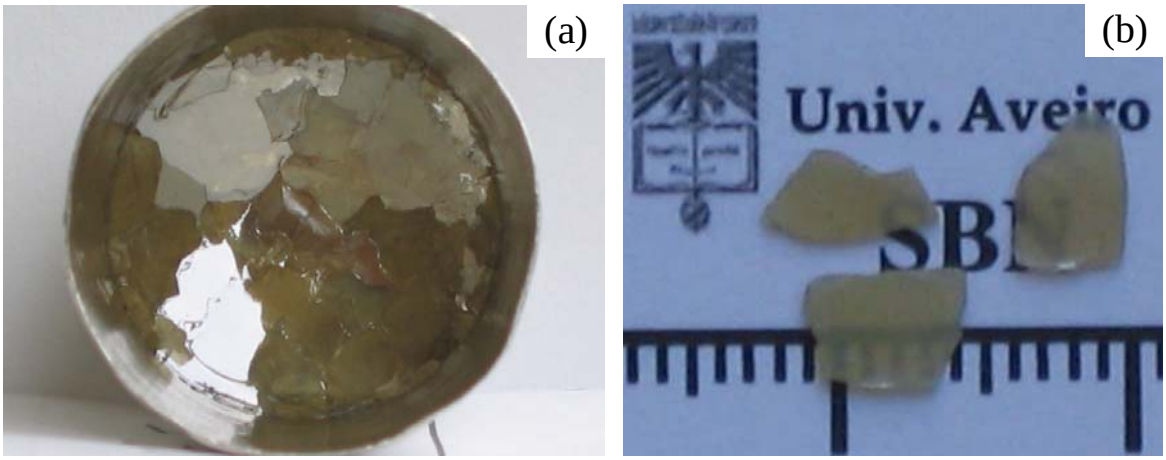

Figure 3.25 (a) Solidified mass of $SrBi_2Nb_2O_9$ crystals and flux inside the Pt crucible (2 cm base diameter) after the growth experiment using thermal profile TP2, and (b) Top view of the as-grown and cleaned SBN crystals showing platelet morphology (1 division = 1 mm).

Figure 3.25(b) shows the micrographs of the typical as-grown acid-cleaned SBN crystal platelets. As observed, large yellowish SBN single crystals with rectangle shape, smooth surfaces and dimensions of ~ 5 × 5 × 0.4 mm^3 were grown for the first time in this work, by using the boron-modified flux and thermal profile TP2. The lateral dimensions of produced crystals are similar to those observed for SBT (see Table 3.1 for comparison), but the thickness of the grown platelets (~ 400 μm in most cases) is twice the value obtained for SBT crystals obtained using the same thermal profile. In addition, SBN crystals are translucent and yellowish, a different coloration from that observed in SBT crystals.

As observed in the case of SBT, the SBN crystals with highest quality, that is, of the perfectly rectangular shape and free of cracks, were somewhat smaller, ~ 2 × 2 × 0.1 mm^3. These were the ones selected for crystallographic and ferroelectric characterization.

Crystal growth and morphology

Both SBN and SBT single crystals were grown under similar conditions and exhibit identical crystal structure with the same space group. They are distinguished by the change of Ta by Nb in the BO_6 octahedra (see Fig. 1.9 in section 1.3.2). As in SBT, the crystal morphology of SBN crystals is also dominated by large [001] facets, which are also supposed to correspond to the lowest energy surfaces. This indicates a faster growth of the crystals parallel to *ab*-plane, compared to that along the [001] direction. However, SBN crystals achieve a greater thickness as compared to that of SBT crystals, suggesting a growth rate along the [001] direction greater than that exhibited by SBT crystals.

For understanding such growth rate differences, detailed information about the local growth mechanism of each face is required. In fact, in spite of the similarities between SBT and SBN systems, several parameters affecting the mass transport through the melt (*e.g.*, viscosity, solute diffusion coefficients, etc.) and the processes occurring at the crystal solution interface (*e.g.*, adsorption coefficients of solute on the crystal surface, surface diffusion coefficients of solute, and solute integration energy in the crystal structure) are expected to be different, thereby accounting for a different growth behavior. Moreover, solubility and consequently supersaturation are probably different in both systems. Further studies are indeed necessary for clarifying this issue.

3.3.2. X-ray diffraction and x-ray topography analysis

The crystalline structure and crystallographic orientation of the grown SBN single crystals were studied by XRD and x-ray topography techniques at room temperature. Figure 3.26(b) shows the XRD pattern of a rectangular SBN crystal platelet where only (00*l*) plane reflections are observed in reflection geometry perpendicular to the crystal major face (see section 2.4.1 and Fig. 2.5 for better understanding). In this way, highly oriented SBN single crystal platelets (with *c*-axis perpendicular to the major face) were successfully produced.

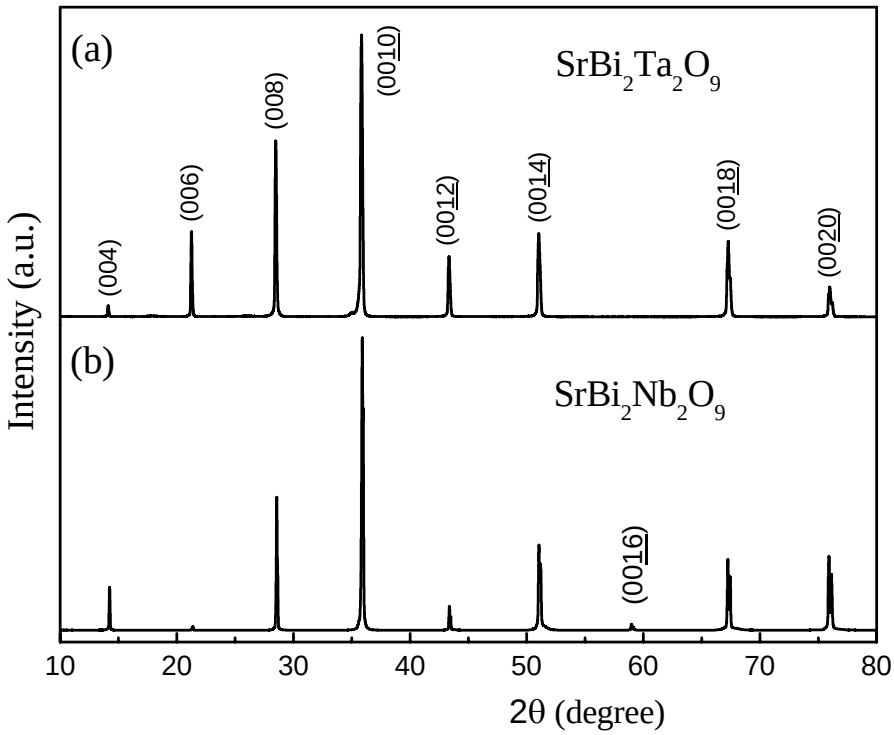

Figure 3.26 X-ray diffraction spectra of perfect *c*-axis oriented (a) $SrBi_2Ta_2O_9$ and (b) $SrBi_2Nb_2O_9$ single crystal platelets in reflection geometry perpendicular to the crystal major face and obtained using thermal profile TP2. The Miller indexes for the (00*l*) plane reflections are included.

For comparison, the XRD spectrum obtained for the SBT crystal is also included in Fig. 3.26(a). Although, similar reflections are observed in both cases, associated with the same space group $A2_1am$, the relative intensity of some reflections differs from one pattern to another, *i.e.*, the (00$\underline{1}$6) plane reflection is not noticeable in the spectrum for SBT and appears in the spectrum for SBN, also the relative intensity of the (006) plane reflection is quite different for SBT and SBN, almost vanished in the second case. Therefore, in spite of the huge similarity of the XRD patterns of these structurally identical systems, each pattern represents a fingerprint for distinguishing SBT from SBN single crystals. Pseudo-tetragonal lattice parameters were also estimated for the SBN crystals using the orthorhombic space group $A2_1am$, and the result obtained [$a \approx 5.513(1)$ Å, $b \approx 5.512(1)$ Å and $c \approx 25.043(4)$ Å] is in a good agreement with the reported data.[34]

X-ray topography measurements were also performed on small SBN single crystals, where the narrow sides of the rectangular shaped crystals were also observed to be oriented along the orthorhombic [110] direction [45º to both *a*- and *b*-axes] with the [001] direction (*c*-axis) lying perpendicular to the crystal major face, similarly to that obtained in SBT single crystals (see section 3.2.2). A uniform contrast was observed over all the surface of the SBN crystals with misorientation smaller than 0.5º.

3.3.3. Dielectric, ferroelectric and piezoelectric properties

Dielectric characterization

Figures 3.27(a) and 3.27(b) show the temperature dependence of the dielectric permittivity upon cooling at several frequencies (from 1 kHz to 1 MHz) measured in the *ab*-plane (along the [110] direction) and along the *c*-axis (the [001] direction), respectively, in the SBN single crystals. The maximum of dielectric permittivity corresponding to the ferroelectric-paraelectric phase transition is clearly observed at $T_C \approx 440$ ºC in both cases. However, contrary to that observed in SBT crystals, the T_C obtained in SBN crystals is in a good agreement with previous reports in ceramics.[27,35] Furthermore, neither a frequency dispersion of the transition temperature nor thermal hysteresis upon heating and cooling were observed in the permittivity curves along both directions.

The anisotropy in the temperature dependence of the dielectric permittivity along the [110] and the [001] directions can be better seen by plotting together both curves at the frequency of 10 kHz, as shown in Fig. 3.28. Similarly to SBT crystals, the maximum permittivity of SBN in the *ab*-plane (~ 2700) is about an order of magnitude greater than that along *c*-axis (~ 220). However, the maximum permittivity obtained for SBN crystals in the *ab*-plane is about twice the value obtained for SBT crystals (see Fig. 3.17 for SBT). On the other hand, the maximum permittivity in the *ab*-plane of the SBN crystals exceeds significantly those of bulk SBN ceramics (~ 1100 at T_C).[27,35]

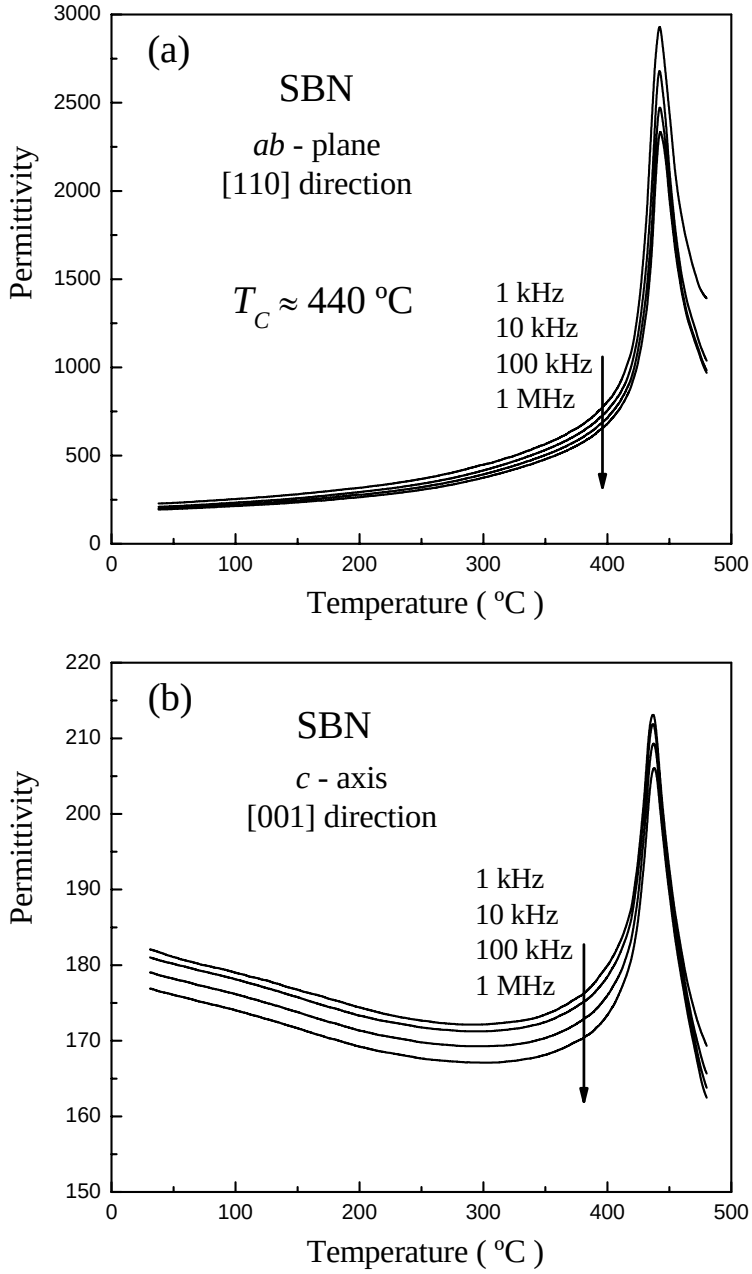

Figure 3.27 Temperature dependence of the dielectric permittivity upon cooling at several frequencies (from 1 kHz to 1 MHz in the sequence indicating by the arrows) along the (a) [110] (*ab*-plane) and the (b) [001] (*c*-axis) directions in the $SrBi_2Nb_2O_9$ single crystal.

As mentioned above, the measurements in the *ab*-plane of the SBN crystals were performed along the [110] direction, that is, at 45º with respect to the polarization direction (*a*-axis). As such, a dielectric permittivity averaged for both *a*- (polarization direction) and *b*-axes (non-polar direction) was measured, as described by the Eq. 3.3. Additionally, the small peak observed around T_C in the temperature dependence of permittivity along *c*-axis

should be of the extrinsic character due to, probably, slight inclination from the [001] direction during the crystal preparation for electrical characterization.

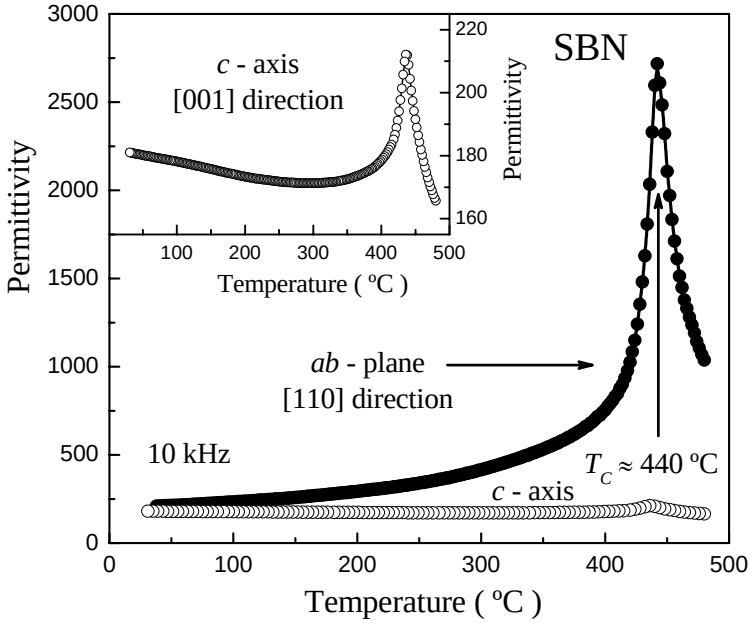

Figure 3.28 Temperature dependence of the dielectric permittivity upon cooling at 10 kHz along the [110] (*ab*-plane) and the [001] (*c*-axis) directions in the $SrBi_2Nb_2O_9$ single crystal.

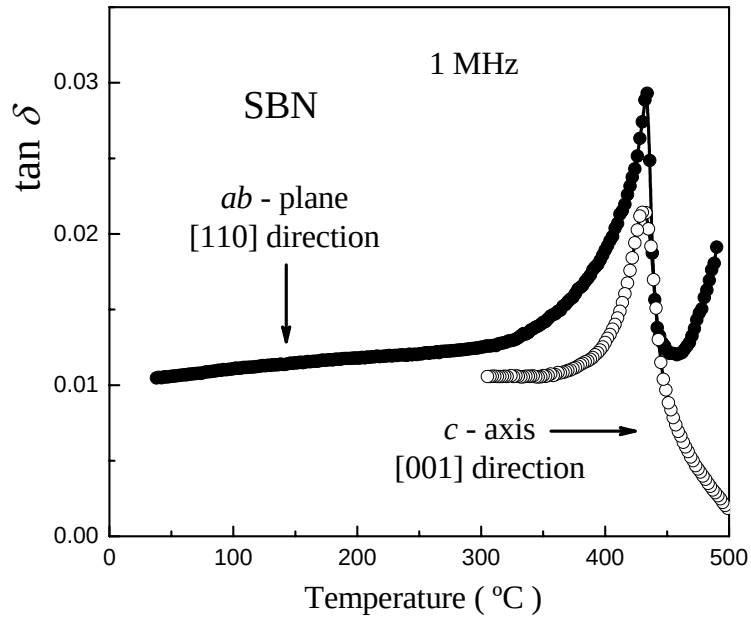

Figure 3.29 Temperature dependence of the dielectric losses (tanδ) upon cooling at 1 MHz along the [110] (*ab*-plane) and the [001] (*c*-axis) directions in the $SrBi_2Nb_2O_9$ single crystal.

Figure 3.29 compares the temperature behavior of the dielectric losses (tanδ) upon cooling at 1 MHz in the *ab*-plane and along *c*-axis in SBN single crystals, where a similar behavior is observed in both cases. The temperature of tanδ peak is obtained at $T_C \approx 435$ ºC, close to the value observed at the permittivity peak but ~ 5 ºC lower. The loss factor was measured both below and above T_C, not revealing significant disturbance due to *dc* conductivity as already observed on the SBT crystals. The low values of tanδ (< 0.04 both above and below T_C) also confirm a low defect concentration and the high quality of the SBN crystals.

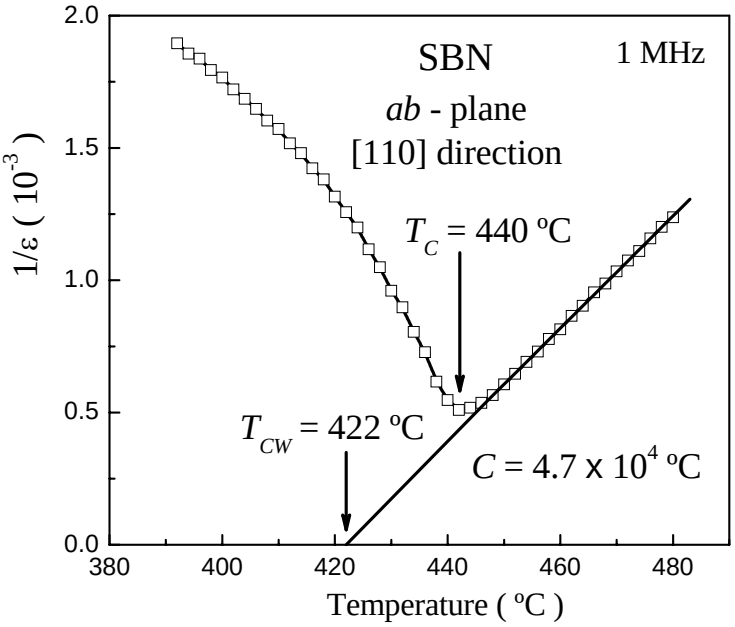

Figure 3.30 Linear relationship between inverse permittivity and temperature near T_C in $SrBi_2Nb_2O_9$ single crystal along the [110] direction at 1 MHz. C is the Curie constant, T_C is the Curie temperature and T_{CW} is the Curie-Weiss temperature.

Figure 3.30 shows a linear relationship between inverse permittivity and temperature, both above and below T_C, for the curve measured in the *ab*-plane at 1 MHz in the SBN single crystal. The Curie constant was determined from the slope of the straight line above T_C ($C = 4.7 \times 10^4$ ºC) and T_{CW} was 422 ºC, approximately. The Curie constant in SBN crystals is of the same order of magnitude as that previously obtained for SBT single crystals. The slope of 1/ε(T) dependence below T_C is approximately two times greater than that above T_C, which is characteristic of the 2nd-order phase transition. However, as discussed in the case of SBT crystals, the case of SBT, the possibility of the 1st-order phase

transition in this material cannot be excluded due to the significant difference between T_{CW} and T_C (~ 18 ºC). More data are also required to clarify the type of the ferroelectric phase transition in SBN.

Ferroelectric characterization

The P-E hysteresis loops in SBN crystals were measured both along *c*-axis ([001] direction) and in the *ab*-plane (parallel to [110] direction), similarly to SBT single crystals. Figure 3.31 shows the room temperature P-E hysteresis loop (curve with open circles) measured along the [110] direction, where a slim loop with no saturation of the polarization was obtained for a maximum applied electric field of ~ 100 kV/cm. The small values for the remanent polarization ($P_r \approx 1.2$ μC/cm^2) and coercive field ($E_C \approx 17$ kV/cm) thus obtained suggest that the measured hysteresis loop is really far from what it is expected in SBN single crystals,[35] *i.e.*, the coercive field reported for SBN is much greater than that for SBT in ferroelectric thin films,[36-38] which was reported to be $E_C \approx 22$ kV/cm for SBT single crystals in section 3.2.4. Thus, higher electric fields seem to be needed for domains switching and saturation of the polarization. However, electric fields higher than 100 kV/cm resulted in the electrical breakdown of the crystals. Therefore, the saturated hysteresis loops could not be achieved in SBN crystals.

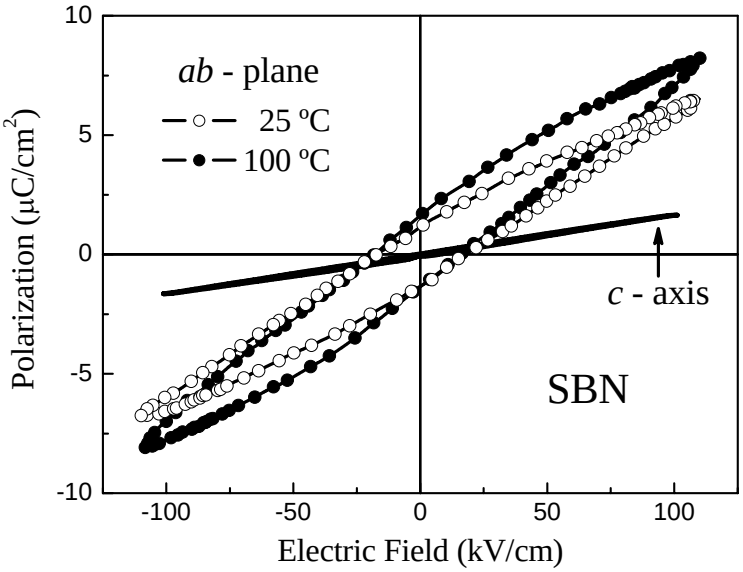

Figure 3.31 P-E hysteresis loops measured along the [110] direction (*ab*-plane) at (○) 25 ºC and (●) 100 ºC, as well as along the [001] direction (*c*-axis), in $SrBi_2Nb_2O_9$ single crystals.

To decrease the energy associated with domains wall switching and to attempt to obtain saturated hysteresis in SBN crystals, the measuring temperature was raised to 100 ºC and the hysteresis loop was measured again (see the loop with solid circles in Fig. 3.31). However, even in this case, no saturated hysteresis loops were obtained for the same maximum applied electric field of ~ 100 kV/cm, and the hysteresis show again a slim shape with low values of P_r and E_C.

Nevertheless, the anisotropy in the P-E hysteresis of SBN single crystals is clearly corroborated by comparing the hysteresis loops along the [001] direction (straight solid line in Fig. 3.31) with that parallel to the [110] direction. As observed, only a linear P-E behavior with vanishing spontaneous polarization and coercive field was obtained for measurements along the [001] direction (*c*-axis), similarly to that of SBT single crystals. Therefore, in spite of the non-saturated hysteresis loop along the [110] direction, this result confirms that P_S vector in the SBN structure also lies entirely in the *ab*-plane and no polarization is obtained perpendicular to the bismuth oxide layers.

Piezoelectric characterization

The piezoelectric characterization of SBN crystals was performed along the [100], [110] and [001] directions, after preparing the crystals in a similar way as in the SBT case, that is, embedded in araldite and poled at E_P = 60 kV/cm, as described in section 2.4.7. Figures 3.32(a) and 3.32(b) show the frequency (*f*) dependence of the longitudinal d_{33} coefficient and phase using an *ac* voltage of V_{ac} = 100 V ($E_{ac} \approx$ 3 kV/cm) in the frequency range from 500 Hz to 5 kHz, and measured along the [100] direction of the SBN single crystal. Similarly to that observed in SBT crystals, a strong frequency dispersion of d_{33} was also found in SBN crystals in this frequency range with clear mechanical resonances that can not be associated with common vibration modes appearing in a piezoelectric resonator, but rather being of the extrinsic character due to, probably, clamping of the small SBT crystal with soft araldite used for the piezoelectric measurements, as explained for SBT crystals in section 3.2.4. In this case, the resonance frequencies also depend on the way the assembly SBN crystal - araldite was positioned in the sample holder.

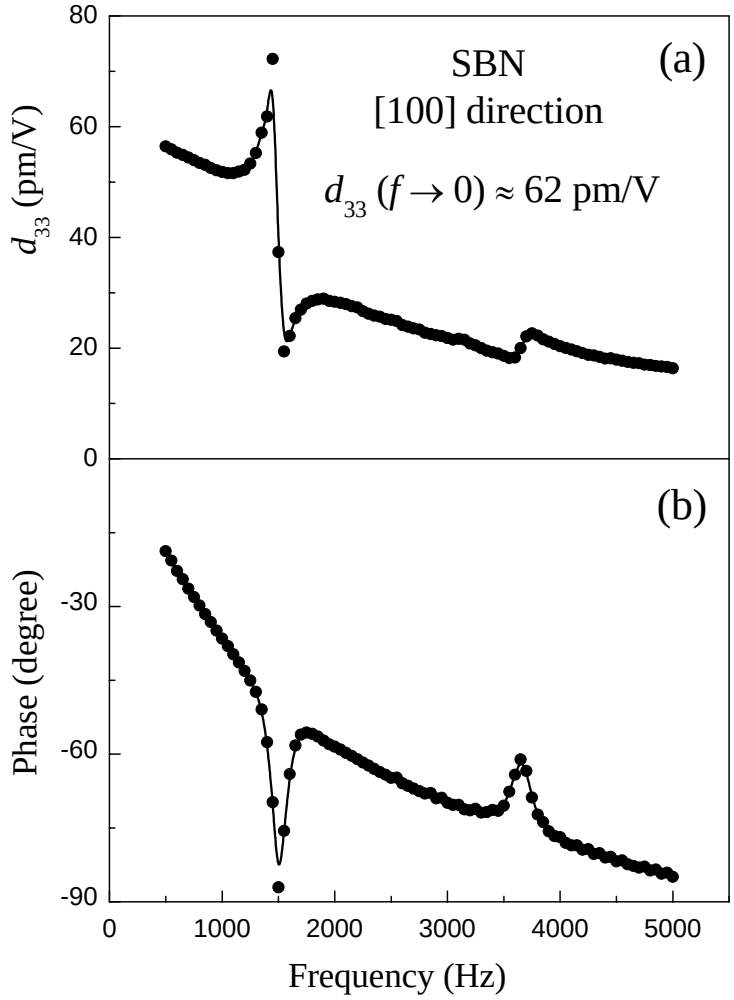

Figure 3.32 Frequency dependence of (a) the piezoelectric coefficient d_{33} and (b) the phase measured along the [100] direction in $SrBi_2Nb_2O_9$ single crystal using an *ac* voltage of V_{ac} = 100 V (E_{ac} ≈ 3 kV/cm). The value estimated for low-frequency d_{33} is indicated.

Taking into account the above arguments, the value of d_{33} coefficient when the measuring frequency extrapolates to zero ($f \rightarrow 0$) was estimated to be d_{33} ≈ 62 pm/V for SBN crystals along the [100] direction, that is twice the value obtained for SBT crystals along the same direction (see section 3.2.4). Figure 3.33 shows the linear relationships between the strain and the amplitude of the applied *ac* voltage at several frequencies along the [100] direction, which is expected in piezoelectric crystals when the applied electric field is lower than the crystal coercive field. The value of d_{33} coefficient for each frequency is calculated from the slope of the straight line and included in the figure.

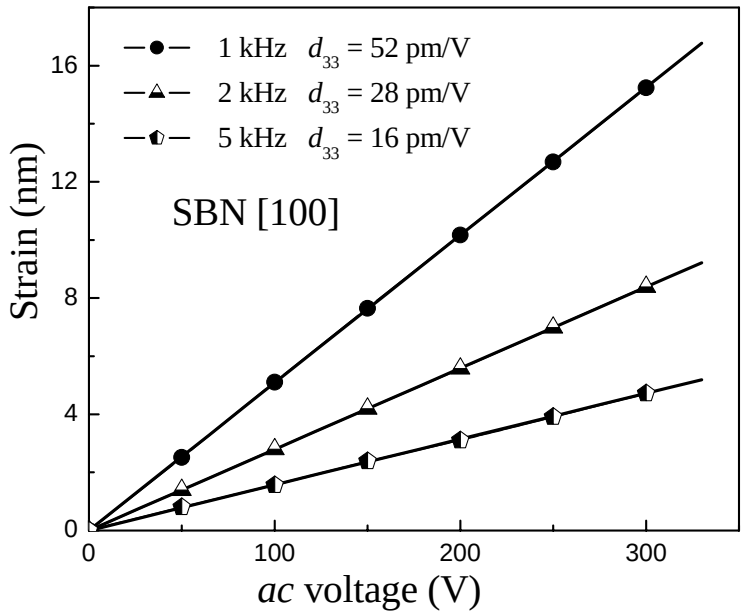

Figure 3.33 Linear relationships between the strain and the amplitude of the *ac* voltage at different frequencies (1, 2 and 5 kHz), measured along the [100] direction in $SrBi_2Nb_2O_9$ crystals. The calculated d_{33} coefficients at different frequencies are indicated.

Similar strong frequency dispersion of the d_{33} coefficient, including some minor mechanical resonances, was observed along the [110] direction in the same frequency range from 500 Hz to 5 kHz, depending on the assembly SBN crystal - araldite positioning in the sample holder, too. Figure 3.34 shows the behavior of the calculated d_{33} coefficient with the *dc* poling filed (piezoelectric hysteresis loop), obtained along the [100] (loop with open circles) and the [110] (loop with solid circles) directions (see section 2.4.7 for experimental details). In both cases, the hysteretic behavior of the d_{33} coefficient with the *dc* poling field was confirmed. In the case of the crystal measured along the [100] direction (open circles) the maximum poling field that could be applied without electrical breakdown was even far from the electric field necessary to switch ferroelectric domains, thus, the measured d_{33} values were around that previously reported for the poled crystal (see Fig. 3.32) and no hysteresis was observed. On the other hand, the value of poling field at which d_{33} vanishes could be measured satisfactorily along the [110] direction and estimated to be $E_C \approx 55$ kV/cm for SBN crystals. This value can be assumed to be closed to the real coercive field of SBN crystals.

It should be mentioned that it was not possible to measure saturated loops from P-E hysteresis loops in SBN crystals, and no reliable data exist for the coercive field of SBN in

the literature. However, the coercive field obtained in our measurements for SBN crystals is at least more than twice the value obtained for SBT crystals (see section 3.2.4). This is in a qualitative agreement with the reported data of SBT and SBN thin films.[36-38]

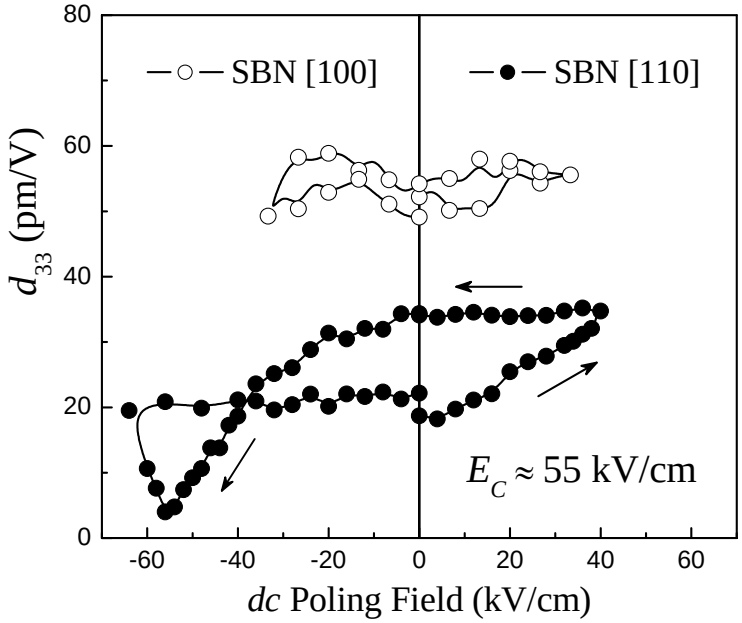

Figure 3.34 Dependence of the piezoelectric coefficient d_{33} with the *dc* poling field along the (○) [100] and the (●) [110] directions in $SrBi_2Nb_2O_9$ crystals. The estimated crystal coercive field (E_C) is also indicated.

Contrary to that observed in SBT crystals, the value for d_{33} along the [110] direction for SBN single crystals (again in a low-frequency limit, $f \rightarrow 0$) was estimated to be $d_{33} \approx 38$ pm/V, which is smaller than the value obtained along the [100] direction. This confirms the anisotropy expected between the [110] and the [100] directions (ferroelectric polarization direction) in the d_{33} coefficient of BLSF crystals, as suggested by Harnagea *et al.*[32] Nevertheless, the differences observed between SBT and SBN crystals require further studies with an improved experimental setup.

Finally, very small values of d_{33} coefficient were obtained along the [001] direction, probably, due to slight inclination of the crystal from the [001] direction during the crystal preparation. This confirms that the P_S vector in the SBN structure also lies in the *ab*-plane (along the [100] direction) and neither polarization, nor piezoelectric activity, are obtained along the [001] direction (*c*-axis), as discussed earlier for SBT.

3.4. Summary

In summary, this chapter was devoted to the growth and characterization of high-quality SBT and SBN single crystals, produced by a high-temperature self-flux solution method and using a Bi_2O_3 flux added with a small amount of B_2O_3. The largest crystals with sizes of ~ 7 × 5 × 0.2 and 5 × 5 × 0.4 mm^3 for SBT and SBN, respectively, were obtained with an optimized thermal profile that included a gradually accelerated slow cooling process. The anisotropic growth morphology of the crystals with layered habit was correlated with its crystallographic structure. XRD and x-ray topography analyses reveal highly oriented single crystal platelets with the [001] direction (*c*-axis) lying perpendicular to the major face, whereas the narrow sides of the rectangular shaped crystals were oriented along the [110] and $[1\bar{1}0]$ directions (45º to both *a*- and *b*-axes) of the orthorhombic $A2_1am$ phase.

The first reliable measurements of the domain structure of high-quality SBT single crystals were reported by piezoresponse force microscopy. A domain system of coexisting 90º and 180º domains in SBT single crystals, forming a well-defined "herringbone" structure with mostly flat 90º domain walls oriented along the [110] direction, was clearly observed. The widths of 90º domains (twins) forming laminar structures lie in the range of 0.7 - 1.5 μm, whereas 180º domain walls, oriented parallel to the [100]-direction (polar axis), exhibited a periodicity of about 250 to 500 nm. Formation of the observed complex domain pattern was attributed to a two-stage phase transition process involving separate ferroelastic and ferroelectric phase transitions in SBT.

The high-quality of the grown SBT and SBN single crystals was also confirmed by dielectric, ferroelectric and piezoelectric measurements, which were conducted in the *ab*-plane (along the [110] direction) and along the *c*-axis (the [001] direction), demonstrating the large anisotropy in the intrinsic properties of both crystals. Clear ferro-paraelectric phase transitions were observed at T_C = 355 ºC and 440 ºC for SBT and SBN, respectively. The maximum permittivity measured in the *ab*-plane was about an order of magnitude greater than that along *c*-axis in both cases. The Curie constant ≈ 4.4 × 10^4 ºC (SBT) and ≈ 4.7 × 10^4 ºC (SBN) was derived from the dielectric vs. temperature curve. The low

dielectric losses (tan $\delta < 0.04$) in the temperature range from room temperature to ~ 500 ºC confirm low defect concentration and high quality of the single crystals.

Saturated hysteresis loop was obtained along the [110] direction for SBT crystals, from which the values of the spontaneous polarization and the coercive field were estimated as ≈ 14 μC/cm^2 and ≈ 22 kV/cm, respectively, thus allowing estimation of spontaneous polarization ≈ 20 μC/cm^2 along the polar axis in this material. However, for SBN crystals, saturated hysteresis loop was not obtained even when applying a maximum electric field of 100 kV/cm, neither at room temperature, nor at 100 ºC. The loops show slim behavior with very low remanent polarization, far from that expected in this material. The longitudinal piezoelectric coefficient d_{33} measured along the [100] direction (polar-axis) was estimated to be ≈ 30 and 62 pm/V for SBT and SBN, respectively. The coercive field for SBN was estimated from the piezoelectric measurements as $E_C \approx 55$ kV/cm.

3.5. References

[1] B. Sih, J. Tang, M. Dong and Z.-G. Ye, "Ferroelectric $SrBi_2Ta_2O_9$ Single-Crystal Growth and Characterization". *J. Mater. Res.* **16** [6] (2001) 1726-1733.

[2] N. Nagasawa, A. Machida, A. Ami and M. Suzuki, "Growth of $Bi_2SrTa_2O_9$ Single Crystals using the Self-Flux Method". *J. Ceram. Soc. Jpn.* **106** [5] (1998) 477-482.

[3] A. Machida, N. Nagasawa, T. Ami and M Suzuki, "Domain Motion of ferroelectricity of $Bi_2SrTa_2O_9$ Single Crystals Under an *ac*-Voltage Electric Field". *Jpn. J. Appl. Phys.* **37** [2A] (1999) 795-799.

[4] H. Amorin, M. E. V. Costa, A. L. Kholkin and J. L. Baptista, "Electrical Properties of $SrBi_2Ta_2O_9$ Single Crystals Grown by Self-Flux Solution". *J. Eur. Ceram. Soc.* **24** [6] (2004) 1535-1539.

[5] D. Elwell and H. J. Scheel, "Crystal Growth from High Temperature Solution". Academic Press, London (1975).

[6] M. Dong and Z.-G. Ye, "High-Temperature Solution Growth and Characterization of the Pierz-/Ferroelectric (1-*x*) $Pb(Mg_{1/3}Nb_{2/3})O_3 - x\ PbTiO_3$ [PMNT] Single Crystals". *J. Cryst. Growth* **209** [1] (2000) 81-90.

[7] Y. Shiohara and A. Endo, "Crystal Growth of Bulk High-Tc Superconducting Oxide Materials". *Mater. Sci. Eng. R* **19** [1-2] (1997) 1-86.

[8] A. D. Rae, J. G. Thompson and R. L. Withers, "Structure Refinement of Commensurately Modulated Bismuth Strontium Tantalate, $Bi_2SrTa_2O_9$". *Acta Crystallogr., Sect. B: Struct. Sci.* **48** [4] (1992) 418-428.

[9] Y. Shimakawa, Y. Kubo, Y. Nakagawa, S. Goto, T. Kamiyama, H. Asano and F. Izumi, "Crystal Structure and Ferroelectric Properties of $ABi_2Ta_2O_9$ (A = Ca, Sr and Ba)". *Phys. Rev. B* **61** [10] (2000) 6559-6564.

[10] I. K. Bdikin, I. M. Shmytko, A. M. Balbashov and A. V. Kazansky, "Twinning of $LaGaO_3$ Single-Crystals". *J. Appl. Crystallogr*. **26** (1993) 71-76.

[11] I. Bdikin, A. Maljuk, S. Watauchi, I. Tanaka, and G. Emel'chenko, "X-ray Topography Investigation of $La_{2-x}Sr_xCuO_4$ Single Crystals". *Physica C* **336** [3-4] (2000) 244-248.

[12] C. H. Hervoches, J. T. S. Irvine and P. Lightfoot, "Two High-Temperature Paraelectric Phases in $Sr_{0.85}Bi_{2.1}Ta_2O_9$". *Phys. Rev. B* **64** [10] (2001) 100102.

[13] S. Kamba, J. Pokorny, V. Porokhonsky, J. Petzelt, M. P. Moret, A. Garg, Z. H. Barber and R. Zallen, "Ferroelastic Phase in $SrBi_2Ta_2O_9$ and Study of the Ferroelectric Phase-Transition Dynamics". *Appl. Phys. Lett.* **81** [6] (2002) 1056-1058.

[14] A. Onodera, K. Yoshio and H. Yamashita, "Structural Study of Intermediate Phase in Layered Perovskite $SrBi_2Ta_2O_9$ Single Crystal". *Jpn. J. Appl. Phys.* **42** [9B] (2003) 6218-6221.

[15] Y. Ding, J. S. Liu and Y. N. Wang, "Ferroelectric Switching Mechanism in $SrBi_2Ta_2O_9$". *Appl. Phys. Lett.* **79** [7] (2001) 1015-1017.

[16] X. Zhu, J. Zhu, S. Zhou, Q. Li, Z. Liu and N. Ming, "Domain Structures and Planar Defects in $SrBi_2Ta_2O_9$ Single Crystals Observed by Transmission Electron Microscopy". *Appl. Phys. Lett.* **78** [6] (2001) 799-801.

[17] D. Su, J. S. Zhu, Y. N. Wang, Q. Y. Xu and J. S. Liu, "Different Domain Structures and their Effects on Fatigue Behaviour in Bi_3TiTaO_9 and $SrBi_2Ta_2O_9$ Ceramics". *J. Appl. Phys.* **93** [8] (2003) 4784-4787.

[18] N. A. Pertsev, J. Novak and E. K. H. Salje, "Long-Range Elastic Interactions and Equilibrium Shapes of Curved Ferroelastic Domain Walls in Crystals". *Philos. Mag. A* **80** [9] (2000) 2201-2213.

[19] A.G. Khachaturyan, "Theory of Structural Transformations in Solids". John Wiley & Sons, New York (1983).

[20] J. M. Perez-Mato, M. Aroyo, A. Garcia, P. Blaha, K. Schwarz, J. Schweifer and K. Parlinski, "Competing Structural Instabilities in the Ferroelectric Aurivillius Compound $SrBi_2Ta_2O_9$". *Phys. Rev. B* **70** [21] (2004) 214111.

[21] H. Amorín, V. V. Shvartsman, A. L. Kholkin and M. E. V. Costa, "Ferroelectric and Dielectric Anisotropy in High-Quality $SrBi_2Ta_2O_9$ Single Crystals". *Appl. Phys. Lett.* **85** [23] (2004) 5667-5669.

[22] T. Mitsui and J. Furuichi, "Domain Structure of Rochelle Salt and KH_2PO_4". *Phys. Rev.* **90** [2] (1953) 193-202.

[23] N. A. Pertsev and G. Arlt, "Internal-Stresses and Elastic Energy in Ferroelectric and Ferroelastic Ceramics – Calculations by the Dislocation Method". *Ferroelectrics* **123** [1-2] (1991) 27-44.

[24] A. Yu. Emelyanov, N. A. Pertsev and E. K. H. Salje, "Effect of Finite Domain-Wall Width on the Domain Structures of Epitaxial Ferroelectric and Ferroelastic Thin Films". *J. Appl. Phys.* **89** [2] (2001) 1355-1366.

[25] A. L. Kholkin, K. G. Brooks and N. Setter, "Electromechanical Properties of $SrBi_2Ta_2O_9$ Thin Films". *Appl. Phys. Lett.* **71** [14] (1997) 2044-2046.

[26] J.-H. Ko, A. Hushur, S. Kojima, B. C. Sih and Z.-G. Ye, "Acoustic Anomalies and Central Peak in $SrBi_2Ta_2O_9$ Single Crystals Studied by Micro-Brillouin Scattering". *Appl. Phys. Lett.* **81** [21] (2002) 4043-4045.

[27] E. C. Subbarao, "A Family of Ferroelectric Bismuth Compounds". *J. Phys. Chem. Solids* **23** (1962) 665-676.

[28] Y. Shimakawa, Y. Kubo, Y. Nakagawa, T. Kamiyama, H. Asano and F. Izumi, "Crystal Structure and Ferroelectric Properties of $SrBi_2Ta_2O_9$ and $Sr_{0.8}Bi_{2.2}Ta_2O_9$". *Appl. Phys. Lett.* **74** [13] (1999) 1904-1906.

[29] H. Irie, M. Miyayama and T. Kudo, "Electrical Properties of a Bismuth Layer-Structured $BaBi_4Ti_5O_{18}$ Single Crystal". *J. Am. Ceram. Soc.* **83** [11] (2000) 2699-2704.

[30] H. Irie and M. Miyayama, "Dielectric and Ferroelectric Properties of $SrBi_4Ti_4O_{15}$ Single Crystals". *Appl. Phys. Lett.* **79** [2] (2001) 251-253.

[31] R. E. Newnham, R. W. Wolfe and J. F. Dorrian, "Structural Basis of Ferroelectricity in the Bismuth Titanate Family". *Mater. Res. Bull.* **6** [10] (1971) 1029-1040.

[32] C. Harnagea, A. Pignolet, M. Alexe and D. Hesse, "Piezoresponse Scanning Force Microscopy: What Quantitative Information can we Really Get out of Piezoresponse Measurements on Ferroelectric Thin Films". *Integr. Ferroelectr.* **44** (2002) 113-124.

[33] D. Royer and V. Kmetik, "Measurement of Piezoelectric Constants using an Optical Heterodyne Interferometer". *Electron. Lett.* **28** [19] (1992) 1828-1830.

[34] S. M. Blake, M. J. Falconer, M. McCreedy and P. Lightfoot, "Cation Disorder in Ferroelectric Aurivillius Phases of the Type $Bi_2ANb_2O_9$ (A = Ba, Sr, Ca)". *J. Mater. Chem.* **7** [8] (1997) 1609-1613.

[35] Y. Shimakawa, Y. Kubo, Y. Tauchi, T. Kamiyama, H. Asano and F. Izumi, "Structural Distortion and Ferroelectric Properties of $SrBi_2(Ta_{1-x}Nb_x)_2O_9$". *Appl. Phys. Lett.* **77** [17] (2000) 2749-2751.

[36] H. Watanabe, T. Mihara, H. Yoshimori and C. A. Paz de Araujo, "Preparation of Ferroelectric Thin-Films of Bismuth Layer Structured Compounds". *Jpn. J. Appl. Phys.* **34** [9B] (1995) 5240-5244.

[37] R. R. Das, P. Bhattacharya, W. Perez and R. S. Katiyar, "Effect of Ca on Structural and Ferroelectric Properties of $SrBi_2Ta_2O_9$ and $SrBi_2Nb_2O_9$ Thin Films". *Ceram. Int.* **30** [7] (2004) 1175-1179.

[38] G. González-Aguilar, M. E. V. Costa and I. M. M. Salvado, "Environmentally Safe Synthesis of $SrBi_2Ta_2O_9$ and $SrBi_2Nb_2O_9$ Thin Films". *J. Phys. IV France* **128** (2005) 41-44.

Chapter 4

Processing and Characterization of Textured $SrBi_2Ta_2O_9$ Ceramics

4.1. Introduction

The aim of this chapter is to study the processing and characterization of textured $SrBi_2Ta_2O_9$ (SBT) ceramics with improved performances of dielectric and ferroelectric properties. Textured SBT ceramics were prepared by templated grain growth (TGG) using the grown SBT single crystals as anisometric templates, as described in Chapter 2 (section 2.3). In fact, the selection and preparation of the template particles is a subject of special interest in TGG, since the texture development and the template growth during ceramics annealing strongly depends on the liquid phase content as well as on the number, size, distribution and initial orientation of the template particles.[1] Usually, template particles with suitable dimensions to be used as seeds for TGG are obtained by molten salt or hydrothermal synthesis methods. However, SBT is very difficult to be obtained by these methods and, thus, the large SBT single crystals presented in Chapter 3 were used to prepare the required seeds for TGG (see section 2.3.1).

Several parameters were firstly considered in order to achieve a high degree of texture in the seeded SBT ceramics, *e.g.*, the amount of liquid phase, the templates/matrix ratio or the processing and sintering conditions like the uniaxial pressure, the sintering temperature and time, etc. The importance of all these parameters was carefully examined from the literature reports on several materials, including ferroelectric ceramics (*e.g.*, perovskites and BLSFs, see section 1.5.3). Two different uniaxial pressures for shaping the green samples were selected, for evaluating the effect of the initial template orientation on the final texture degree, whereas several sintering conditions were used aiming at to produce dense ceramics with high degree of texture and enhanced properties.

Different amounts of Bi_2O_3 excess were tested in this work as liquid phase former. In absence of liquid phase a negligible template boundary migration into the polycrystalline matrix was observed, whereas extensive grain growth with highly textured microstructures was demonstrated in ceramics containing a small (3 wt%) amount of Bi_2O_3 excess. Large amount of liquid phase (≥ 5 wt%) resulted in ceramics with high porosity and low density, which deteriorates dielectric and ferroelectric properties. Furthermore, a noteworthy difference in the template growth was not observed between 3 and 5 wt% of Bi_2O_3 excess.

Therefore, 3 wt% of Bi_2O_3 as liquid phase was selected as a promising condition for TGG of SBT ceramics, being the results of this chapter focused in seeded SBT ceramics with 3 wt% of Bi_2O_3.

The template/matrix ratio was also scanned in the range up to 5 wt% of templates. Higher amount of templates as seeds were seen to result in ceramics with lower degree of texture and higher porosity, due to the early impingement of the templates. Therefore, the seeded SBT ceramics mainly discussed in this chapter were prepared with 5 wt% of templates, though other amounts are also considered for comparative purposes.

The experimental results are discussed in separated sections as follows: first, the effect of the initial processing parameters on the final density and degree of texture of seeded and unseeded SBT ceramics is discussed. Then, the microstructure evolution is analyzed and correlated with the processing parameters via a stereological analysis and also using a quantitative texture analysis based on the orientation distribution function of the large anisometric templates. The anisotropy in the dielectric and ferroelectric properties of the seeded SBT ceramics and its dependence on the degree of texture are demonstrated in the next section and compared to those of unseeded SBT ceramics. Finally, the spatial distribution of the polarization vector in randomly oriented and textured BLSF materials is modeled, and the values of the spontaneous polarization for SBT ceramics are predicted from this theoretical approach as a function of the degree of texture.

4.2. Ceramics Processing and X-Ray Characterization

4.2.1. Densification results

Table 4.1 summarizes the density results of unseeded and seeded SBT samples prepared with 3 wt% of Bi_2O_3, and processed under different pressing and sintering conditions. In the case of seeded samples, an amount of 5 wt% of templates was used. These are the representative specimens of the produced SBT ceramics which showed the most prominent microstructure and degree of texture, and hence, they were selected for the study of the dielectric and ferroelectric anisotropy. The theoretical density (TD) value of 8.78 g/cm^3 for SBT[2] was used to calculate the relative density (ρ_r) of each sample as the ratio of the measured density to the TD.

Table 4.1 Final density (ρ) and relative density (ρ_r)* of the 5 wt% seeded (SBT3Bi5T) and unseeded (SBT3Bi) SBT ceramics with 3 wt% of Bi_2O_3 excess, consolidated under different uniaxial pressure and sintered under different conditions.

Sintering Temperature (ºC)	Sintering Time (hours)	Unseeded SBT3Bi 150 MPa		Seeded SBT3Bi5T 150 MPa		Seeded SBT3Bi5T 300 MPa	
		ρ (g/cm^3)	ρ_r (%)*	ρ (g/cm^3)	ρ_r (%)*	ρ (g/cm^3)	ρ_r (%)*
1150	24	8.27	94	8.54	97	8.20	93
1250	0	8.22	94	8.22	94	8.17	93
1250	0.25	8.29	94	8.37	95	8.25	94
1250	1	8.46	96	8.55	97	8.28	94
1250	2	8.56	97	8.52	97	8.18	93
1250	24	8.41	96	8.32	95	8.02	91
1350	24	-	-	8.27	94	-	-

* Ratio of the measured density to the theoretical density of SBT, ρ_{Th} = 8.78 g/cm^3.

Firstly, it must be pointed out that the higher uniaxial pressure resulted in higher green densities in the seeded samples, *i.e.*, the seeded samples uniaxially pressed at 300 MPa showed higher green densities (~ 62% TD, density relative to the theoretical density), than those uniaxially pressed at 150 MPa (~ 56% TD). However, no significant difference in the green densities of the unseeded and seeded SBT samples was observed after the application of the isostatical pressing of ~ 200 MPa to all the uniaxially pressed specimens at the used different uniaxial pressures. The green densities of the samples were around 60% TD in all cases. Thus, from the point of view of the packing of the templates and of the matrix particles in the green state, apparent comparable starting conditions for sintering seemed to be established for all specimens.

After sintering, densities higher than 90% TD were obtained in all the sintered samples (see Table 4.1). The presence of templates in the seeded ceramics does not significantly affect the final density of the samples processed under similar sintering conditions, as demonstrated by the density values reported for SBT3Bi and SBT3Bi5T both pressed at 150 MPa. Moreover, it was also observed that the sintered seeded samples (SBT3Bi5T) pressed at 300 MPa exhibit a somewhat lower density than when pressed at 150 MPa. Table 4.1 shows a trend for a slight decrease of density for long sintering times.

4.2.2. X-ray diffraction analysis and Lotgering factor

The crystalline phase and degree of texture of the seeded and the unseeded SBT ceramics were studied via XRD analysis recorded on the polished cross-sections parallel (//P) and perpendicular (⊥P) to the pressing direction, as schematically shown in Fig. 2.13. In order to perform the XRD study, most of the sintered samples need to be first polished to remove a second phase appearing near the surface due to the evaporation of bismuth by sintering at high temperatures. In spite of the 3 wt% of Bi_2O_3 excess, the prolonged heating at 1250 ºC in air was propitious for bismuth losses near the sample surface. Figure 4.1(a) shows, as example, the XRD pattern scanned over the as-sintered surface ⊥P for the seeded SBT3Bi5T ceramic uniaxially pressed at 150 MPa and sintered at 1250 ºC during 24 hours. The reflections obtained in this pattern were indexed and the phase present was identified as isostructural to the bismuth-free $Sr_{2.83}Ta_5O_{15}$ tetragonal phase (space group *P*4*mbm*).[3]

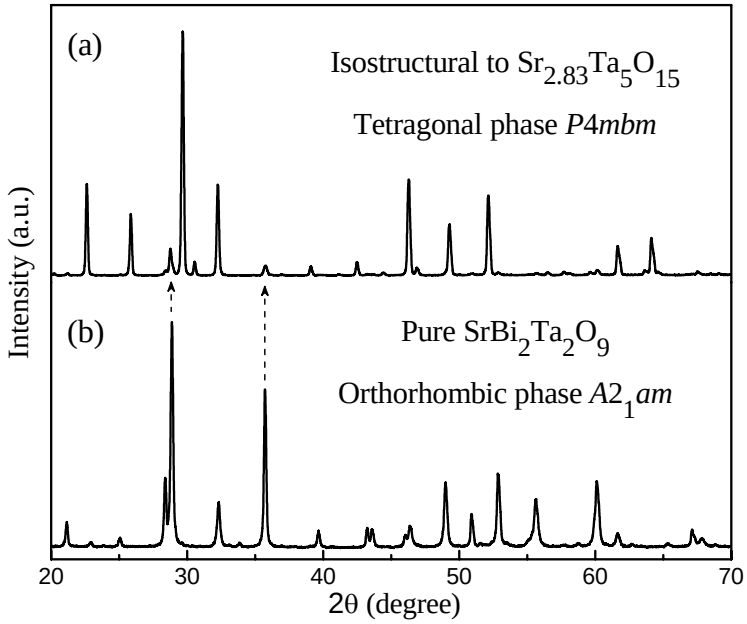

Figure 4.1 XRD patterns for (a) the as-sintered surface ⊥P and (b) the cross-section ⊥P after polishing to remove the second phase of the surface, in the seeded SBT3Bi5T ceramic uniaxially pressed at 150 MPa and sintered at 1250 ºC during 24 hours. The dashed lines indicate small peaks corresponding to SBT phase.

Figure 4.1(b) shows the XRD pattern of the polished cross-section ⊥P of the same sample after removing the second phase by polishing the specimen at ~ 100 μm inside the bulk and away from the as-sintered surface. As observed, only the peaks corresponding to

the SBT orthorhombic phase (space group $A2_1am$)[2] were obtained, confirming that the bulk phase of the sintered ceramics is pure SBT phase. The dashed lines in Fig. 4.1 indicate some small peaks corresponding to the SBT phase which were also observed in the XRD pattern of the as-sintered surface.

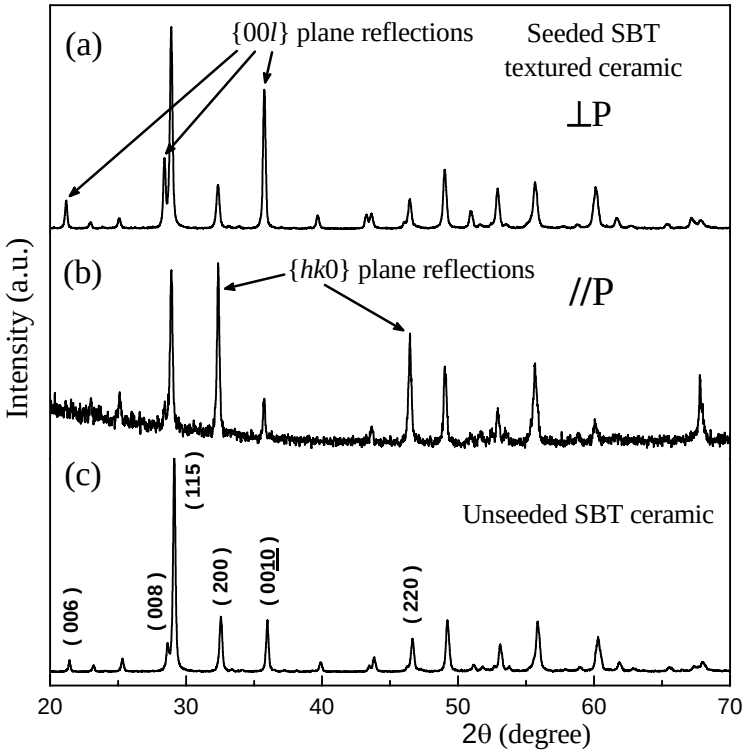

Figure 4.2 XRD patterns scanned on the cross-sections (a) ⊥P and (b) //P, in the seeded SBT3Bi5T ceramic uniaxially pressed at 150 MPa and sintered at 1250 ºC during 24 hours. (c) The pattern for the unseeded SBT3Bi ceramic processed under similar conditions is also included for comparison.

Figure 4.2(a,b) shows the XRD patterns recorded on the cross-sections ⊥P and //P, respectively, in the seeded SBT3Bi5T ceramic uniaxially pressed at 150 MPa and sintered at 1250 ºC during 24 hours. For comparison, the XRD pattern of the unseeded SBT3Bi ceramic processed under the same conditions is also included in Fig. 4.2(c). The lattice planes (*hkl*) associated to the reflections whose relative intensity changes significantly among the patterns are also pointed out. It can be observed that the diffractions from the {00*l*} planes of the SBT structure have a meaningful intensity in the XRD pattern on the cross-section ⊥P, while the diffraction peaks from the {*hk*0} planes, specifically the (200)

and (220) lattice planes, are stronger in the XRD pattern scanned on the cross-section //P. This result confirms a crystallographic texture in the seeded SBT ceramics.

Samples pressed at 150 MPa and sintered at different temperatures for 24 hours

For comparative purposes, Figure 4.3 shows the XRD patterns recorded on the cross-sections ⊥P of SBT3Bi5T samples pressed at 150 MPa and sintered at 1150 ºC, 1250 ºC and 1350 ºC for 24 hours. The lattice planes associated to the reflections whose relative intensity changes significantly among the patterns are also pointed out. With increasing sintering temperature, diffraction peaks from {00*l*} planes progressively dominate the patterns, accounting for the most intensive peak of the spectrum for the seeded sample sintered at 1350 ºC for 24 hours. However, in spite of being a dense ceramic (94% TD), this sample showed very low mechanical integrity and thus was not considered for further dielectric and ferroelectric characterization.

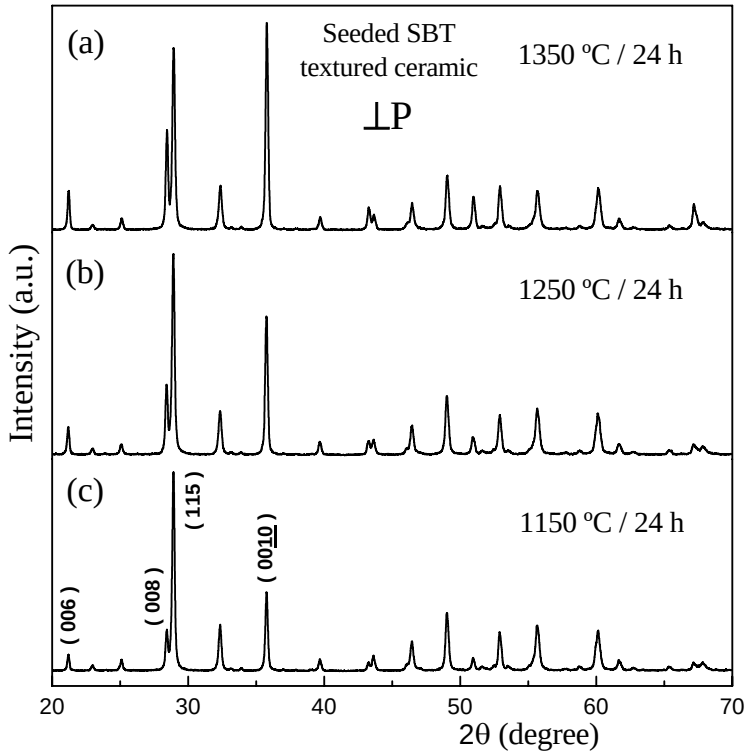

Figure 4.3 XRD patterns scanned on the cross-section ⊥P for seeded SBT3Bi5T ceramics uniaxially pressed at 150 MPa and sintered at (a) 1350 ºC, (b) 1250 ºC, and (c) 1150 ºC during 24 hours.

Samples pressed at 300 MPa and sintered at 1250 ºC for different sintering times

Aiming at increasing the initial alignment of the template particles inside the powder matrix, the ceramics were pressed under a higher uniaxial pressure of 300 MPa, thus allowing the pressure effect on the degree of texture to be evaluated. Figure 4.4 shows the XRD patterns recorded on the cross-section ⊥P for seeded SBT3Bi5T ceramics uniaxially pressed at 300 MPa and sintered at 1250 ºC for 0, 2 and 24 hours. With increasing sintering time, diffraction peaks from {00*l*} planes progressively dominate the patterns, accounting for the most intensive peak of the spectrum for the seeded sample sintered at 1250 ºC during 24 hours.

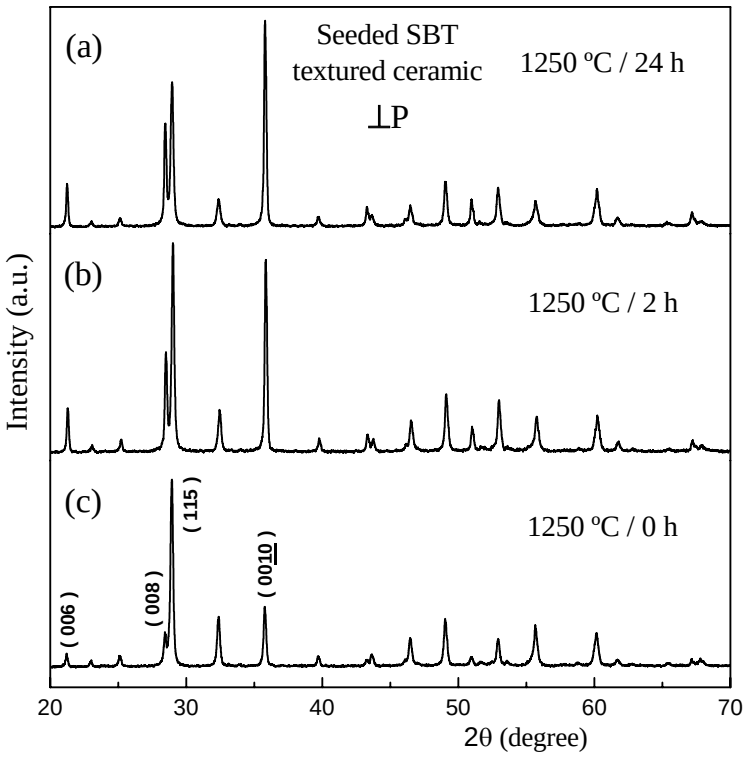

Figure 4.4 XRD patterns scanned on the cross sections ⊥P for seeded SBT3Bi5T ceramics uniaxially pressed at 300 MPa and sintered at 1250 ºC during (a) 24, (b) 2, and (c) 0 hours.

It has been reported that during densification very little or no template growth occurs, at least until the density approach to 90% TD.[4] In our ceramics, the values of relative density reported in Table 4.1 showed densities above 90% TD in all the sintered specimens, thereby indicating that density constrains for TGG process do not exist in such samples. Therefore, the continuous increment of the diffractions peaks from the {00*l*} planes observed for sintered seeded ceramics reflects the occurrence of TGG resulting in

higher volume fraction of textured material with *c*-axis parallel to the pressing direction, as will be further discussed in the next section 4.3.

Figure 4.5(a-c) compares the XRD patterns recorded on the cross-section ⊥P of unseeded SBT3Bi samples uniaxially pressed at 150 MPa and sintered at 1250 ºC for 0 and 24 h, with the one corresponding to the seeded SBT3Bi5T ceramic pressed at 300 MPa and sintered at 1000 ºC for 1 h. This seeded ceramic has a low density of ~ 80% TD. The XRD patterns are practically indistinguishable, thus indicating that the samples are equivalent regarding crystallographic texture, that is, unseeded samples did not suffer significant texture modification whereas the seeded sample did not start yet to develop texture. In this case, the seeded sample with only 80% TD may be considered at an early stage of the TGG process with porosity and a low grain connectivity inhibiting the template growth.

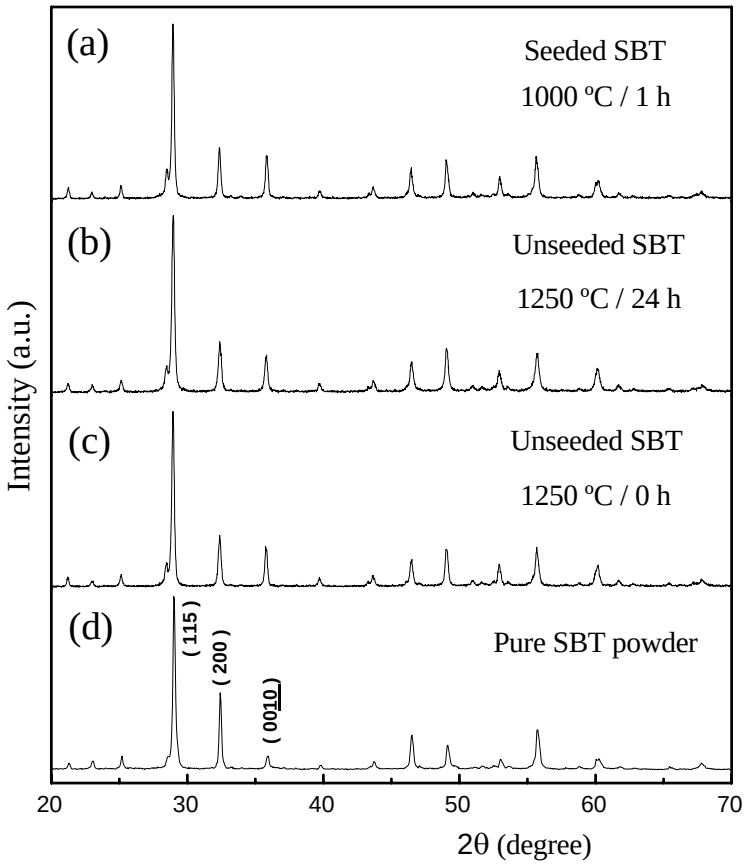

Figure 4.5 XRD patterns scanned on the cross sections ⊥P for (a) the seeded SBT3Bi5T sample uniaxially pressed at 300 MPa and sintered at 1000 ºC for 1 h, and unseeded SBT3Bi ceramics uniaxially pressed at 150 MPa and sintered at 1250 ºC during (b) 24 h and (c) 0 h. (d) For comparison the pattern of the SBT powder calcined at 950 ºC for 3 h is included.

In the unseeded SBT3Bi specimens [Fig. 4.5(b,c)], a small increase in the (00$\underline{1}$0) peak and a small decrease in the (200) peak with respect to the randomly oriented SBT powder [Fig. 4.5(d)] can be observed, suggesting that the sintered unseeded samples are not entirely randomly oriented but there exists a weak crystallographic texture, probably due to some matrix grains alignment during the consolidation of the green compact by uniaxial pressing and later sintering.

Table 4.2 Lotgering factor, *f* (%), for unseeded and seeded SBT ceramics with 3 wt% of Bi_2O_3 excess, processed under different uniaxial pressures and sintering conditions. The $f_{(00l)}$ factors were calculated using Eq. 2.8 for the (00*l*) plane reflections of the XRD patterns taken on the cross sections ⊥P.

Sintering Temperature (ºC)	Sintering Time (hours)	Unseeded	5 wt% Seeded		3 wt% Seeded
		150 MPa		300 MPa	
1250	0	8.4	11	13	-
1250	0.25	8.4	13	19	-
1250	1	8.5	15	27	12
1250	2	8.6	17	36	18
1250	24	8.9	25	46	26

Table 4.2 summarizes the Lotgering factor (*f*) calculated using Eq. 2.8 for the (00*l*) plane reflections of the XRD patterns obtained on the cross sections ⊥P of seeded and unseeded SBT ceramics with 3 wt% of Bi_2O_3 excess and processed under different pressing and sintering conditions. The effect of the initial uniaxial pressure is compared for a series of samples pressed at 150 MPa and 300 MPa.

Influence of the uniaxial pressure on the degree of texture

Figure 4.6 shows the dependence of the Lotgering factor on the sintering time for seeded SBT3Bi5T samples sintered at 1250 ºC, and that of the unseeded SBT3Bi samples, for comparison. Whereas unseeded ceramics show a Lotgering factor lower than 10% even after 24 hours of sintering time, seeded ceramics reach a maximum $f \approx 25\%$ for samples uniaxially pressed at 150 MPa and $f \approx 46\%$ for samples pressed at 300 MPa. For short sintering time (0 hours) a similar degree of orientation was obtained in seeded samples

corresponding to both pressure conditions, very close to that observed in the early stage of the TGG process (seeded SBT3Bi5T sample sintered at 1000 ºC for 1 hour, $f \approx 10\%$). When the sintering time increases, the seeded ceramics exhibit an initial fast texturing rate which tends to saturate after 2 hours.

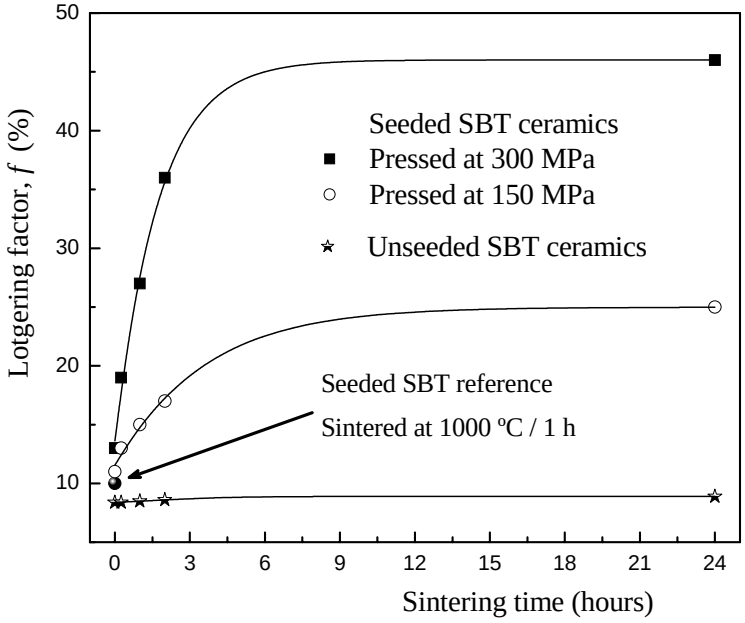

Figure 4.6 Effect of the uniaxial pressure on the dependence of the texture development (*Lotgering factor*) with the sintering time of seeded and unseeded SBT3Bi5T ceramics sintered at 1250 ºC. The value obtained for the seeded SBT3Bi5T specimen sintered at 1000 ºC during 1 hour is included as reference.

The higher is the uniaxial pressure in the green samples, the higher seems to be the initial orientation of the templates, resulting in a higher degree of texture in the sintered samples. Nevertheless, the *f* values obtained in this work are lower than those typically reported for textured ceramics produced by other more elaborated texturing techniques like tape casting or extrusion.[5-7]

According to Table 4.2, the 5 wt% seeded SBT ceramics result in a higher degree of texture as compared with the 3 wt% seeded SBT samples both pressed at 300 MPa. Higher amounts of templates (> 5 wt%) were seen to result in a lower degree of texture. In fact, nearly fully textured ceramics have been achieved in other systems using only 5 wt% of templates.[8] Therefore, based on all these observations, SBT ceramics prepared with 3 wt%

of Bi_2O_3 excess and 5 wt% of templates (SBT3Bi5T) uniaxially pressed at 300 MPa were selected for further studies.

4.2.3. Pole figure analysis

Pole figure measurements, the most common method to evaluate the distribution of a specific crystallographic orientation in bulk materials, were performed in the seeded and unseeded SBT ceramics. In this study, the seeded specimens were disks with axisymmetric texture about the normal to the disks major face, which is the axis parallel to the pressing direction (the texture axis in this case). Here, the preferred orientation direction, *i.e.*, the crystal direction preferentially aligned with the texture axis, is the [001] direction. This kind of texture development is predictable since the uniaxial pressing can only align the basal planes of the SBT templates perpendicular to the pressing direction, thus the rotational alignment of the templates in the plane ⊥P should be random. For measuring axisymmetric texture under this configuration, the pole figures of diffraction peaks from planes normal to the preferred orientation direction [(00*l*) diffraction planes in this case] are usually displayed.

Figure 4.7(a,b) shows the pole figures of the (115) and (008) diffraction planes, respectively, obtained from the cross-section ⊥P of the seeded SBT3Bi5T sample pressed at 150 MPa and sintered at 1250 ºC during 24 hours, as the samples rotate about two orthogonal axes ω and β (see section 2.5.2 and Fig. 2.14). The (115) diffraction is included in this study because it is the most intense reflection in the XRD pattern of a randomly oriented SBT material. For comparison, the pole figures of the same diffraction peaks for the unseeded SBT3Bi sample processed under similar pressing and sintering conditions are presented in Fig. 4.7(c,d). In this case, a uniform pole density with no significant texture is observed in both diffractions for the unseeded SBT3Bi specimen [see the small intensity of the (008) diffraction in the entire pole figure of Fig. 4.7(d)], which is typical of materials with near randomly oriented crystallites.

On the other hand, a large distribution of (008) diffraction with a maximum of about one order of magnitude at the center of the pole figure with respect to the edge is clearly observed for the seeded SBT3Bi5T sample [see Fig. 4.7(b)]. Both pole figures [for (008)

and (115) diffractions in Fig. 4.7(a,b)] show non-uniform pole density and the increase of the (008) intensity supports the idea of having a textured material with axisymmetric texture, where the crystallographic *c*-axis is preferably oriented along the pressing direction (texture direction). The difference in the intensity recorded for the (008) diffraction plane in Fig. 4.7(b) with respect to that in Fig. 4.7(d) is related with the higher volume fraction of templated grains with *c*-axis preferentially aligned along the texture axis and their lattice (00*l*) planes in reflection geometry in the seeded SBT3Bi5T sample.

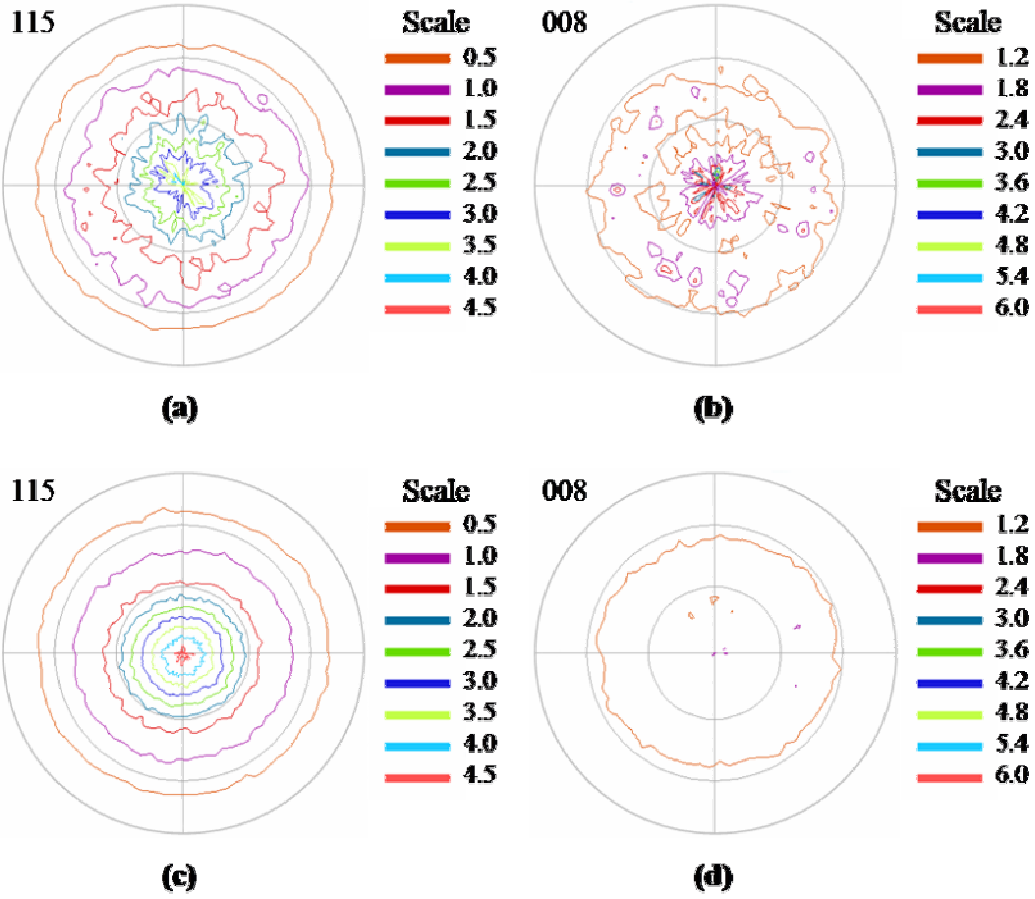

Figure 4.7 Pole figures of the (115) and (008) diffraction planes obtained from the cross-section ⊥P of the (a)-(b) seeded SBT3Bi5T and (c)-(d) unseeded SBT3Bi ceramics, both pressed at 150 MPa and sintered at 1250 ºC for 24 hours.

In order to quantify the texture, the pole figure of materials with axisymmetric texture can also be represented as a plot of the intensity versus ω at fixed β, as explained in section 2.5.2. In this case, the volume fraction of textured material with preferred crystallographic direction at a certain angle with respect to the texture axis is measured.

Figure 4.8 shows the angular dependence of the intensity of the (00$\underline{1}$0) and the (115) diffraction planes in the range -90º ≤ ω ≤ 90º for the seeded SBT3Bi5T samples uniaxially pressed at 300 MPa and sintered at 1250 ºC for different sintering times. There is an evident modification in the widths and on the height of the (00$\underline{1}$0) diffraction profiles with the increase of the sintering time. When the sintering time increases, the intensity of the (00$\underline{1}$0) diffraction in the vicinity of ω = 0º increases, becoming higher than the (115) diffraction for 24 hours of sintering time. The orientation distribution profile of the (00$\underline{1}$0) diffraction drops in all cases when increasing ω, reaching the maximum value (*M*) at ω = 0º. This indicates not only that the templates grow in such a way that most of the grains are oriented with *c*-axis within ~ 20º about the texture axis, but also that the number of grains with orientations in the vicinity of the texture axis and contributing to the XRD profile for low ω values increases with increasing of the sintering time.

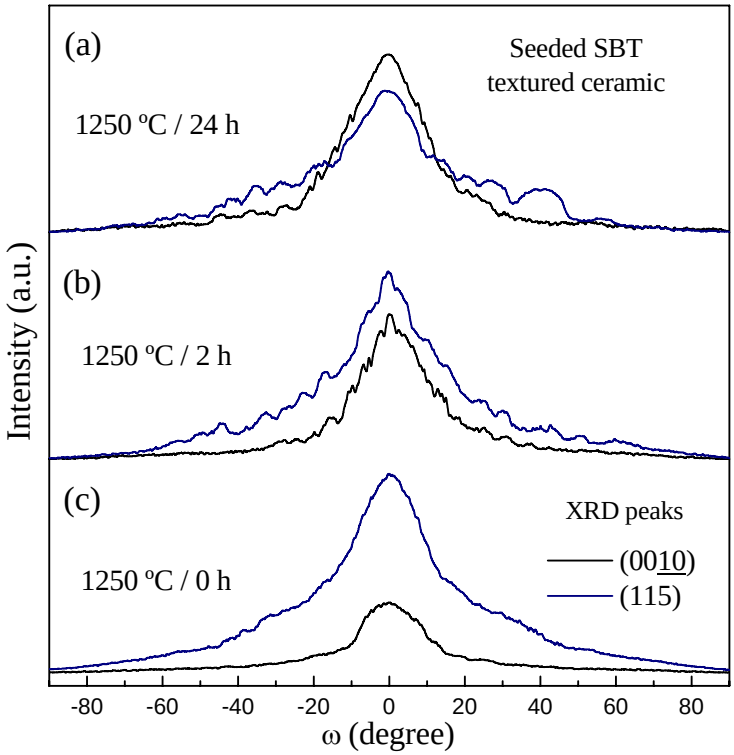

Figure 4.8 Angular dependence of the intensity of the (00$\underline{1}$0) and the (115) diffraction peaks in the range -90º ≤ ω ≤ 90º for the seeded SBT3Bi5T specimens pressed at 300 MPa and sintered at 1250 ºC during (a) 24, (b) 2 and (c) 0 hours.

On the other hand, there is a significant difference in the width of the (00$\underline{1}$0) profiles with increasing sintering time. While intensities 5 times smaller (*M*/5) are reached at

$|\omega| = 15^o$ for the specimens with 0 hours of sintering time, the value of $|\omega|$ for *M*/5 increases to 20^o and 22^o for the specimens with 2 and 24 hours of sintering times, respectively. This behavior is related with the orientation distribution of grains in each sample, which will be further discussed in the next section 4.3.3, using a stereological analysis.

Several small peaks were observed in the angular range of $|\omega| \leq 20^o$ for the (00$\underline{10}$) diffraction and $30^o \leq |\omega| \leq 50^o$ for the (115) diffraction. It is believed that the appearance of such peaks in these distributions is related to the statistic of the present XRD data, since in 1 mm^2 of incidence region over the sample there exist less than 100 template grains, as will be shown in the SEM results.

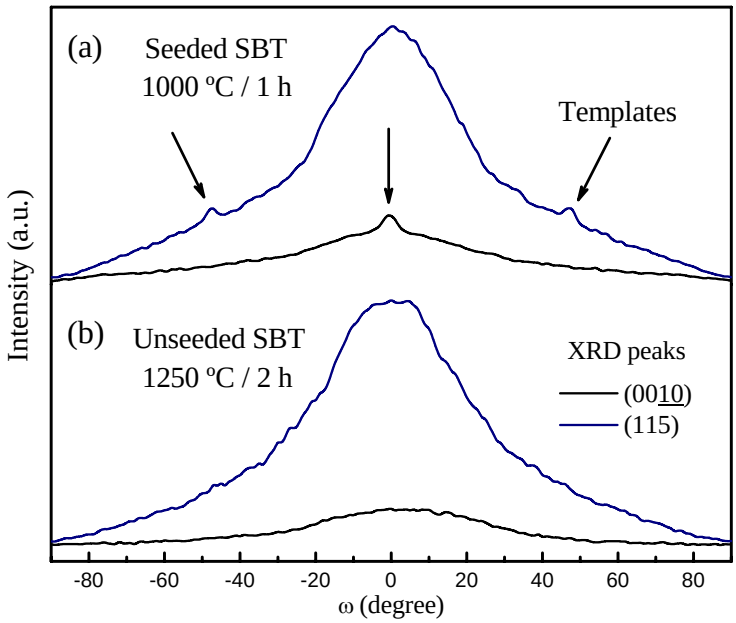

Figure 4.9 Angular dependence of the intensity of the (00$\underline{10}$) and (115) diffraction peaks in the range of $-90^o \leq \omega \leq 90^o$ for (a) the seeded SBT3Bi5T sample pressed at 300 MPa and sintered at 1000 ºC for 1 h, and (b) the unseeded SBT3Bi sample sintered at 1250 ºC for 2 h.

On the other hand, the angular dependence of the intensity of the (00$\underline{10}$) and (115) diffraction peaks for the unseeded SBT3Bi sample sintered at 1250 ºC for 2 hours (used as a standard) and for the seeded SBT3Bi5T sample sintered at 1000 ºC for 1 hour (sample in which no significant TGG has occurred) were plotted in Fig. 4.9. The main differences in these two plots is the small peak appearing around $\omega = 0^o$ for the (00$\underline{10}$) diffraction and $|\omega| \approx 50^o$ for the (115) diffraction in Fig. 4.9(a), very close to the angle between the [001] and the [115] directions in the orthorhombic structure of SBT. These small peaks are

associated to the well-oriented templates in the seeded SBT3Bi5T samples, confirming an adequate orientation distribution of the original templates in the green samples.

In the unseeded SBT3Bi sample, the distributions of intensity of the (00$\underline{1}$0) and the (115) diffraction peaks are in a good agreement with the pole figure shown in Fig. 4.7(c,d). That is, uniform pole densities with maximum values at $\omega = 0^o$ in both cases. When TGG occurs in seeded SBT3Bi5T ceramics, the distribution of orientations around $\omega = 0^o$ for the (00$\underline{1}$0) diffraction start to dominate the profile, being the highest peak for 24 hours of sintering time, while the intensity for the (115) diffraction still dominating the profile for $|\omega| > 20^o$ because the intensity of the (115) diffraction peak would have to be maximal around $|\omega| = 52^o$, which is the angle between the [001] and the [115] directions calculated taking into account the orthorhombic symmetry (space group $A2_1am$) of the SBT system.[2] For texture higher than those presented in our samples, it should be expected that the (115) diffraction shows a concentric ring around $|\omega| = 52^o$ in the pole figures.

4.3. Microstructure and Texture Analysis

4.3.1. Microstructure evolution

In unseeded SBT ceramics sintered under similar processing conditions as those of seeded SBT, that is, uniaxial pressure of 150 MPa and sintering at 1250 ºC from 0 to 24 h, a microstructure showing dense platelet grain morphology without significant porosity was observed [see Fig. 4.10], in a good agreement with the high densities reported in section 4.2.1. Small, anisometric and well-faceted matrix grains were obtained, with a maximum length size of ~ 15 μm and thickness of ~ 4 μm, as documented in Fig. 4.10 for a sample sintered at 1250 ºC during 24 hours (the micrograph with the scale of 100 μm was included for later comparison with those of seeded SBT ceramics).

Almost all BLSF materials show plate-like grain morphology to minimize the energy associated with the grain boundaries.[5] As in $Bi_4Ti_3O_{12}$, another BLSF crystal, SBT (00*l*) facets develop more extensively during the sintering process, thus indicating to be the ones possessing the lower surface energy. As a result, a plate-like grain morphology develops with major faces parallel to the (00*l*) crystal planes.

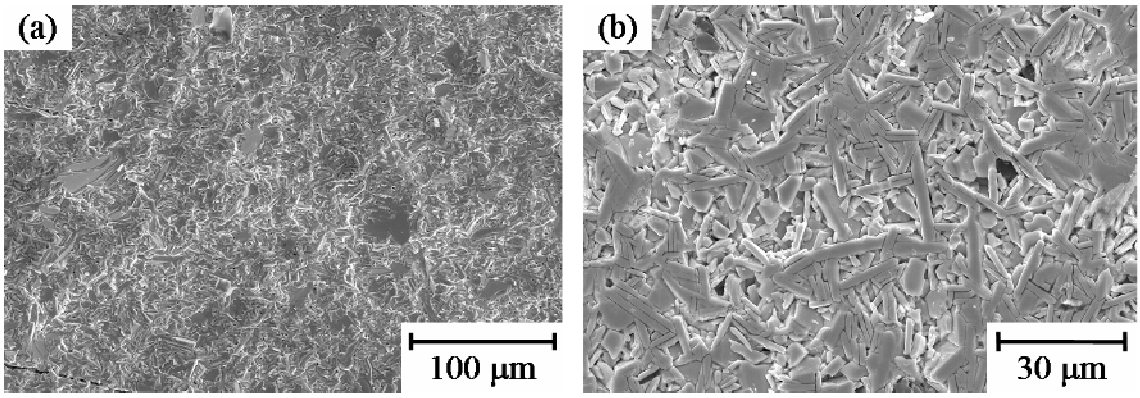

Figure 4.10 SEM micrographs of the polished and acid etched unseeded SBT3Bi specimen uniaxially pressed at 150 MPa and sintered at 1250 ºC for 24 hours.

Figure 4.11(a) shows a cross-section //P of the seeded SBT3Bi5T ceramic uniaxially pressed at 300 MPa and sintered at 1000 ºC for 1 hour, in which the matrix is still porous and has density around 80% TD. As observed, anisotropic template growth is limited since grain connectivity and porosity do not favour the close contact between matrix grains and templates.[9] As shown before, this sample did not start yet developing a crystallographic texture, being this stage regarded as the initial stage of the TGG process, *i.e.*, the matrix grains are lower than 1 μm, the template particles are homogeneously distributed, and the average template size is ~ 42 μm in length by 8.4 μm in thickness, giving an initial aspect ratio (AR) of ~ 5.

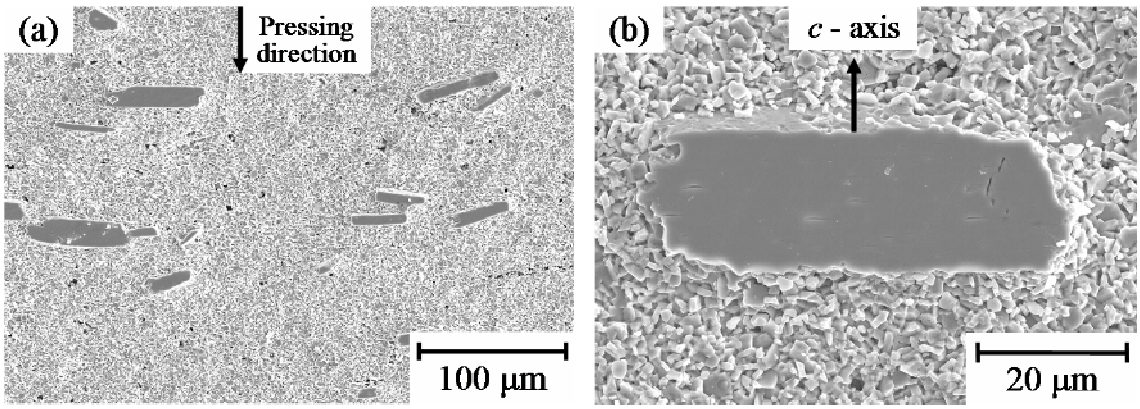

Figure 4.11 SEM micrographs of (a) a cross-section //P of the seeded SBT3Bi5T ceramic uniaxially pressed at 300 MPa and sintered at 1000 ºC for 1 hour, and (b) a single SBT template surrounded by matrix grains, showing the *c*-axis orientation.

Figure 4.11(b) shows an image of a single template surrounded by matrix grains in the same cross-section //P, in such a way that the *c*-axis is aligned parallel (or nearly

parallel) to the vertical axis of the micrograph as indicated in the figure. Although there exist a few misoriented templates [see Fig. 4.11(a)], most of them display a similar *c*-axis projection, in which their major face is nearly perpendicular to the uniaxial pressing direction, and thus, *c*-axis is aligned parallel to the pressing direction.

For accessing the influence of the liquid phase on the final microstructure of the sintered ceramics, the microstructures of seeded SBT ceramics with and without Bi_2O_3 excess were evaluated. Figure 4.12 shows the cross-section //P of the 5 wt% seeded SBT ceramic prepared without Bi_2O_3 excess (liquid phase former), uniaxially pressed at 300 MPa, and sintered at 1250 ºC for 2 hours. The microstructure of such specimen consists of very few large anisometric grains with an average size close to that of the original templates [see Fig. 4.11(a) for comparison], which are distributed in a matrix of small and randomly oriented grains. A negligible template boundary migration into the polycrystalline matrix has thus occurred in this case.

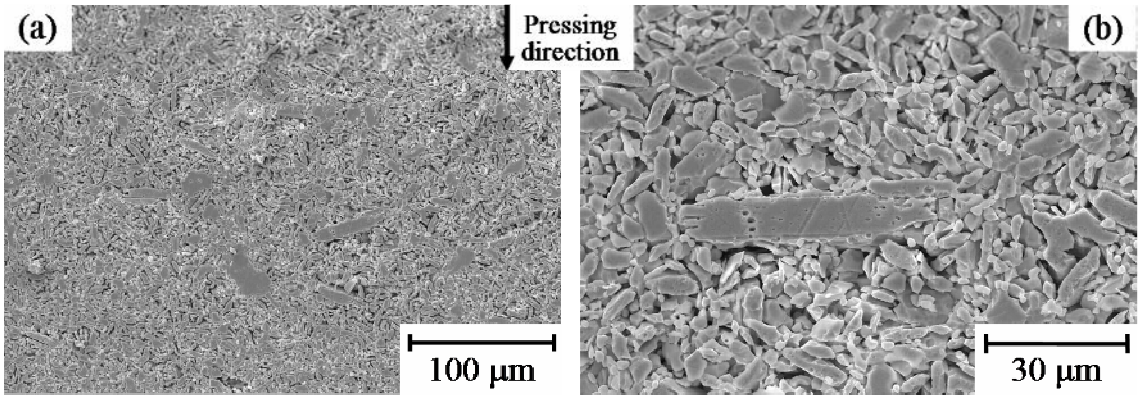

Figure 4.12 SEM micrographs on the polished and acid etched cross-section //P of the 5 wt% seeded SBT5T ceramic with no Bi_2O_3 excess, uniaxially pressed at 300 MPa and sintered at 1250 ºC for 2 hours.

Comparing this image to that corresponding to a seeded ceramic produced with the same amount of templates and under the same sintering conditions, but added with 3 wt% of Bi_2O_3 excess, a completely different microstructure is observed [see Fig. 4.14(c)]. The seeded sample with 3 wt% of Bi_2O_3 excess has developed a high volume fraction of large anisometric grains, which were grown by consuming small and randomly arranged grains from the matrix. This Ostwald ripening-type process was allowed by the Bi_2O_3 excess. The dimensions of the large anisometric grains are far above those of the original templates.

These results demonstrate that the Bi_2O_3 excess plays a crucial role as a liquid phase medium which enhances mass transfer processes in the TGG of SBT ceramics.

Samples pressed at 150 MPa and sintered at different temperatures for 24 hours

Figure 4.13(a,b) shows the textured microstructures of the polished and acid etched cross-sections //P that result from seeded SBT3Bi5T samples uniaxially pressed at 150 MPa and sintered at 1150 ºC and 1250 ºC, respectively, for 24 hours. The microstructures thus obtained are quite different from that of the seeded SBT ceramic with no Bi_2O_3 excess [compare Figs. 4.12(a) and 4.13(a,b)]. In this case, a bimodal microstructure dominated by a great number of interconnected large and anisometric grains is clearly observed in both samples, although its amount is larger in the case of the sample sintered at 1250 ºC. These large grains, which were not observed in unseeded SBT3Bi ceramics [see Fig. 4.10(a) for comparison], display a plate-like morphology similar to the original template, with a final average length of ~ 90 μm and average thickness of ~ 14 μm, for the sample sintered at 1250 ºC for 24 hours. This is about twice the dimensions of the initial seeds.

Figure 4.13(c) shows an amplified region of the Fig. 4.13(a), where the matrix grains surrounding the large anisometric grains can be observed for the seeded SBT specimen sintered at 1150 ºC for 24 hours. These small grains are the matrix grains from which the templates are grown. Hence, the large template particles consume the small and randomly arranged matrix grains, as reported in many other systems.[1,8]

Figure 4.13(d) shows the SEM micrograph of the polished and acid etched ⊥P top surface that result from the seeded SBT3Bi5T sample sintered at 1250 ºC for 24 h, for a comparative purpose. In this case, a bimodal microstructure is also evidenced, although the templates are revealed as square sections of solid grains with dimensions of ~ 90 × 90 μm^2. Thus, it may be concluded that the large grains are plate-like anisotropic grains, similar to the SBT templates, but two times larger than the initial seeds.

Figures 4.13(a) and 4.13(b) while revealing that the final volume fraction of large anisometric grains largely exceeds that of initial templates, also demonstrate that the volume fraction of large grains increases with the increasing sintering temperature. As discussed before, these phenomena take place in presence of liquid phase but not in its

absence. It is suggested that a decrease in the viscosity of the liquid phase with increasing temperature may account for these results since its favors matrix grain rearrangement and mass transport, which are considered to be relevant factors for anisometric grain growth in TGG processes.[8-10] It must be also pointed out that the increasing amount of large anisometric grains that follow the increase of sintering temperature is accompanied by an increase of the ceramic crystallographic texture as revealed in Fig. 4.3. As reported in Table 4.2 and Fig. 4.6, the best Lotgering factor obtained for seeded SBT3Bi5T ceramics pressed at 150 MPa was only 25% in spite of the great amount of large grains, due to the misorientation of the initial templates.

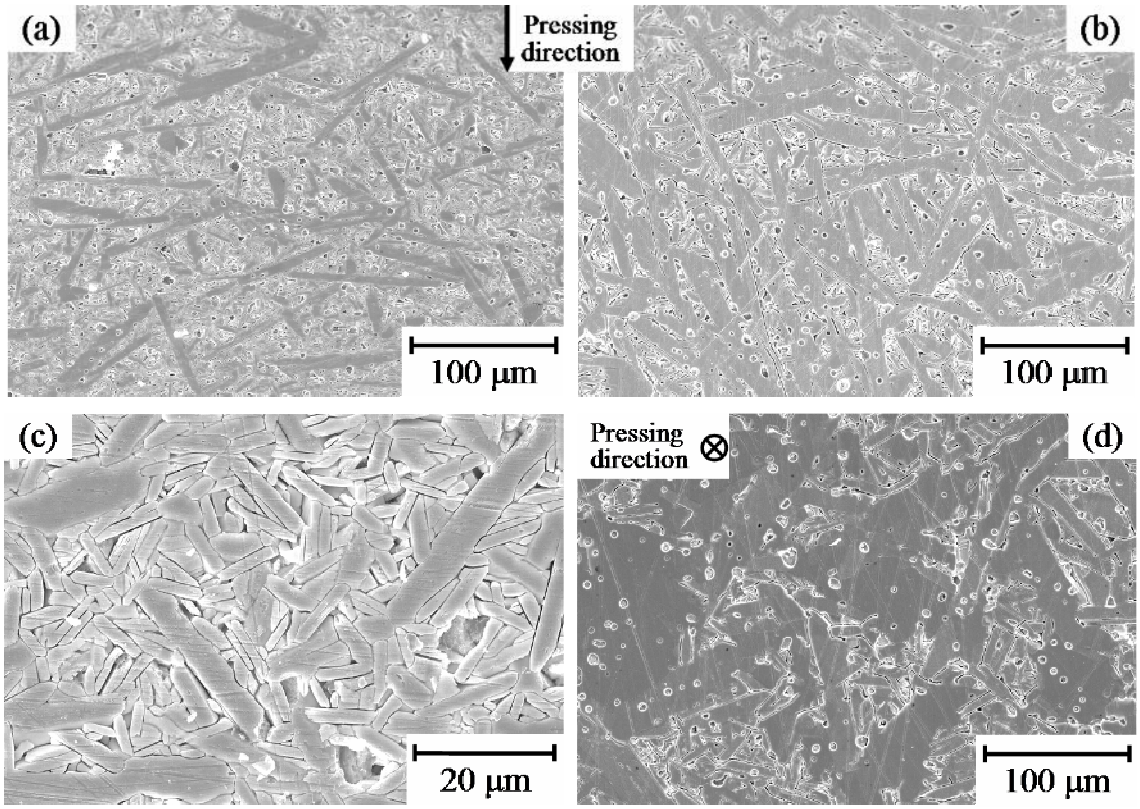

Figure 4.13 SEM micrographs on the polished and acid etched cross-section //P of the seeded SBT3Bi5T ceramic uniaxially pressed at 150 MPa and sintered at (a) 1150 ºC and (b) 1250 ºC during 24 hours. (c) Amplified section of the figure (a) showing the small grains surrounding the large anisometric grains. (d) SEM micrograph on the polished and acid etched ⊥P top surface of the same specimen of figure (b), in this case the pressing direction is pointing ⊥ to the figure plane (⊗).

Samples pressed at 300 MPa and sintered at 1250 ºC for different sintering times

In order to increase the initial degree of orientation of the plate-like templates in the matrix for improving the degree of texture, a higher uniaxial pressure of 300 MPa was applied to the seeded SBT3Bi5T specimens, and the evolution of the microstructure for different sintering times at 1250 ºC was followed. Figure 4.14 shows the development of the textured microstructure during sintering of seeded SBT3Bi5T ceramics at 1250 ºC, after 0, 1, 2 and 24 hours. When increasing the sintering time, the templates particles grow significantly along the length direction for short sintering times until template impingement, while the matrix grains coarsen gradually. This is in a good agreement with results reported for alumina, where TGG was proposed to occur in three stages:[9,11,12] densification, rapid radial growth of individual template particles until impingement, and slower growth by template thickening, as schematically represented in Fig. 1.13.

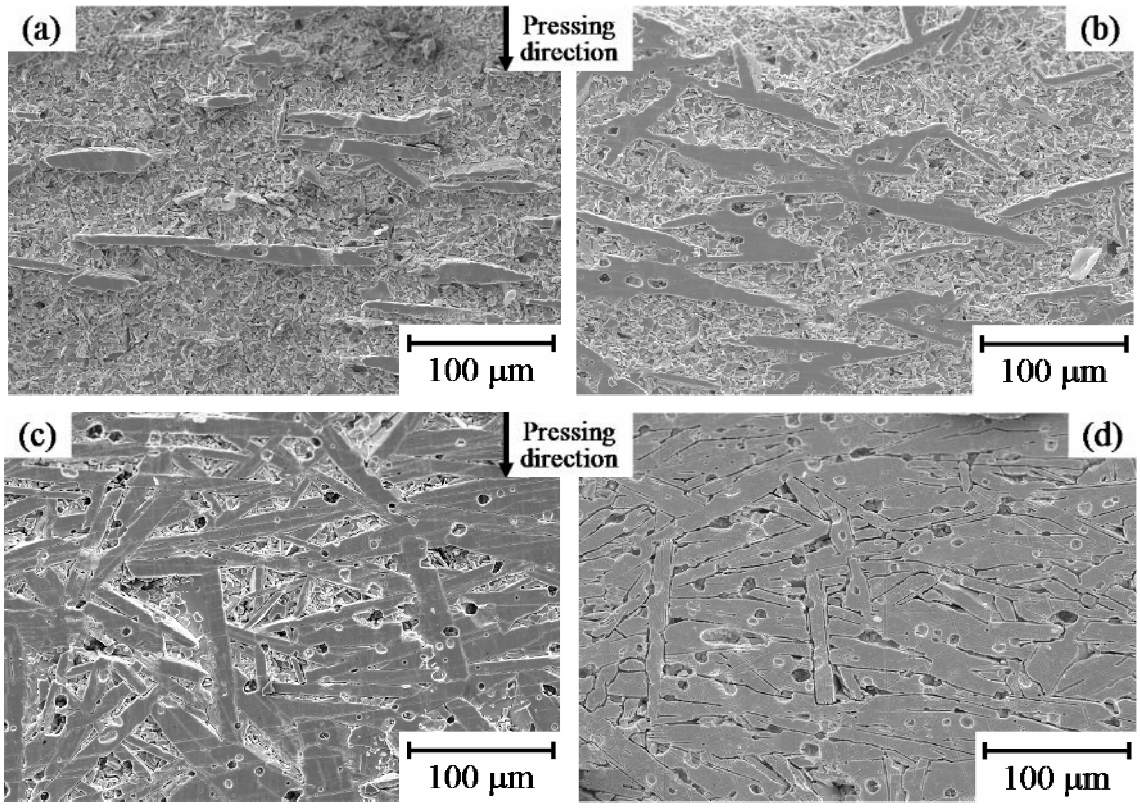

Figure 4.14 SEM micrographs on the polished and acid etched cross-section //P of the seeded SBT3Bi5T ceramic uniaxially pressed at 300 MPa and sintered at 1250 ºC for (a) 0 h, (b) 1 h, (c) 2 h and (d) 24 hours.

The time evolution of the microstructure depicted by Fig. 4.14 also reveals an increasing amount of oriented grains with their major faces perpendicular to the uniaxial pressing direction. This may explain the observed increasing crystallographic texture with the increasing sintering time, as shown in Fig. 4.4. In the present samples, after sintering at 1250 ºC for 0 h the microstructure shows a few large grains that correspond roughly to the initial concentration of seed crystals. However, their average size has significantly increased to ~ 74 × 9 μm^2 and has been accompanied by the corresponding increase (about 60%) of the aspect ratio from AR ≈ 5 (initial stage) to AR ≈ 8. Similar to bismuth titanate ceramics textured by TGG, the template growth morphology may be ascribed to the anisotropy of grain boundary energies.[5] Thus, the preferred lateral growth of the templates maximizes the area of the faces perpendicular to the *c*-axis, which appear to be those with lower surface energy. Although slowed by matrix coarsening, the template lateral growth continues until templates impinge each other after sintering at 1250 ºC for 2 hours (see also Table 4.3). At this point the average size of the large anisometric grains is ~ 88 × 11 μm^2, while the aspect ratio still at AR ≈ 8.

On the other hand, the comparison of Figs. 4.13(b) and 4.14(d) allows evaluating the effectiveness of the uniaxial pressure for conditioning the ceramic texture: it is clearly observed that the higher pressure (300 MPa) resulted in a larger amount of anisometric grains aligned with their major faces perpendicular to the pressing direction.

Figure 4.15 illustrates the impingement of several large anisometric grains surrounded by small matrix grains in a cross-section //P of the seeded SBT3Bi5T ceramic pressed at 300 MPa and sintered at 1250 ºC for 2 hours. The edges of the large grains terminate abruptly on the major faces of other large grains. Besides, some of the matrix grains that grow too large to be consumed and that still are misaligned with respect to the templates also impinge upon the large anisometric grains. For longer sintering times, due to impingement, the large anisotropic grains stop to grow along the length direction while getting thicker, mainly through the aligned matrix grains, giving place to a decrease of the aspect ratio until AR ≈ 6.7. Their average size was of ~ 91 × 13.5 μm^2 for the samples sintered during 24 hours. At this stage, some porosity concentrated near the template particle boundary also limits the grain growth, as observed in Fig. 4.14.

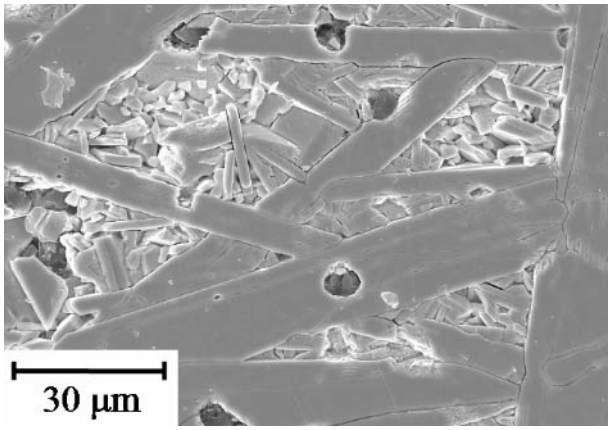

Figure 4.15 Cross-section //P of the seeded SBT3Bi5T ceramic uniaxially pressed at 300 MPa and sintered at 1250 ºC for 2 hours, showing the impingement of several large anisometric grains surrounding by small matrix grains.

4.3.2. Stereological analysis

The measured values of the average length, thickness and the calculated aspect ratio for large and small anisotropic grains in seeded SBT3Bi5T samples sintered at 1250 ºC from 0 to 24 hours are reported in Table 4.3. The average length and thickness for small and large grains were determined through a stereological analysis by creating the corresponding histogram and fitting it with a normal distribution, as explained in the section 2.5.4. The aspect ratio for the large anisometric grains was calculated by dividing the average length by the average thickness.

Table 4.3 Microstructure morphology parameters of the seeded SBT3Bi5T ceramics uniaxially pressed at 300 MPa and sintered under different conditions: Average length, thickness, aspect ratio and volume fraction corresponding to the large anisometric grains, and average length and thickness for the matrix grains, determined by stereological analysis.

Sintering Temperature (ºC)	Sintering Time (hours)	Volume Fraction f_v	Small Grains (µm)		Large Grains (µm)		Aspect Ratio
			Length	Thickness	Length	Thickness	
1000	1	0.05	1.0	0.5	42	8.4	5.0
1250	0	0.09	5.6	1.5	74	9.1	8.1
1250	0.25	0.14	6.7	1.9	77	9.2	8.3
1250	1	0.21	7.5	2.1	80	10.1	7.9
1250	2	0.53	9.7	2.6	88	11.2	7.8
1250	24	0.62	14.6	3.8	91	13.5	6.7

The volume fraction of textured material, f_v, has been also included in Table 4.3. For calculating f_v, the large anisometric grains were considered as textured material while the remaining small grains were assumed as randomly oriented. This volume fraction increases from ~ 9% after 0 hours to ~ 62% after 24 hours of sintering time. In the case of the seeded SBT specimen sintered at 1000 ºC for 1 hour, the calculated volume fraction of large anisometric grains was ~ 5%, in a good agreement with the initial amount of templates added to the SBT powder for TGG. Therefore, the previous assumption that this sample might be assumed to be at the initial stage of the TGG process is confirmed.

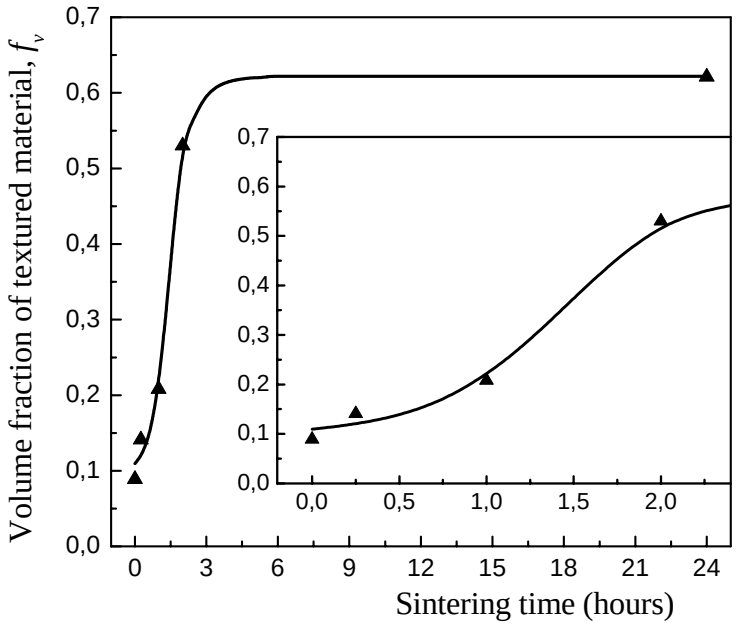

Figure 4.16 Sintering time dependence of the volume fraction of textured material obtained by stereological analysis of SEM images in seeded SBT3Bi5T ceramics pressed at 300 MPa and sintered at 1250 ºC. The inset corresponds to the enlargement of the initial curve region.

Figure 4.16 shows how the volume fraction of textured material changes with the sintering time. Due to the template growth, a fast increase in the volume fraction of large anisometric grains from ~ 9% after 0 h to ~ 53% after 2 hours is observed, and then, f_v stars to saturate following a sigmoid function. The anisotropic TGG occurs mainly in the first 2 hours of sintering time when sintered at 1250 ºC (see inset in Fig. 4.16 for better visualization). However, a small amount of this volume fraction corresponds to misaligned grains with respect to the texture plane, that is, the plane perpendicular to the pressing direction. Nevertheless, most of these grains have a misorientation lower than 20º, as obtained from the pole figure measurements, and thus, they are expected to contribute to

the improvement of the dielectric and ferroelectric properties measured along any direction perpendicular to the pressing direction.

Nucleation of new large anisometric grains

Generally it was believed that the texture development during TGG occurs only by the growth of the large, anisometric and well-oriented templates throughout the matrix, consuming the small and randomly arranged neighbor matrix grains, without contribution from the rearrangement or the preferential development of texture in the matrix grains, as reported in TGG of textured alumina.[11,13] Thus, the limits of the template growth and texture development should be controlled by the geometry, concentration and alignment of the original templates. According to such assumption, the volume fraction of textured material (considering only template particles) should be directly related to the number of original templates,[11]

$$f_v = N\, V_T \tag{4.1}$$

where N is the initial number of templates in 1 cm^3 and V_T the average volume of a single template particle in cm^3. Therefore, when template growth occurs, V_T increases and according to Eq. 4.1 f_v should increase linearly with V_T.

Figure 4.17 shows the dependence of f_v on V_T, which was calculated using the average length and average thickness of large anisotropic grains reported in Table 4.3 and assuming a plate-like morphology for the large grains. The slope of the curve corresponds to the number of large anisometric grains per 1 cm^3. As observed, instead of a continuous linear relation between the volume fraction of textured material and the calculated average volume of a single large grain, two distinct slopes are identified in this plot, one for short sintering times up to 1 hour and a higher slope for longer sintering times.

This result suggests that the number of large grains per 1 cm^3 in the final stage of the TGG process increased with respect to the number of original templates. This can be also stated by comparing Fig. 4.14 from (a) to (d), even taking into account the increase of the large grains length and thickness. The number of large grains per 1 cm^3 obtained from this plot was: $N_o \approx 2.7 \times 10^6$ cm^{-3} for short sintering times and $N_f \approx 1 \times 10^7$ cm^{-3} for longer

sintering times (both with correlation coefficient greater than 0.96). Thus, the number of large anisometric grains at the late stage of the TGG process is almost 4 times greater than the value obtained in the early stage. The number of original templates per 1 cm^3 was also experimentally evaluated by taking into account the initial average particle dimensions (~ 42 × 8.4 μm^2) and the original 5 wt% of templates mixed with the initial SBT powder. The value thus obtained, $N = (3.3 \pm 0.5) \times 10^6$ cm^{-3}, is in a good agreement with N_o.

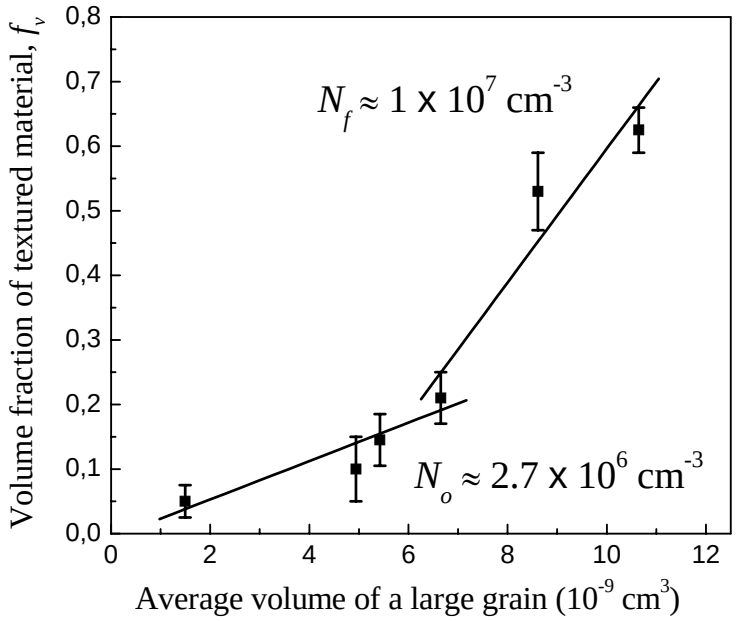

Figure 4.17 Correlation between the volume fraction of textured material and the calculated average volume of a large anisometric grain in seeded SBT3Bi5T ceramics pressed at 300 MPa and sintered at 1250 ºC from 0 to 24 h. N is the number of large grains per 1 cm^3.

Therefore, besides the growth of the original templates throughout the polycrystalline matrix, new large grains evolve from the matrix and grow after 1 hour of sintering time, acquiring similar platelet morphology with a fast growth along the *ab*-plane and similar alignment with their major face nearly perpendicular to the uniaxial pressing direction. A mechanism other than the growth of the original templates should operate in this case.

The study of the aspect ratio distributions for different sintering times gives also some information about the existence of new large grains independent of the original templates. Figure 4.18 shows several histograms corresponding to the AR distributions of large anisometric grains, weighted by their frequency, in the cross-sections //P of the seeded SBT3Bi5T ceramics uniaxially pressed at 300 MPa and sintered at 1250 ºC for

different sintering times. These histograms were fitted with normal distributions which allowed determining the mean AR and the full width at the half-maximum (FWHM) of each curve. The mean AR values thus obtained differ from those reported in Table 4.3 for the same specimens because the average AR reported in Table 4.3 were calculated dividing the average length by the average thickness also reported in this Table.

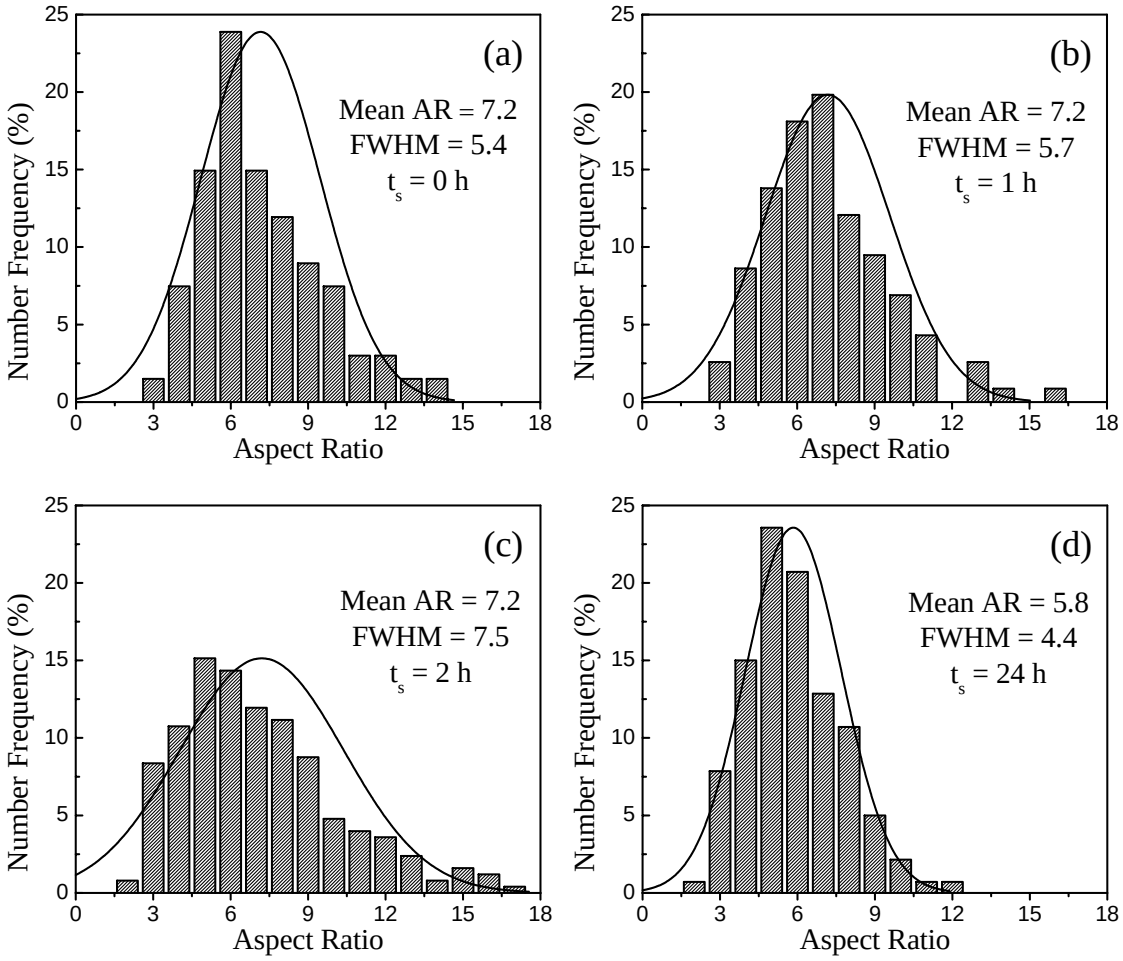

Figure 4.18 Histogram plots of the aspect ratio distribution fitted with a normal distribution (solid curve) corresponding to the large anisometric grains of seeded SBT3Bi5T ceramics pressed at 300 MPa and sintered at 1250 ºC for (a) 0 h, (b) 1 h, (c) 2 h and (d) 24 hours. *AR* is the aspect ratio, *FWHM* is the full-width at half-maximum, and t_s is the sintering time.

In spite of the observed difference between the mean and the average AR, both show a similar behavior with the increasing sintering time, that is, an approximately constant value (mean AR ~ 7.2) until the large grain impingement occurs at ~ 2 hours of sintering time, and then a decrease to ~ 5.8 for 24 hours of sintering time. However, the most important behavior in these distributions is that, in spite of the constant mean AR value

obtained from 0 to 2 hours of sintering time, a considerably broadening of the distribution is observed with the increasing sintering time, which is reflected by the increasing FWHM value from 5.4 for 0 hours to 7.5 for 2 hours of sintering time. This increase in the FWHM value is associated to the intrinsic nucleation and growth of new large grain from the matrix before impingement, resulting in a wider distribution of the AR with increasing sintering time. Finally, the subsequent growth after impingement occurs mainly by grain thickening, resulting now in the narrowing of the distribution for longer sintering times as shown in Fig. 4.18(d) for 24 hours of sintering time.

Figure 4.19 shows two SEM images with small matrix grains between large grains and having face-to-face contact in seeded SBT3Bi5T specimens pressed at 300 MPa and sintered at 1250 ºC for 0 and 2 hours. This grain alignment may have been originally induced by the pressing process itself or, as proposed by Watanabe *et al.*[14] in bismuth titanate textured ceramics, by the rearrangement of the small matrix grains. It is suggested that the aligned templates induce the alignment of the matrix grains by rotation during the early stage of the TGG process. Those small grains that are situated close to the templates rotate to share the low-energy surface, that is, the major surface, thus influencing the rotation of other matrix grains that are farther from the template interface, as pointed out by Horn *et al.*[5] Recently, Sakuma *et al.*[15] have demonstrated this mechanism of matrix grain rearrangement assisted by templates with different composition and crystal structure from that of the matrix powder in BLSF materials. Sato *et al.*[16] reported as well a similar effect in β-SiC materials, where two contacting grains showing a small difference in their orientations readjusted to the same orientation and bonded to form an elongated grain.

The previously discussed results concerning (i) the effect of the presence of Bi_2O_3 excess as liquid phase, (ii) the effect of the increasing sintering temperature, and (iii) the effect of the increase of the uniaxial pressure indicate that the template alignment and the liquid phase characteristics are important parameters governing the nucleation of secondary anisometric grains from the matrix. The higher uniaxial pressure (300 MPa) combined with a suitable amount of Bi_2O_3 excess (3 wt%) and sintering temperature (1250 ºC) seemed to be the best experimental conditions for improving the initial template alignment and induce the matrix grain rearrangement, which, assisted by a liquid phase of adequate viscosity, allowed the nucleation of new large anisometric grains. These findings

are in line with the proposals of Hong *et al.*[12] for exploring the nucleation of large grains from the matrix in textured mullite, and with the suggestions from Suvaci *et al.*[9] that liquid phase promotes the rearrangement and alignment of the matrix grains in textured alumina.

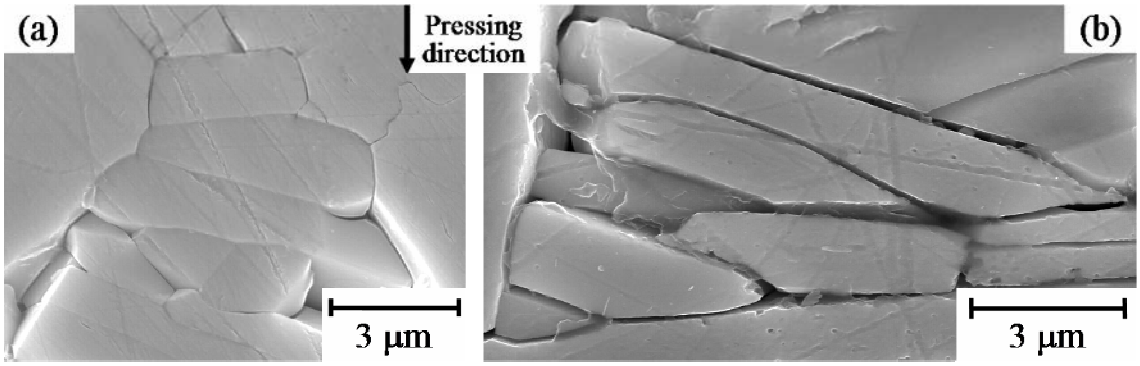

Figure 4.19 SEM micrographs of aligned matrix grains acquired on cross-sections //P of seeded SBT3Bi5T ceramics pressed at 300 MPa and sintered at 1250 ºC for (a) 0 and (b) 2 h.

Kinetics of templated grain growth

As mentioned above, the kinetics of grain boundary migration in TGG is increased by introducing a liquid phase in the template boundary. In most cases of TGG, the template growth has been suggested to be controlled by a mechanism of mass transport by diffusion through the liquid phase,[4,10,17] *i.e.*, the polycrystalline matrix grains are dissolved and then deposited on the lowest energy surface of the templates.[1] To access the rate-controlling process for template grain growth, that is, whether it is controlled by diffusion through the liquid phase or by the interfacial reaction at the solid/liquid interface, the magnitude of $R_t^n - R_o^n$ (where R_t and R_o are the average template radii at time t and zero, respectively, and n is the growth exponent that determines the governing grain growth law)[18] must be plotted against the sintering time. Lay reported the cubic growth kinetics for diffusion-controlled grain growth in the presence of a liquid phase, using the following equation,[19]

$$R_t^3 - R_o^3 = 1.05 K_m \, t_s \tag{4.2}$$

where K_m is the growth kinetic constant at a given sintering temperature and t_s is the sintering time. This cubic law was observed to be independently fulfilled by the length (L) and by the thickness (T) of the large anisometric grains, in the seeded SBT3Bi5T ceramics uniaxially pressed at 300 MPa and sintered at 1250 ºC in the sintering time period between

0 and 2 h, before template impingement, as shown in Fig. 4.20. Error bars displayed in the plots were calculated from the standard deviation in each case and the correlation coefficients for the fit of the length and the thickness were 0.98 and 0.99, respectively. For longer sintering times the model did not fit the cubic law due to template impingement.

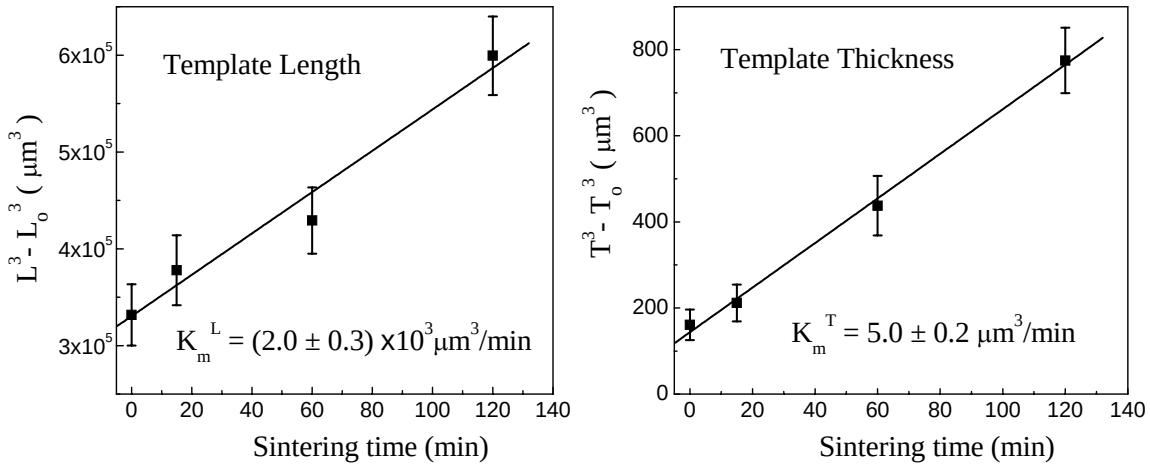

Figure 4.20 Growth of the large anisometric grains: (a) Length and (b) Thickness follow a cubic rate law for seeded SBT3Bi5T ceramics pressed at 300 MPa and sintered at 1250 ºC from 0 to 24 hours. K_m is the growth kinetic constant.

The value of the length growth kinetic constant is $K_m^L = 2.0 \times 10^3$ μm^3/min, being of the same order of magnitude of that reported for textured alumina and PMN-PT crystals.[4,17] On the other hand, the thickness growth kinetic constant K_m^T is three orders of magnitude smaller (5.0 μm^3/min) in this sintering time period. The fulfillment of the Lay´s law by both the length and the thickness growth suggests that the mechanism for the growth of the large anisotropic grains in seeded SBT textured ceramics is controlled by mass diffusion through the liquid phase medium.

It is worth noting that for a diffusion-controlled template growth in the presence of liquid phase, the viscosity of the liquid phase constrains the mass transfer processes. Therefore, this mechanism is in a good agreement with the observed increase in the volume fraction of large anisometric grains in seeded SBT3Bi5T pressed at 150 MPa when increasing the sintering temperature from 1150 to 1250 ºC, since the resulting decrease of the liquid phase viscosity is expected to speed up the mass transport and thus the rate of grain growth. Nevertheless, it is not safe to unambiguously assign a particular growth

mechanism based simply on the experimental growth exponent and further studies are needed to confirm this mechanism of template growth.[18]

4.3.3. Orientation distribution function and quantitative texture analysis

As mentioned in section 2.5.5, the texture analysis using only the *Lotgering* factor does not provide enough information about the distribution of grain orientation,[20] which can be a key in the understanding of the processing-texture and more important texture-property relationships. In fact, it only reflects the percentage quantity of material with the (00*l*) planes perpendicular to the scanned surface in the XRD experiment, thus, scarce information about the distribution of grain orientation is obtained. On the other hand, if the grain morphology can be correlated with a particular crystallographic direction or plane of the studied material, an orientation distribution of the anisotropic grains stereologically determined can be used to quantify the degree of texture throughout the *r* (*texture factor*) and f_v (*volume fraction* of textured material) parameters.[21,22] Therefore, more important than the degree of texture in piezoelectric materials determined by the *Lotgering* factor is the knowledge of the distribution of grain orientation, since the grains with some small misorientation regarding the texture axis may also contribute to the spontaneous polarization, thus enhancing the ferroelectric properties along a specific direction.

The orientation distribution of large anisotropic grains in seeded SBT3Bi5T ceramics pressed at 300 MPa was obtained from the stereological analysis by measuring the number frequency of large grains with their major axis oriented at a given angle ω with respect to the texture plane, and fitted using the March-Dollase equation described in section 2.5.5 by a least-squares method. In this case, f_v was set equal to 1 in order to quantify the degree of alignment of the large anisotropic grains throughout the *r* parameter (*texture factor*), which is associated with the width of the orientation distribution function. The equation obtained by setting f_v = 1 in the March-Dollase equation (Eq. 2.10) describes the probability distribution function introduced originally by March in 1932 and utilized by Dollase in his later work.[23]

$$F(1, r, \omega) = \left(r^2 \cos^2 \omega + \frac{\sin^2 \omega}{r} \right)^{-\frac{3}{2}} \tag{4.3}$$

The normalization to the unity of the March probability distribution function (Eq. 4.3) was obtained by dividing this equation by its boundary condition at $\omega = 0$, that is,

$$F^N(1,r,\omega) = \frac{\left(r^2\cos^2\omega + \frac{\sin^2\omega}{r}\right)^{-\frac{3}{2}}}{F(1,r,0)} = \frac{\left(r^2\cos^2\omega + \frac{\sin^2\omega}{r}\right)^{-\frac{3}{2}}}{\frac{1}{r^3}} \qquad (4.4)$$

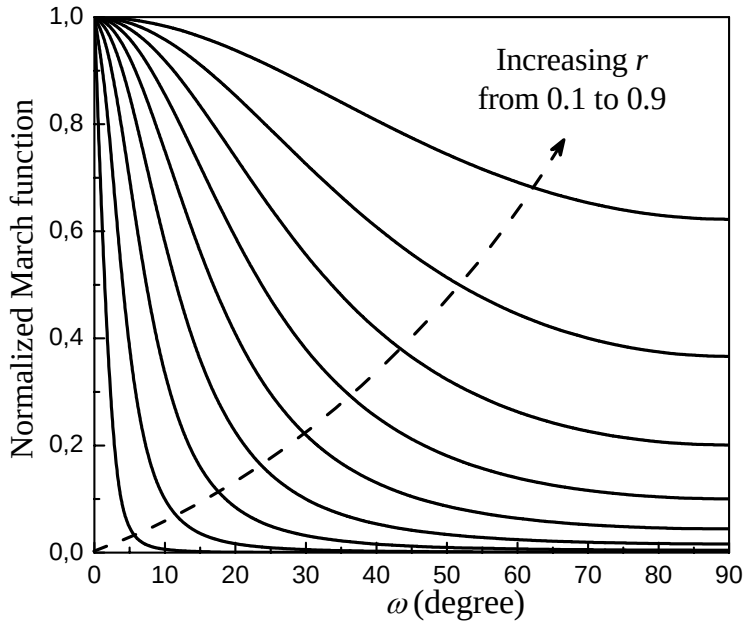

Figure 4.21 Calculated dependence of the normalized March function for different values of the r parameter in the range $0.1 \leq r \leq 0.9$, using Eq. 4.4.

Equation 4.4 was used to fit the normalized orientation distributions of large anisotropic grains. Figure 4.21 shows the ω dependence of this normalized March probability function, F^N, with the value of the r parameter in the range $0.1 \leq r \leq 0.9$. The higher is the texture of the material, the narrower is the orientation distribution and thus the smaller is the r value. For randomly oriented materials, the normalized orientation distribution is equal to the unity for the full range of ω and thus $r = 1$. Highly textured ceramics obtained by TGG have shown r values smaller than 0.2.[22]

Figure 4.22 shows the normalized orientation distribution of large anisometric grains for seeded SBT3Bi5T ceramics uniaxially pressed at 300 MPa and sintered at (a) 1000 ºC for 1 hour (this condition was considered as corresponding to the initial stage of the TGG

process, and thus, this curve describes the orientation distribution of the original templates) and at (b-f) 1250 ºC from 0 to 24 hours of sintering time. Each distribution was normalized to the unity by dividing it by the number frequency of large grains with orientation equal to zero, $\omega = 0$. For each case, a texture factor, *r*, was searched so as to produce the best fitting of the normalized March function (Eq. 4.4) to the experimental values. The March fits to the data are plotted in Fig. 4.22 for each distribution as a solid line, being the correlation coefficients better than 0.99 for all the fits, except for the distribution of original templates [Fig. 4.22(a)] that shows a correlation coefficient above 0.97, demonstrating the suitability of the March-Dollase distribution function for fitting stereologically measurable data.

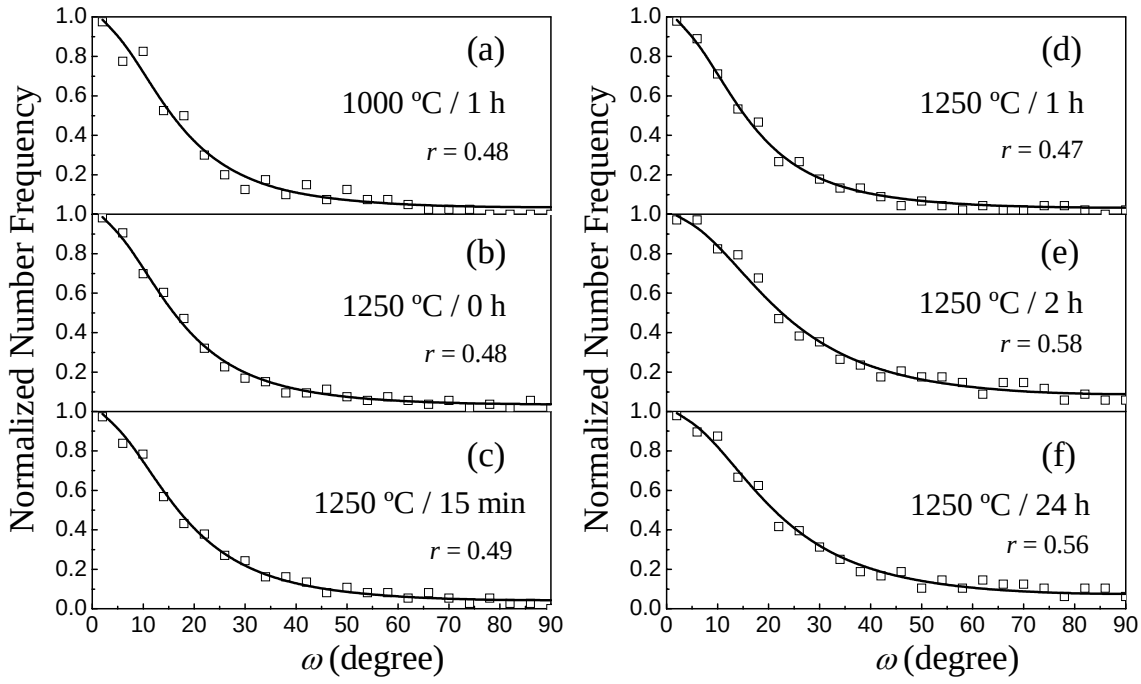

Figure 4.22 Normalized orientation distribution of large anisometric grains and their March fits in seeded SBT3Bi5T ceramics pressed at 300 MPa and sintered at (a) 1000 ºC for 1 hour (original templates) and (b) 1250 ºC for 0 h, (c) 15 min, (d) 1 h, (e) 2 h and (f) 24 hours. Square open symbol stands for the experimental data and solid lines for March fits. ω is the platelet orientation angle.

As expected, the maximum value of the distributions occurs at $\omega = 0$ and the number frequency of large grains drops with increasing ω, reaching 0.2 (that is 5 times lower than the value for $\omega = 0$) at $\omega \sim 30^o$ of the texture axis. Moreover, a noticeable increase in the widths of the profiles occurs when the sintering time increases beyond 1 hour at 1250 ºC. Figure 4.23(a) allows comparing the profiles corresponding to 0 and 2 h of sintering time.

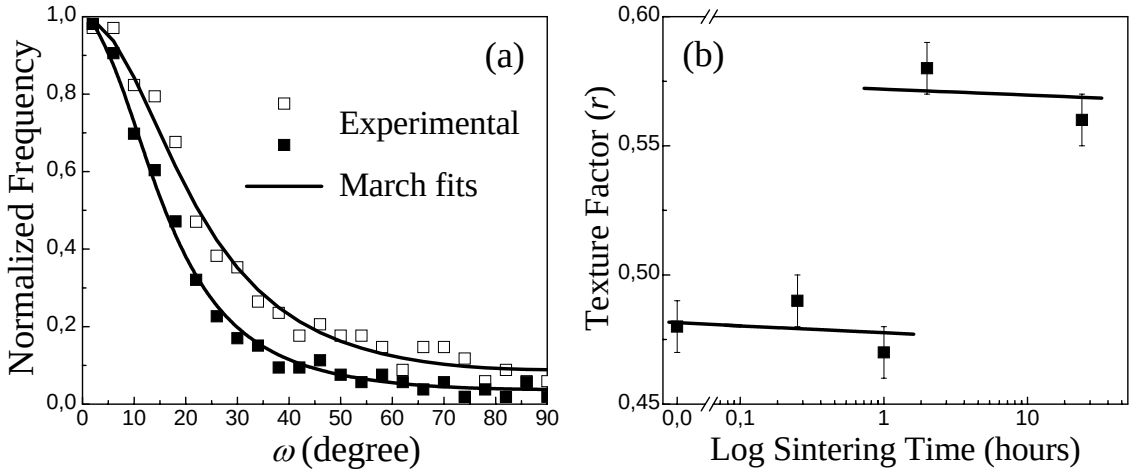

Figure 4.23 (a) Comparison of the width of the normalized orientation distribution of large anisometric grains corresponding to seeded SBT3Bi5T ceramics pressed at 300 MPa and sintered at 1250 ºC during (■) 0 h and (□) 2 h (the solid lines represent March fits). (b) Texture factor (*r*) as a function of the logarithm of the sintering time.

Figure 4.23(b) shows the *r* values of seeded SBT3Bi5T ceramics uniaxially pressed at 300 MPa and sintered at 1250 ºC as a function of the sintering time. A step increase of the *r* value from ~ 0.49 for short sintering times to ~ 0.58 for 2 and 24 hours of sintering times is clearly observed. For the specimen sintered at 1000 ºC for 1 hour, which was considered as the initial stage of the TGG process and where the distribution is associated to the original templates, the value obtained for the texture factor was $r = 0.48$, very close to that obtained for the specimens sintered at 1250 ºC from 0 to 1 hour. Thus, within this range of sintering times the degree of orientation of large grains remains approximately constant. The relatively high *r* values obtained in the present work reflect mainly the effectiveness of the used processing technique for template alignment. It is believed that an *r* value improvement will be achieved by using other more complex texturing techniques.

If texture development during TGG was controlled only by the growth of the templates throughout the matrix, consuming the small and randomly oriented grains, as primarily proposed by Messing *et al*. in many other systems,[11,13,22] then a nearly constant *r* value should be obtained for the different sintering times, being the texture factor of the sintered specimens the result of the original templates texture factor. The sudden increase in the texture factor for 2 or more hours of sintering time is probably related with the nucleation and growth of the new large grains in the final stage of the TGG process, as discussed in the previous section 4.3.2. Nevertheless, some experimental aspects, such as

the lower size limit and the AR condition for selecting a measurable large grain, need to be taken into account in this method in order to have a more accurate result.

4.4. Dielectric and Ferroelectric Properties

4.4.1. Dielectric characterization

Unseeded SBT ceramics

Figure 4.24(a) shows the temperature dependence of dielectric permittivity upon heating for several frequencies (from 1 kHz to 1 MHz) obtained for the unseeded SBT3Bi ceramic sintered at 1250 ºC for 2 h. The maximum of dielectric permittivity corresponding to the ferroelectric-paraelectric phase transition is clearly observed at $T_m \approx 300$ ºC, in a good agreement with previous reports on stoichiometric SBT ceramics.[24,25] Small thermal hysteresis of about 1 ºC were observed in the permittivity curves upon heating and cooling, as shown in the inset of Fig. 4.24(a) for 1 and 10 kHz, which is within the experimental error. Figure 4.24(b) shows the temperature dependence of the dielectric losses ($\tan\delta$) upon heating in the same frequency range, where the peak corresponding to the ferroelectric-paraelectric phase transition is only visible at 1 MHz [see inset of Fig. 4.24(b)]. The temperature of $\tan\delta$ peak is also obtained at $T_m \approx 300$ ºC, with dielectric losses lower than 0.02 from room temperature up to 400 ºC at 1 MHz.

SBT is believed to belong to the displacive-type ferroelectrics with a near 2nd-order phase transition from paraelectric to ferroelectric state at T_C (Curie temperature), as shown in section 3.2.4. The absence of frequency dispersion at the transition temperature observed in Fig. 4.24(a), together with the matching values of T_m from permittivity and $\tan\delta$ curves as well as the small thermal hysteresis in permittivity, confirms the close to a 2nd-order phase transition in the unseeded SBT ceramics, where T_m can be estimated to be close to T_C. Similar behavior of the temperature dependences of dielectric permittivity and losses for several frequencies (from 1 kHz to 1 MHz) were obtained for all the unseeded SBT specimens under different sintering conditions, which are summarized in Table 4.4.

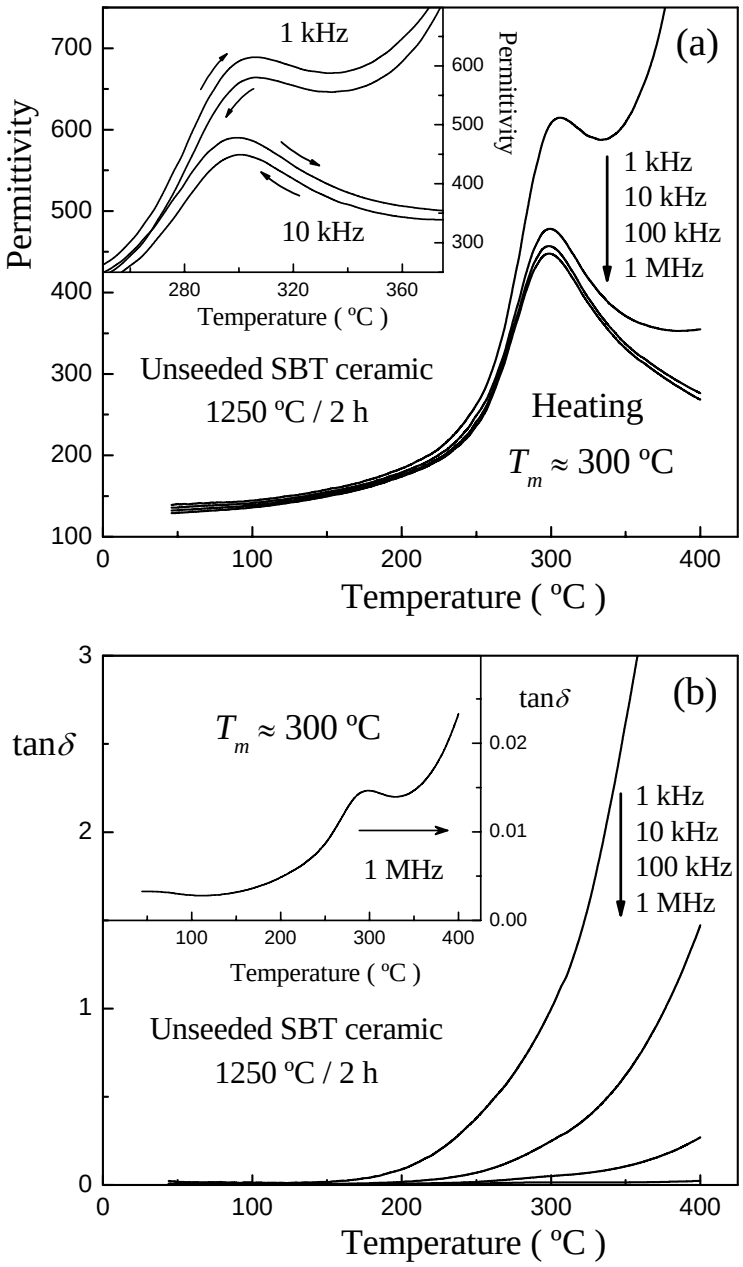

Figure 4.24 Temperature dependence of (a) dielectric permittivity and (b) dielectric losses (tanδ) upon heating for several frequencies (from 1 kHz to 1 MHz as indicated by the arrows) for the unseeded SBT3Bi ceramic sintered at 1250 ºC for 2 hours. The inset in (a) shows the thermal hysteresis upon heating and cooling for 1 and 10 kHz, and in (b) gives the tanδ peak at 1 MHz corresponding to the ferroelectric phase transition.

The room temperature and maximum permittivities for 10 kHz are around 135 and 480, respectively, with dielectric losses lower than 0.02, for most of the samples, except for the unseeded SBT3Bi specimen sintered at 1250 ºC for 24 hours whose maximum permittivity decreases to ~ 400. As previously referred, the long sintering process of the

sample at 1250 ºC is followed by some bismuth losses which are known to deteriorate dielectric properties. The unseeded SBT specimen sintered at 1250 ºC for 2 hours will be used as a reference for further comparison with the textured seeded SBT ceramics.

Table 4.4 Results from the dielectric characterization of unseeded SBT3Bi ceramics for different sintering conditions. T_m is the transition temperature obtained from the permittivity curve, the dielectric permittivity (ε_r) is reported at room temperature (RT) as well as at T_m (maximum permittivity) at 10 kHz, and the dielectric loss ($\tan\delta$) is reported at T_m (1 MHz).

Sintering Temperature (ºC)	Sintering Time (hours)	T_m (ºC)	ε_r (10 kHz)		$\tan\delta$ at T_m (1 MHz)
			RT	Maximum	
1150	2	320	140	495	0.014
1150	24	317	130	475	0.018
1250	2	300	135	480	0.015
1250	24	293	130	405	0.020

The small downwards shift of the transition temperature with increasing sintering temperature and time, *i.e.*, from 320 ºC (1150 ºC / 2 h) to 300 ºC (1250 ºC / 2 h) and to 293 ºC (1250 ºC / 24 h) may be ascribed to different degree of internal stresses in the fine-grained ceramics, which develop during cooling down from the sintering temperature and affect the intrinsic properties of ferroelectric materials.[26] These internal stresses are related to the grain size and grain distributions, as well as to the formation of 90º domains.[27] Similar grain-size effect on the Curie temperature has been reported in other ferroelectric systems.[27-29] Moreover, for the samples sintered at 1250 ºC, it is believed that compositional fluctuations and the bismuth loss due to long sintering times and high sintering temperature may also contribute for this T_m shift. This discussion will be further resumed for the analysis of the seeded SBT specimens.

Figure 4.25 shows the linear relationship between the inverse permittivity (at 1 MHz) and temperature, above and below T_m, in the unseeded SBT3Bi ceramic sintered at 1250 ºC for 2 hours. The permittivity curve at 1 MHz was selected for this study since it is the one having the lower contribution from the low frequency dispersion above T_m up to 400 ºC, as observed in Fig. 4.24(a). This linear relationship in the proximity of T_m is known as the Curie-Weiss law previously described in section 1.2.3 (Eq. 1.7), which is satisfied in most

(non-relaxor) ferroelectrics. The Curie constant was determined from the slope of the straight line above T_m (C = 5.5 × 10^4 ºC) while T_{CW} was ~ 175 ºC. It is worth noting that the C value is similar to that reported in section 3.2.4 for SBT single crystal. On the other hand, the slope of 1/ε(T) dependence below T_m is approximately two times greater than that above T_m, which is also characteristic of a 2nd-order phase transition. Similar results were obtained in all unseeded SBT specimens.

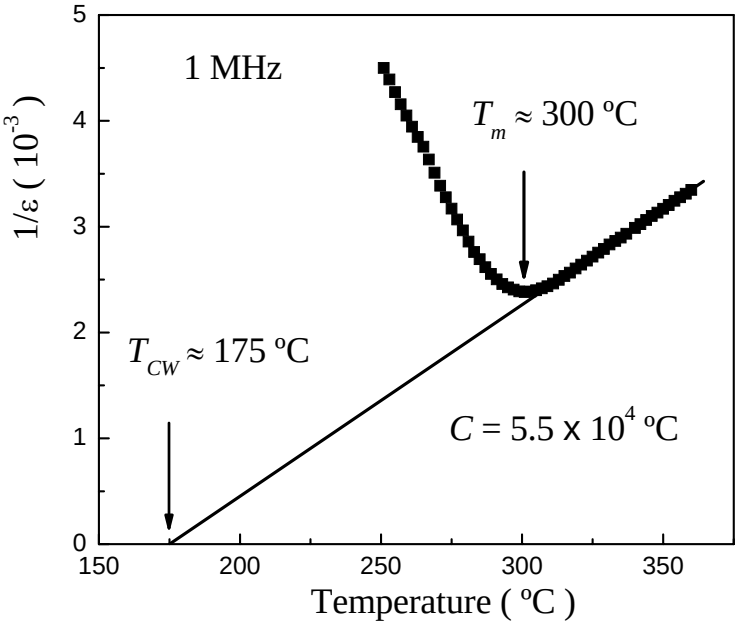

Figure 4.25 Temperature dependence of the inverse dielectric permittivity near T_m at 1 MHz, in the unseeded SBT3Bi ceramic sintered at 1250 ºC for 2 hours. C is the Curie constant, T_m is the transition temperature and T_{CW} is the Curie-Weiss temperature.

Seeded SBT ceramics

The dielectric characterization of the seeded SBT3Bi5T ceramics is discussed for the samples uniaxially pressed at 300 MPa, since they demonstrated the highest texture. Figure 4.26 shows the temperature dependence of permittivity for several frequencies upon heating for seeded SBT3Bi5T ceramics sintered at 1250 ºC for 0 and 24 hours, when the electric field is applied parallel to the pressing direction (E//P), *i.e.*, perpendicular to the favorable direction of polarization. For comparative purposes, the curve obtained for the unseeded SBT3Bi ceramic sintered at 1250 ºC for 2 hours is also included.

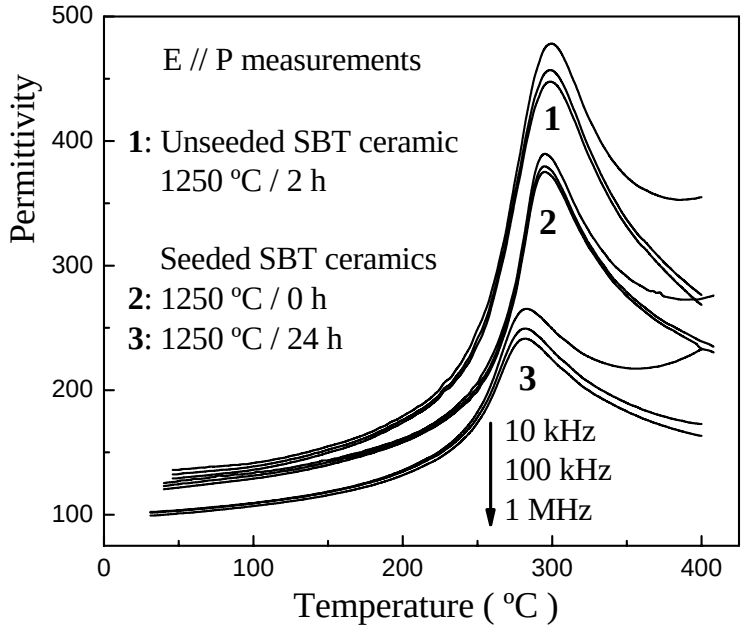

Figure 4.26 Temperature dependence of dielectric permittivity for several frequencies (from 10 kHz to 1 MHz as indicated by the arrows) for the unseeded SBT3Bi ceramic sintered at 1250 ºC for 2 hours and the seeded SBT3Bi5T ceramic sintered at 1250 ºC for 0 and 24 h, when the electric field is applied parallel to the pressing direction (E//P).

The unseeded SBT ceramic exhibit room temperature and maximum permittivities at 10 kHz of ~ 135 and ~ 480, respectively, while the transition temperature was at 300 ºC as mentioned before. When increasing the sintering time at 1250 ºC, the room temperature and maximum permittivities at 10 kHz of the seeded SBT3Bi5T samples decrease from ~ 125 and ~ 390 for 0 hours to ~ 100 and ~ 265 for 24 hours of sintering time, respectively, followed by a downwards shift of the transition temperature from 295 ºC to 282 ºC (see also Table 4.5). The decrease observed in the peak of dielectric permittivity is related to the improvement of the degree of texture of the seeded SBT ceramics with increasing sintering time. The contribution from the highly polarizable *ab*-plane of the plate-like grains diminishes due to the favorable alignment of large anisometric grains with their major face (crystallographic *ab*-plane of the SBT structure) perpendicular to the applied electric field.

It must be referred that, as observed in unseeded ceramics, the thermal hysteresis in the permittivity curves upon heating and cooling for seeded SBT3Bi5T specimens was also ~ 1 ºC. Moreover, no significant frequency dependence of the transition temperature was observed in all the seeded SBT samples, being the behavior of the temperature dependence of permittivity for several frequencies (from 1 kHz to 1 MHz) very similar for all the cases.

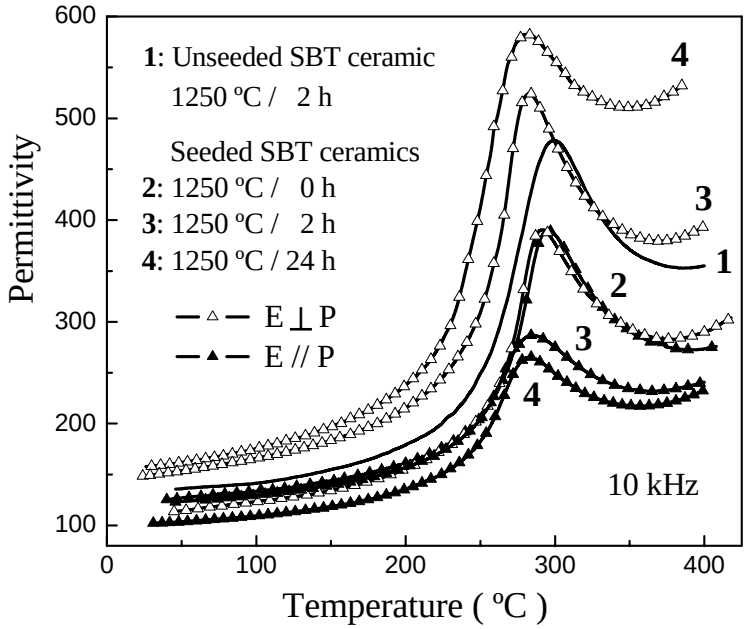

Figure 4.27 Anisotropy in the temperature dependence of the dielectric permittivity at 10 kHz, measured with E//P and E⊥P, for seeded SBT3Bi5T ceramics sintered at 1250 ºC for 0, 2 and 24 hours. For comparison, the dielectric curve at 10 kHz for the unseeded SBT3Bi ceramic sintered at 1250 ºC for 2 hours is also included.

Figure 4.27 compares the temperature dependence of permittivity at 10 kHz obtained in seeded SBT3Bi5T samples sintered at 1250 ºC for 0, 2 and 24 hours, when the electric field is applied parallel (E//P) and perpendicular (E⊥P) to the pressing direction. For comparison, the dielectric curve for the unseeded SBT3Bi ceramic sintered at 1250 ºC for 2 hours is also included in the plot. Anisotropy in the dielectric permittivity at room temperature as well as at the transition temperature can be observed in the seeded SBT samples (see also Table 4.5). This anisotropy is scarcely evident in the seeded SBT samples sintered during 0 h, whose curves (measured with E//P and E⊥P) stay below that of the unseeded SBT sample. However, when the sintering time increases to 2 h and to 24 h, the anisotropy becomes strongly enhanced due to the increasing degree of texture, *i.e.*, for 24 h of sintering time the room temperature and maximum permittivities increase from ~ 100 and ~ 265 to ~ 160 and ~ 580 when measured with E//P and E⊥P, respectively.

The permittivity value obtained for the seeded SBT ceramic sintered at 1250 ºC for 2 and 24 hours (measured with E⊥P) exceeds those of the unseeded one which are roughly isotropic, not depending on the direction of the applied electric field. In the case of seeded samples, there is a positive contribution from the highly polarizable *ab*-plane of the plate-

like grains, due to the favorable alignment of the large anisometric grains with their major faces (crystallographic *ab*-plane) parallel to the applied electric field.

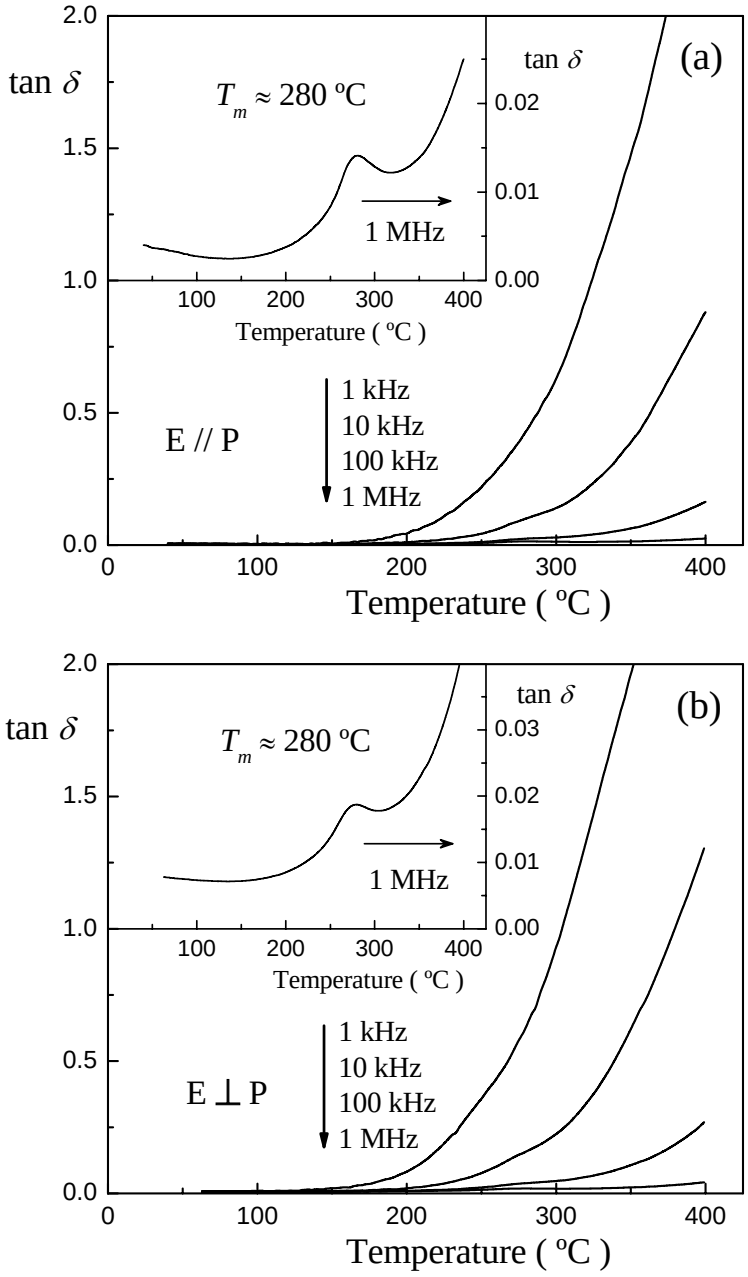

Figure 4.28 Temperature dependence of dielectric loss (tanδ) upon heating for several frequencies (from 1 kHz to 1 MHz as indicated by the arrows), measured with (a) E//P and (b) E⊥P, for seeded SBT3Bi5T ceramics sintered at 1250 ºC for 2 h. The inset gives the tanδ peak at 1 MHz in both cases, which corresponds to the ferro-paraelectric phase transition.

Figure 4.28 shows the temperature dependence of dielectric losses (tanδ) for several frequencies (from 1 kHz to 1 MHz) when the electric field is applied (a) parallel (E//P) and (b) perpendicular (E⊥P) to the pressing direction, for the seeded SBT3Bi5T ceramic sintered at 1250 ºC during 2 hours. Once again, the peak corresponding to the ferroelectric-paraelectric phase transition can be only observed at 1 MHz [see insets in Fig. 4.28], as already referred in the unseeded ceramics. However, in the case of seeded ceramics, the temperature corresponding to tanδ peak is observed at $T_m \approx 280$ ºC, which is around 3 to 5 ºC lower than the value obtained from permittivity measurements in this sample (see also Table 4.5). Similar temperature dependences of the dielectric loss for several frequencies (from 1 kHz to 1 MHz) were obtained in all the seeded SBT specimens.

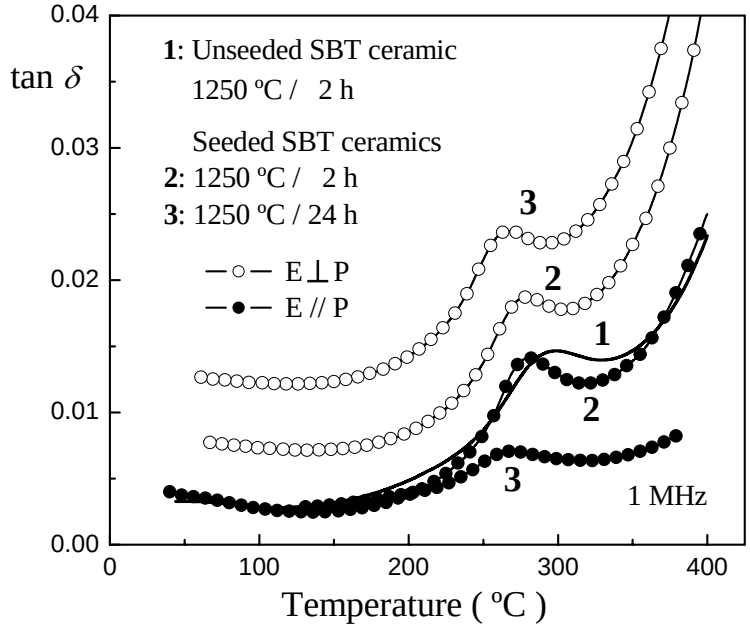

Figure 4.29 Anisotropy in the temperature dependence of the dielectric loss (tanδ) at 1 MHz, measured with E//P and E⊥P, for seeded SBT3Bi5T ceramics sintered at 1250 ºC for 2 and 24 hours. For comparison, the tanδ curve for the unseeded SBT3Bi ceramic sintered at 1250 ºC for 2 hours is also included.

The anisotropy in tanδ curve at 1 MHz for seeded SBT3Bi5T ceramic sintered at 1250 ºC for 2 and 24 h, when the electric field is applied parallel (E//P) and perpendicular (E⊥P) to the pressing direction is better observed in Fig. 4.29. For comparison, the curve corresponding to the unseeded SBT3Bi specimen sintered at 1250 ºC for 2 hours is also included in this plot. As observed in permittivity data, the temperature of tanδ peak also

decreases with increasing sintering time. In addition, the anisotropy of the dielectric loss at room temperature as well as at the transition temperature can be observed in the seeded samples. The higher losses were obtained when measurements were performed with E⊥P due to the higher conductivity in the *ab*-plane of the BLSF materials,[30,31] while the lower losses were obtained with E//P, because in this case the Bi_2O_2 layers are perpendicular to the electric field direction.

Table 4.5 summarizes the results of the dielectric characterization of the seeded SBT3Bi5T specimens obtained under different pressing and sintering conditions, when the electric field is applied parallel (E//P) and perpendicular (E⊥P) to the pressing direction. The anisotropy in the average room temperature and maximum permittivities, as well as in the dielectric losses, can be clearly observed. This anisotropy is greater in the samples with a higher uniaxial pressure because these samples showed a higher degree of texture.

Table 4.5 Results from the dielectric characterization of seeded SBT3Bi5T ceramics uniaxially pressed at 150 and 300 MPa for different sintering conditions, and measured with the electric field applied parallel (E//P) and perpendicular (E⊥P) to the pressing directions. T_m is the transition temperature obtained from the permittivity curves, dielectric permittivity (ε_r) is reported at room temperature (RT) as well as at T_m (maximum permittivity) at 10 kHz, and dielectric looses (tanδ) are reported at T_m (1 MHz).

Sintering Temperature (ºC)	Sintering Time (hours)	T_m (ºC)		ε_r (10 kHz)				tanδ at T_m (1 MHz)	
				RT		Maximum			
		E // P	E ⊥ P	E // P	E ⊥ P	E // P	E ⊥ P	E // P	E ⊥ P
Pressure 150 MPa									
1150	24	298	300	125	128	412	512	0.012	0.014
1250	24	288	290	110	145	288	560	0.016	0.027
Pressure 300 MPa									
1250	0	295	292	125	115	390	390	0.015	0.014
1250	0.25	294	293	120	122	375	405	0.016	0.017
1250	1	290	289	115	135	340	430	0.015	0.016
1250	2	285	283	118	150	285	525	0.014	0.019
1250	24	282	281	100	160	265	582	0.007	0.024

The downwards shift of the transition temperature with the increase of the sintering time is observed again, *i.e.*, $T_m \approx 295$ ºC for the sample sintered at 1250 ºC during 0 h, but decreases to 282 ºC after 24 hours (Table 4.5). Moreover, the seeded sample sintered at 1250 ºC for 2 h has $T_m \approx 285$ ºC, which is 15 ºC lower than the value obtained for the unseeded sample ($T_m \approx 300$ ºC) sintered under the same conditions (Table 4.4). This result agrees with a grain-size dependence of the transition temperature, that is, in seeded SBT ceramics stresses develop during the TGG process and become stored in the impinged large anisometric grains. Such internal stresses in the impinged large grains increase the free energy of the ferroelectric phase, thus decreasing the transition temperature.[28]

4.4.2. Ferroelectric characterization

The ferroelectric characterization of the seeded SBT3Bi5T ceramics was performed on the specimens uniaxially pressed at 300 MPa, since they demonstrated the highest texture and anisotropy in the dielectric properties. Figure 4.30 shows the room temperature P-E hysteresis loops (at 50 Hz) using progressively increasing applied electric fields (E_m), for the seeded SBT3Bi5T ceramic sintered at 1250 ºC for 2 hours and measured with the electric field applied parallel (E//P) and perpendicular (E⊥P) to the pressing direction. Anisotropy in the hysteresis loops can be clearly observed by comparing the two plots as well as the values of remanent (P_r) and spontaneous (P_S) polarizations along both directions, which are also reported in the figure for the loops obtained with $E_m \approx 150$ kV/cm (see also Table 4.6). The coercive field was the same in both cases, $E_C = 26$ kV/cm.

Figure 4.31 shows the dependence of P_r and P_S with the applied electric field (at 50 Hz), obtained from progressive hysteresis loops, when the electric field is applied parallel (E//P) and perpendicular (E⊥P) to the pressing direction. Once again, the anisotropy in the P_r and P_S values can be clearly seen in this plot, although, it should be noted that none of the two parameters is saturated for a maximum applied electric field of 150 kV/cm, which exceeds more than five times the coercive field of this sample. In addition, further increase of the applied electric field beyond this maximum value gives rise to the electrical breakdown in most of the samples.

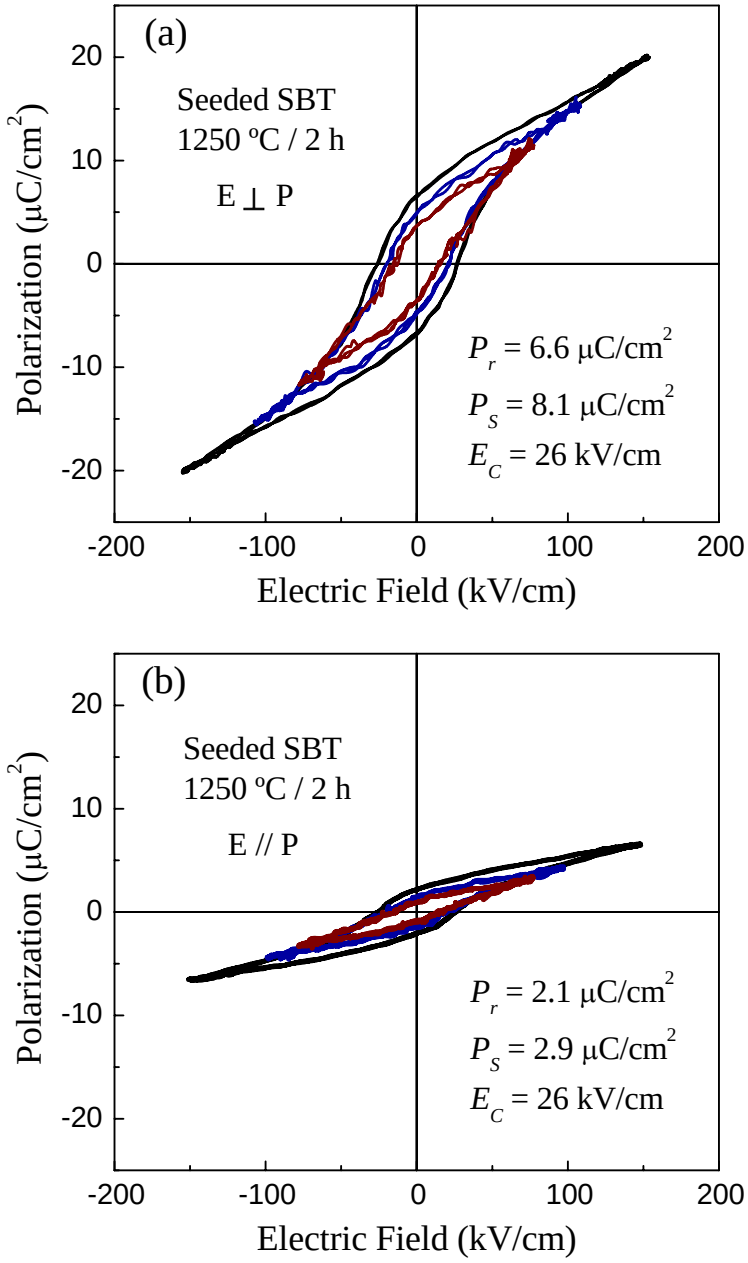

Figure 4.30 Room temperature P-E hysteresis loops measured with (a) E⊥P and (b) E//P for a maximum applied electric field of 150 kV/cm in seeded SBT3Bi5T ceramics sintered at 1250 ºC for 2 hours. The values for the remanent (P_r) and the spontaneous (P_S) polarization as well as the coercive field (E_C) obtained from the hysteresis loop at 150 kV/cm are included in both cases.

Similar dependences of P_r and P_S values on the applied electric field (at 50 Hz) until $E_m \approx 150$ kV/cm have been obtained for all the seeded SBT samples measured with both applied field configurations, that is, E//P and E⊥P. Figure 4.32 shows a comparison of the room temperature P-E hysteresis loops at $E_m \approx 150$ kV/cm for the seeded SBT3Bi5T

ceramics sintered at 1250 ºC for different sintering times and measured with E//P and E⊥P. For comparison, the loop obtained for the unseeded SBT3Bi ceramic sintered at 1250 ºC for 2 hours is also included in the three graphs. The textured samples show a strong anisotropy in the hysteresis loops when measured with E//P and E⊥P, which is higher for the specimens with higher degree of texture, *i.e.*, those sintered during 2 and 24 hours.

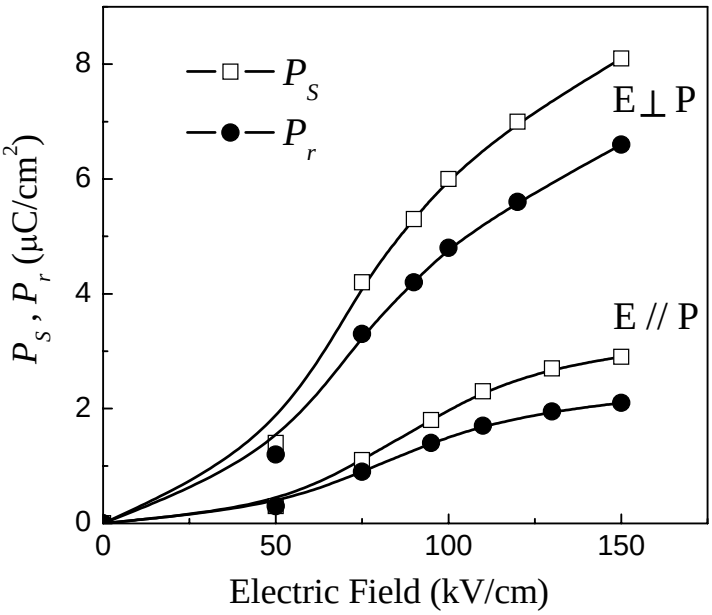

Figure 4.31 Dependence of the remanent (P_r) and the spontaneous (P_S) polarization on the electric field, when it is applied parallel (E//P) and perpendicular (E⊥P) to the pressing direction, in the seeded SBT3Bi5T ceramic sintered at 1250 ºC for 2 hours.

The polarization vector in the SBT orthorhombic structure lies entirely along the *a*-axis.[32] Accordingly, the observed increase of P_S and P_r values for the textured ceramics when E⊥P is used, may be explained as an increased contribution from the highly polarizable *ab*-plane allowed by the favorable alignment of the large anisometric grains with their major faces (crystallographic *ab*-plane) parallel to the applied electric field. This contribution is expected to further increase with the ceramic degree of texture. For the sample where E//P, the above mentioned contribution is partly lost and the permittivity and polarization values decreases.

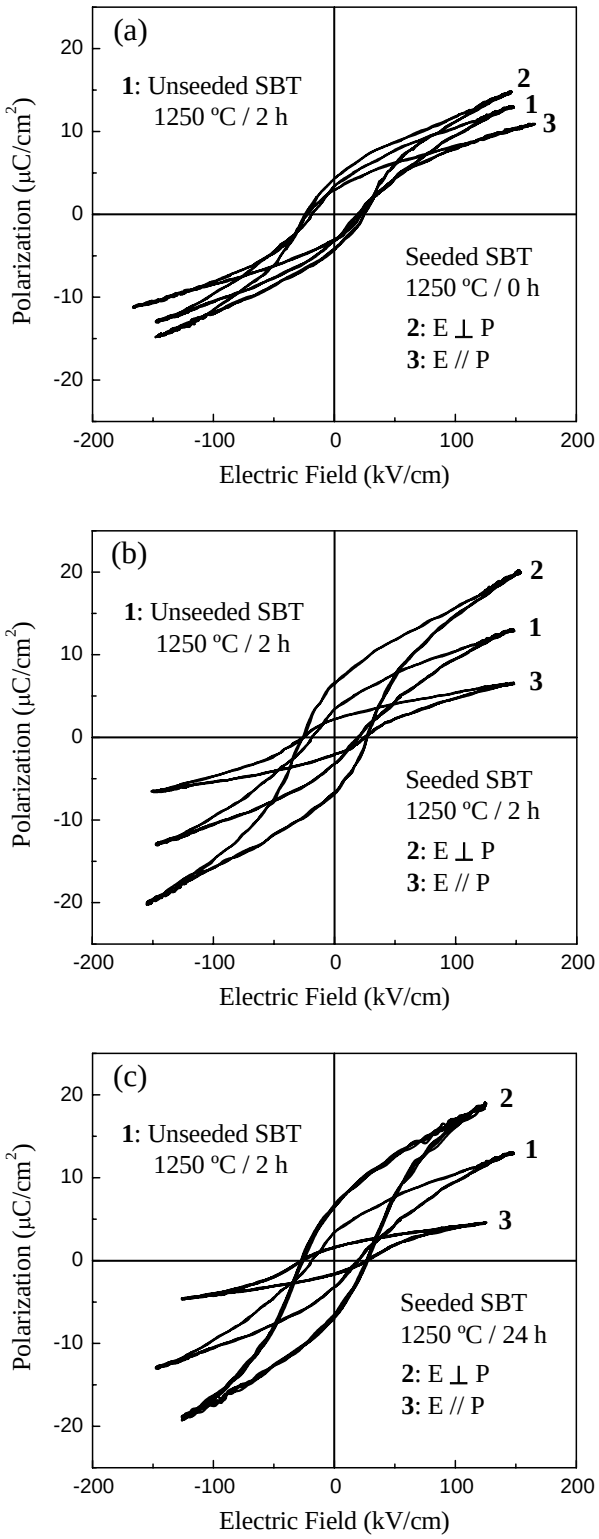

Figure 4.32 Room temperature P-E hysteresis loops obtained at $E_m \approx 150$ kV/cm with E⊥P and E//P in seeded SBT3Bi5T ceramics sintered at 1250 ºC during (a) 0, (b) 2 and (c) 24 h. The hysteresis loop obtained for the unseeded SBT3Bi ceramic sintered at 1250 ºC for 2 h is also included for comparison.

Table 4.6 summarizes the results of the ferroelectric characterization for the seeded SBT3Bi5T specimens sintered at 1250 ºC from 0 to 24 hours, when the electric field is applied parallel (E//P) and perpendicular (E⊥P) to the pressing direction. The results for the unseeded SBT3Bi ceramic sintered at 1250 ºC for 2 hours are also included.

The permittivity for high electric fields, ε^E, was determined from the slope of the linear segment that back to the polarization axis in the P-E hysteresis loop at high electric fields [dashed line in Fig. 1.6(a)] and using the Eq. 1.8, as described in the section 1.2.5. As mentioned in that section, at very low as well as at very high electric fields, when all the domains have switched in the direction of the electric field, the material behaves like an ordinary dielectric and the permittivity obtained from the P-E hysteresis loop must be similar to that obtained from dielectric measurements at room temperature using the same frequency. The high ε^E values obtained for $E_m \approx 150$ kV/cm with both configurations, E//P and E⊥P, being far above the permittivity values obtained from dielectric measurements at room temperature (see Table 4.5), also indicate that polarization from the hysteresis loops was not saturated. It should be mentioned that even when dielectric measurements were performed from 1 kHz to 1 MHz (far above the 50 Hz used in the P-E hysteresis loops), the frequency dispersion of room temperature permittivity is too weak for predicting ε_r values (at 50 Hz) comparable with the ε^E values determined from the hysteresis loops.

The anisotropy in the P_r, P_S and ε^E values measured at $E_m \approx 150$ kV/cm can be also observed in Table 4.6 when the degree of texture of seeded SBT3Bi5T ceramics increases. These parameters become enhanced for E⊥P but decrease if E//P, due to the opposite contribution from the highly polarizable *ab*-plane for these two cases. On the other hand, the coercive field does not show anisotropy when measured parallel and perpendicular to the pressing direction, but it increases from 20 to 27 kV/cm with the increasing sintering time. It is important to emphasize that the E_C obtained for the unseeded SBT3Bi specimen (20 kV/cm) is very close to that obtained in SBT single crystals (see section 3.2.4). The maximum P_S of 8.9 μC/cm^2 measured with E⊥P for 24 h of sintering time is still far from the value estimated for the SBT single crystal in section 3.2.4 ($P_S \approx 20$ μC/cm^2).

Table 4.6 Results from the room temperature P-E hysteresis loops measured with the electric field applied parallel (E//P) and perpendicular (E⊥P) to the pressing directions in the unseeded SBT3Bi ceramic sintered at 1250 ºC for 2 h and seeded SBT3Bi5T ceramics pressed at 300 MPa and sintered at 1250 ºC from 0 to 24 h. P_r and P_S are the remanent and spontaneous polarization, respectively, E_C is the coercive field, and ε^E is the permittivity under high electric field, all reported for a maximum electric field of E_m = 150 kV/cm.

Sintering Temperature (ºC)	Sintering Time (hours)	P_r (μC/cm^2)		P_S (μC/cm^2)		E_C (kV/cm)		ε^E	
		E // P	E ⊥ P	E // P	E ⊥ P	E // P	E ⊥ P	E // P	E ⊥ P
Unseeded SBT3Bi									
1250	2	3.3		5.3		20		590	
Seeded SBT3Bi5T									
1250	0	3.1	4.2	4.2	5.4	22	24	470	700
1250	0.25	2.9	4.5	4.0	5.6	23	23	425	762
1250	1	2.8	4.9	4.0	5.9	23	24	386	790
1250	2	2.1	6.6	2.9	8.1	26	26	280	876
1250	24	1.6	7.0	2.1	8.9	27	27	225	950

These results indicate that dielectric and ferroelectric properties are considerably improved in the textured SBT ceramics when measured with E⊥P, as compared to the unseeded SBT samples, and that highly anisotropic properties can be thus achieved. Next section is focused on the prediction of the texture - property relationships in BLSF materials, especially in textured SBT ceramics.

4.5. Texture - Property Relationships in BLSF materials

The final section of this chapter is devoted to describe the spatial distribution of the polarization vector for both randomly oriented and textured BLSF materials, so as to predict the corresponding theoretical spontaneous polarization. This quantitative model uses the texture analysis accomplished via the orientation distribution function, described in section 4.3.3, for the calculation of the expected P_S as a function of the degree of texture.

4.5.1. Theoretical approach

It is well known that piezoelectric properties of ferroelectric materials depend on the orientation of the spontaneous polarization relative to the direction of the applied electric field, and thus can not be fully exploited in randomly oriented polycrystalline materials. For instance, in uniaxial ferroelectrics where the polarization vector (*P*) is confined to one axis and only two antiparallel domain states are allowed (180º Domain Wall Switching or DWS), the net polarization for a randomly oriented ceramic under the application of a poling electric field along a specific direction is obtained by averaging over the available spatial distribution of the polarization vector of each grain in the semi-sphere of solid angle 2π around the direction of the electric field (*z*-axis), as schematically illustrated in Fig. 4.33(a).[33] In this case, the spatial distribution of polarization for misoriented grains can be expressed as $P_o \cos\theta$, where P_o is the spontaneous polarization of each grain (which is assumed to be a single crystal) and θ is the angle between P_o and the electric field direction. Thus, the net polarization along the *z*-axis is given by (in spherical coordinates),

$$\langle P \rangle_{random} = \frac{\int_0^{\frac{\pi}{2}} P_o \cos\theta \left(\sin\theta \, d\theta\right)}{\int_0^{\frac{\pi}{2}} \sin\theta \, d\theta} = \frac{P_o}{2} \tag{4.5}$$

However, in BLSF materials the polarization is basically confined to a plane, allowing not only two antiparallel domain states (180º DWS) but also two perpendicular domain states in the plane (90º DWS).[34] Takenaka *et al.*[34] have calculated for the first time the expected polarization for perfectly textured and randomly oriented $Bi_4Ti_3O_{12}$ ceramics, considering two configurations of domain wall switching, that is, only 180º DWS and both 180º and 90º DWS. Ferroelastic 90º domains (twins) in BLSF are related to the interchange of the crystallographic *a* and *b*-axes in the *ab*-plane of the orthorhombic structure.

In BLSF materials, the grains grow in anisotropic form showing platelet morphology with the major face of the plate-like grain parallel to the *ab*-plane and perpendicular to the *c*-axis of the pseudo-tetragonal structure.[5-7,15] Thus, the spatial distribution of the polarization vector of each grain in a randomly oriented ceramic under the application of a

poling electric field is described by two angles in the semi-sphere of solid angle 2π around the direction of the electric field (*z*-axis). These angles are: θ - the angle between the major face of the platelet grain and the electric field direction, and φ - the angle between the polar vector (P_o) within the plane of the major face and the projection of the electric field vector (*z*-axis) in the same plane, as schematically illustrated in Fig. 4.33(b).

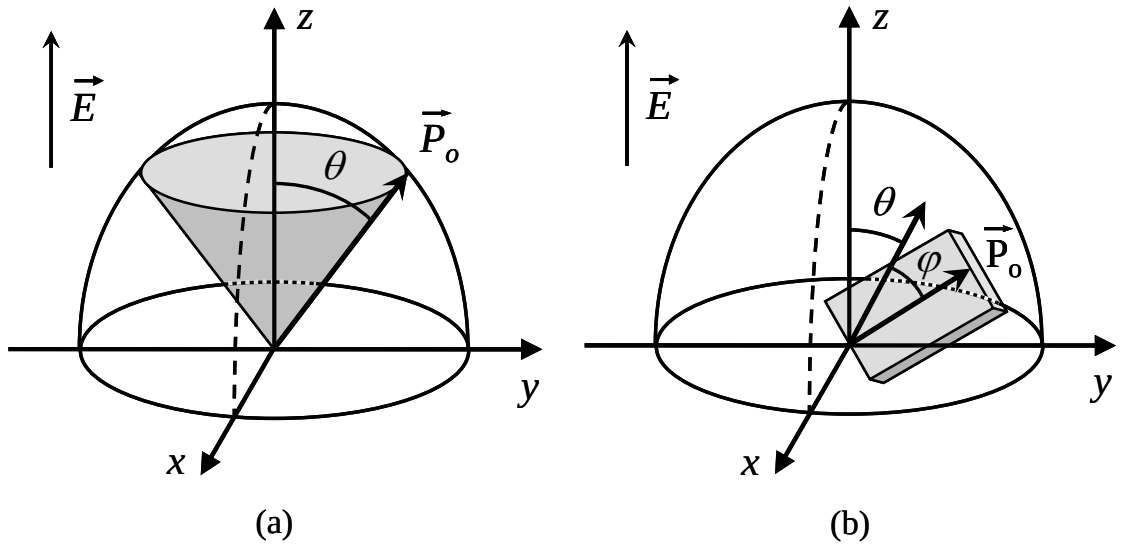

Figure 4.33 Spatial distributions of the polarization vector in ferroelectric materials with (a) uniaxial symmetry (*P* is confined to one axis and only 180º DWS is allowed), and (b) platelet grain morphology (*P* is confined to a plane allowing both 180º and 90º DWS), in the semi-sphere of solid angle 2π around the electric field direction (taken along the *z*-axis).

In this model, the polarization is considered entirely along the *a*-axis in the *ab*-plane of the structure, as is the case of SBT, although, for BLSF materials where *m* is odd (see section 1.3.2) the small component of the spontaneous polarization appearing along the *c*-axis has also to be taken into account in the calculation. Furthermore, each grain in the randomly oriented or partially textured ceramic is assumed to act independently from adjacent grains. Thus, the cooperative effect of domain switching and the elastic coupling at the grain boundary which tend to pin domain switching are neglected in the calculations as well as the mechanical strain accompanying 90º DWS which also clamps domain switching. It is also assumed in the case of both 180º and 90º DWS that the polarization vector under the application of a poling electric field will assume the orientation closest to the projection of the electric field vector in the plane of the grain major face.

Therefore, the spatial distribution of polarization for misoriented grains according to the Fig. 4.33(b) can be expressed as $P(\theta,\varphi) = P_o \cos\theta \cos\varphi$, and the net polarization along the *z*-axis is given by (considering some symmetry elements),

$$\langle P \rangle_{random} = \frac{\int_0^{\frac{\pi}{2}} \int_0^{\Phi} P_o \left(\cos\theta \sin\theta \, d\theta\right) \cos\varphi \, d\varphi}{\int_0^{\frac{\pi}{2}} \int_0^{\Phi} \sin\theta \, d\theta \, d\varphi} \tag{4.6}$$

The value of Φ in the upper limit of the integration for the φ angle depends on if only 180º DWS is considered ($\Phi = \pi/2$) or both 180º and 90º DWS are considered ($\Phi = \pi/4$). Therefore, the net polarization in a randomly oriented BLSF ceramic is,

$$\langle P \rangle_{random} = \begin{cases} \dfrac{P_o}{\pi} & (180^o \text{ DWS}) \\ \dfrac{\sqrt{2}\, P_o}{\pi} & (180^o \text{ and } 90^o \text{ DWS}) \end{cases}$$

In textured ceramics, the spontaneous polarization is enhanced by the alignment of the polar vector of each grain along a preferential direction (texture direction). To model the effect of the degree of texture in the net polarization along this preferential direction, the orientation distribution of anisometric grains must be quantified and introduced in the integration procedure. In this case, the March-Dollase (MD) function (Eq. 2.10) has been selected as a model equation to fit and quantify the measured orientation distribution of large anisometric grains, as previously described in the section 4.3.3. The MD function is a real probability distribution function which satisfied the normalization condition,

$$\int_0^{\frac{\pi}{2}} F(f_v, r, \theta) \sin\theta \, d\theta = 1 \tag{4.7}$$

Therefore, the expected polarization in textured BLSF ceramics can be theoretically modeled by introducing the MD function into the Eq. 4.6,

$$P^{Theor}(f_v, r) = \frac{\int_0^{\frac{\pi}{2}} \int_0^{\Phi} F(f_v, r, \theta)\, P_o \left(\cos\theta \sin\theta\, d\theta\right) \cos\varphi\, d\varphi}{\int_0^{\frac{\pi}{2}} \int_0^{\Phi} F(f_v, r, \theta) \sin\theta\, d\theta\, d\varphi} \tag{4.8}$$

from which is obtained,

$$P^{Theor}(f_v, r) = A \int_0^{\frac{\pi}{2}} F(f_v, r, \theta)\, P_o \cos\theta \sin\theta\, d\theta \tag{4.9}$$

where,

$$A = \begin{cases} \dfrac{2}{\pi} & (180^o \text{ DWS}) \\ \dfrac{2\sqrt{2}}{\pi} & (180^o \text{ and } 90^o \text{ DWS}) \end{cases}$$

The maximum expected polarization as a function of the experimentally determined f_v and r parameters can be predicted from the Eq. 4.9 in textured BLSF ceramics.

In fully textured BLSF materials (f_v = 1 and r = 0), even when the major faces of all platelet grains are parallel to each other, the polarization vector lies completely in the plane parallel to the major face of platelet grains, but still randomly distributed within the plane. In this case, the net polarization under the application of a poling electric field along a specific direction in the texture plane is given by,

$$\langle P \rangle_{fully\ textured} = \frac{\int_0^{\Phi} P_o \cos\varphi\, d\varphi}{\int_0^{\Phi} d\varphi} \tag{4.10}$$

where Φ in the upper limit of the integration depends on if only 180º DWS is considered ($\Phi = \pi/2$) or both 180º and 90º DWS are considered ($\Phi = \pi/4$). Therefore, the net polarization in a fully textured BLSF ceramic is,

$$\langle P\rangle_{fully\ textured} \begin{cases} \frac{2}{\pi}P_o & (180^o\ \text{DWS}) \\ \frac{2\sqrt{2}}{\pi}P_o & (180^o \text{ and } 90^o\ \text{DWS}) \end{cases}$$

4.5.2. Comparison between predicted and experimental polarization in SBT textured ceramics

Figure 4.34 shows an example of the linear dependence of the predicted values for the maximum expected polarization (P^{Theor}), considering only 180º DWS, on the volume fraction of textured material (f_v) in textured SBT ceramics having a different degree of alignment of the template grains, which is represented through the *r* parameter as described in section 4.3.3. To P_o was attributed the value of 20 μC/cm^2, which is the spontaneous polarization of the SBT single crystal as reported in section 3.2.4.

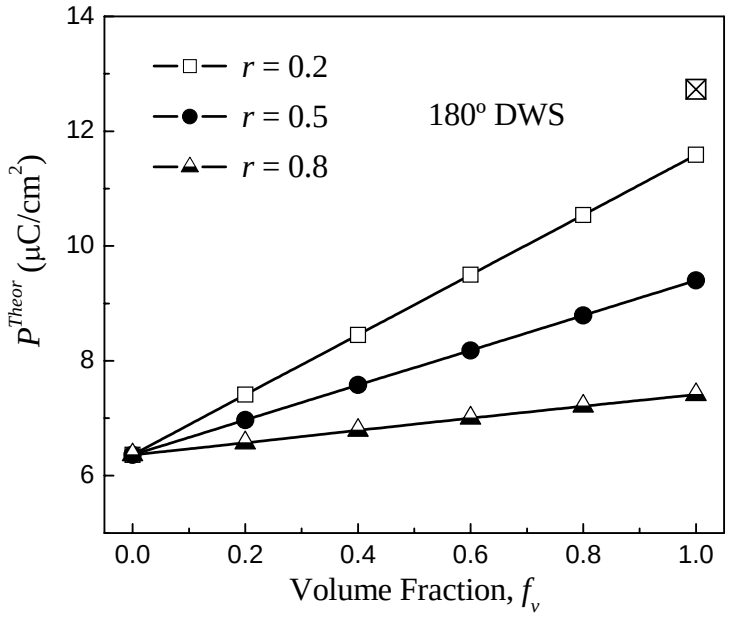

Figure 4.34 Predicted values for the maximum expected polarization, P^{Theor} (Eq. 4.9), as a function of the volume fraction of textured material (f_v) in partially textured SBT ceramics having different values of the *r* parameter (□) *r* = 0.2, (●) *r* = 0.5 and (▲) *r* = 0.8, and assuming P_o = 20 μC/cm^2 and only 180º DWS. (⊠) Predicted P^{Theor} for the fully textured SBT ceramic with only 180º DWS.

It is noteworthy that both parameters (f_v and *r*) are crucial for obtaining high values of P_S in textured ceramics, so that, not only to grow of a great amount of platelet grains

during the TGG process, but rather to induce a high alignment of the original templates during the fabrication of the green samples. The predicted maximum polarization for randomly oriented, $\langle P \rangle_{random}$ (f_v = 0 or r = 1) and fully textured, $\langle P \rangle_{fully\ textured}$ (f_v = 1 and r = 0), SBT ceramics, assuming P_o = 20 μC/cm^2, were determined to be,

$$\langle P \rangle_{random} = \begin{cases} 6.4\ \mu C/cm^2 & (180^o\ DWS) \\ 9.0\ \mu C/cm^2 & (180^o \text{ and } 90^o\ DWS) \end{cases}$$

and

$$\langle P \rangle_{\text{fully textured}} = \begin{cases} 12.7\ \mu C/cm^2 & (180^o\ DWS) \\ 18.0\ \mu C/cm^2 & (180^o \text{ and } 90^o\ DWS) \end{cases}$$

Therefore, only 90% of the P_S for SBT single crystal can be theoretically obtained in fully textured SBT ceramics (considering both 180º and 90º DWS), since the distribution of the polarization vector within the texture plane can not be inhibited during TGG.

The results predicted by the model underlying the Eq. 4.9 and the experimental P_S values obtained from P-E hysteresis loops when E⊥P (see Table 4.6) are both plotted in Fig. 4.35 as a function of the volume fraction (f_v) of textured material (see Table 4.3). The calculated data yield the maximum polarization that can be ideally obtained for a given set of f_v and r parameters if it is considered the configuration of only 180º DWS or that with both 180º and 90º DWS. P_o = 20 μC/cm^2 was used as the spontaneous polarization of each grain, the same as that reported for the SBT single crystal in section 3.2.4.

The calculated polarizations for both configurations (only 180º DWS or both 180º and 90º DWS) are considerably higher than the measured P_S, in particular for low f_v values. Several reasons may explain this result, including porosity, grain size, and mostly the poor continuity in the polarization during switching due to the randomly oriented grains, which effectively decrease the measured P_S as suggested by Duran *et al*. in $Sr_{0.53}Ba_{0.47}Nb_2O_6$ textured ceramics.[33] Randomly oriented grains effectively decrease the measured polarization at lower f_v values by interfering with the domain switching. Nevertheless, with

the increasing degree of texture, experimental P_S approaches to the predicted values, exceeding the values predicted for only 180º DWS for $f_v > 0.5$. This result suggests that there exist both contributions to the polarization, *e.g.*, 180º and 90º DWS, and that the higher degree of texture enhances the cooperative switching of ferroelectric domains in well-oriented grains with good connectivity. Further experimental results obtained for $f \sim 1$ are necessary to confirm this assumption.

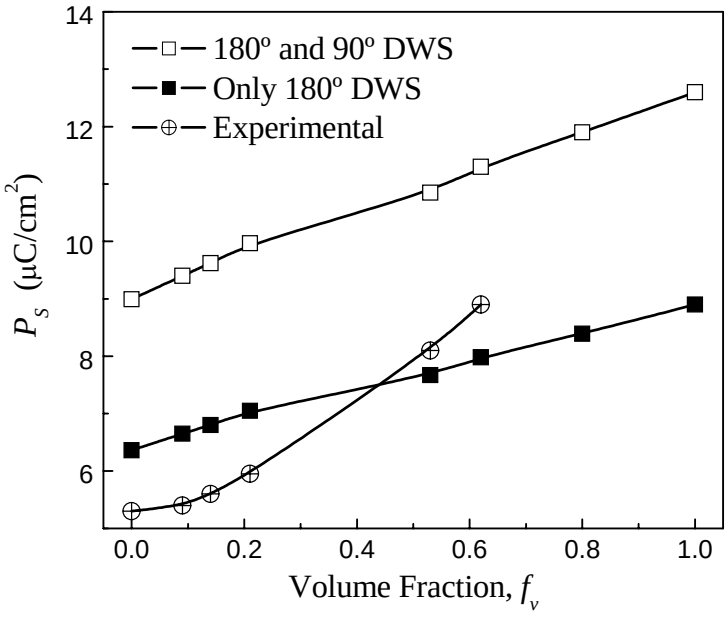

Figure 4.35 Predicted values for the maximum expected spontaneous polarization (P_S) as a function of the volume fraction of textured material (f_v) assuming (■) only 180º DWS and (□) both 180º and 90º DWS. (⊕) Experimental P_S obtained from the P-E hysteresis loops with E⊥P in the seeded SBT3Bi5T ceramics (see Table 4.6).

4.6. Summary

In summary, this chapter was dedicated to the processing and characterization of textured $SrBi_2Ta_2O_9$ ceramics with improved performances of dielectric and ferroelectric properties along a particular direction. The studies were focused on seeded SBT ceramics prepared by templated grain growth using 3 wt% of Bi_2O_3 excess as liquid phase and 5 wt% of anisometric SBT templates, as these were identified as promising conditions for TGG. The effects of the processing and sintering conditions including uniaxial pressure, the sintering temperature and time, etc., on the final density, degree of texture and microstructure evolution of both seeded and unseeded SBT ceramics were studied and

discussed. The texture development was examined by XRD and pole figure analyses, which confirmed a crystallographic texture in seeded SBT samples. Lotgering factor was determined in all cases showing an increase with the increasing sintering temperature and time, whereas the higher uniaxial pressure used for shaping the green samples resulted in ceramics with higher degree of texture.

A bimodal microstructure with a high amount of large anisometric grains was obtained after sintering the seeded SBT ceramics at 1250 ºC for 2 h. The large grains were similar in shape to the original templates but two times larger than the initial seeds. Most of the large grains with *c*-axis perpendicular to the major face were preferentially oriented with the normal to the major face within ~ 20º about the texture axis (the pressing direction). When increasing the sintering time and temperature, the template particle grow significantly faster along the length direction until the template impingement occurs while the matrix grains coarsen gradually. The volume fraction of oriented material increases from ~ 9% after 0 hours to ~ 62% after 24 hours of sintering time. The alignment of the templates particles induces alignment of the matrix grains, given rise to nucleation of new large anisometric grains that evolve from the matrix independent of the original seeds. The number of large anisometric grains per 1 cm^3 increases from 2.7×10^6 cm^{-3} for short sintering times to 1×10^7 cm^{-3} for longer sintering times. The growth of the large grains in seeded SBT textured ceramics seemed to be controlled by a mechanism of mass transport by diffusion through the liquid phase.

Anisotropy in the dielectric and ferroelectric properties of the seeded SBT specimens at room temperature as well as at the transition temperature, and its dependence on the degree of texture were demonstrated. Enhanced dielectric and ferroelectric properties were measured perpendicularly to the uniaxial pressing direction for the seeded samples sintered at 1250 ºC for 2 and 24 hours, with permittivity and polarization values exceeding those of the unseeded SBT ceramics which are roughly isotropic, not depending on the direction of the applied electric field. The ferro-paraelectric phase transition temperature decreases with increasing the sintering temperature and time in both seeded and unseeded SBT ceramics, probably due to internal stresses associated with the grain size and grain distributions. The Curie constant was determined to be ~ 5.5×10^4 ºC, in a good agreement with the results in

SBT single crystals, and the maximum P_S of 8.9 μC/cm^2 was measured with E⊥P for 24 h of sintering time, far from the value estimated for SBT single crystal ($P_S \approx 20$ μC/cm^2).

A quantitative model was presented for the prediction of the maximum P_S in both randomly oriented and textured BLSF materials, using a texture analysis accomplished via the orientation distribution of large anisometric grains. The March-Dollase equation was selected to fit the measured orientation distribution and the spatial distribution of the polarization vector in platelet grains of BLSF materials was discussed. The calculated data yield the maximum P_S that can be ideally obtained for a given set of f_v and r parameters whether 180º DWS or (180º and 90º) DWS configurations are considered. The results were applied to the case of the textured SBT ceramics, and the predicted values for P_S as a function of the degree of texture were compared with those obtained from the hysteresis loops. The experimental P_S approaches to the predicted values with the increasing degree of texture, exceeding the values predicted for 180º DWS configuration when $f_v > 0.5$.

4.7. References

[1] G. L. Messing, S. Trolier-McKinstry, E. M. Sabolsky, C. Duran, S. Kwon, B. Brahmaroutu, P. Park, H. Yilmaz, P. W. Rehrig, K. B. Eitel, E. Suvaci, M. M. Seabaugh and K. S. Oh, "Templated Grain Growth of Textured Piezoelectric Ceramics". *Crit. Rev. Solid State Mater. Sci.* **29** [2] (2004) 45-96.

[2] JCPDS-ICDD, Powder Diffraction File No. 49-0609.

[3] JCPDS-ICDD, Powder Diffraction File No. 87-0030.

[4] E. Suvaci, K.-S. Oh and G. L. Messing, "Kinetics of Template Growth in Alumina during the Process of Templated Grain Growth (TGG)". *Acta Mater.* **49** [11] (2001) 2075-2081.

[5] J. A. Horn, S. C. Zhang, U. Selvaraj, G. L. Messing and S. Trolier-McKinstry, "Templated Grain Growth of Textured Bismuth Titanate". *J. Am. Ceram. Soc.* **82** [4] (1999) 921-926.

[6] T. Takeuchi, T. Tani and Y. Saito, "Piezoelectric Properties of Bismuth Layer-Structured Ferroelectric Ceramics with a Preferred Orientation Processed by the Reactive Templated Grain Growth Method". *Jpn. J. Appl. Phys.* **38** [9B] (1999) 5553-5556.

[7] S. H. Hong, S. Trolier-McKinstry and G. L. Messing, "Dielectric and Electro mechanical Properties of Textured Niobium-Doped Bismuth Titanate Ceramics". *J. Am. Ceram. Soc.* **83** [1] (2000) 113-118.

[8] M. M. Seabaugh, I. H. Kerscht and G. L. Messing, "Texture Development by Templated Grain Growth in Liquid-Phase-Sintered Alpha-Alumina". *J. Am. Ceram. Soc.* **80** [5] (1997) 1181-1188.

[9] E. Suvaci, M. M. Seabaugh and G. L. Messing, "Reaction-Based Processing of Textured Alumina by Templated Grain Growth". *J. Eur. Ceram. Soc.* **19** [13-14] (1999) 2465-2474.

[10] E. M. Sabolsky, G. L. Messing and S. Trolier-McKinstry, "Kinetics of Templated Grain Growth of $0.65Pb(Mg_{1/3}Nb_{2/3})O_3 - 0.35PbTiO_3$". *J. Am. Ceram. Soc.* **84** [11] (2001) 2507-2513.

[11] E. Suvaci and G. L. Messing, "Critical Factors in the Templated Grain Growth of Textured Reaction-Bonded Alumina". *J. Am. Ceram. Soc.* **83** [8] (2000) 2041-2048.

[12] S.H. Hong and G. L. Messing, "Development of Textured Mullite by Templated Grain Growth". *J. Am. Ceram. Soc.* **82** [4] (1999) 867-872.

[13] M. M. Seabaugh, G. L. Messing and M. D. Vaudin, "Texture development and microstructure evolution in liquid-phase-sintered alpha-alumina ceramics prepared by templated grain growth". *J. Am. Ceram. Soc.* **83** [12] (2000) 3109-3116.

[14] H. Watanabe, T. Kimura and T. Yamaguchi, "Sintering of Plate-Like Bismuth Titanate Powder Compacts with Preferred Orientation". *J. Am. Ceram. Soc.* **74** [1] (1991) 139-147.

[15] Y. Sakuma and T. Kimura, "Mechanisms of Texture Development in Bismuth Layer-Structured Ferroelectrics Prepared by Templated Grain Growth". *J. Electroceram.* **13** [1-3](2004) 537-541.

[16] H. Sato, N. Otsuka, G. L. Liedl and S. Mansour, "Formation of Elongated Particles in Beta-SiC Compacts". *Mater. Lett.* **4** [3] (1986) 136-144.

[17] P. T. King, E. P. Gorzkowski, A. M. Scotch, D. J. Rockosi, H. M. Chan and M. P. Harmer, "Kinetics of {001} $Pb(Mg_{1/3}Nb_{2/3})O_3$ - 35 mol% $PbTiO_3$ Single Crystals Grown by Seeded Polycrystal Conversion". *J. Am. Ceram. Soc.* **86** [12] (2003) 2182-2187.

[18] M. Kitayama, K. Hirao, M. Toriyama and S. Kanzaki, "Modeling and simulation of grain growth in Si_3N_4 - I. Anisotropic Ostwald ripening". *Acta Mater.* **46** [18] (1998) 6541-6550.

[19] K. W. Lay, "Grain Growth in UO_2–Al_2O_3 in the Presence of a Liquid Phase". *J. Am. Ceram. Soc.* **51** [7] (1968) 373-376.

[20] J. L. Jones, E. B. Slamovich and K. J. Bowman, "Critical Evaluation of the Lotgering Degree of Orientation Texture Indicator". *J. Mater. Res.* **19** [11] (2004) 3414-3422.

[21] M. S. Sandlin, C. R. Peterson and K. J. Bowman, "Texture Measurement on Materials Containing Platelets using Stereology". *J. Am. Ceram. Soc.* **77** [8] (1994) 2127-2131.

[22] M. M. Seabaugh, M.D. Vaudin, J. P. Cline and G. L. Messing, "Comparison of Texture Analysis Techniques for Highly Oriented α-Al_2O_3". *J. Am. Ceram. Soc.* **83** [8] (2000) 2049-2054.

[23] W. A. Dollase, "Correction of Intensities for Preferred Orientation in Powder Diffractometry: Application of the March Model". *J. Appl. Crystallogr.* **19** [4] (1986) 267-272.

[24] Y. Shimakawa, Y. Kubo, Y. Nakagawa, T. Kamiyama, H. Asano and F. Izumi, "Crystal Structure and Ferroelectric Properties of $SrBi_2Ta_2O_9$ and $Sr_{0.8}Bi_{2.2}Ta_2O_9$". *Appl. Phys. Lett.* **74** [13] (1999) 1904-1906.

[25] Y. Noguchi, M. Miyayama and T. Kudo, "Effect of Bi Substitution at the Sr Site on the Ferroelectric Properties of Dense Strontium Bismuth Tantalate Ceramics". *J. Appl. Phys.* **88** [4] (2000) 2146-2148.

[26] G. Arlt, D. Hennings and G. Dewith, "Dielectric-Properties of Fine-Grained Barium-Titanate Ceramics". *J. Appl. Phys.* **58** [4] (1985) 1619-1625.

[27] M. H. Frey and D. A. Payne, "Grain-Size Effect on Structure and Phase Transformations for Barium Titanate". *Phys. Rev. B* **54** [5] (1996) 3158-3168.

[28] T. Hiroshima, K. Tanaka and T. Kimura, "Effects of Microstructure and Composition on the Curie Temperature of Lead Barium Niobate Solid Solutions". *J. Am. Ceram. Soc.* **79** [12] (1996) 3235-3242.

[29] V. Tura, L. Mitoseriu, C. Papusoi, T. Osaka and M. Okuyama, "Investigation of Grain-Size Influence on the Ferroelectric-to-Paraelectric Phase Transition in $BaTiO_3$ Ceramics by Means of AC Calorimetry". *Jpn. J. Appl. Phys.* **37** [4A] (1998) 1950-1954.

[30] S. K. Kim, M. Miyayama and H. Yanagida, "Electrical Anisotropy and Plausible Explanation for Dielectric Anomaly of $Bi_4Ti_3O_{12}$ Single Crystal". *Mater. Res. Bull.* **31** [1] (1996) 121-131.

[31] H. Irie, M. Miyayama and T. Kudo, "Electrical Properties of a Bismuth Layer-Structured $Ba_2Bi_4Ti_5O_{18}$ Single Crystal". *J. Am. Ceram. Soc.* **83** [11] (2000) 2699-2704.

[32] A. D. Rae, J. G. Thompson and R. L. Withers, "Structure Refinement of Commensurately Modulated Bismuth Strontium Tantalate, $Bi_2SrTa_2O_9$". *Acta Crystallogr., Sect. B: Struct. Sci.* **48** [4] (1992) 418-428.

[33] C. Duran, S. Trolier-McKinstry and G. L. Messing, "Dielectric and Piezoelectric Properties of Textured $Sr_{0.53}Ba_{0.47}Nb_2O_6$ Ceramics Prepared by Templated Grain Growth". *J. Mater. Res.* **18** [1] (2003) 228-238.

[34] T. Takenaka and K. Sakata, "Grain-Orientation and Electrical-Properties of Hot-Forged $Bi_4Ti_3O_{12}$ Ceramics". *Jpn. J. Appl. Phys.* **19** [1] (1980) 31-39.

General Conclusions and Future Work

The knowledge of $SrBi_2Ta_2O_9$ and $SrBi_2Nb_2O_9$ intrinsic properties, including the anisotropy of the dielectric, ferroelectric and piezoelectric properties, domain structure and phase transitions, are important prerequisite for the understanding of the distinct effects observed to date in SBT and SBN thin films. As referred above, this has motivated an important part of this thesis work focused on the growth and properties study of SBT and SBN single crystals. Moreover, stressed by the current interest in developing lead-free piezoelectric materials for high-temperature applications, this work also explored the use of the grown crystals for producing textured SBT ceramics, thereby allowing to understand the texture - property relationships in this material. As a result, the main conclusions of this thesis work may be summarized as follows:

5.1. $SrBi_2Ta_2O_9$ and $SrBi_2Nb_2O_9$ Single Crystals

- High-quality SBT and SBN plate-like single crystals were successfully grown by high-temperature self-flux solution method, allowing the study of their intrinsic properties which are required for applications in various microelectronic devices. The same optimized thermal profile was successful for growing large single crystals of both compositions, with the sizes of ~ $7 \times 5 \times 0.2$ and $5 \times 5 \times 0.4$ mm^3 for SBT and SBN, respectively, though the greater thickness of SBN crystals accounts for some difference in the various parameters ruling the crystal growth of both systems. The narrow sides of the platelet crystals were oriented along the [110] and $[1\bar{1}0]$ directions of the orthorhombic structure with the [001] direction (*c*-axis) lying perpendicular to the major face.

- Piezoelectric force microscopy allowed the observation of coexisting 90º and 180º domain walls in SBT single crystals, which form a well-defined "herringbone" structure with mostly flat 90º walls. These flat 90º walls oriented parallel to the ⟨110⟩-direction, which were not observed to date in ceramics and thin films, were explained by considering the energy associated to elastic fields of very long range produced by the wall bending. The formation of such complex domain structure in SBT crystals, which was attributed to the presence of separate ferroelastic and ferroelectric phase transitions in SBT, may have a significant impact on the physical properties of this system.

- The high-quality of the grown SBT and SBN single crystals was also confirmed by dielectric, ferroelectric and piezoelectric measurements, demonstrating a large anisotropy in the intrinsic properties of both crystals. The maximum permittivity measured in the *ab*-plane was an order of magnitude greater than that along *c*-axis, and significantly exceeded that of bulk ceramics in both cases. The displacive-type ferro-paraelectric phase transition of SBT and SBN systems seemed to be intermediate between the 1st- and the 2nd-order.

- The saturated hysteresis loop obtained along the [110] direction and the linear P-E behavior revealed along the [001] direction in SBT crystals confirms that the spontaneous polarization vector lies entirely in the *ab*-plane of the SBT structure. P_S was estimated as $\approx$ 20 $\mu C/cm^2$ along the polar *a*-axis in SBT. Though saturated hysteresis loops were not reached for a maximum applied electric field of 100 kV/cm in SBN crystals, their ferroelectric anisotropy was demonstrated, too.

- Piezoelectric coefficients d_{33} exceeding those reported for ceramics and thin films have been measured along the [100] direction (polar-axis) of both crystals ($d_{33} \approx$ 30 and 62 pm/V for SBT and SBN, respectively). The measured d_{33} is believed to be smaller than the real value corresponding to the crystal free of any stress and constrain due to the sample holder. A correction factor that relates the real d_{33} value to the measured one could not be determined due to the complex configuration of the crystal embedded in araldite.

5.2. Textured $SrBi_2Ta_2O_9$ Ceramics

- Textured SBT ceramics were prepared by templated grain growth using anisometric SBT templates. The orientation of the original templates in the green pressed samples was seen to be enhanced when increasing the uniaxial pressure, thereby improving the degree of texture of the sintered ceramics. Seeded SBT specimens with 3 wt% of Bi_2O_3 excess as liquid phase former and 5 wt% of templates revealed the highest degree of texture with improved performance of the dielectric and ferroelectric behavior.

- The crucial role of the liquid phase and of the templates in the TGG process was demonstrated in the microstructure of the seeded specimens: whereas a large amount of anisometric grains having a similar platelet shape but with the size twice as that of the

starting templates was developed in the seeded samples having liquid phase, a negligible template boundary migration occurred in the absence of Bi_2O_3 excess. Moreover, the presence of aligned templates induced the alignment of the small matrix grains and created proper conditions for the nucleation of new large anisometric grains within the matrix, displaying platelet morphology with similar alignment as the original templates. The lateral growth of these large anisometric grains is therefore preferred to maximize the area of the faces perpendicular to the *c*-axis, which appear to be those with low surface energy, until the template impingement occurs. The mechanism of templated grain growth in the seeded SBT ceramics seemed to be controlled by the diffusion through the liquid phase.

- Anisotropy in the dielectric and ferroelectric properties was demonstrated in the seeded SBT samples with enhanced properties measured perpendicularly to the uniaxial pressing direction, due to the greater contribution from the highly polarizable *ab*-plane of large anisometric grains with their major faces parallel to the applied electric field. In this case, the permittivity and spontaneous polarization values exceed those of the unseeded SBT ceramics which are roughly isotropic and do not depend on the applied electric field direction. The observed downwards shift of the transition temperature with the increasing sintering temperature and time was ascribed to different degree of internal stresses, which probably develop during the TGG process and become stored in the impinged large grains, though compositional fluctuations and bismuth losses for long sintering times and at high sintering temperature may also contribute to this shift.

- The maximum spontaneous polarization that can be ideally obtained in randomly oriented or in partially textured SBT ceramics was predicted by a quantitative model which takes into account the configuration of only 180º domain wall switching (DWS) or that corresponding to both 180º and 90º DWS. In the present case of textured SBT ceramics, the experimental P_S measured from the hysteresis loop approaches the values predicted by the model when increasing the degree of texture, and exceeds the predicted values when the volume fraction of textured material is above 0.5, if only the 180º DWS is considered. Both contributions to the polarization, *e.g.*, 180º and 90º DWS, are thus suggested to take place in the textured SBT ceramics. Moreover, this model can be applied to other BLSF materials for predicting the maximum expected P_S as a function of the degree of texture in ceramics and thin films.

5.3. Future Work

The results obtained in this thesis work emerged from a systematic examination of the intrinsic properties of SBT and SBN single crystals, as well as from the study of the texture - property relationships in textured SBT ceramics. However, further studies regarding these two subjects are required to answer some unsolved questions in this work. Accordingly, the future work should be focused in the following issues.

SBT and SBN Single Crystals

- The growth morphology of the obtained SBT and SBN single-crystals was compared, and several factors related to the crystal growth were suggested as possible reasons accounting for the observed difference in the growth rates along the [001]-direction (*c*-axis). However, a deeper understanding of the growth mechanism requires a detailed study of the growth conditions such as: flux viscosity, supersaturation, solute diffusion, etc. Such study is generally expected to benefit the knowledge on crystal growth in the BLSF family and, particularly, to allow the growth of thicker SBT crystals.

- The obtained complex domain pattern in SBT crystals was attributed to separate ferroelastic and ferroelectric phase transitions in SBT. It is believed that different thermal treatments of the grown crystals may clarify the relation between the observed twinned domain structure and the ferroelastic phase above T_C observed in SBT, *i.e.*, using a very slow cooling through the ferro-paraelastic transition, as well as a quenching from ~ 750 ºC down to room temperature. In addition, the domain structure of the SBN crystals should be investigated in detail by piezoelectric force microscopy to reveal the unknown domain pattern of this ferroelectric crystal.

- The experimental setup used for piezoelectric characterization must be improved for allowing measurements in stress-free crystals and for obtaining d_{33} as well as d_{31} and d_{15} piezoelectric coefficients, which are very important for the complete study of the piezoelectric properties. Moreover, many other fundamental properties of SBT and SBN systems should be exploited by characterizing the grown crystals like electromechanical, elastic and electro-optical coefficients.

SBT Textured Ceramics

- Although textured SBT ceramics were successfully obtained by TGG, the degree of texture evaluated via the Lotgering factor shows values lower than those typically reported for fully textured ceramics produced by other more elaborated texturing techniques like tape casting and extrusion. Therefore, such texturing techniques must be introduced in the TGG process of SBT ceramics for enhancing the degree of texture, thus improving the dielectric and ferroelectric properties.

- Transmission electron microscopy (TEM) studies may be performed to confirm the crystallographic orientation of the large anisometric grain with *c*-axis perpendicular to the major face, and to determine the thickness and composition of the liquid layer at the interface between templates and matrix grains, which would help to achieve a greater understanding of the mechanism for the growth of the large anisotropic grains.

- The model presented for the prediction of the maximum P_S in randomly oriented and textured BLSF materials must be improved in the case where *m* is odd, by considering the small component of the P_S appearing along the *c*-axis in the calculation.

List of Publications of the Thesis

1. **H. Amorín**, M. E. V. Costa, A. L. Kholkin and J. L. Baptista, "Electrical Properties of $SrBi_2Ta_2O_9$ Single Crystals Grown by Self-Flux Solution". *J. Eur. Ceram. Soc.* **24** [6] (2004) 1535-1539.
2. **H. Amorín**, M. E. V. Costa and A. L. Kholkin, "Microstructure and Electrical Properties of $SrBi_2Ta_2O_9$ Ceramics Processed by Templated Grain Growth". *Mater. Sci. Forum* **455-456** (2004) 35-39.
3. **H. Amorín**, V. V. Shvartsman, G. Trolliard, M. Manier, J.-P. Mercurio, A. L. Kholkin and M. E. V. Costa, "Investigation of Domain Structure of $SrBi_2Ta_2O_9$ Single Crystals via Polarized Optical and Piezoelectric Force Microscopy". *Integr. Ferroelectr.* **62** (2004) 215-220.
4. **H. Amorín**, V. V. Shvartsman, A. L. Kholkin and M. E. V. Costa "Ferroelectric and Dielectric Anisotropy in High-Quality $SrBi_2Ta_2O_9$ Single Crystals". *Appl. Phys. Lett.* **85** [23] (2004) 5667-5669.
5. **H. Amorín**, I. K. Bdikin, V. V. Shvartsman, M. E. V. Costa and A. L. Kholkin, "X-ray Characterization and Domain Structure of High-Quality $SrBi_2Ta_2O_9$ Single-Crystals Grown by Self-Flux Solution Method". *Integr. Ferroelectr.* **68** (2004) 259-268.
6. **H. Amorín**, A. L. Kholkin and M. E. V. Costa, "Texture Development and Dielectric Properties of $SrBi_2Ta_2O_9$ Ceramics Processed by Templated Grain Growth". *J. Eur. Ceram. Soc.* **25** [12] (2005) 2453-2456.
7. **H. Amorín**, R. S. Martins, A. L. Kholkin and M. E. V. Costa, "Structural and Electrical Characterization of Ferroelectric $SrBi_2Nb_2O_9$ Single Crystals Grown by High-Temperature Self-Flux Solution". *Ferroelectrics* **320** (2005) 43-50.
8. **H. Amorín**, V. V. Shvartsman, I. K. Bdikin, M. E. V. Costa, A. L. Kholkin and N. A. Pertsev, "Ferroelectric Domains and Twinning in High-Quality $SrBi_2Ta_2O_9$ Single Crystals". *Appl. Phys. Lett.* (2006) In Press.
9. **H. Amorín**, A. L. Kholkin and M. E. V. Costa, "Texture - Property Relationships in Bi-Layered Ferroelectric Ceramics: A Case Study of $SrBi_2Ta_2O_9$". *Mater. Sci. Forum* (2005) In Press.
10. **H. Amorín**, I. K. Bdikin, A. L. Kholkin and M. E. V. Costa, "Growth and Characterization of Ferroelectric $SrBi_2Ta_2O_9$ Single Crystals via High Temperature Self-Flux Solution Method". *Phys. Solid State* (2006) In Press.